Summer 8-2022

Manufacturing and Characterization of Continuous Nanofiber-Reinforced Composites

Lucas Barry
University of Nebraska-Lincoln, lucas.barry@huskers.unl.edu

MANUFACTURING AND CHARACTERIZATION OF CONTINUOUS NANOFIBER-REINFORCED COMPOSITES

by

Lucas Patrick Barry

A DISSERTATION

Presented to the Faculty of

The Graduate College at the University of Nebraska

In Partial Fulfillment of Requirements

For the Degree of Doctor of Philosophy

Major: Mechanical Engineering and Applied Mechanics

Under the Supervision of Professor Yuris A. Dzenis

Lincoln, Nebraska

August 2022

MANUFACTURING AND CHARACTERIZATION OF CONTINUOUS NANOFIBER-REINFORCED COMPOSITES

Lucas Barry, Ph.D.

University of Nebraska, 2022

Advisor: Yuris Dzenis

Fiber-reinforced composite laminates are some of the most advanced structural materials available. However, delamination remains a critical challenge due to its prevalence in structures and ability to cause catastrophic failure. Recently, high-temperature composites are at the forefront of polymer-matrix composites research, but they are prone to microcracking followed by delamination. Nanoreinforcement of interfaces by continuous nanofibers has been proposed earlier at UNL and produced increased interlaminar fracture resistance in conventional advanced composites. However, no studies have yet been conducted on emerging high-temperature composites. Also, there is insufficient information on the translatability of observed modes I and II interlaminar fracture toughness improvements to the structural performance level. The main objectives of this dissertation were to explore feasibility of nanofiber-based delamination suppression in high-temperature laminates and to study translation of delamination suppression via nanofiber-interleaving to the performance of composite structural volumes.

Unidirectional carbon/epoxy and carbon/cyanate ester composites were reinforced with continuous nanofiber interleaves electrospun from polyacrylonitrile or polyimide, and their fracture mechanics performance was characterized and compared. Significant improvements in modes I and II fracture resistance were demonstrated with the high-temperature material for the first time. The improvements in material properties were also

translated to the structural performance of laminates with and without holes and L-shaped composites. Nanofiber-reinforced specimens continued to perform better than pristine specimens, and the high-temperature material showed greater improvements.

To mimic the controlled anisotropy and high fiber volume fraction of traditional advanced laminates, laminated nanocomposites reinforced with aligned, continuous nanofibers were fabricated and characterized. Results prove the feasibility of manufacturing nanolaminates with distinct oriented plies, high nanofiber volume fractions, and improved properties.

Lastly, feasibility of nanofiber structure tailoring with graphene nanoribbons and MXenes was explored. It was shown that incorporation of MXene nanoparticles can lead to significant improvements in the graphitic structure of the templated carbon nanofibers.

Overall, this dissertation provides novel results on continuous nanofiber-reinforcement of high-temperature composites and advanced composite structures. The knowledge gained will contribute to the extension of electrospun nanofibers from the laboratory to industrial applications.

“Everyone you will ever meet knows something you don’t.”

Bill Nye

ACKNOWLEDGEMENTS

The completion of this degree would not have been possible without the help of several important people in my life. Firstly, I want to express my tremendous gratitude to my advisor Dr. Yuris Dzenis, who has provided guidance and motivation throughout this long process. I also want to thank my other advisory committee members: Dr. Jeffrey Shield, Dr. Ruqiang Feng, and Dr. Srivatsan Kidambi. They were very flexible and supportive of my process. I also learned a great deal from the other professors who taught my classes. In addition, I would like to extend a special thank you to Dr. Alexander Sinitskii and his group for supplying the GNRs and MXenes. Lastly, the Department of Mechanical & Materials Engineering and the College of Engineering as a whole provided me with an exceptional opportunity to obtain a valuable degree in a field that I am passionate about. For that, I will be forever grateful.

Along with my professors, my lab mates have taught me more than they know, and they each have done something, no matter how small it may seem, that helped me progress with my research. To Taylor Stockdale, Dimitry Papkov, Iakov Golman, Abdelrahman Elsayed, Iurii Zubkov, Preston Noll, Emmanuel Mensah, Mikhail Kartashov, Justin Busnot, and Sabrina Leseul, thank you. I would also like to recognize Pacific Engineering, Inc, who invested their time and money in me so I could gain invaluable knowledge and experience. My gratitude must also be extended to the Air Force Office of Scientific Research for their partial funding support.

Lastly, I cannot forget my family and friends. I have received constant support from many friends during my time in both graduate and undergraduate school. To my parents and sister, thank you for your endless love and always believing in me. You three played the largest role in shaping who I am today. Most importantly, I want to

acknowledge my wonderful wife. These last four years have been a journey, and you have provided unending support throughout all the ups and downs. You have loved me unequivocally, and I look forward to our life to come, especially as we begin to build a family together. I am eternally thankful to have you in my life.

TABLE OF CONTENTS

CHAPTER 1. INTRODUCTION 1
1.1 Advanced Composite Materials 1
1.1.1 Historical Remarks 1
1.1.2 Classification of Fiber-Reinforced Composites 4
1.1.3 Manufacturing of Continuous Fiber-Reinforced Composites 5
1.1.4 Applications of Fiber-Reinforced Polymer Matrix Composites 8
1.2 High-Performance Polymer Matrix Composites 10
1.2.1 Reinforcing Fibers 10
1.2.2 Polymer Resins 13
1.2.3 Recent Developments in High-Temperature Resins and Composites 17
1.2.4 Failure in Advanced Laminated Composites 19
1.3 Nanotechnology and Composites 21
1.4 Continuous Nanofibers 23
1.5 Nanofiber-Reinforcement of Interfaces in Advanced Composite Laminates 28
1.6 Summary and Overall Goals of the Dissertation 30
1.7 Organization of the Dissertation 31
CHAPTER 2. CONTINUOUS NANOFIBER REINFORCEMENT OF LAMINATED COMPOSITE STRUCTURES FOR HIGH-TEMPERATURE APPLICATIONS: REVIEW AND TECHNICAL PROBLEM IDENTIFICATION 34
2.1 Advantages of Laminated Composites 35
2.2 Mechanics of Laminated Composites 37
2.3 Mechanisms of Delamination 42
2.4 Delamination Suppression Methods 46
2.4.1 Laminate Design 46
2.4.2 Edge Design 47
2.4.3 Interleaving 48
2.4.4 Matrix Toughening 49
2.5 Continuous Nanofiber Reinforcement of Interfaces 51
2.6 High-Temperature Composites 54
2.7 Microcracking and Delamination in High-Temperature composites 57
2.8 Toughening of High-Temperature Resins 60
2.9 High-Temperature Nanofibers 62
2.10 Structural Sources of Delamination 67
2.11 Testing Methods for Composite Structures 69
2.12 Summary and Technical Problem Formulation 71

CHAPTER 3. INTERLAMINAR FRACTURE TOUGHNESS TESTING OF ELECTROSPUN NANOFIBER-REINFORCED COMPOSITES 74
3.1 Experimental Methods 75
3.1.1 Composite Materials and Manufacturing 75
3.1.2 Nanofiber Materials and Electrospinning Process 79
3.1.3 Specimen Preparation and Interlaminar Fracture Toughness Testing 81
3.2 Mode I Interlaminar Fracture Toughness Testing Results 84
3.2.1 Mode I Interlaminar Fracture Toughness Data Analysis 86
3.2.2 Discussion of Mode I Interlaminar Fracture Toughness Testing Results 90
3.3 Mode II Interlaminar Fracture Toughness Testing Results 111
3.3.1 Mode II Interlaminar Fracture Toughness Data Analysis 112
3.3.2 Discussion of Mode II Interlaminar Fracture Toughness Testing Results 114
3.4 Summary of Interlaminar Fracture Toughness Testing Results 123
3.5 Conclusions 126
CHAPTER 4. NANOFIBER REINFORCEMENT OF COMPOSITE STRUCTURES 128
4.1 Experimental Methods 129
4.1.1 Materials 129
4.1.2 Electrospinning Parameters 130
4.1.3 Laminate Specimen Manufacturing and Testing 131
4.1.4 Open-Hole Tension Specimen Manufacturing and Testing 132
4.1.5 L-bend Specimen Manufacturing and Testing 133
4.1.6 X-Ray Computed Tomography 136
4.1.7 DMA Testing 136
4.1.8 List of Materials and Structures Tested 138
4.2 Results of multidirectional Laminate Testing 139
4.2.1 Discussion of Laminate Tensile Testing Results 141
4.3 Open-Hole Tensile Testing Results 150
4.3.1 Discussion of Open-Hole Tensile Testing Results 152
4.4 Results of L-bend Testing 167
4.4.1 L-bend Data Analysis 169
4.4.2 Discussion of L-bend Testing Results 174
4.5 DMTA Testing and Discussion of Results 183
4.6 Conclusions 188
CHAPTER 5. ELECTROSPINNING OF ALIGNED NANOFIBER CONFIGURATIONS FOR LAMINATED NANOCOMPOSITES 191
5.1 Review and Identication of Technical Problem 191
5.1.1 Polymer Matrix Nanocomposites 191
5.1.2 Bulk Nanofiber-Reinforced Composites 192

5.1.3 Aligned Nanofiber-Reinforced Composites 195
5.1.4 Summary and Problem Formulation 197
5.2 Experimental Methods 198
5.2.1 Materials 198
5.2.2 Electrospinning 199
5.2.3 Orientation and Diameter Analysis 203
5.2.4 Nanocomposite Manufacturing 204
5.2.5 Specimen Preparation and Testing 204
5.2.6 High-Speed Video Observation 208
5.3 Results of the Nanofiber Alignment Investigation 209
5.4 Analysis of the CNF/Epoxy Nanocomposite Fabrication and Mechanical Characterization 217
5.4.1 Discussion 222
5.5 Analysis of the Cyanate Ester Matrix Nanocomposite Fabrication and Mechanical Characterization 227
5.5.1 Discussion 229
5.6 High-Speed Video Observation of Jet Instabilities and Nanofiber Deposition 237
5.7 Conclusions 238
CHAPTER 6. SUMMARY AND FUTURE WORK 242
6.1 Conclusions 242
6.1.1 Continuous Nanofiber-Reinforcement of High-Temperature Composite Laminates 242
6.1.2 Translation of Material Improvements via Nanofiber-Reinforcement to Composite Structures 244
6.1.3 Nanofiber Alignment and Developed Laminated Nanocomposites Reinforced with Continuous Nanofibers 245
6.1.4 Templated Carbon Nanofibers with Nanomaterials to Improve Graphitic Structure 246
6.2 Future Directions 248
6.2.1 Continuous Nanofiber-Reinforced Composite Structures 248
6.2.2 Electrospinning Aligned Nanofibers for Laminated Nanocomposites 249
6.2.3 Templated Carbon Nanofibers 249
REFERENCES 251
APPENDIX A – DATA FROM INTERLAMINAR FRACTURE TOUGHNESS TESTING 296
APPENDIX B – NANOCOMPOSITE MANUFACTURING 298
B.1. DETERMINATION OF FIBER VOLUME FRACTION 301
APPENDIX C – TABULATED RESULTS OF THE NANOFIBER ALIGNMENT INVESTIGATION 303
APPENDIX D – CONTINUOUS NANOFIBERS TEMPLATED WITH CARBON-BASED NANOMATERIALS 305
D.1. METHODS OF IMPROVING STRUCTURE AND MECHANICAL PROPERTIES OF NANOFIBERS 305

D.1.1. Post-Processing Treatment....305
D.1.2. Adding Nanoreinforcement....307
D.1.3. Adding Templating Agent....308
D.1.4. Summary and Problem Formulation....309
D.2. EXPERIMENTAL METHODS....311
D.2.1. Materials....311
D.2.2. Electrospinning....313
D.2.3. Stabilization and Carbonization....313
D.2.4. Raman Spectroscopy....314
D.3. RESULTS....315
D.3.1. Graphene Nanoribbons Results....315
D.3.2. MXenes Results....322
D.4. CONCLUSIONS....326

LIST OF FIGURES

Figure 1.1: Specific strength versus specific stiffness of some isotropic materials and various advanced composite materials. B represents boron fiber. For composites, 0 represents aligned fibers, 1 represents fibers in the following arrangement: 50% at 0°, 40% at ±45°, and 10% at 90°, 2 represents a balanced laminate with equal layers of fibers at 0°, ±45°, and 90°.[7] 3
Figure 1.2: Typical types of fiber reinforcement.[1] 4
Figure 1.3: (a) Influence of reinforcement type and quantity on composite performance.[1] (b) Tensile properties of fiber, matrix, and unidirectional, continuous fiber-reinforced composite.[8] 5
Figure 1.4: (a) Unidirectional continuous fiber lamina. (b) Effect of fiber and matrix on mechanical properties. (c) Unidirectional and quasi-isotropic lay-ups.[8] 7
Figure 1.5: (a) Volkswagen xl1 carbon fiber body parts.[5] (b) Boeing 787 Dreamliner commercial airplane.[1] 8
Figure 1.6: Global composites market share in 2020, separated by end use.[12] 9
Figure 1.7: U.S. advanced composites market size, separated by product type.[12] 10
Figure 1.8: Specific strength and modulus of some commercially important fibers.[1] 11
Figure 1.9: Applications of polymer matrix carbon fiber composites.[14] 13
Figure 1.10: Transverse microcrack in a laminated composite developed after thermal and mechanical cycling. The material is carbon fiber-reinforced bismaleimide.[23] 19
Figure 1.11: Graphene sheet being rolled into a carbon nanotube.[39] 22
Figure 1.12: Typical electrospinning process. 24
Figure 1.13: (A) Comparison of a commercial carbon fiber and an electrospun nanofiber. Comparison of (B) vapor-grown commercial carbon nanofibers and (C) electrospun carbon nanofibers showing much better uniformity and purity. (D and E) Highly aligned unidirectional and orthogonal continuous nanofibers produced with the gap method. (F) Cross section view of a nanocrystalline zirconia nanofiber with applications in ultra-tough ceramics.[52] 25
Figure 1.14: Specific energy to failure versus specific true strength for some commercial fibers and materials. Diamonds represent as-spun polyacrylonitrile (PAN) nanofibers. The arrow density indicates approximate nanofiber diameters (see scale bar). The colored area represents the strength/toughness region occupied by traditional materials.[58] 27
Figure 1.15: Concept of interleaving nanofibrous veils in between the primary reinforcing layers, resulting in a nanofiber-enhanced composite laminate with tough interlayers.[64] 29
Figure 2.1: Stresses on a 3D element.[71] 38
Figure 2.2: (a) Difference between an isotropic and an orthotropic plate. (b) Definition of the material (1-2) and x-y coordinate systems.[72] 39
Figure 2.3: Physical significance of the anisotropic stress-strain relations.[71] 42
Figure 2.4: The three different modes of fracture that are distinguished according to the direction of the applied load with respect to the crack plane.[73] 43
Figure 2.5: The free edge effects in a cross-ply $[0°/90°]_S$ laminate under uniaxial tension. *Note that the x_1, x_2, and x_3 axes are equivalent to the x, y, and z axes.[34] 44
Figure 2.6: The free edge effects in an angle-ply $[\pm 45°]_S$ laminate under uniaxial tension. *Note that the x_1, x_2, and x_3 axes are equivalent to the x, y, and z axes.[34] 45
Figure 2.7: Free-edge delamination suppression concepts.[3] 47
Figure 2.8: (a) Schematic of interleaving in a cross-ply laminate.[78] (b) Interleaving suppresses delamination development at the lamina interface.[80] 49
Figure 2.9: (left) Advanced laminated composite with nanofiber-reinforced interfacial layer. (right) In situ observation of interlaminar toughening nanomechanisms including Velcro-like crack bridging by nanofibers.[41] 53
Figure 2.10: Crack density compared with accelerated thermal cycles for graphite fabric/PMR-25 polyimide laminates.[11] 58

Figure 2.11: Microscopic damage in a G40-800/5260 carbon fiber/bismaleimide $[\pm 45/90]_S$ laminate (ε=1.6%).[95] 59
Figure 2.12: Illustration of two-step method for synthesizing polyimides and chemical structures of some commonly used diamines and dianhydrides.[105] 65
Figure 2.13: Features prone to delamination owing to direct through thickness loading: (a) lug fitting and (b) rib-to-skin joint.[33] 68
Figure 2.14: Features prone to delamination owing to geometry: (a) taper and (b) curved section in bending.[33] 68
Figure 2.15: Features prone to delamination owing to discontinuities: (a) ply drop and (b) free edge.[33] 69
Figure 2.16: (a) Sources of delamination.[45] (b) Measured delamination in an L-shaped laminate specimen.[115] (c) SEM micrographs of through-thickness bearing damage showing noticeable delamination.[116] 69
Figure 3.1: (left) Schematic assembly of the two-chamber press-clave for composite curing.[136] (right) Carver, Inc. model 2699 press-clave without the assembly inserted. 77
Figure 3.2: (left) MTS 810 servo-hydraulic load frame with an Instron 8800 controller. (right) Instron 5966 screw-driven load frame. 78
Figure 3.3: Process of electrospinning directly onto prepreg plies before curing. (a) Electrospinning setup. (b) Prepreg ply covered with nanofibers. (c) SEM image of electrospun NFs. (d) resin impregnation of the NF mat, which shows how the resin naturally wetted the NF mats after being left at room temperature for several weeks. 80
Figure 3.4: Typical dimensions, layup, and geometry for the DCB specimens.[32] 82
Figure 3.5: Typical dimensions, layup, and geometry for the ENF specimens.[32] 83
Figure 3.6: Representative curves for the DCB results of the carbon/epoxy materials. 85
Figure 3.7: Representative curves for the DCB results on the carbon/CE materials. 85
Figure 3.8: Example (left) and measured (right) plot of the crack length vs. the 1/3 power of the compliance. The measured plot came from the DCB data on the RS3C-PI12-1 specimen. 88
Figure 3.9: Mode I interlaminar crack resistance curves. 89
Figure 3.10: Mode I strain energy release rates. 89
Figure 3.11: Mode I critical stress intensity factors. 90
Figure 3.12: SEM images showing the wettability of (a) PAN NFs with epoxy, (b) PI NFs with epoxy, (c) PAN NFs with epoxy, and (d) PI NFs with CE resin. The black dots in (c) are the particulate modifiers that were added by the manufacturer to increase the toughness of the CE resin. (e) cross-section of a DCB PMTF3-PAN1 specimen. The red arrows indicate the NF-reinforced interlayer while the blue arrows indicate the pristine interlaminar regions. (f) cross-section of a DCB pristine PMTF3 specimen. (g) cross-section of a DCB PMTF3-PI10 specimen. In (f) and (g), the double-sided arrows represent the approximate thickness of the interlaminar region at the midplane. 92
Figure 3.13: (a and b) SEM micrographs of the RS3C-PI12 DCB specimen cross-section. Mode I crack propagation would have occurred into the page. (c and d) Cross-sections of pristine (c) PMTF3 and (d) RS3C DCB specimens. Crack propagation would have occurred from left to right. All double-sided arrows represent the thickness of the interlaminar region at the midplane. 93
Figure 3.14: Carbon/epoxy mode I crack propagation. 94
Figure 3.15: Carbon/CE mode I crack propagation. 95
Figure 3.16: SEM micrographs of the mode I interlaminar fracture surface of carbon/epoxy pristine and PAN1 specimens. The crack propagation followed the direction of the arrows. 96
Figure 3.17: SEM micrographs of the mode I interlaminar fracture surfaces of carbon/CE pristine and PI12 specimens. 96
Figure 3.18: SEM micrographs of the mode I interlaminar fracture surface of a RS-3C-PI12 specimen. 97
Figure 3.19: SEM images showing the mode I interlaminar crack paths and fracture surfaces of carbon/epoxy specimens. Crack propagation occurred from left to right. 98
Figure 3.20: SEM micrographs of the mode I interlaminar fracture surface for a PMTF3-PAN1 specimen. 100
Figure 3.21: Carbon/epoxy DCB fracture surfaces. Crack propagation occurred from left to right. 101

Figure 3.22: Carbon/CE mode I interlaminar fracture surfaces. Crack propagation occurred from left to right. The arrows indicate striping patterns due to alternating stable and unstable crack growth. A matrix dominated failure zone is outlined in the PI12 specimen. 102
Figure 3.23: Cross-section of a PMTF3-PAN1 DCB specimen. The double-sided arrow represents the thickness of the NF-reinforced interlaminar region. The red dashed arrows in (b) represent potential crack paths that would lead to carbon fiber bridging. 104
Figure 3.24: Unstable mode I crack propagation in a pristine carbon/epoxy specimen. 104
Figure 3.25: Mode I interlaminar fracture surface of (a) pristine and (b & c) PAN1 carbon/epoxy specimens. Crack propagation occurred from left to right. 105
Figure 3.26: Mode I interlaminar fracture surface of (a) pristine and (b & c) PI12 carbon/CE specimens. Crack propagation occurred from left to right. 106
Figure 3.27: Cured carbon/CE ply surfaces covered partially by PI NFs. The plies were cured in an oven without any added pressure. 107
Figure 3.28: SEM micrographs of the (a & b) PMTF3-PAN1 and (c & d) RS3C-PI12 NF mats. (e) schematic of mode I crack growth through the NF-reinforced interlaminar region.[91] (f) DCB experimental setup. 108
Figure 3.29: (a) PAN cyclization reaction.[157] (b) Heating of PAN-co-PS fibers in isothermal conditions at 190°C in air.[157] 109
Figure 3.30: A PAN nanofiber mat (a) before and (b) after baking in oven at 350°F for 2 hours and being fractured in tension by hand. 110
Figure 3.31: Section of a PI NF mat (a) before and (b) after baking in an oven at 350°F for 2 hours between two glass plates. 111
Figure 3.32: (a) Carbon/epoxy representative and (b) carbon/CE stress-displacement curves from the ENF tests. 112
Figure 3.33: Mode II critical strain energy release rates. 114
Figure 3.34: Mode II critical stress intensity factors. 114
Figure 3.35: SEM micrographs of the (a and b) PMTF3-PAN1 and (c and d) RS3C-PI6 NF mats. (e) schematic of mode II crack growth through the NF-reinforced interlaminar region.[91] (f) ENF experimental setup. 117
Figure 3.36: Mode II interlaminar fracture surfaces for the carbon/epoxy material. (a, d, and e) pristine, (b and f) PAN1, (c) PAN2. The red box outlines the end of the pre-crack, while the red lines show the approximate location where the cracks terminated after the drastic drop in load. The green box indicates a shear hackle pattern. 118
Figure 3.37: Mode II interlaminar fracture surfaces of the carbon/CE material. The red box outlines the end of the pre-crack, while the red lines show the approximate location where the cracks terminated after the drastic drop in load. The green boxes show shear hackle patterns between carbon fibers. 119
Figure 3.38: Mode II interlaminar fracture surface of a PMTF3-PAN1 specimen. The crack propagation direction was from left to right. 120
Figure 3.39: Mode II interlaminar fracture surface of a RS3C-PI7 specimen. The crack propagation direction was from left to right. 121
Figure 3.40: Mode II interlaminar crack paths of carbon/epoxy specimens. 122
Figure 3.41: SEM micrographs showing the mode II crack paths of carbon/CE specimens. Crack propagation occurred from left to right. 122
Figure 4.1: Rotated coefficients of mutual influence (extension-shear coupling) for unidirectional plies of the (left) carbon/epoxy and (right) carbon/CE materials. 130
Figure 4.2: (a) Schematic of open-hole tension test specimen.[180] (b) Untested open-hole tensile specimen. (c) Open-hole tensile testing setup. 133
Figure 4.3: Chronological manufacturing procedure for L-bend panels: (a) aluminum angle, (b) composite layup, (c) vacuum-bagged layup, (d) sealed and vacuum pressurized layup, (e) Thermo Scientific HERATherm oven and MTI vacuum, (f) cured panel. 135
Figure 4.4: (a) Curved beam strength test specimen geometry (SI units).[193] (b) curved beam in four-point bending.[193] (c) Experimental setup for curved beam strength test. 136

Figure 4.5: (a) Representative DMA specimen. (b) DMA specimen loaded in 3PB fixture. (c) Mettler Toledo DMA 1 STARe system. 137
Figure 4.6: Representative stress-strain curves for the laminate tensile tests. The sharp drop in strain in the PI6 curve is due to the extensometer edges slipping. 140
Figure 4.7: Laminate tensile strength results. 140
Figure 4.8: Laminate tensile modulus results. 141
Figure 4.9: Laminate failure strain results. 141
Figure 4.10: Representative SEM images of (a & b) the PMTF3-PAN1 and (c & d) the RS3C-PI6. 142
Figure 4.11: SEM micrographs of ±12° interfaces in untested laminate specimens: (a) pristine PMTF3, (b & c) PMTF3-PAN1, (d) pristine RS3C, and (e & f) RS3C-PI6. 143
Figure 4.12: Laminate tensile test failure codes and examples of two common failure modes.[120] 144
Figure 4.13: Failure modes of the carbon/epoxy $[\pm 12/0]_S$ pristine and PAN1 laminate specimens. 145
Figure 4.14: Failure modes of the carbon/CE $[12_2/-12_2/0]_S$ pristine and PI6 laminate specimens. 146
Figure 4.15: Edges of failed carbon/epoxy $[\pm 12/0]_S$ laminate specimens: (a) pristine and (b) PAN1. Crack propagation occurred in the downward direction. 147
Figure 4.16: Edges of failed carbon/CE $[12_2/-12_2/0]_S$ laminate specimens: (a) pristine and (b) PI6. Crack propagation occurred in the downward direction. 148
Figure 4.17: (a) Interlaminar crack at a ±12° interface in a failed PMTF3-PAN1 laminate specimen. (b & c) Fracture surfaces near the PMTF3-PAN1 interlaminar region. 149
Figure 4.18: (a) Interlaminar crack at a ±12° interface in a failed RS3C-PI6 laminate specimen. (b & c) Fracture surfaces near the PI6 interlaminar region. 150
Figure 4.19: Representative stress-strain curves for the open-hole tensile tests 151
Figure 4.20: Open-hole tensile strength results. 151
Figure 4.21: Open-hole tensile modulus results. 152
Figure 4.22: Open-hole tensile failure strain results 152
Figure 4.23: Acceptable open-hole tensile failure modes.[180] 153
Figure 4.24: Failed carbon/epoxy open-hole tension specimens: (a) PMTF3 pristine and (b) PMTF3-PAN1. 154
Figure 4.25: Failed carbon/CE open-hole tension specimens: (a) RS3C pristine and (b) RS3C-PI6. 155
Figure 4.26: Different failure mechanisms observed in open-hole tensile specimens: (a) brittle, (b) pull-out, and (c) delamination.[176] (d) Schematic of outer 45/90/-45 plies separating from the 0° plies and pulling out in a notched quasi-isotropic laminate.[33] 156
Figure 4.27: Edge delamination in failed open-hole tensile specimens: (a) PMTF3 pristine, (b) PMTF3-PAN1, (c) RS3C pristine, (d) RS3C-PI6. 157
Figure 4.28: Hole edges in failed carbon/epoxy open-hole tensile specimens: (a) pristine and (b, c, & d) PAN1. Figure (d) shows some fractured NFs 158
Figure 4.29: Hole edges in failed carbon/CE open-hole tensile specimens: (a) pristine and (b, c, & d) PI6. Figures (c) and (d) show signs of matrix toughening and NF bridging. 159
Figure 4.30: Edges of failed carbon/epoxy open-hole tensile specimens: (a) pristine and (b) PAN1. Crack propagation occurred in the downward direction. 160
Figure 4.31: Edges of failed carbon/CE open-hole tensile specimens. (a) pristine and (b) PI6. Crack propagation occurred in the downward direction. 160
Figure 4.32: SEM images of interlaminar cracks at ±12° interfaces of tested carbon/epoxy open-hole tensile specimens: (a & b) pristine and (c, d, e, & f) PAN1. 161
Figure 4.33: SEM images of interlaminar cracks at ±12° interfaces of tested carbon/CE open-hole tensile specimens: (a) pristine and (b, c, & d) PI6. 162
Figure 4.34: X-ray CT scans of carbon/epoxy open-hole tensile specimens. (a) untested and (b) tested PMTF3 pristine. (c) untested and (d) tested PMTF3-PAN1. 163
Figure 4.35: X-ray CT scans of carbon/epoxy open-hole tensile specimens. 164
Figure 4.36: X-ray CT scans of carbon/CE open-hole tensile specimens. (a) untested and (b) tested RS3C pristine. (c) untested and (d) tested RS3C-PI6. Carbon fiber failure is outlined in red. 165
Figure 4.37: X-ray CT scans of carbon/CE open-hole tensile specimens. 166

Figure 4.38: Curved laminate configurations and failure modes.[209] 168
Figure 4.39: Different L-bend loading configurations that induce delamination at the curve. (a) ref. [211] (b) ref. [172] (c) ref. [209] (d) ref. [193]. 169
Figure 4.40: Curved beam strengths of the L-bend specimens. 171
Figure 4.41: Typical load-displacement responses for (a) unidirectional and (b) multidirectional specimens.[193] 173
Figure 4.42: Representative interlaminar tensile stress-displacement curves for the L-bend tests. 174
Figure 4.43: Interlaminar tensile strengths determined from the L-bend tests. 174
Figure 4.44: SEM micrographs of a PAN1 NF mat that was used to reinforce the interfaces between every 2 plies in the carbon/epoxy L-bend specimens. 175
Figure 4.45: SEM micrographs of a PI8 NF mat that was used to reinforce the interfaces between every 4 plies in the carbon/CE L-bend specimens. 176
Figure 4.46: Edge view of delamination in carbon/epoxy L-bend specimens during testing when crosshead displacement was at 8 mm: (a) pristine (8mm) and (b) PAN1 (12mm). The value in parentheses indicates the maximum crosshead displacement during the test on that specimen. 177
Figure 4.47: Edge view of delamination in carbon/CE L-bend specimens during testing when crosshead displacement was at 12 mm: (a) pristine and (b) PI8. Both specimens were tested to 12mm displacement. 177
Figure 4.48: SEM images of the curved edge of tested carbon/epoxy L-bend specimens: (a & b) PMTF3 pristine and (c, d, & e) PMTF3-PAN1. Image (b) shows a transverse crack that has propagated through the resin-rich interlaminar region, which would be a great candidate for NF-reinforcement. Image (d) shows an interlaminar crack that initiated at a large void and has propagated through the NF reinforced interlaminar region. Image (e) shows evidence of NF bridging across an interlaminar crack. 178
Figure 4.49: SEM images of the edges of carbon/CE L-bend specimens. (a) RS3C pristine specimen, (b) untested RS3C-PI8 specimen, and (c & d) tested RS3C-PI8 specimen. Figures (b) and (d) show clear evidence of nanofiber bridging in both the untested and tested RS3C-PI8 specimens. 179
Figure 4.50: X-ray CT scan of untested carbon/epoxy L-bend specimens. 180
Figure 4.51: X-ray CT scan of untested carbon/CE L-bend specimens. 181
Figure 4.52: Some definitions of glass transition temperature from DMA.[214] 184
Figure 4.53: Storage modulus data from the DMA testing. 187
Figure 4.54: Damping ratio results from DMA tests. 187
Figure 5.1: (a) E-SPIN nanofiber unit used to electrospin aligned nanofibers. (b) Experimental setup for electrospinning aligned NFs. (c) Schematic of electrospinning setup using a rotating cylinder collector. .200
Figure 5.2: Definition of fiber orientation angle ϕ 204
Figure 5.3: Experimental setup for tensile testing of CNF/epoxy nanolaminates with digital image correlation data collection. 205
Figure 5.4: (a) CNF/epoxy nanolaminate speckled dogbone specimen. (b-d) Digital image correlation axial strain data throughout a tensile test of a CNF/epoxy nanolaminate. 206
Figure 5.5: (top) Actual shape of a dogbone specimen and (bottom) the estimated shape, which was used to determine the approximate width of the specimen over the gauge length L. 207
Figure 5.6: (a & b) Neat AroCy-L10 CE resin specimens before and after failure. (c & d) PAN-CP-6% nanolaminate specimen before and after failure. 207
Figure 5.7: Experimental setup for capturing high-speed video of the electrospinning process. 209
Figure 5.8: SEM images of NF mats spun with different substrate speeds. 210
Figure 5.9: Directionality histograms obtained with Fiji and used to determine the dispersion values: (left) 6.4 m/s and (right) 37.7 m/s. 211
Figure 5.10: Results of the substrate speed study. 212
Figure 5.11: (a) A “random” PAN nanofiber mat electrospun onto a stationary collector. (b) SEM image of a unidirectional carbon fiber preform manufactured by Sigmatex. Directionality histograms corresponding to the SEM images of the (c) PAN NF mat and the (d) CF preform. The dispersion values obtained from (c) and (d) are 28.06° and 2.52°, respectively. The fp and gp values for the PAN NF mat are 0.2628 and 0.2241, respectively. The fp and gp values for the CF mat are 0.6764 and 0.6725, respectively. 212

Figure 5.12: Directionality histograms obtained from NF mats spun for (left) 60 min and (right) 30 min. 213
Figure 5.13: Results of the spin time study. 214
Figure 5.14: Results of the substrate width study. 215
Figure 5.15: Results of the voltage study. 216
Figure 5.16: Results of the polymer concentration study. 216
Figure 5.17: SEM micrographs of aligned (a & b) as-spun, (c) oxidized, and (d) carbonized PAN NFs. The average diameter of the as-spun PAN nanofibers was 627 ± 165 nm. The average diameter of the stabilized fibers was 517 ± 90 nm. The average diameter of the carbonized fibers was 355 ± 87 nm. 218
Figure 5.18: Directionality histograms obtained using FIJI for the (a) as-spun, (b) stabilized, and (c) carbonized PAN nanofiber mats. The respective standard deviations of the fitted Gaussian curves for these three mats were ±11.52°, ±16.27°, and ±11.07°. The orientation parameters fp and gp for the as-spun mat were 0.805 and 0.763, respectively. The orientation parameters fp and gp for the stabilized mat were 0.780 and 0.716, respectively. The orientation parameters fp and gp for the carbonized mat were 0.737 and 0.677, respectively. 218
Figure 5.19: Stress-strain curves for the neat epoxy resin and the CP-19%-Si specimens. 219
Figure 5.20: Stress-strain curves for the unidirectional CNF/epoxy specimens. 220
Figure 5.21: Representative stress-strain curves for the neat epoxy resin and CNF/epoxy nanocomposites. 221
Figure 5.22: Tensile strength and modulus results for the neat epoxy resin and CNF/epoxy nanocomposites. 222
Figure 5.23: Failure strain and toughness results for the neat epoxy resin and CNF/epoxy nanocomposites. 222
Figure 5.24: Fracture surface of a neat EPON828 specimen. The dashed line separates the epoxy and the layer of spray paint that was applied for DIC. 223
Figure 5.25: Fracture surface of a UD-10%-noSi specimen. 223
Figure 5.26: Fracture surface of a UD-10%-Si specimen. 224
Figure 5.27: Fracture surface of a UD-22%-Si specimen. 225
Figure 5.28: Fracture surface of a CP-19%-Si nanolaminate specimen. 225
Figure 5.29: Fracture surface of a CP-19%-Si nanolaminate specimen. These images show the failure mechanisms of the 0° plies. 226
Figure 5.30: Fracture surface of a CP-19%-Si nanolaminate specimen. The images show the failure mechanisms of the 90° plies. 226
Figure 5.31: Representative stress-strain curves for the neat CE resin and the CE-matrix nanolaminates. 228
Figure 5.32: Tensile strength and Young's modulus values for the cyanate ester matrix nanolaminates compared to the neat resin. 228
Figure 5.33: Failure strain and toughness values for the cyanate ester matrix nanolaminates compared to the neat resin. 229
Figure 5.34: SEM micrographs of the aligned PAN NF mats used to manufacture the PAN/CE nanolaminates. 229
Figure 5.35: SEM micrographs of the aligned PI NFs used to manufacture the PI/CE nanolaminates. 230
Figure 5.36: Directionality histograms obtained using FIJI for aligned (a) PAN and (b) PI nanofiber mats. 230
Figure 5.37: Photographs showing the transparencies of the CE resin matrix nanolaminates compared to the neat CE resin. The three stars are drawn on the sheet of paper behind each material. 231
Figure 5.38: (a) as-spun random PAN NF mat that was sheared with scissors. (b) PAN NF mat baked at 350°F for 3 hours between two pieces of glass and broken in tension by hand. 232
Figure 5.39: Fracture surface of a neat AroCy-L10 CE resin specimen. 232
Figure 5.40: Fracture surfaces of (a) PAN-CP-6% and (b) PAN-CP-12% nanolaminate specimens. 233
Figure 5.41: Fracture surface of a PAN-45-20% nanolaminate. 234
Figure 5.42: Fracture surfaces of a PI-CP-30% nanolaminate specimen. 234
Figure 5.43: Fracture surfaces of a PI-45-30% nanolaminate specimen. 235

Figure 5.44: Molecular structures of APS-C2 (6FDA/BPDA/6FOBDA = 80/20/100) and Matrimid® 5218.[278] 236
Figure 5.45: (a) APS-C2 polyimide powder. (b) AroCy-L10 resin mixed with Co^{3+} AcAc and nonylphenol catalysts. (c) APS-C2 mixed with CE resin at a 13.6% weight ratio (11.7% PI VF). (d) That same mixture after curing. 237
Figure 5.46: Single frames from videos taken with a Samsung Galaxy S8+ at 480 fps of PAN 10wt% + DMF with a 20 gauge needle with cylinder speeds of approximately (a) 1800 RPM, (b) 2400 RPM, and (c) 3300 RPM. (d) Frame from a 1000 fps high-speed video taken with the Redlake camera while electrospinning onto a stationary plate. The arrows indicate the needle tips. 238

Figure A.1: DCB data for the carbon/epoxy material reinforced with PAN NFs. 297
Figure A.2: DCB data for the carbon/epoxy material reinforced with PI NFs. 297
Figure A.3: DCB data for the carbon/CE material. 298
Figure B.1: MTI GSL-1700X tube furnace in which nanofibers were carbonized. 299
Figure B.2: Aligned PAN NF mats. (top) as-spun. (bottom left) folded over once to create a $[0_2]$ layup. (bottom right) folded over twice to create a $[0_4]$ layup. The fiber direction is horizontal. 300
Figure B.3: CNF/epoxy composite manufacturing steps: (a) as-spun layup on a silicon wafer, (b) as-spun layup sandwiched between silicon wafers, (c) carbonized layup before resin impregnation, and (d) cured CNF/epoxy composite. 301
Figure B.4: PAN/CE nanolaminate manufacturing. (a) PAN $[0_4/90_4]$ preform, (b) PAN $[0_4/90_4]$ preform partially impregnated with AroCy-L10 CE resin, (c) the preform fully impregnated with resin before curing, and (d) the cured $[0_4/90_4]$ nanolaminate. 301
Figure D.1.3.1: (a) Schematic of nanotoughening mechanism in CNT-modified nanofibers.[310] (b) TEM image of a graphene oxide templated carbon nanofiber.[291] 309
Figure D.2.1.1: Schematic of manufacturing process for GNR-reinforced carbon nanofibers.[290] 312
Figure D.2.1.2: Schematic of manufacturing process for MXene-reinforced carbon nanofibers.[312] 312
Figure D.2.4.1: Horiba Scientific LabRAM HR Evolution Raman spectrometer. 315
Figure D.3.1.1: Raman spectra of powdered (a) PAN and (b) graphene nanoribbons. (c) SEM image of a bundle of GNRs. 316
Figure D.3.1.2: Optical microscope image of 10wt% PAN + 1% (wt% of PAN) GNR in DMF solutions (a) before sonication and (b) after sonication. 317
Figure D.3.1.3: Optical microscope image of the 10wt% PAN + 1% (wt% of PAN) GNR in DMF after sonication and evaporation of DMF solvent 318
Figure D.3.1.4: Locations of obtained spectra for (a) an aligned PAN+1%GNR fiber "dark spot," (b) a random PAN+1%GNR fiber (not a dark spot: PAN only), and (c) a random pristine PAN fiber. 318
Figure D.3.1.5: (a) Raman spectra of as-spun PAN+1%GNR PAN only spots. (b) optical microscope image of a PAN+1%GNR PAN only location. The vertical lines indicate points or ranges of relevant vibrational modes. 319
Figure D.3.1.6: (a) Optical microscope image of a large "dark spot" in a PAN+1%GNR nanofiber. (b) SEM micrograph of a bulge in a fiber from the same mat. 319
Figure D.3.1.7: (a) Raman spectra of as-spun PAN+1%GNR "dark spots." SEM images of PAN+1%GNR (b) random and (c) aligned nanofibers. The vertical lines indicate points or ranges of relevant vibrational modes. 320
Figure D.3.1.8: Raman spectra of as-spun GNR dark spots and carbonized pristine PAN nanofibers. 322
Figure D.3.2.1: SEM images of PAN+2%MXene nanofibers. (b) Dispersion pattern of Ti_3C_2 shown by EDS mapping where Ti is red. 323
Figure D.3.2.2: TEM image of a PAN+2%MXene nanofiber. 323
Figure D.3.2.3: Qualitative comparison of the average Raman spectra for carbonized pristine PAN and PAN+2%MXene nanofibers 324
Figure D.3.2.4: Average Raman spectrum for carbonized pristine PAN NFs showing the four fitted Lorentzian curves. The vertical lines indicate points or ranges of relevant vibrational modes. 325

Figure D.3.2.5: Average Raman spectrum for carbonized PAN+2%MXene NFs showing the four fitted Lorentzian curves. The vertical lines indicate points or ranges of relevant vibrational modes. 325
Figure D.4.1: Average Raman spectra of as-spun aligned PAN+1%GNR “dark spots,” carbonized PAN+2%MXene, and carbonized pristine PAN random nanofibers.....327

LIST OF TABLES

Table 1.1: Advantages/disadvantages of advanced composites.[11] 9
Table 1.2: Properties and applications of high-performance fibers.[13] 12
Table 1.3: Types and applications of thermoplastic polymers.[16] 14
Table 1.4: Types and applications of thermosetting polymers.[16] 14
Table 1.5: Comparison of certain properties of thermoset and thermoplastic resins.[17] 15
Table 2.1: Tensor versus contracted notation for stresses and strains. *Note that γij represents engineering shear strain whereas εij $(i \neq j)$ represents tensor shear strain.[71] 38
Table 2.2: Physical modifiers used to investigate toughening of cyanate ester resin.[25] 61
Table 3.1: Material properties of unidirectional, orthotropic plies of both the carbon/epoxy and carbon/CE materials. All values were determined experimentally except for $E1$ and $G12$ of the carbon/CE material, which was provided by the manufacturer. *Manufacturer data. 78
Table 3.2: Electrospinning parameters used to manufacture NF interleaves that produced positive mode I IFT results. 80
Table 3.3: Electrospinning parameters used to manufacture NF interleaves that produced positive mode II IFT results. 81
Table 3.4: Materials testing using the DCB procedure. 82
Table 3.5: Materials tested using the ENF procedure. 84
Table 3.6: Carbon (or graphite)/epoxy mode I IFT results. 123
Table 3.7: Carbon/CE and other high-temperature mode I IFT results. *Thermoplastic matrix. 124
Table 3.8: Carbon/epoxy mode II IFT results, along with values from the literature. **350°F dry and 270°F wet service capability. 125
Table 3.9: Carbon/CE mode II IFT results, along with another value of a high-temperature matrix composite from the literature. *Thermoplastic matrix. 126
Table 4.1: Electrospinning parameters used to fabricate the NF interleaves for the laminate and open-hole tensile specimens. 131
Table 4.2: Electrospinning parameters used to fabricate the NF interleaves for the L-bend specimens. 131
Table 4.3: List of materials and structures tested with the carbon/epoxy material. 138
Table 4.4: List of materials and structures tested with carbon/CE material. 139
Table 4.5: Porosity results from the x-ray CT data of untested open-hole laminate specimens. 167
Table 4.6: Porosity results for untested L-bend specimens. 182
Table 4.7: Porosity results for tested L-bend specimens. 182
Table 4.8: DMA results for specimens that were not post cured. *It is unclear which definition was used. 188
Table 4.9: DMA results for specimens that were post cured at 450°F for 2 hours. *It is unclear which definition was used. 188
Table 4.10: Results of laminate tensile testing. 189
Table 4.11: Results of open-hole tensile testing. 189
Table 4.12: Results of L-bend testing. 189
Table 5.1: Electrospun nylon nanofiber-reinforced composites.[60] 194
Table 5.2: The electrospinning parameters used for the study on nanofiber alignment using the rotating cylinder method. *The flow rates were varied for the voltage study to produce continuous electrospinning. 200
Table 5.3: Electrospinning parameters used to fabricate aligned PAN NFs for the CNF/epoxy nanocomposites. *These mats were used to reinforce the UD-22%-Si nanocomposite. 201
Table 5.4: Electrospinning parameters used to fabricate aligned NFs for the CE matrix nanocomposites. 201
Table 5.5: List of materials tested. 207
Table 5.6: Mechanical testing results for the neat epoxy resin and CNF/epoxy nanocomposites. 239
Table 5.7: Mechanical testing results for the neat CE resin and CE-matrix nanolaminates. 240

Table A.1: Electrospinning parameters for NF interleaves that produced negative DCB results.....296
Table A.2: Electrospinning parameters for NF interleaves that produced negative ENF results. 296
Table B.1: Carbonization schedule. The time column indicates the time it took for the oven to go from the temperature in the same row to the temperature in the following row. 299
Table C.1: Results of the substrate speed study. 303
Table C.2: Results of the spin time study.....303
Table C.3: Results of the substrate width study. 303
Table C.4: Results of the voltage study, showing the different flow rates used. 304
Table C.5: Results of the polymer concentration study.....304
Table D.2.1.1: List of materials tested.....313
Table D.2.2.1: Electrospinning parameters used to fabricate random and aligned NFs. 313
Table D.3.2.1: Quantitative comparison of the Raman spectra characteristics for pristine PAN and PAN+2%MXene nanofibers.....326

CHAPTER 1. INTRODUCTION

1.1 ADVANCED COMPOSITE MATERIALS

1.1.1 Historical Remarks

A composite material can be defined as a combination of two or more materials that exhibits a blend of its constituents' properties. In some cases, composites can even exhibit properties *greater* than those of its constituents alone.[1] Most often, composites are composed of a structural reinforcement and a matrix. Composite materials have been used for thousands of years for structural applications. Since their development, they have come a long way, making them some of the most advanced structural materials available today. The advantages of current advanced composite materials, including their low weight, high strength, and durability, make them an extremely prolific research topic in the materials science field.

Perhaps the earliest known examples of composites are the mud bricks reinforced with straw used as building materials across ancient Mesopotamia and Sumer as early as 4900 B.C.[1] Straw maintained its status as a reinforcing material in other ancient composite structures, such as boats and pottery.[2] Ancient Egyptians invented plywood by bonding strips of wood together at different orientations, which improved strength and decreased swelling due to absorption of water.[3] Later, the famous Mongol bows (1200 C.E.) were made from a combination of wood, bone, and "animal glue" that were pressed and wrapped in birch bark. These bows were strong and flexible, which increased their firepower and accuracy. In fact, they existed as the most powerful weapon on earth until the invention of gunpowder.[2] As technologies and manufacturing processes developed,

new composite materials with better properties and even broader applications came about.

Before scientists developed plastics, natural resins derived from plants and animals were the only source of binders and composite matrices. At the start of the twentieth century, plastics, or synthetic polymers, including vinyl, polystyrene, phenolic, and polyester, were developed to offer better properties than natural resins. However, plastics needed reinforcement to provide enough strength and rigidity for structural applications. In 1935, the first glass fiber was developed by Owens Corning. When combined with a plastic polymer matrix, this fiberglass created an incredibly strong and lightweight material.[2] This was the birth of the fiber-reinforced polymer (FRP) industry as we know it.

Soon, due to the demand created by the Second World War, the FRP industry experienced substantial growth. As the need for lightweight materials, especially to build military aircraft, increased, composites extended from the lab to actual production. Besides being light and strong, fiberglass composites were also transparent to radio waves, making them ideal for use in sheltering electronic radar equipment (radomes).[2] The lightweight applications of these composites were abundant in the military, but after the war, they remained at the forefront of the material world, expanding their uses to commercial boats and aircraft.[4] Industry innovators also developed new manufacturing methods and infrastructure.[2]

Since fibers are the main load-bearing component of FRPs, improving their strengths and stiffnesses will ultimately do the same for the composite.[5] This established the need to develop higher strength and stiffer fibers. Although glass fibers were and

continue to be the most commonly used in FRPs, there was a need for a fiber that could improve properties even further.[5] This led to the development of carbon fiber in the 1960s, which paved the way for new technologies in the aerospace industry due to carbon fiber's increased stiffness.[5,6] In the 1970s, DuPont developed the aramid fiber known as Kevlar®, which has become the standard in ballistic armor due to its high tenacity.[2] At the same time, other fibers, such as quartz, ceramic, and those based on several different polymers, were being developed. However, as their manufacturing costs dropped throughout the 1990s, carbon fiber-reinforced polymers (CFRPs) became much more widespread. Their applications extended to other industries, including sports and recreation. In fact, from 1998 to 2006, CFRP use doubled in the world market.[6] Today, advanced composites are defined as those reinforced with carbon, high-strength glass, ceramic, or high-performance polymer fibers due to their enhanced structural properties, namely high specific strength and stiffness.

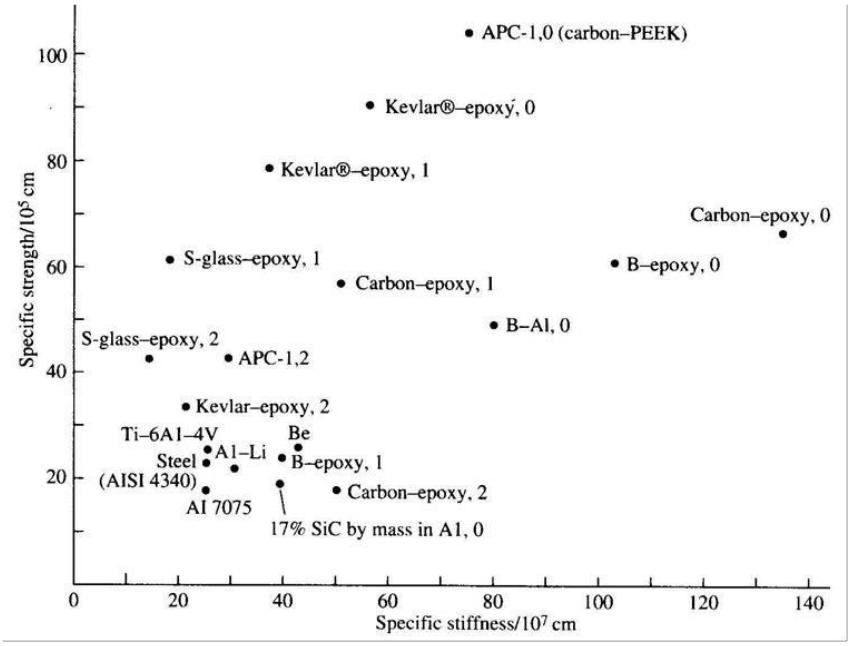

Figure 1.1: Specific strength versus specific stiffness of some isotropic materials and various advanced composite materials. B represents boron fiber. For composites, 0 represents aligned fibers, 1 represents fibers in the following arrangement: 50% at 0°, 40% at ±45°, and 10% at 90°, 2 represents a balanced laminate with equal layers of fibers at 0°, ±45°, and 90°.[7]

1.1.2 Classification of Fiber-Reinforced Composites

Although composites can have metal or ceramic matrices, polymer matrix composites (PMCs) are the most widespread. Metal matrix composites (MMCs) and ceramic matrix composites (CMCs) have unique properties and applications, but PMCs cost less and are relatively simple to manufacture.[6] Also, PMCs are lighter than MMCs and CMCs, making them more applicable to lightweight structural applications in industries such as aerospace.

Although polymer resins reinforced with particles can provide improved properties compared to the polymer alone, fiber reinforcement is much more common for structural applications. Fiber-reinforced polymers (FRPs) can be classified by fiber length and orientation. They can be reinforced with either short, discontinuous or long, continuous fibers. Discontinuous fibers can either be aligned or randomly oriented in polymer matrices, while continuous fibers are almost always aligned, whether that be in unidirectional or woven layers. Some hybrid fiber-reinforced composites can even have two or more types of fiber reinforcement.[5]

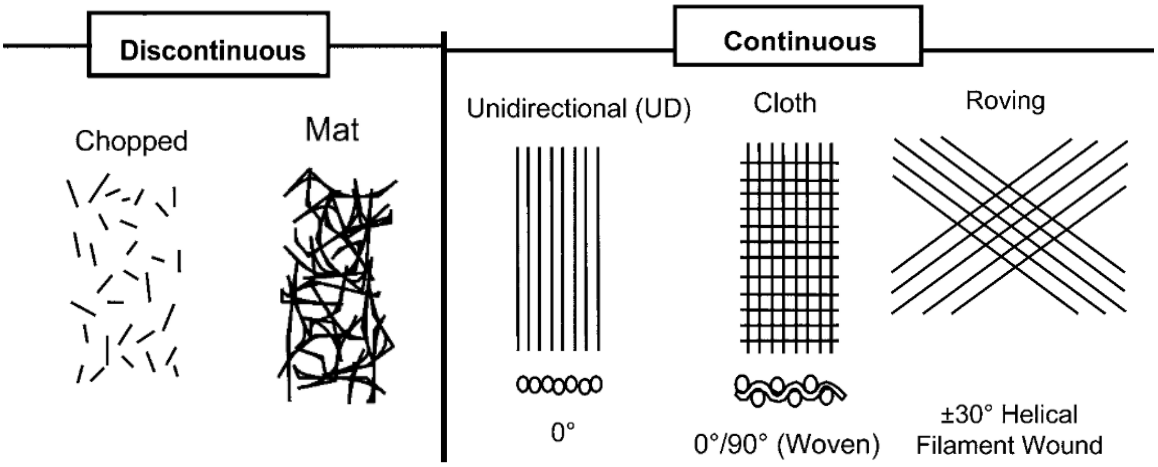

Figure 1.2: Typical types of fiber reinforcement.[1]

Although there are many types of FRPs, most structural applications require high strength and stiffness, which are provided by the reinforcing fibers. In FRPs, the fibers are the main load-bearing component, while the role of the matrix is to secure the fibers in place, protect them from damage, and transfer loads to the fibers, which can support high tensile loads but are much weaker in transverse directions. Since the fibers carry most of the load, increasing their volume fraction (VF) will inherently increase the performance of the composite. Because stress concentrations can be created at fiber edges, continuous fibers minimize the number of stress concentration sites. Continuous fibers also inhibit the growth of cracks through brittle matrices more effectively than discontinuous fibers.[5] For these reasons, advanced structural composites are always reinforced with continuous aligned fibers, which allows for the highest fiber volume fractions and structural properties.

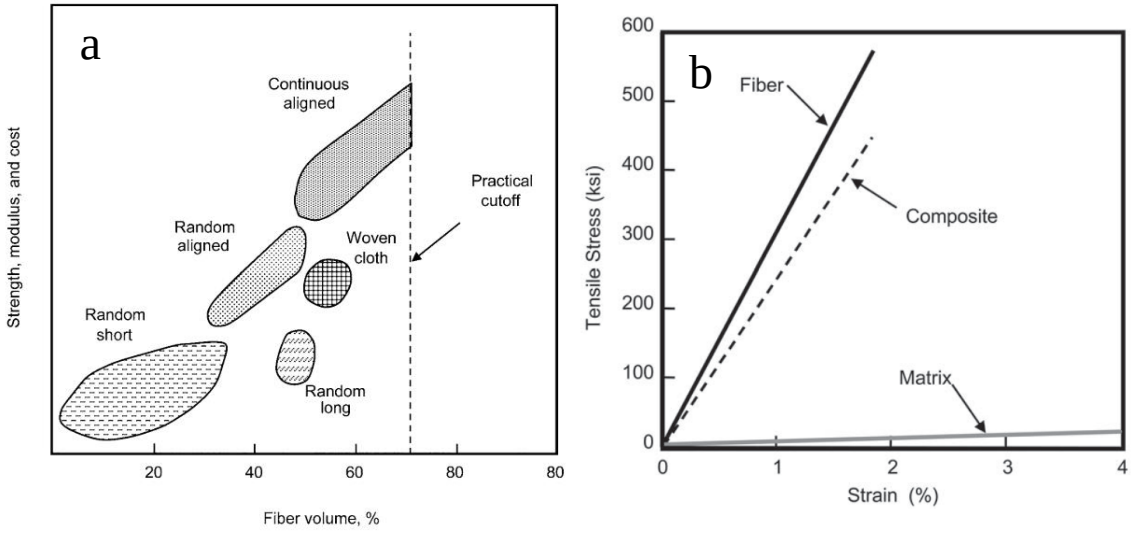

Figure 1.3: (a) Influence of reinforcement type and quantity on composite performance.[1] (b) Tensile properties of fiber, matrix, and unidirectional, continuous fiber-reinforced composite.[8]

1.1.3 Manufacturing of Continuous Fiber-Reinforced Composites

To accommodate for a wide variety of uses, continuous fiber-reinforced composites can be produced via a multitude of different manufacturing processes. One

common technique involves the use of prepregs (short for “pre-impregnated” sheets of fibers impregnated with uncured resin). Composite parts formed from prepreg can be cured in an autoclave, a press clave, or simply under vacuum.

Another class of composite fabrication techniques combines dry fiber sheets, or preforms, and liquid resin. There are several methods for impregnating the dry fibers with resin. Perhaps the most straight-forward is called the hand layup process, which can be used in combination with vacuum bag molding. Vacuum infusion, in which vacuum is used to pull liquid resin through a preform layup, is another popular choice. Vacuum is also used to pull resin during the vacuum-assisted resin transfer molding (VARTM) process, in which resin is pressurized and “pushed” through the preform mold with the assistance of “pulling” from the vacuum. If the vacuum is removed, the process is simply called resin transfer molding (RTM).[5]

Another type of manufacturing method is called filament winding. This process involves dipping tows of dry fibers in a liquid resin bath and winding them onto a rotating mandrel before curing. Because of its nature, filament winding can only be used to create bodies of revolution, such as cylinders, spheres, shafts, and cones. However, its applications include pressure vessels, rocket motor casings, engine cowlings, and drive shafts. End fittings are typically wound into the structure, which produces efficient and strong joints.[1]

There are a few other common fabrication methods, including injection molding, pultrusion, and compression molding. Injection and compression molding allow for large, curved parts to be made, making their uses in the automotive, marine, and aerospace industries popular. Parts produced via the pultrusion process are limited to those with a

constant cross-section.[1] These processes require relatively expensive equipment, and are generally used for industrial-scale production rather than for R&D.

When it comes to advanced composites, unidirectional fiber-reinforced layers, called plies, are normally utilized as building blocks and stacked to create a composite *laminate.* Plies are usually oriented at different directions to balance the load carrying capability. One example of this is called a quasi-isotropic layup (see **Figure 1.4**c), which means the laminate is balanced with an equal number of plies in the 0, +45, -45, and 90 degree directions.[8] Choice of layup, along with the type of fiber and matrix used, provides added design flexibility and tailorability to meet the structural strength and stiffness requirements.[9] Due to their enhanced and tailorable mechanical properties, composite laminates have become the most common type of fiber-reinforced composites for several applications, namely those in industries that require lightweight structural materials.

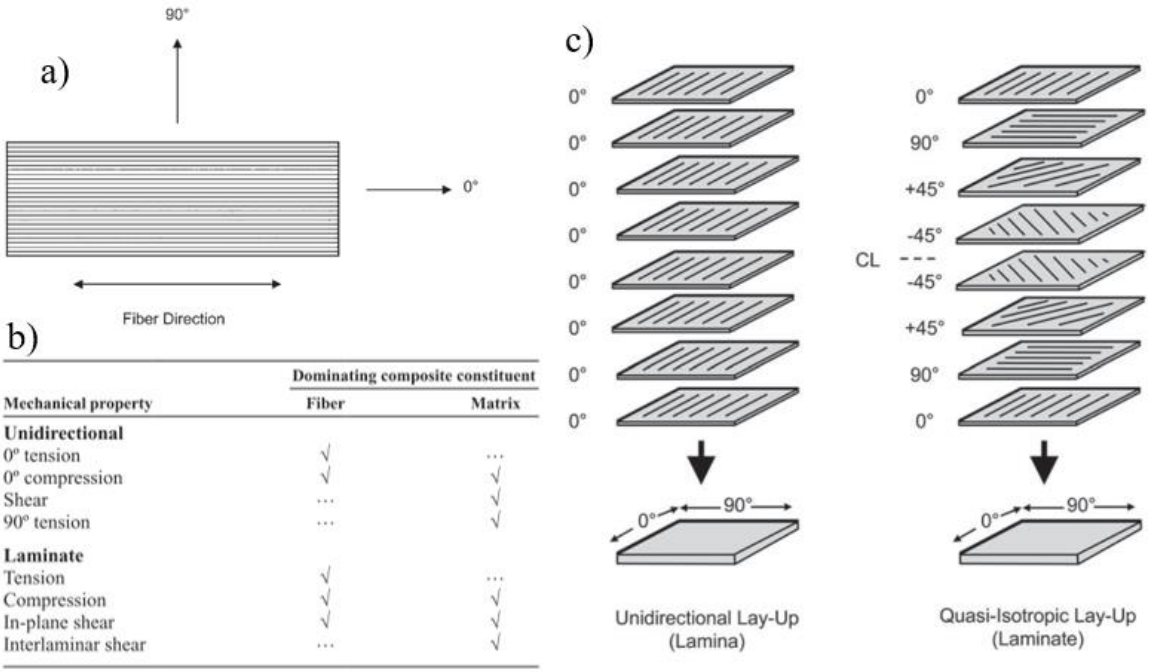

Mechanical property	Dominating composite constituent: Fiber	Matrix
Unidirectional		
0° tension	√	…
0° compression	√	√
Shear	…	√
90° tension	…	√
Laminate		
Tension	√	…
Compression	√	√
In-plane shear	√	√
Interlaminar shear	…	√

Figure 1.4: (a) Unidirectional continuous fiber lamina. (b) Effect of fiber and matrix on mechanical properties. (c) Unidirectional and quasi-isotropic lay-ups.[8]

1.1.4 Applications of Fiber-Reinforced Polymer Matrix Composites

Advanced composites are some of the most state-of-the-art and widely used structural materials to date. They have applications across several fields, including civil infrastructure, military and defense, space exploration, land, sea, and air transportation, mechanical industry, energy, healthcare, and recreation.[5] Composites are so widespread due to their abundant advantages over other structural materials, including light weight, tailorability of properties, fatigue and corrosion resistance, and reduced assembly costs due to fewer parts and fasteners.[1,6,10] These excellent properties give fiber-reinforced composites limitless applications across several industries.

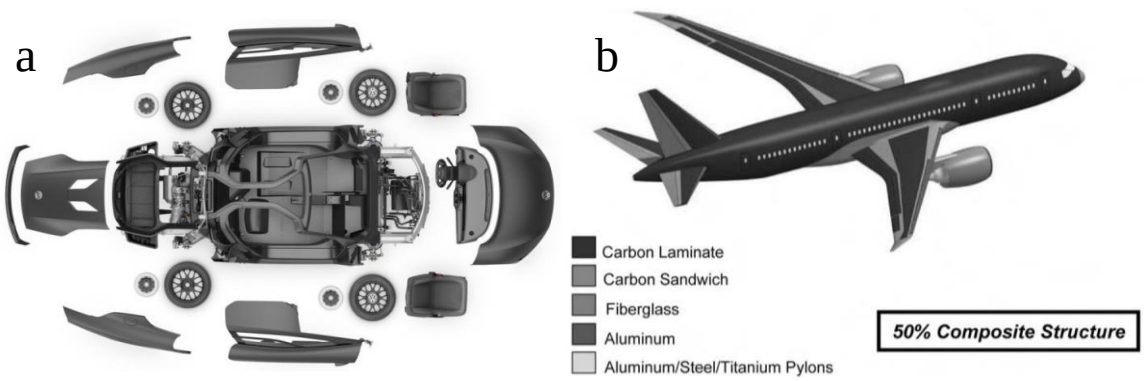

Figure 1.5: (a) Volkswagen xl1 carbon fiber body parts.[5] (b) Boeing 787 Dreamliner commercial airplane.[1]

Although composites possess several critical advantages over other structural materials, they also have some shortcomings. These include higher raw material and manufacturing costs, especially for high-performance fibers, potential adverse temperature or moisture effects, repair difficulties compared to metals, poor out-of-plane strength, and susceptibility to impact damage and delamination, or ply separations.[1] Nonetheless, the advantages of composites far outweigh their shortcomings, which makes them preferred materials for lightweight structural applications.

Table 1.1: Advantages/disadvantages of advanced composites.[11]

Advantages	*Disadvantages*
Weight reduction High strength or stiffness to weight ratio	Cost of raw materials and fabrication
Tailorable properties Can tailor strength or stiffness to be in the load direction	Transverse properties may be weak
Redundant load paths (fiber to fiber)	Matrix is weak, low toughness
Longer life (no corrosion)	Reuse and disposal may be difficult
Lower manufacturing costs because of less part count	Difficult to attach
Inherent damping	Analysis is difficult
Increased (or decreased) thermal or electrical conductivity	Matrix subject to environmental degradation

In recent years, the global composites market has experienced steady growth. In 2020, the market size was estimated at USD 86.4 billion. It is expected to advance at a compound annual growth rate (CAGR) of 6.6% from 2021 to 2028 due to increased demand for advanced materials in numerous industries, such as automotive, transportation, wind energy, aerospace, and defense.[12] However, the COVID-19 pandemic and its impact on the global supply chain has recently reduced demand in several end-use applications.

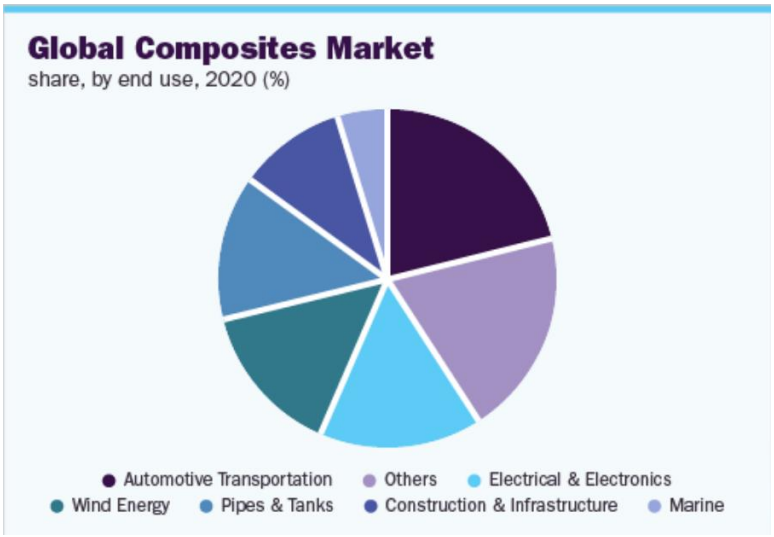

Figure 1.6: Global composites market share in 2020, separated by end use.[12]

As trade restrictions enacted due to the pandemic are eased and material and fabrication costs continue to decrease, the situation is expected to recover, and the prominence of composites will continue to increase, which should restore the growth trajectory of the market, as shown in **Figure 1.7**.[12] This is exciting for both composite researchers and manufacturers.

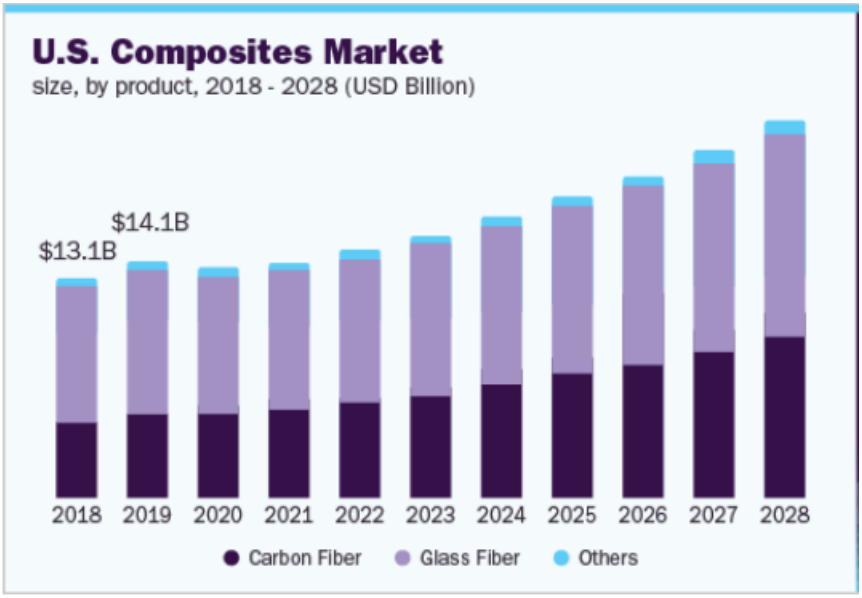

Figure 1.7: U.S. advanced composites market size, separated by product type.[12]

1.2 HIGH-PERFORMANCE POLYMER MATRIX COMPOSITES

1.2.1 Reinforcing Fibers

There are several different types of high-performance commercial fibers that can be used as reinforcement in polymer matrix composites. Most prominently, these include boron, aramid (Kevlar®), ultra-high molecular weight polyethylene (UHMWPE or Spectra®), ceramic, glass, and carbon. These fibers exhibit much higher specific tensile strengths and moduli than metals such as steel and aluminum (see **Figure 1.8**), which is what allows fiber-reinforced, polymer matrix composites to achieve high mechanical performance.

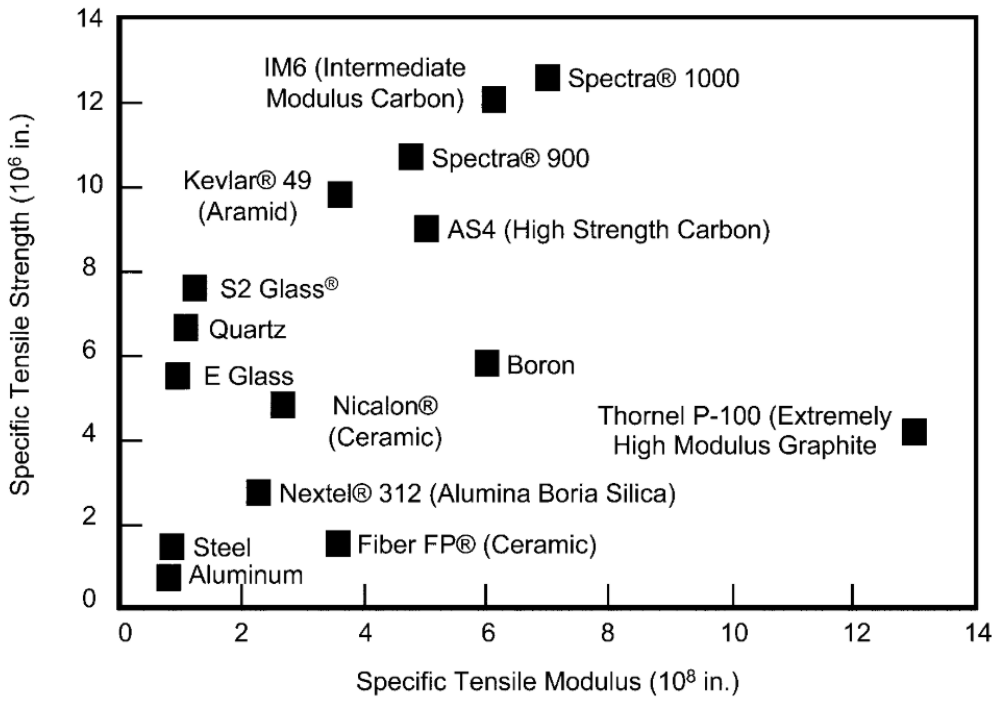

Figure 1.8: Specific strength and modulus of some commercially important fibers.[1]

Boron fibers were the first high-performance reinforcement for use in structural composite materials. Boron/epoxy composites possess enhanced compression properties and have been used in the sporting goods industry, but their high production costs have limited their use.[11] Aramid fiber-reinforced composites exhibit high impact and tensile strength, but they are often hybridized with carbon or glass fibers due to their low compressive strength.[5] UHMWPE fibers are extremely strong, stiff, durable, and cut resistant, but their low crystalline melting point limits their high-temperature applications.[11] Ceramic fibers have much higher thermal stabilities, which enables their use in demanding industrial, automotive, and aerospace environments, but manufacturing methods can be complicated and expensive.[11]

On the other hand, glass is the most commonly used reinforcing fiber due to its versatile properties and low cost of manufacturing. Glass fibers can possess excellent strength and durability, thermal stability, resistance to impact, and good chemical,

friction, and wear properties.[5] However, lots of fiberglass composites are reinforced with discontinuous fibers, which are not adequate for advanced structural applications.

Table 1.2: Properties and applications of high-performance fibers.[13]

Fiber	Young's Modulus (GPa)	Tensile Strength (GPa)	Diameter (μm)	Applications
Steel	200	2.8	90–400	Tire cords, piano wire
Ceramic (Al_2O_3-based, SiC-based)	350–380	1.7–5	10–20	Ceramic-matrix composites, high-temperature aerospace applications
Aramid	65–130	2.8–3.4	12	Body armor, bullet-proof vests, tire cords, sporting equipment, polymer-matrix composites
Nylon	6	1	20–40	Tire cords, polymer-matrix composites
Carbon	180–600	2.2–3.8	7–10	Automotive, aerospace, sporting equipment, polymer-matrix composites
Glass (silica-based)	70	1.8–3.4	8–14	Fiber optics, polymer-matrix composites

Nearly as common as glass, carbon fibers are used for applications that require higher stiffnesses.[5] Carbon fiber-reinforced polymers (CFRPs) were first used primarily in the aerospace sector. Today, however, CFRPs can be found in pressure vessels, energy production, cars, and even sports equipment, including golf clubs and tennis raquets.[6] They have become some of the most popular materials of choice for advanced lightweight structural applications.

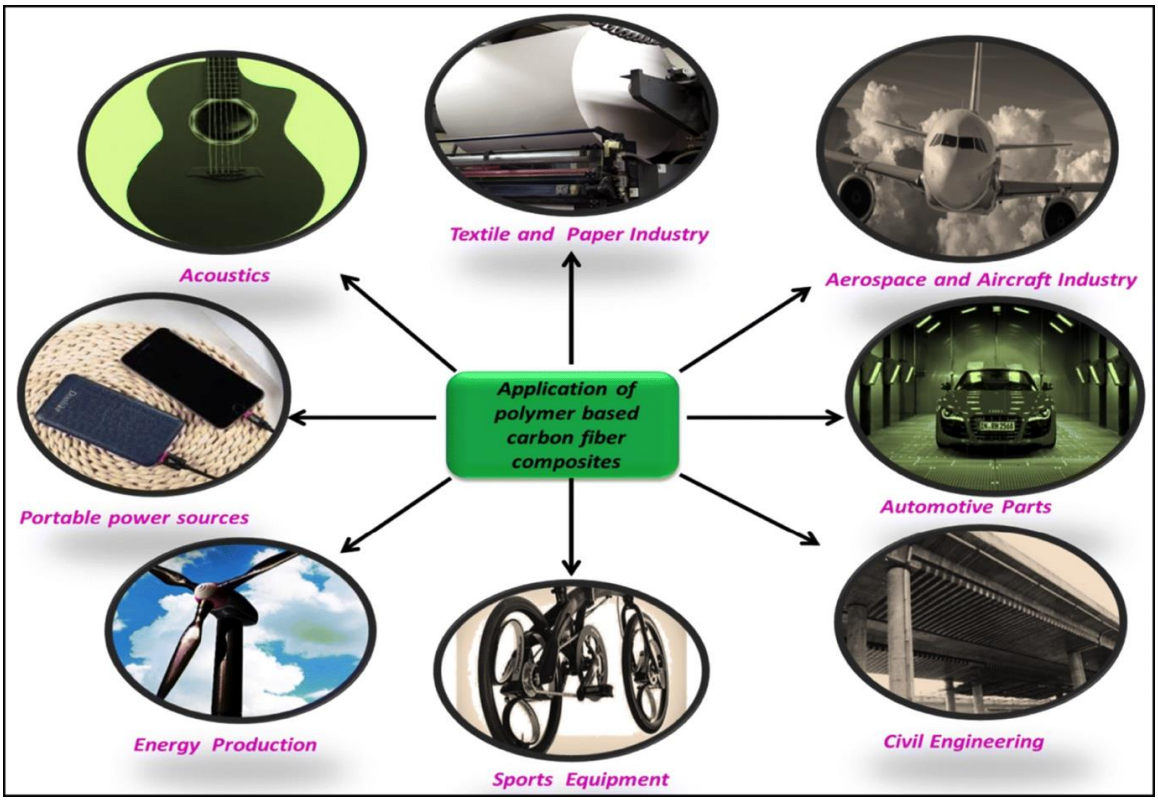

Figure 1.9: Applications of polymer matrix carbon fiber composites.[14]

Although high-performance fibers exhibit ultrahigh specific tensile strengths and moduli, all of them are brittle. In fact, most high-strength commercial fibers fail at strains lower than 2.5%, and high-modulus fibers typically fail at strains below 1%.[1] Since this brittleness is transferred to the performance of fiber-reinforced composites, there is a desire to develop fibers with increased failure strains.

1.2.2 Polymer Resins

In composite materials, the polymer matrix, or resin, can be classified by its type, which fits into one of two categories: thermoset (TS) or thermoplastic (TP) polymer. The main difference between the two is how they react to heat. For thermoplastics, the temperature-dependent solidification process is reversible, meaning they can be softened and remolded when heated. When thermosets are cured, however, they form a solid, three-dimensional crosslinked structure with strong chemical links across different

thermosetting molecules. Such structure impedes the motion of the polymer molecules[15] and causes the melting point to increase beyond the decomposition temperature, meaning thermosets cannot be melted later for remolding.[16]

There are a number of different types of thermoplastic and thermosetting polymers, each with their own unique sets of advantages and applications. **Table 1.3** and **Table 1.4** outline some common types of thermoplastics and thermosets and their applications.

Table 1.3: Types and applications of thermoplastic polymers.[16]

Thermoplastic	Properties and applications
Polyamide (nylon)	Tough and relatively hard material used for power tool casings, curtain rails, bearings, gear components, and clothes
Polymethyl Methacrylate (PMMA, acrylic)	Stiff, durable, and hard plastic that polishes to a sheen, used for signage, aircraft fuselage, windows, bathroom sinks, and bathtubs
Polyvinyl Chloride (PVC)	Tough and durable material that is commonly used for pipes, flooring, cabinets, toys, and general household and industrial fittings
Polypropylene	Light, yet hard material that scratches fairly easily, with excellent chemical resistance, used for medical and laboratory equipment, string, rope, and kitchen utensils
Polystyrene (PS)	Light, stiff, hard, brittle, waterproof material used mainly for rigid packaging
Polytetrafluoroethylene (PTFE, Teflon)	Very strong and flexible material used for non-stick cooking utensils, machine components, gears, and gaskets
Low-density Polythene (LDPE)	Tough, relatively soft, chemical resistant material used for packaging, toys, plastic bags, and film wrap
High-density Polythene (HDPE)	Stiff, hard, chemical resistant material used for plastic bottles and casing for household goods

Table 1.4: Types and applications of thermosetting polymers.[16]

Thermoset	Properties and applications
Epoxy resin	Hard material that is brittle without extra reinforcement. Used for adhesives and bonding of materials
Melamine formaldehyde	Hard, stiff, and strong, with decent chemical and water resistance, used for work surface laminates, tableware, and electrical insulation
Polyester resin	Hard, stiff, and brittle when unlaminated. Used for

	encapsulation, bonding, and casting
Urea formaldehyde	Hard, stiff, strong, and brittle used primarily in electrical devices due to its good electrical insulation properties
Polyurethane	Hard, strong, and durable material used in paint, insulating foam, shoes, car parts, adhesives, and sealants
Phenol formaldehyde resin (PF)	Strong, heat and electrical-resistant material used in electrical items, sockets and plugs, car parts, cookware, and precision-made industrial parts

In general, thermoplastics can provide high-strength, flexibility, and opposition to shrinking. They are generally tougher and more impact-resistant than thermosets, and their recyclability is highly advantageous for "green" applications. However, although their melting points can be relatively high, most thermoplastic resins exhibit low glass transition temperatures. Because the glass transition temperature normally governs the upper threshold of usable temperatures, thermoplastics are usually limited to low-temperature applications. Another challenge that limits their uses is their high cost of manufacturing.

On the other hand, thermosetting resins can be manufactured at relatively low costs. They are generally hard and stiff and possess higher glass transition temperatures than thermoplastics.[16] **Table 1.5** compares some of the characteristics of thermosets and thermoplastics.

Table 1.5: Comparison of certain properties of thermoset and thermoplastic resins.[17]

Feature/Property	Thermoplastics	Thermosets
Molecular structure	Linear polymer: weak molecular bonds in a straight-chain formation	Network polymers: high level of crosslinking with strong chemical molecular bonds
Melting point	Melting point lower than the degradation temperature	Melting point higher than the degradation temperature
Mechanical	Flexible and elastic. High resistance to impact (10x more than thermosets). Strength comes from crystallinity	Inelastic and brittle. Strong and rigid. Strength comes from crosslinking.
Polymerization	Addition polymerization:	Polycondensation

	repolymerized during manufacture (before processing)	polymerization: polymerized during processing
Microstructure	Comprised of hard crystalline and elastic amorphous regions in its solid state	Comprised of thermosetting resin and reinforcing fiber in its solid state
Size	Size is expressed by molecular weight	Size is expressed by crosslink density
Recyclability	Recyclable and reusable by the application of heat and/or pressure	Non-recyclable
Chemical resistance	Highly chemical resistant	Heat and chemical resistant
Crack repair	Cracks can be repaired easily	Difficult to repair cracks
Process thermal aspect	Melting thermoplastics is endothermic	Crosslinking thermosets is exothermic
Service temperature	Lower continuous use temperature (CUT) than thermosets	Higher CUT than thermoplastics
Solubility	Can dissolve in organic solvents	Do not dissolve in organic solvents

One of the most common and widely used thermosets is epoxy resin. The term "epoxy" refers to a broad group of reactive compounds that are categorized by an oxirane or epoxy ring. The presence of this functional group deems a molecule an epoxide, but the molecular base can vary widely, hence the diversity in the applications of epoxy resins.[18] Epoxies adhere well to most additives and reinforcements, enabling more efficient load transfer to fibers. They possess high strength and stiffness, rigidity, chemical and solvent resistance, electrical insulation, and relatively low toxicity.[18] Due to these excellent properties, epoxy resins, along with other thermosets, dominate today's advanced composites market. However, they are relatively brittle, making them susceptible to damage, microcracking, and delamination, all of which can lead to catastrophic failure. In addition, the glass transition temperatures of epoxies range from 150 to 220° C.[18] This is higher than glass transition temperatures of most thermoplastic resins, but is still insufficient for truly high-temperature applications.

1.2.3 Recent Developments in High-Temperature Resins and Composites

In the last few decades, the United States Department of Defense (DoD) has become increasingly interested in composite materials with increased service temperatures.[19] Polymer matrix composites suitable for high-temperature use would mainly find applications in the aerospace sector, e.g., in high-speed fighter skins, engines, missile nose cones, nozzle flaps, and fins.[20] This demand has led to the development of several new polymers that exhibit unique properties at high temperatures, although only a few have overcome the costs and challenges of manufacturing to see success.[21] Among these high-temperature resins are both thermoplastic and thermoset polymers.

The high-temperature, thermoplastic amorphous polymers include polyethersulfone (PES) and polyetherimide (PEI) and the semi-crystalline polymers include polyether-ether-ketone (PEEK) and polyether-ketone-ketone (PEKK).[21,22] Thermoplastic resins possess unique qualities, including increased delamination resistance, high damage tolerance, low moisture absorption, and excellent chemical resistance. Unlike thermosets, thermoplastics do not require a curing reaction, so processing can be performed faster. Thermoplastics have desirable qualities when it comes to environmental concerns, such as low toxicity, repairability, and near infinite shelf-life.[11] High-temperature thermoplastics are of interest in the aerospace industry because they sometimes have higher service temperatures than traditional epoxy-based resins and are less brittle than high-temperature thermosets. These properties give them potential for use in structural composites. However, these thermoplastics still have lower glass transition temperatures than novel high-temperature thermosets. Additionally, there is a lack of manufacturing infrastructure for thermoplastic composites, which require

completely different processing principles and equipment. These are the main reasons why the large-scale use of high-temperature thermoplastic resins has yet to be realized.[11]

The high-temperature thermoset polymers include polyimides (PIs), bismaleimides (BMIs), and cyanate esters (CEs). Due to the well-defined and supported manufacturing processes for thermoset-matrix composites and the demand for lightweight materials with higher service temperatures in aerospace and defense, high-temperature thermosets have the potential to become the future of the advanced composites industry. However, these resins are typically inelastic and brittle. In fact, their high curing temperatures can evoke transverse microcracks throughout the composite, as shown in **Figure 1.10**. Such microcracks in thermoset composites are typically caused by thermal and/or mechanical cycling, but in high-temperature composites, they can also develop due to residual stresses and differential shrinking after the curing process.[23,24] The higher cure temperatures cause higher residual thermal stresses and strains, which correlate with increased microcrack densities. Laminates cured at higher temperatures show a greater tendency to delaminate, contain wider and more crooked cracks, and form networks of cracks,[24] making them especially susceptible to damage during use. A number of chemical and physical approaches to increase the toughness of these resins have been explored (see more detailed technical review in CHAPTER 2).[20,21,25–30] However, most of these methods ended up being detrimental to either the thermal or structural properties of the resins. In addition, most approaches required modifications of composite processing and manufacturing that led to significantly increased costs. Consequently, the challenge of microcracking in high-temperature thermosets has yet to be overcome. Diminishing the development of microcracks while maintaining the strong

thermo-oxidative properties and well-established thermoset manufacturing processes is a critical advancement necessary to improve the applicability of high-temperature thermoset resins.

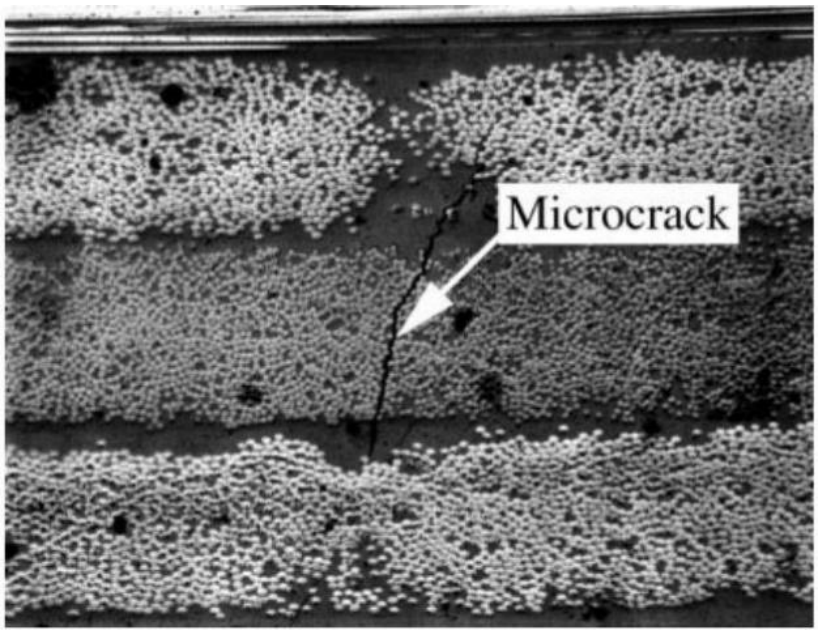

Figure 1.10: Transverse microcrack in a laminated composite developed after thermal and mechanical cycling. The material is carbon fiber-reinforced bismaleimide.[23]

1.2.4 Failure in Advanced Laminated Composites

Fiber-reinforced laminates experience several unique failure modes because they are highly anisotropic and heterogeneous (have multiple constituents with different mechanical properties). These failure modes include matrix cracking, fiber breakage, and debonding. As fibers fail and cracks grow and coalesce, local changes in stiffness occur. This causes a degradation of the effective mechanical properties of the composite. Therefore, all advanced fiber-reinforced composites exhibit gradual damage behavior. In general, composites are relatively damage tolerant, but for safety critical applications, suppression of early damage is essential.

Since the reinforcing fibers have extremely strong tensile strengths compared to the matrix, fiber failure is the preferred failure mode. However, since most thermosetting

resin matrices are brittle, the presence of microcracks in composites can result in catastrophic failure, making matrix fracture a concerning topic.[31]

When matrix cracking occurs in the resin-rich interlaminar planes, composite laminates experience a unique, critical failure mechanism called delamination, or the separation of the adjacent plies. Delamination cracks can be initiated by voids or contaminants in the layup and can propagate easily through the brittle polymer matrix during loading. Normal and/or shear interlaminar stresses can occur due to direct out-of-plane loadings,[32] but they can also be induced under in-plane loadings as a result of the mismatch of material properties between consecutive plies. These interlaminar stresses can even exhibit singular trends near certain discontinuities and structural design features, such as free edges or curves (see detailed technical review in CHAPTER 2).[4,33–35] In high-temperature composites, delamination is even more of an issue due to the increased susceptibility of high-temperature resins to microcracking combined with higher residual thermal stresses in these composites. As delamination cracks propagate, ultimate failure will occur, oftentimes at lower external loads than expected.[33]

Since delamination can lead to catastrophic failure, several methods have been developed in an attempt to suppress it by reducing and/or supporting the high interlaminar stresses (see detailed technical review in CHAPTER 2). Most of these techniques caused detrimental effects to the structural properties of the laminates. Most have also significantly increased manufacturing time and expenses.[36] Interleaving ductile layers between the load-bearing composite plies was shown to improve interlaminar fracture toughness. However, insertion of thick, ductile layers led to substantial increase of weight and decreases of in-plane properties, namely specific strength and stiffness,

which are the main advantages of composites.[37] Thus, increasing the delamination resistance while maintaining the excellent lightweight structural properties of advanced composite laminates remains a critical challenge.

1.3 NANOTECHNOLOGY AND COMPOSITES

Nanomaterials (NMs) are materials that possess internal or external structures with at least one nanoscale (1-1000 nm) dimension. Due to their tailorable mechanical, physiochemical, and biological characteristics resulting in enhanced performance over their bulk counterparts, NMs are at the forefront of materials research. Nanocomposite (NC) materials are multi-phase materials that incorporate at least one component with a nanoscale dimension. Although the combinations are limitless, NCs often combine nanoparticles (0D), nanofibers (1D), nanoplatelets (2D), nano-networks (3D), or a blend of these with a bulk metal, ceramic, or polymer matrix material. The mixture and morphology of NCs are determined by the material properties required for a desired application.[38]

Nanomaterials composed of carbon, such as carbon nanotubes (CNTs), show the potential as composite reinforcement because they are some of the stiffest and strongest materials ever synthesized.[39] After the first synthesis of carbon nanotubes in 1991 and the discovery of their extraordinary mechanical properties, research surrounding all types of CNTs and their applications increased.[40] Matrices reinforced with CNTs have shown to exhibit increased strength as well as useful functional properties such as electrical and thermal conductivity.[39,40] However, after more than three decades of intense research, the high strength of CNTs has yet to effectively translate into composite strength to obtain “super nanocomposites”, and it is unclear whether this translation is even possible.[41]

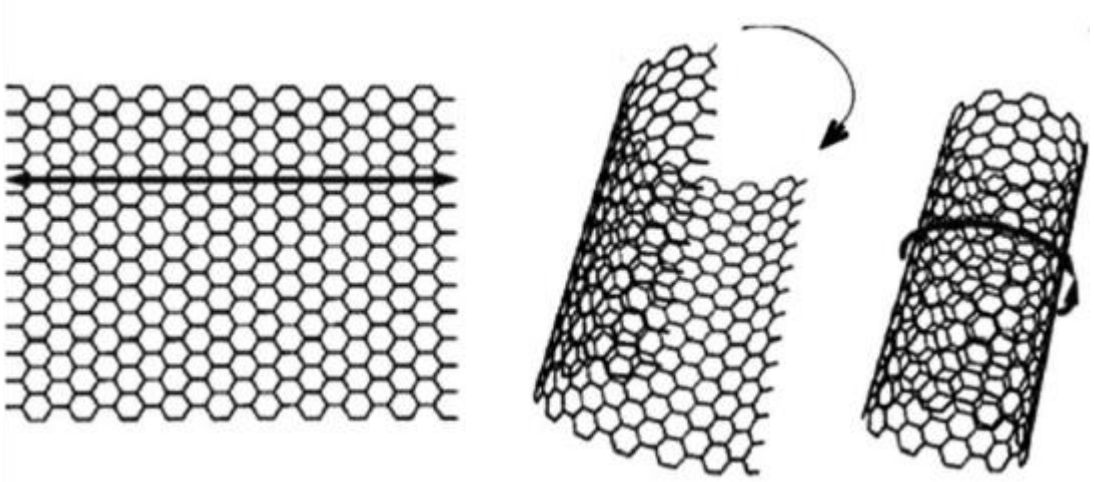

Figure 1.11: Graphene sheet being rolled into a carbon nanotube.[39]

In general, carbon nanomaterials can be explored to suppress delamination in composite laminates. One example of this involves the addition of carbon nanotubes (CNTs) to the polymer matrix or on the carbon fiber surfaces, which can enhance the interlaminar fracture toughness (IFT).[31,42,43] However, considering CNTs are among the stiffest and toughest structures ever synthesized, improvements were expected to be much greater.[39] There is also no guarantee that the CNTs will bridge interlaminar cracks, which is a significant toughening mechanism. Vapor grown carbon nanofibers (VGCNFs) have also been explored for enhancements of IFT.[44] However, VGCNFs are usually not uniform and have relatively low aspect ratios, which reduces their reinforcement efficiency. In addition, bottom-up synthesis and purification of VGCNFs and CNTs are very costly and can critically increase the cost of bulk composite applications.

The difficulties with CNTs and other nanoparticles are related to their discontinuity. CNTs have a tendency to agglomerate when dispersed in a polymeric medium.[39] Other nanomaterials, such as graphene and nanoclays, can also experience non-uniform dispersion. Other common issues noted when incorporating CNTs and other nanoparticles into composites are ineffective load transfer due to their discontinuous

morphologies and weak interfacial bonds, low particle volume fraction, and lack of tailorability and controlled anisotropy.[41] Although alignment of nanomaterials within polymer matrices can provide significantly enhanced load carrying capacity,[45] nanoparticles are difficult to orient due to their discontinuous nature.

Another potential detriment to CNTs is their ability to be inhaled by humans due to their small size. This can cause adverse effects to the pulmonary system.[38] Further research is necessary to determine the safest way to incorporate CNTs into industrial environments.[39]

Many of the problems that arise with CNTs are due to their discontinuity. Therefore, it is likely that a continuous nanomaterial would solve most of these issues and provide a more effective reinforcement in structural composites.

1.4 CONTINUOUS NANOFIBERS

Fibers with nanoscale diameters are an emerging class of nanomaterials that possess unique advantages for composite applications. They can be produced through a multitude of nanomanufacturing methods, which can be classified as either bottom-up or top-down. Bottom-up methods consist of vapor deposition and self-assembly. Top-down methods include melt spinning, gel spinning, centrifugal spinning, phase separation, drawing, interfacial polymerization, and template synthesis.[46,47] Nanofibers produced from bottom-up methods are generally discontinuous, while top-down methods usually produce continuous nanofibers. The continuity of continuous nanofibers differentiates them from other nanomaterials, such as carbon nanotubes, and, subsequently, allows them to overcome many of the challenges that discontinuous nanomaterials face.

Although several methods can produce continuous nanofibers, electrospinning is the most popular. Electrospinning is a cost-efficient, top-down nanomanufacturing process in which a polymer solution is subjected to a high voltage. As the solution is fed through a spinneret, the electric potential allows the charged polymer to overcome surface tension, emitting a thin jet of solution. As the jet is drawn by the electric field, it experiences several types of instabilities.[48] These instabilities promote rapid jet thinning, while continuous solvent evaporation leads to jet solidification and production of dry, ultra-fine, continuous nanofibers. By altering solution parameters (viscosity, polymer molecular weight, conductivity), process parameters (applied voltage, spinneret-to-collector distance, solution flow rate), and environmental parameters (temperature, relative humidity), continuous polymer fibers with diameters ranging from several nanometers to a few micrometers can be obtained.[49,50]

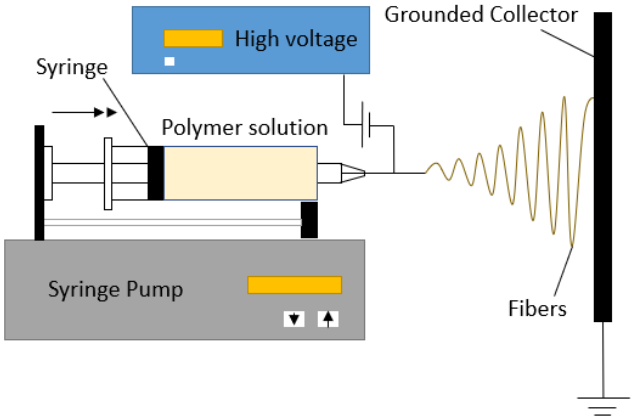

Figure 1.12: Typical electrospinning process.

The method of electrospinning has developed over the last century and a half or so. In 1887, Charles V. Boys discovered that a viscoelastic liquid could be drawn into fibers in the presence of an external electric field. In 1902, the first two patents for electrospinning were filed by John Cooley and William Morton. In 1938, electrospun NFs were first implemented in the Soviet Union for use in air filters, known as

"Petryanov filters." However, it was not until the mid-1990s that the technique really took off. Several research groups, including Dzenis lab at the University of Nebraska-Lincoln, demonstrated that numerous different organic polymers could be electrospun into NFs. Continuous carbon and ceramic nanofibers have also been produced from electrospun precursors. This made the newly coined "electrospinning" process the method of choice for producing long, continuous, nanoscale fibers.[51]

The electrospinning process provides a versatility that enables almost any soluble polymer to be spun into ultra-fine, continuous nanofibers. Several variations of the process allow for the manufacturing of different configurations and morphologies of electrospun NFs, which is extremely challenging for other nanomaterials such as CNTs or VGCNFs.[52] In the last few decades, the ability to electrospin new materials with a variety of structures paved the way for the development of new applications, including catalysis, sensors, filtration, "smart" materials, biomedicine, and energy harvesting, conversion, and storage.[53,54] Recently, industrial production of NFs has increased thanks to new manufacturing technology, enabling downstream commercial products.[51]

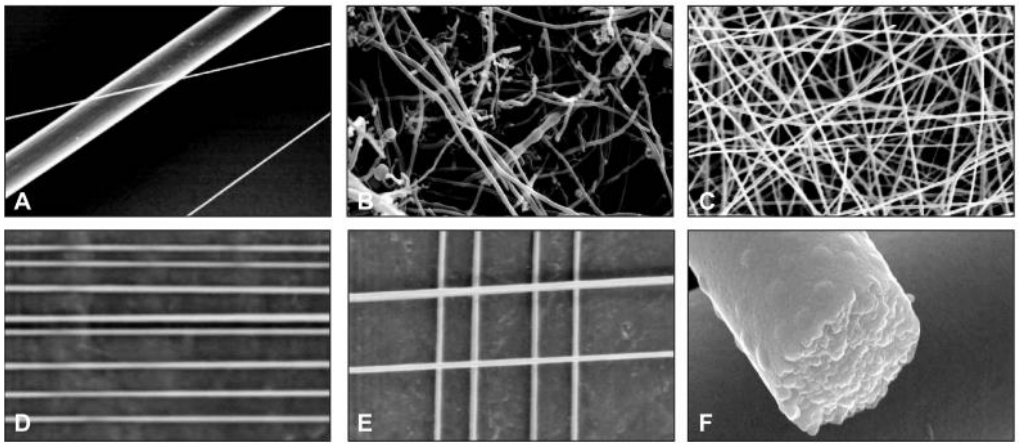

Figure 1.13: (A) Comparison of a commercial carbon fiber and an electrospun nanofiber. Comparison of (B) vapor-grown commercial carbon nanofibers and (C) electrospun carbon nanofibers showing much better uniformity and purity. (D and E) Highly aligned unidirectional and orthogonal continuous nanofibers produced with the gap method. (F) Cross section view of a nanocrystalline zirconia nanofiber with applications in ultra-tough ceramics.[52]

Continuous electrospun nanofibers are generally expected to exhibit enhanced mechanical properties while maintaining distinct advantages over other materials. Their nanoscale dimensions can lead to increased molecular alignment and decreased defect density, which can grant them improved mechanical performance over commercial fibers.[55] Continuous nanofibers also possess ultrahigh surface area-to-volume ratios, which can increase interfacial bond strength and enhance load transfer, making nanofibers promising applicants to reinforce composites.[41,56] The continuity of nanofibers can improve their handling and characterization while avoiding potential health hazards inherent to other discontinuous nanomaterials (e.g. nanoparticles, nanotubes, whiskers).[57]

Perhaps the most impressive property of electrospun nanofibers is their ability to exhibit simultaneous improvements in strength, modulus, and toughness at ultrafine diameters, as shown in **Figure 1.14**. In contrast to most structural materials, including high-performance fibers, which show increases in strength at the expense of failure strain, polyacrylonitrile (PAN) nanofibers electrospun at the University of Nebraska-Lincoln showed increases in strength without any statistical decrease in strain at failure.[58] This unique property was due to the high molecular alignment and low crystallinity within the polymer NFs.[58]

In addition to PAN NFs, electrospun polyimide (PI) nanofibers exhibited similar size-dependent mechanical properties.[59] These PI NFs can be particularly useful for high-temperature applications due to their high glass-transition temperatures. However, there are limited studies on their use as reinforcement in composites to date.

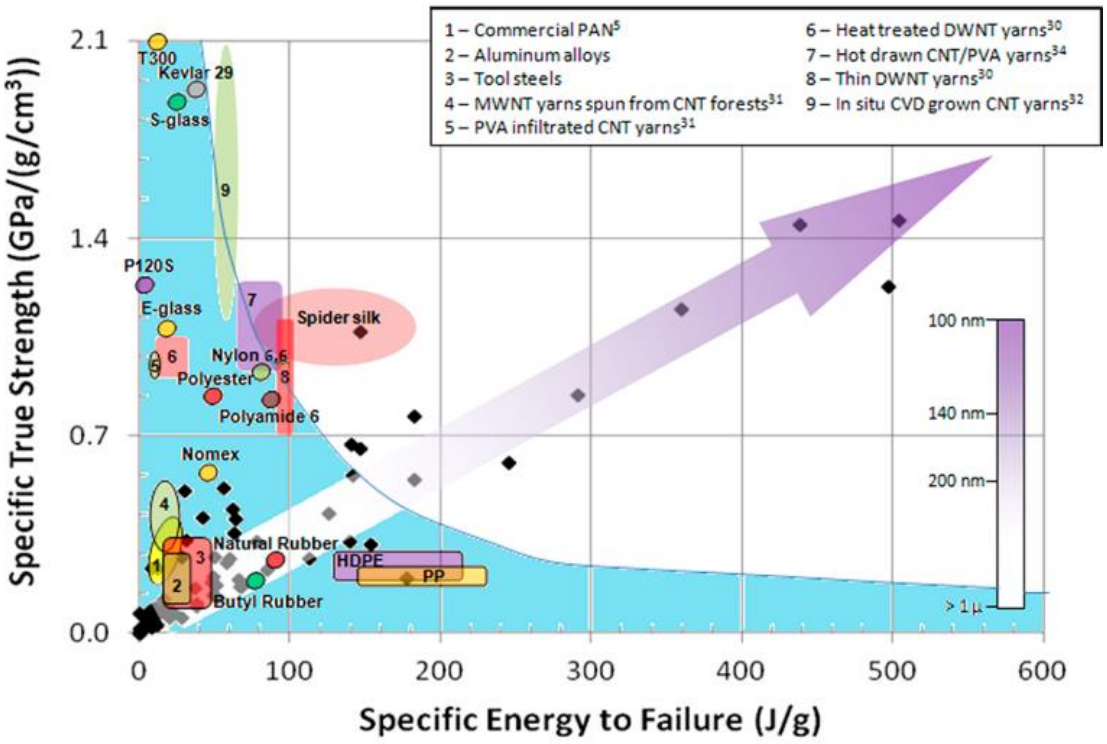

Figure 1.14: Specific energy to failure versus specific true strength for some commercial fibers and materials. Diamonds represent as-spun polyacrylonitrile (PAN) nanofibers. The arrow density indicates approximate nanofiber diameters (see scale bar). The colored area represents the strength/toughness region occupied by traditional materials.[58]

Several polymer materials have been electrospun into continuous nanofibers and used as bulk reinforcement in polymer matrix nanocomposites,[60] but the "super" properties exhibited by NFs themselves have yet to be realized in composites. With the development of nanomanufacturing techniques to better control the alignment, morphologies, diameters, and mass production of continuous nanofibers comes the ability to produce nanofiber-reinforced composites with enhanced structural properties. In addition, improving the mechanical properties of individual nanofibers could lead to the development of next-generation structural applications.[56]

1.5 NANOFIBER-REINFORCEMENT OF INTERFACES IN ADVANCED COMPOSITE LAMINATES

In addition to primary reinforcement of polymer matrices, continuous nanofibers also have the ability to serve as secondary reinforcement in composite laminates. Recently, significant interest has been focused on the nanoreinforcement of laminated composites. Nanomaterials have the potential to provide significant delamination suppression by toughening the thin, resin-rich interlayer between plies while maintaining the high in-plane properties of laminated composites.

Although adding CNTs and VGCNFs to composite laminates can increase delamination resistance, the most promising method, which was developed in part by researchers at the University of Nebraska-Lincoln, involves the use of continuous electrospun nanofiber sheets to reinforce the interfaces between plies.[61] This marked the foundation of a new field of advanced composites research.

Continuous electrospun nanofiber "interleaves" can significantly increase interlaminar fracture toughness, but they can also improve in-plane properties because they add negligible weight and thickness and serve as a secondary reinforcement.[45,61,62] Continuous NFs are also more likely to bridge across the interlaminar crack,[63] which increases the energy needed for it to grow. Since hundreds of polymers can be electrospun into continuous nanofibers, the optimal polymer can be chosen based on the matrix material and requirements of the application. Electrospinning can also be easily integrated into existing laminate manufacturing methods through either direct collection onto composite plies or post-spinning application of nanofiber mats. These factors differentiate continuous NF interleaves from previous interleaf materials and other nanoreinforcements.

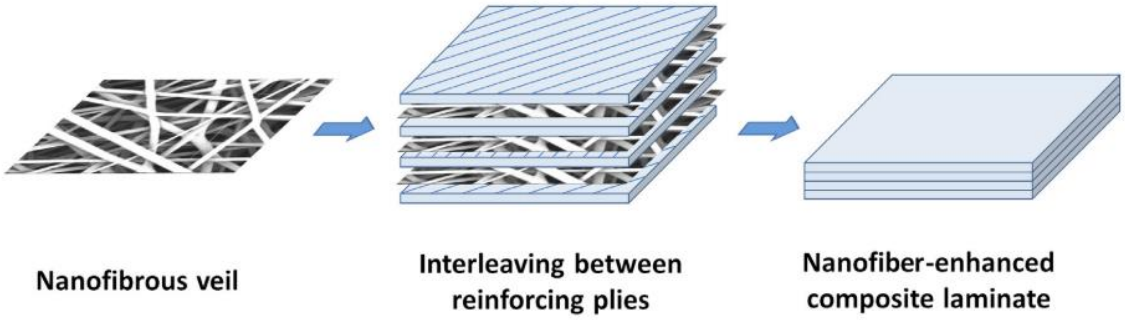

Figure 1.15: Concept of interleaving nanofibrous veils in between the primary reinforcing layers, resulting in a nanofiber-enhanced composite laminate with tough interlayers.[64]

Up to now, several studies have been performed investigating different electrospun NF materials for improving modes I and II interlaminar fracture toughness of conventional advanced laminated composites, such as carbon/epoxy laminates.[45] However, as mentioned above, emerging high-temperature applications require the use of composites with high service temperatures, which are particularly susceptible to microcracking and delamination. To the best of our knowledge, interlaminar reinforcement of high-temperature composites with continuous nanofibers has not yet been studied. The development of novel, high-temperature, nanotoughened materials could help lead the charge in developing next-generation composite laminates for a broad range of emerging and new applications.

In addition to pure mode I and II interlaminar fracture toughening, continuous nanofiber reinforcement can improve in-plane, bending, impact, compression after impact, tension, and fatigue performance of laminated composites.[45,65–68] Certain design features, such as holes, curves, and joints, that are prominent in composite structures are especially prone to delamination. In addition to direct out-of-plane structural loadings, interlaminar stresses in such features can be caused by a combination of material anisotropy *and* geometric discontinuities (see detailed technical review in CHAPTER 2).

Nonetheless, studies regarding the translation of material improvements observed as a result of nanofiber reinforcement in simple, pure-mode fracture tests to actual complex composite structures are extremely limited. Since composite structures experience much more complex, 3D stress states, this translation is not trivial. To expand the use of continuous electrospun NFs in advanced composite laminates for structural applications, the effectiveness of NF interleaves in composite structures must be investigated.

1.6 SUMMARY AND OVERALL GOALS OF THE DISSERTATION

Fiber-reinforced, polymer-matrix laminates are some of the most advanced structural materials available today. They offer enhanced specific strength and stiffness, fatigue and corrosion resistance, and tailorability of properties compared to isotropic metallic alloys. However, their anisotropic mechanics leads to the unique and critical failure mechanism of delamination. Although several methods have been developed to suppress delamination, perhaps the most promising is the use of electrospun nanofiber reinforcement at ply interfaces. Although several studies have proved nanofiber ability to suppress delamination in conventional carbon/epoxy composites, mechanical results on composites made from high-temperature resins reinforced with novel high-temperature nanofibers are virtually nonexistent. As a result, the first main goal of this research is to investigate delamination of a high-temperature resin matrix composite reinforced with electrospun NFs, which would be highly applicable to the growing number of high-temperature applications. Results are compared to traditional carbon/epoxy material.

Although NF interleaves have proven an effective interlaminar toughener, material improvements have mostly only been documented based on modes I and II interlaminar fracture toughness and in-plane properties of 2D plates. More investigation

is needed to determine how the toughening effectiveness of NF interleaves translates to 3D structures with design features especially prone to delamination. Thus, the second main goal of this dissertation is to investigate the toughening effect of continuous NF interleaves in composites structures.

Lastly, two exploratory subjects were explored. These include enhancing nanofiber alignment to manufacture and characterize nanolaminated composites and templating carbon nanofibers with two-dimensional nanomaterials to improve their graphitic structure. Introductions and objectives for these two exploratory studies will be provided in their respective sections.

1.7 ORGANIZATION OF THE DISSERTATION

CHAPTER 2 of this dissertation reviews and examines nanofiber reinforcement of laminated composites, particularly for high-temperature applications. The advantages and disadvantages of composite laminates are listed. Delamination and its anisotropic mechanics are discussed. Delamination suppression techniques, including nanofiber-interleaving, and their pros and cons are also reviewed and discussed. High-temperature resins and the methods for toughening them are reviewed, and structural sources of delamination are discussed. Lastly, the summary and technical problem statements for this dissertation are given.

CHAPTER 3 describes a systematic investigation of nanofiber-reinforcement in interlaminar regions of composites. Modes I and II interlaminar fracture toughness (IFT) tests are performed on pristine and NF-reinforced carbon fiber composites. Although IFT tests have been performed on NF-reinforced composites before, a new material combination (cyanate ester matrix with polyimide nanofibers), which is especially

applicable to high-temperature applications, is studied for the first time. The results on this material are compared to those obtained with traditional carbon/epoxy laminates reinforced with polyacrylonitrile nanofibers. This study provides a baseline for the analysis of translation of NF-toughening to composite structures conducted in the next chapter.

In CHAPTER 4, an attempt to extend delamination suppression via NF-interleaving from simple modes I and II failure to more complex structural failure modes is described. NF-reinforcement of structural design features especially prone to delamination is investigated. Manufacturing and mechanical testing of multidirectional laminated plates with and without holes and unidirectional curved L-bend panels are performed on both the carbon/epoxy material (reinforced with polyacrylonitrile NFs) and the carbon/cyanate ester material (reinforced with polyimide NFs) for the first time.

CHAPTER 5 outlines a systematic study of the effects of electrospinning process parameters on the degree of continuous nanofiber alignment. The electrospinning process and its inherent jet instabilities are analyzed via direct high-speed observation. The fabrication and testing, along with associated challenges, of both carbon nanofiber-reinforced epoxy and polymer nanofiber-reinforced high-temperature cyanate ester resin are explained. Results comparing the mechanical properties of pure resin and multiple sets of nanolaminates will be provided.

Finally, CHAPTER 6 of this dissertation summarizes the results of the research and proposes potential future research directions.

In addition, APPENDIX D includes the description of an exploratory study involving the templating of continuous nanofibers with two-dimensional, carbon-based

nanomaterials. Graphene nanoribbons and Ti_3C_2 MXenes are added to polymer solutions in an attempt to produce continuous carbon nanofibers with improved graphitic structures. Graphitic order is characterized with Raman spectroscopy and results are compared to those of pristine carbon nanofibers.

CHAPTER 2. CONTINUOUS NANOFIBER REINFORCEMENT OF LAMINATED COMPOSITE STRUCTURES FOR HIGH-TEMPERATURE APPLICATIONS: REVIEW AND TECHNICAL PROBLEM IDENTIFICATION

Due to their numerous advantages, advanced composites will continue to be popular materials for structural applications. As mentioned before, the most common type of fiber-reinforced composite used for structural applications is a laminate. Although composite laminates possess several critical advantageous properties, their inhomogeneous nature causes them to experience multiple, unique failure mechanisms.

Failure that is confined to the resin-rich phase between plies can be described using linear elastic fracture mechanics (LEFM). In the interlaminar planes, crack propagation can occur through opening (mode I), shearing (mode II), tearing (mode III), or mixed modes.[69] Interlaminar fracture, or delamination, is induced by interlaminar tensile and shear stresses, which are especially high near free edges due to the mismatch in material properties between unidirectional plies oriented at different angles.[35,70] In addition, certain design features of composite structures are especially prone to delamination.[33]

Several methods have been developed to suppress delamination, of which nanofiber-reinforcement of ply interfaces seems to be the most promising. However, NF-reinforcement of the interlaminar regions of laminates has yet to be extended to composite structural elements that experience complex 3D stress states. In addition, delamination suppression studies on high-temperature polymer-matrix composites, which can experience extensive microcracking due to their high curing temperatures and thermomechanical cycling during use, are extremely limited. Successful reinforcement of high-temperature composite structures using electrospun NFs could help develop the next

generation of structural materials. In this Chapter, detailed technical review of the relevant issues is presented and used to formulate the technical problems.

2.1 ADVANTAGES OF LAMINATED COMPOSITES

Composite laminates are comprised of layered plies. Although these plies can be multidirectional, unidirectional (UD) plies allow for the highest fiber volume fractions, which produces the highest mechanical performance. Unidirectional plies, or lamina, are very strong and stiff in the fiber (longitudinal) direction, but they are much weaker in the direction perpendicular to the fibers (transverse) because the load must be supported by the much weaker and softer matrix. While a high-strength fiber might have a tensile strength of 5000-6000 MPa, the tensile strength of a polymer matrix is typically between 35 and 70 MPa. The difference in moduli, which determines inhomogeneous internal stresses, can be equally high or higher. For example, a high modulus carbon fiber can have a modulus of 350-450 GPa, while epoxy resins typically exhibit moduli between 3 and 6 GPa. These differences in strengths and stiffnesses make UD plies highly anisotropic.

Although it would make sense to orient as many fibers as possible along the direction of loading, this is only practical for a handful of applications. In reality, it is usually necessary to balance the load-carrying capability in several different directions, which is why lamination is so popular. Although there are infinitely many potential layups, one popular example is a balanced laminate that has equal numbers of 0°, +45°, -45°, and 90° plies. This is called a *quasi-isotropic* layup because it behaves isotropically under in-plane loadings.[1]

Depending on the requirements of the application, laminate properties can be tailored to meet the structural needs. This is done through altering the layup of the laminate. Although quasi-isotropic layups are common, some applications require more specialized layups. The ability to control the anisotropy of laminates gives them great design flexibility and the potential to be used in a wide variety of applications that are only possible with distinct laminate designs.[11]

In addition to their controlled anisotropy, composite laminates can provide significant weight savings because they exhibit significantly higher specific strengths and stiffnesses compared to other structural materials, such as aluminum and steel.

Laminates are also relatively simple and cheap to manufacture. Fiber alignment must be carefully controlled during composite fabrication. To create a UD ply, or tape, fibers can be directly drawn out from a spool into a fiber tow and coated in resin.[1,11] Automated tape-laying machines are used to carefully align the high-performance fibers and eliminate the possibility of human error. One of the most common methods used for laminate processing involves the stacking of UD fiber preforms impregnated with a controlled amount of tacky, semisolid (B-stage) resin.[1] These pre-impregnated plies, or "prepregs" can also be fabricated by hot melt impregnation, resin filming, or solvent impregnation.[1] Another popular method that uses UD plies as building blocks is called filament winding, in which fibers are wound and layered around a mandrel. This method also creates a lamination effect.

The simplicity, flexibility, cost-effectiveness, and enhanced properties of advanced composites laminates composed of unidirectional plies are what makes them so popular for high-performance applications. However, the lamination of their anisotropic

UD plies creates a heterogeneity that produces complex internal stress distributions, complicated damage evolution, and unique failure mechanisms.

2.2 MECHANICS OF LAMINATED COMPOSITES

Because composite laminates are built from continuous fibers and a matrix, they are inherently heterogeneous. This makes their mechanical analysis complex. The unidirectional plies that serve as laminate building blocks are highly anisotropic, i.e., they respond very differently depending on the direction of the applied load. Therefore, they are considered anisotropic. Understanding of anisotropic mechanics of individual unidirectional plies is critical to understanding of mechanisms and analysis of interlaminar stresses in laminated composites.

For linear elastic materials, generalized Hooke's law can be written as

$$\sigma_{ij} = C_{ijkl}\varepsilon_{kl} \qquad i,j,k,l = 1,2,3$$

where σ_{ij} are the stress components shown on the cube in **Figure 2.1**, C_{ijkl} are the components of the stiffness matrix, and ε_{kl} are the strain components. The contracted notation, which is defined in **Table 2.1**, of generalized Hooke's law can be written as $\sigma_i = C_{ij}\varepsilon_j$ where $i,j = 1,\dots,6$. The inverse of this can be written as $\varepsilon_i = S_{ij}\sigma_j$ where $i,j = 1,\dots,6$ and S_{ij} are the components of the compliance matrix. Here, the strains are defined as

$$\varepsilon_1 = \frac{\partial u}{\partial x} \qquad \varepsilon_2 = \frac{\partial v}{\partial y} \qquad \varepsilon_3 = \frac{\partial w}{\partial z}$$

$$\gamma_{23} = \frac{\partial v}{\partial z} + \frac{\partial w}{\partial y} \qquad \gamma_{31} = \frac{\partial w}{\partial x} + \frac{\partial u}{\partial z} \qquad \gamma_{12} = \frac{\partial u}{\partial y} + \frac{\partial v}{\partial x}$$

where u, v, and w are the displacements in the x, y and z (or 1, 2, and 3) directions.

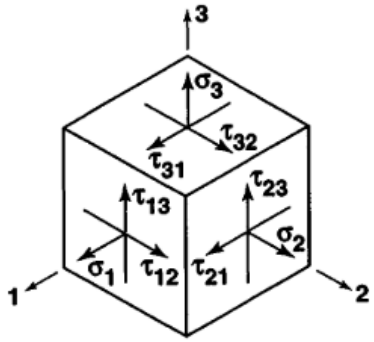

Figure 2.1: Stresses on a 3D element.[71]

Table 2.1: Tensor versus contracted notation for stresses and strains. *Note that γ_{ij} represents engineering shear strain whereas ε_{ij} $(i \neq j)$ represents tensor shear strain.[71]

Stresses		Strains	
Tensor Notation	Contracted Notation	Tensor Notation	Contracted Notation
σ_{11} (σ_1)	σ_1	ε_{11} (ε_1)	ε_1
σ_{22} (σ_2)	σ_2	ε_{22} (ε_2)	ε_2
σ_{33} (σ_3)	σ_3	ε_{33} (ε_3)	ε_3
$\tau_{23} = \sigma_{32}$	σ_4	$\gamma_{23} = 2\varepsilon_{23}$*	ε_4
$\tau_{31} = \sigma_{31}$	σ_5	$\gamma_{31} = 2\varepsilon_{31}$	ε_5
$\tau_{12} = \sigma_{12}$	σ_6	$\gamma_{12} = 2\varepsilon_{12}$	ε_6

The stiffness matrix $[C]$ is a 6x6 matrix, meaning it has 36 constants. However, when the strain energy is considered, it can be shown that $C_{ij} = C_{ji}$. Thus, the stiffness matrix is symmetric and has a maximum of 21 independent components for the most general anisotropic material. For materials with any degree of symmetry, the stiffness matrix can be simplified, and the number of independent constants will be reduced.[71]

Unidirectional plies are defined as orthotropic, meaning they have three mutually orthogonal axes of symmetry. Since they respond differently in 3 perpendicular directions, orthotropic materials have stiffness matrices with 9 independent constants: 3 Young's moduli, 3 shear moduli, and 3 Poisson's ratios. The compliance matrix for an orthotropic material can be written as

$$[S_{ij}] = \begin{bmatrix} \frac{1}{E_1} & -\frac{\nu_{21}}{E_2} & -\frac{\nu_{31}}{E_3} & 0 & 0 & 0 \\ -\frac{\nu_{12}}{E_1} & \frac{1}{E_2} & -\frac{\nu_{32}}{E_3} & 0 & 0 & 0 \\ -\frac{\nu_{13}}{E_1} & -\frac{\nu_{23}}{E_2} & \frac{1}{E_3} & 0 & 0 & 0 \\ 0 & 0 & 0 & \frac{1}{G_{23}} & 0 & 0 \\ 0 & 0 & 0 & 0 & \frac{1}{G_{31}} & 0 \\ 0 & 0 & 0 & 0 & 0 & \frac{1}{G_{12}} \end{bmatrix}.$$

Figure 2.2a shows the difference between an isotropic plate and an orthotropic, unidirectional fiber-reinforced plate. For orthotropic materials, the stiffness in the first principal direction (parallel to the fibers) is much different than those in the second (in-plane) and third (out-of-plane) principal directions, which are perpendicular to the fibers. In some cases, the properties are similar in the second and third principle directions. These materials can be approximated as monotropic, or transversely isotropic, and they will have 5 independent elastic constants.

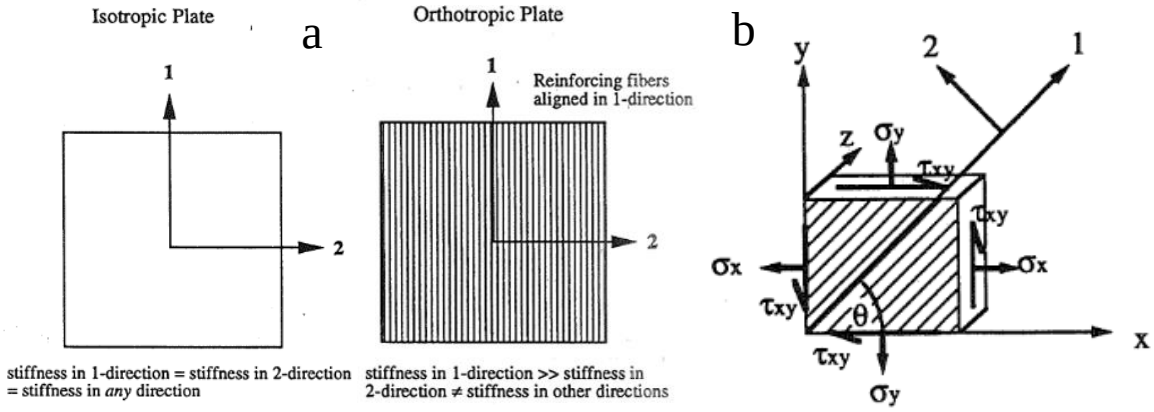

Figure 2.2: (a) Difference between an isotropic and an orthotropic plate. (b) Definition of the material (1-2) and x-y coordinate systems.[72]

For orthotropic lamina in a laminated composite, it is conventional to assume a plane stress condition, meaning $\sigma_3 = \tau_{13} = \tau_{23} = 0$.[71] This reduces the strain-stress relations to

$$\begin{bmatrix} \varepsilon_1 \\ \varepsilon_2 \\ \gamma_{12} \end{bmatrix} = \begin{bmatrix} S_{11} & S_{12} & 0 \\ S_{12} & S_{22} & 0 \\ 0 & 0 & S_{66} \end{bmatrix} \begin{bmatrix} \sigma_1 \\ \sigma_2 \\ \tau_{12} \end{bmatrix} \quad \text{where} \quad S_{11} = 1/E_1 \qquad S_{22} = 1/E_2$$
$$S_{12} = -\nu_{12}/E_1 = -\nu_{21}/E_2 \qquad S_{66} = 1/G_{12} .$$

These relations can be inverted to determine the stress-strain relations

$$\begin{bmatrix} \sigma_1 \\ \sigma_2 \\ \tau_{12} \end{bmatrix} = \begin{bmatrix} Q_{11} & Q_{12} & 0 \\ Q_{12} & Q_{22} & 0 \\ 0 & 0 & Q_{66} \end{bmatrix} \begin{bmatrix} \varepsilon_1 \\ \varepsilon_2 \\ \gamma_{12} \end{bmatrix} \quad \text{where} \quad Q_{11} = \frac{E_1}{1-\nu_{12}\nu_{21}} , \qquad Q_{22} = \frac{E_2}{1-\nu_{12}\nu_{21}} ,$$
$$Q_{12} = \frac{\nu_{12}E_2}{1-\nu_{12}\nu_{21}} = \frac{\nu_{21}E_1}{1-\nu_{12}\nu_{21}} , \qquad Q_{66} = G_{12} .$$

Here, matrix [Q] is called the reduced stiffness matrix. Note that there are only 4 independent elastic constants in these relations because $\nu_{21} = \frac{E_2}{E_1}\nu_{12}$.[71] For the plane-stress condition, these relations are identical for orthotropic and monotropic materials.

If the unidirectional ply is rotated by an angle θ with respect to the applied load, as shown in **Figure 2.2**b, a coordinate transformation is needed to determine the stresses and strain in the x-y system. This can be done with the use of the 3x3 tensorial transformation matrix [T], which can be used for both stresses and strains:

$$\begin{bmatrix} \sigma_1 \\ \sigma_2 \\ \tau_{12} \end{bmatrix} = \begin{bmatrix} \cos^2\theta & \sin^2\theta & 2\sin\theta\cos\theta \\ \sin^2\theta & \cos^2\theta & -2\sin\theta\cos\theta \\ -\sin\theta\cos\theta & \sin\theta\cos\theta & \left(\cos^2\theta - \sin^2\theta\right) \end{bmatrix} \begin{bmatrix} \sigma_x \\ \sigma_y \\ \tau_{xy} \end{bmatrix}$$

With the inverse of [T], the stresses and strains in the x-y system can be converted back to the 1-2 (material) system. Hence:

$$\begin{bmatrix}\sigma_1\\ \sigma_2\\ \tau_{12}\end{bmatrix}=[T]\begin{bmatrix}\sigma_x\\ \sigma_y\\ \tau_{xy}\end{bmatrix}\quad\text{and}\quad\begin{bmatrix}\sigma_x\\ \sigma_y\\ \tau_{xy}\end{bmatrix}=[T]^{-1}\begin{bmatrix}\sigma_1\\ \sigma_2\\ \tau_{12}\end{bmatrix},\quad\begin{bmatrix}\varepsilon_1\\ \varepsilon_2\\ \varepsilon_{12}\end{bmatrix}=[T]\begin{bmatrix}\varepsilon_x\\ \varepsilon_y\\ \varepsilon_{xy}\end{bmatrix}\quad\text{and}\quad\begin{bmatrix}\varepsilon_x\\ \varepsilon_y\\ \varepsilon_{xy}\end{bmatrix}=[T]^{-1}\begin{bmatrix}\varepsilon_1\\ \varepsilon_2\\ \varepsilon_{12}\end{bmatrix}.$$

With some rearrangements, one can obtain the equation

$$\begin{bmatrix}\sigma_x\\ \sigma_y\\ \tau_{xy}\end{bmatrix}=[T]^{-1}[Q]\begin{bmatrix}1&0&0\\ 0&1&0\\ 0&0&2\end{bmatrix}[T]\begin{bmatrix}\varepsilon_x\\ \varepsilon_y\\ \varepsilon_{xy}\end{bmatrix}$$

where a new matrix $[\bar{Q}]$ can be defined as

$$[\bar{Q}]=[T]^{-1}[Q]\begin{bmatrix}1&0&0\\ 0&1&0\\ 0&0&2\end{bmatrix}[T].$$

The 2 arises from the fact that $\gamma_{xy}=2\varepsilon_{xy}$. If $m=\cos\theta$ and $n=\sin\theta$, the components of the stiffness matrix $[\bar{Q}]$ in the new, rotated coordinate system can be defined as

$$\bar{Q}_{11}=Q_{11}m^4+2\left(Q_{12}+2Q_{66}\right)m^2n^2+Q_{22}n^4,$$

$$\bar{Q}_{12}=\left(Q_{11}+Q_{22}-4Q_{66}\right)m^2n^2+Q_{12}\left(m^4+n^4\right),$$

$$\bar{Q}_{22}=Q_{11}n^4+2\left(Q_{12}+2Q_{66}\right)m^2n^2+Q_{22}m^4,$$

$$\bar{Q}_{16}=\left(Q_{11}-Q_{12}-2Q_{66}\right)m^3n+\left(Q_{12}-Q_{22}+2Q_{66}\right)mn^3,$$

$$\bar{Q}_{26}=\left(Q_{11}-Q_{12}-2Q_{66}\right)n^3m+\left(Q_{12}-Q_{22}+2Q_{66}\right)nm^3,$$

$$\bar{Q}_{66}=\left(Q_{11}+Q_{22}-2Q_{12}-2Q_{66}\right)m^2n^2+Q_{66}\left(m^4+n^4\right).$$

The final relationship can be written as

$$\begin{bmatrix}\sigma_x\\ \sigma_y\\ \tau_{xy}\end{bmatrix}=\begin{bmatrix}\bar{Q}_{11}&\bar{Q}_{12}&\bar{Q}_{16}\\ \bar{Q}_{12}&\bar{Q}_{22}&\bar{Q}_{26}\\ \bar{Q}_{16}&\bar{Q}_{26}&\bar{Q}_{66}\end{bmatrix}\begin{bmatrix}\varepsilon_x\\ \varepsilon_y\\ \gamma_{xy}\end{bmatrix}.$$

In orthotropic plies, only normal strains are produced when a load is applied parallel to either of the principle material axes (1-2). However, when a load is applied at a direction not parallel to these axes, the terms $\bar{Q}_{16}$ and $\bar{Q}_{26}$ will also be nonzero, meaning normal stresses can be produced from shear strains and shear stresses can be produced from normal strains. This is called extension-shear coupling.[72] For general anisotropic materials, the physical significance of the stress-strain relationships are shown in **Figure 2.3**.

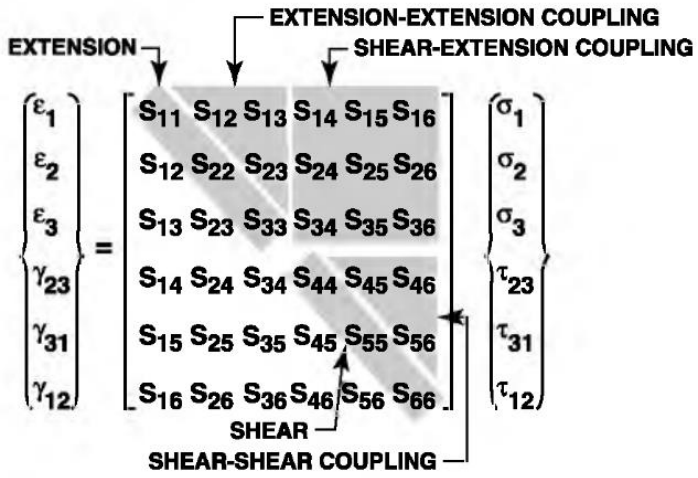

Figure 2.3: Physical significance of the anisotropic stress-strain relations.[71]

When orthotropic laminae are stacked to create a laminate, a special method is required to perform mechanical analysis. This method is called classical lamination theory (CLT). Comprehensive explanations of CLT can be found in many composites textbooks, for example in a classical book by Jones.[3]

2.3 MECHANISMS OF DELAMINATION

Delamination is a critical failure mechanism in composite laminates that occurs when interlaminar cracks initiate in and propagate through the unreinforced planar region between plies. These interlaminar cracks, along with cracks in general, can propagate under three different fracture modes: mode I (opening), mode II (sliding), and mode III

(tearing) (see **Figure 2.4**). Depending on the types of interlaminar stresses a composite laminate experiences, different fracture modes can occur during the delamination fracture process. Although interlaminar cracks can be initiated by defects generated during processing due to locally poor adhesion, contaminants, or voids between plies,[32] they can also originate in the absence of defects. In fact, due to the lamination of highly anisotropic plies, delamination can be caused by high interlaminar stresses, which can approach infinite values at free edges. Although they were originally unexpected and not discovered or analyzed until the 1970s, these "edge effects" are now commonly accepted to be the primary reason for delamination.[70]

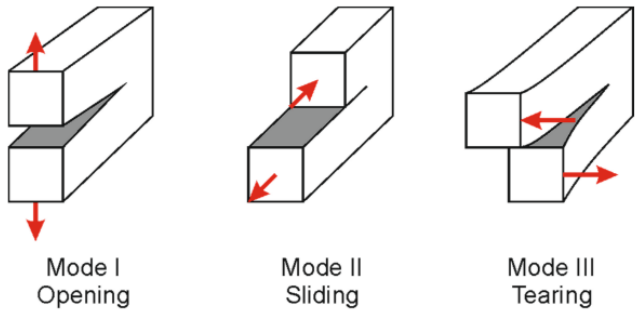

Figure 2.4: The three different modes of fracture that are distinguished according to the direction of the applied load with respect to the crack plane.[73]

Under plane stress loadings, there are two mechanisms that cause interlaminar stresses near edges: mismatch in the Poisson's ratio ν_{xy} and mismatch in the coefficient of mutual influence $\eta_{xy,x}$. The latter defines the shear-extension coupling in an anisotropic ply. Although these mechanisms can occur simultaneously in laminates, they will be described separately for simplicity.

To explain the mechanism of Poisson's ratio mismatch, a cross-ply laminate (plies oriented at either 0° or 90°) can be used as an example because there is no $\eta_{xy,x}$ mismatch (it is zero for both layers). In cross-ply laminates, when a uniaxial external

stress σ_x is applied, the 0° and 90° plies want to deform differently because they possess different Poisson's ratios ν_{xy}. However, since the plies are bonded together, they deform uniformly. This gives rise to a nonzero internal stress σ_y, which can be computed by CLT. Force equilibrium requires that this σ_y is offset with an interlaminar shear stress τ_{yz}, and moment equilibrium requires that an interlaminar peel stress σ_z is distributed at the interface. This mechanism is illustrated in **Figure 2.5**. It should be noted that σ_z (or σ_{33}) exhibits a mathematically singular value at the free edge, making this location extremely prone to delamination onset.[34]

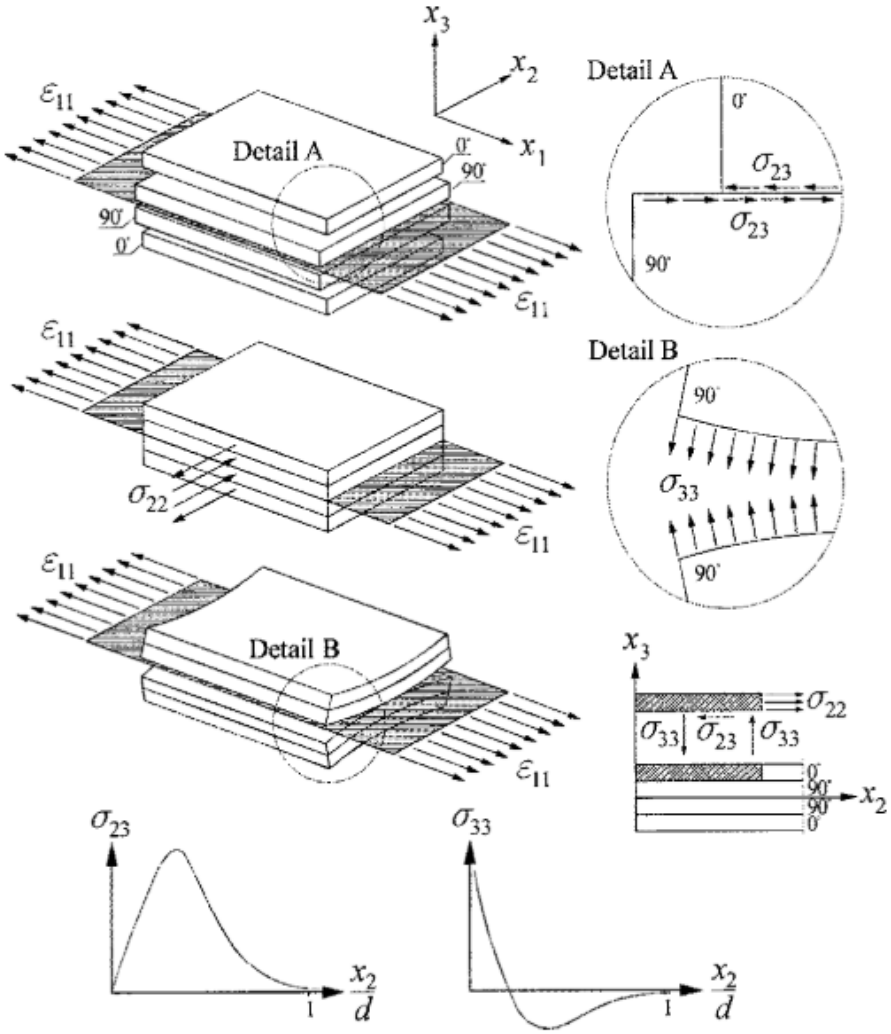

Figure 2.5: The free edge effects in a cross-ply $[0°/90°]_S$ laminate under uniaxial tension. *Note that the x_1, x_2, and x_3 axes are equivalent to the x, y, and z axes.[34]

The mismatch in the coefficient of mutual influence $\eta_{xy,x}$, which represents coupling between extension in the x-direction and shear in the x-y plane, can also contribute to edge delamination. When a $[\pm 45°]_S$ angle-ply laminate is subjected to a uniaxial stress σ_x, there is no mismatch in Poisson's ratio ν_{xy}. However, due to shear-extension coupling, the +45° and -45° plies want to deform differently under the uniaxial stress. Since they are bonded together, they deform uniformly, which induces a shear CLT stress τ_{xy}. To maintain equilibrium, the nonzero τ_{xy} gives rise to the shear stress τ_{xz}, which is distributed along the interlaminar plane between +45° and -45° plies. This mechanism is shown in **Figure 2.6**. Similar to σ_z, the shear interlaminar stress τ_{xz} (or σ_{13}) also shows a singular trend at the free edge.[34]

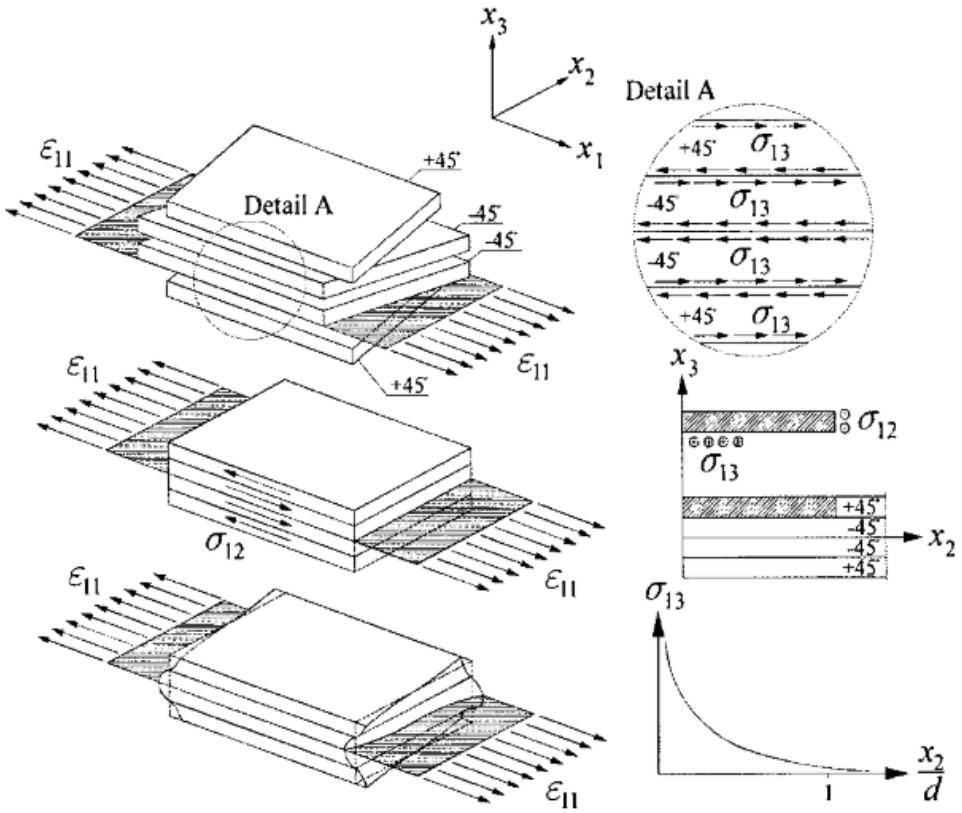

Figure 2.6: The free edge effects in an angle-ply $[\pm 45°]_S$ laminate under uniaxial tension. *Note that the x_1, x_2, and x_3 axes are equivalent to the x, y, and z axes.[34]

In general, the significance of each interlaminar stress depends highly on the layup of the laminate. In cross-ply laminates, τ_{yz} and σ_z are more prominent, while angle-ply laminates usually experience higher τ_{xz} stresses. Laminates with clusters of plies oriented in the same direction experience higher interlaminar shear stresses than those without.[74] However, quasi-isotropic and general laminates can experience all three interlaminar stresses. Regardless of their layup, composite laminates experience high interlaminar stresses near free edges and, therefore, are prone to delamination.

Due to universality of these mechanisms, delamination plays a significant role in in-plane failure. This has been shown by tensile testing of quasi-isotropic laminates at off-axis loadings, where failure initiated at the free edges, and none of the tested specimens reached the expected load predicted by classical lamination theory.[33] Because delamination is pervasive in composite laminates and can cause catastrophic failure, minimizing it has become a hot topic in composites research.

2.4 DELAMINATION SUPPRESSION METHODS

Significant efforts have been made to develop methods to suppress delamination in composite laminates. These can be classified as laminate design, edge design, interleaving, matrix toughening, and continuous nanofiber reinforcement.[36,61]

2.4.1 Laminate Design

The stress distribution in laminates can be modified by altering the ply stacking sequence. An optimized layup can significantly reduce interlaminar stresses while keeping the same global properties. For example, under constant in-plane tension, the interlaminar stress σ_z is much lower in a laminate with a $[15°/45°/-45°/-15°]_S$ layup than that in a laminate with a $[15°/-15°/45°/-45°]_S$ layup. However, there are limitations to

laminate stacking sequence, and substantial interlaminar stresses can still be present in optimized layups.[36,75]

2.4.2 Edge Design

Modifications of edge designs can also help suppress delamination. Since free edges are where interlaminar stresses are the highest, edge reinforcement and modification methods have been developed to account for these high stresses. For edge reinforcement, z-pinning,[76] stitching,[77] edge interleaving,[36] or edge capping[62] techniques have been used. However, these methods are highly dependent on the reinforcing structure,[78] can significantly increase the thickness and/or weight of the part, and are not practical in many structural applications. They also increase the costs and time of manufacturing. Edge modification methods include ply termination or chamfering,[79] notching, and tapering.[3] Although these methods can reduce interlaminar edge stresses, they require extra machining, and the substantial edge modifications may not be suitable in multi-layered laminates.[78] In addition, some of the edge modification methods cause damage to the laminate, which can be detrimental to structural performance.

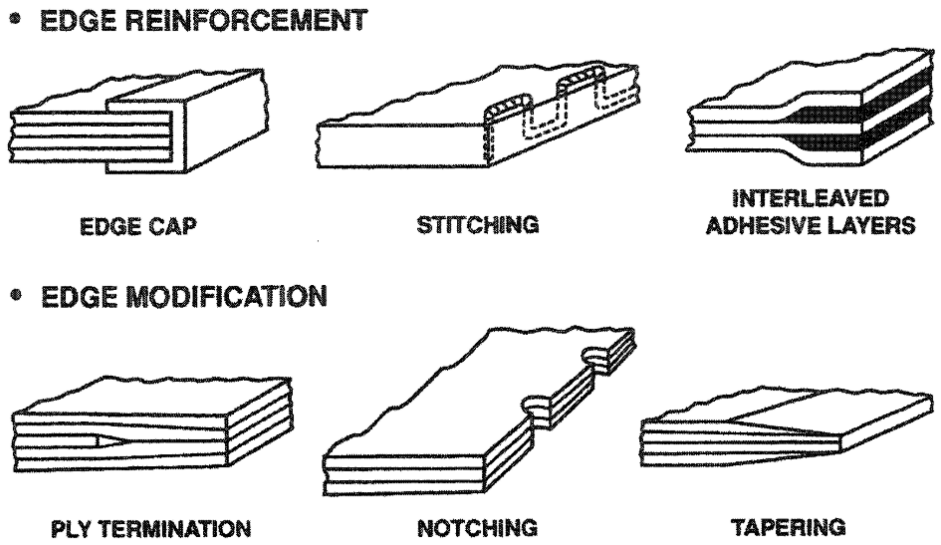

Figure 2.7: Free-edge delamination suppression concepts.[3]

2.4.3 Interleaving

Another method, which somewhat reduces the above issues, is called interleaving. This method involves the addition of a discrete ductile material layer between plies. Interleaving has been shown capable of producing significant enhancements to modes I and II interlaminar fracture toughness, along with improved impact resistance.[80] Several interleaf materials have been used, including thermoplastic films, chopped fibers, glass/epoxy prepreg, thermoset adhesive films,[81] and piezoceramic interlayers.[82] However, these techniques require relatively thick interleaves, which decrease in-plane strength and add weight. The latter decreases the high specific strength and stiffness of fiber-reinforced composites (their main advantages!).[66] In fact, fracture toughness is directly proportional to interleaf thickness, and interleaf effectiveness decreases if its thickness drops below a critical level.[80] For example, thermoplastic particle interleaves can increase thickness by around 20% and decrease in-plane stiffness by 15-20%. Interleaving can also lower the glass transition temperature of the composite.[66] For these reasons, interleaved laminates are seldom used in the advanced composites industry. In fact, commercially available composites that are sold with interleaf material are difficult to find.

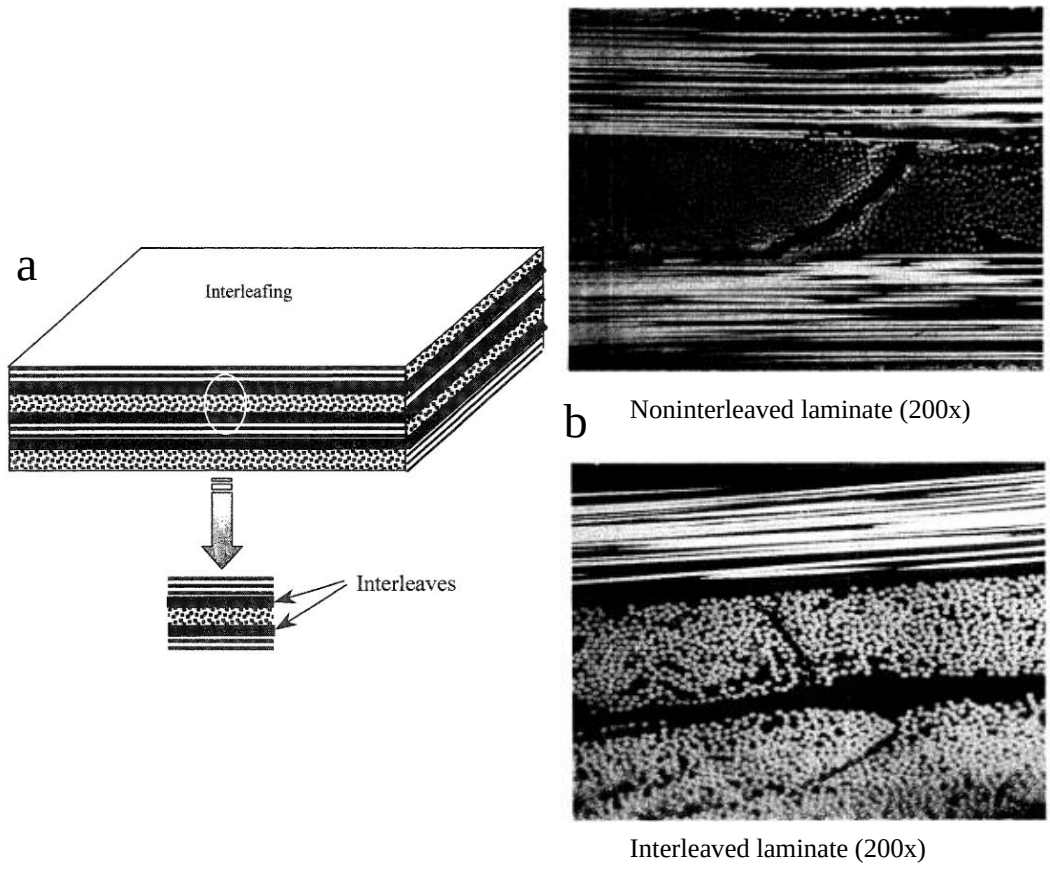

Figure 2.8: (a) Schematic of interleaving in a cross-ply laminate.[78] (b) Interleaving suppresses delamination development at the lamina interface.[80]

2.4.4 Matrix Toughening

Delamination suppression can also be achieved by toughening the polymer resin matrices. Most thermosetting resins have low fracture toughnesses, which makes them susceptible to damage and microcracking. Thus, several methods, most of which involve the addition of micro- or nanoparticles, have been developed to increase the fracture toughness of brittle resins. Although not the original intent of resin toughening, increasing the fracture toughness of the resin itself also provides increased interlaminar fracture toughness in laminates since delamination cracks originate in and propagate through the resin-rich interlaminar region.

These matrix toughening methods can be categorized by particle size. One of the first conventional, larger particles added to brittle resins was rubber, which has been extensively studied.[29] Although the addition of rubber particles can enhance fracture toughness, it can also decrease stiffness, lower the glass transition temperature (T_g), plasticize the matrix, reduce yield strength, and increase the linear thermal expansion coefficient. This significantly limits the applications of rubber particles as a toughening agent in polymer matrices. Other large particles, which were stiffer, such as mica, iron powder, cork, and glass beads have also been added to polymer resins to increase their mechanical performance.[78] Even a "self-healing" particle has been used to increase the fracture toughness of polymer resins.[78] However, some researchers reported a negative effect on impact and compression after impact properties due to insufficient wetting and agglomeration of particles.[67] More importantly, the large sizes of the these particle additives (some as large as 200 μm in diameter, which is comparable to the thickness of an entire fiber-reinforced ply), create large, unreinforced, matrix-dominated volumes. This can significantly reduce the overall fiber volume fraction in laminates. In addition, large interstitial spaces between particles can give cracks ample room to propagate while avoiding the particles entirely.

On the other hand, particles with nanoscale dimensions can have lower effect on the thickness of the laminate and may be fine enough to go between the carbon fibers within the plies. One example of nanotoughening involves the addition of carbon nanotubes (CNTs)[42,43] to the matrix or fiber surface, which can significantly enhance the IFT of laminated composites. However, considering CNTs are among the stiffest and toughest materials ever synthesized, improvements were expected to be much greater.[39]

There is also no guarantee that the CNTs will bridge the interlaminar crack due to their discontinuity. Similar to CNTs, vapor grown carbon nanofibers (VGCNFs)[44] and graphene[83] have been used to toughen polymer resins.[44] However, the addition of these nanoparticles can significantly increase the viscosity of the resin, which leads to issues with impregnation, wetting, and load transfer. In addition, bottom-up synthesis of carbon-based nanomaterials is a time-intensive, costly, and complicated process.[43]

One other nanoparticle that is used to enhance the toughness of polymer resins is silica.[84] Since it is cheaper to produce than carbon nanomaterials, several commercial thermoset resins are reinforced with nanosilica. However, the provided increase in fracture toughness is minimal and should be improved further. In general, particle reinforcement is inherently dependent on a multitude of factors, such as filler volume fraction, particle size, filler aspect ratio, filler modulus, filler strength, and resin-filler adhesion.[78] Lastly, the discontinuity of nanoparticles makes them a potential health hazard.[57]

2.5 CONTINUOUS NANOFIBER REINFORCEMENT OF INTERFACES

One method to suppress delamination that escapes most of the shortcomings discussed above involves the addition of continuous, electrospun nanofibers to the interlaminar region. This pioneering approach was proposed in 1994 and since developed by the Dzenis group at the University of Nebraska-Lincoln (UNL). The first patent for the use of electrospun NFs as interlaminar reinforcement was issued in 2001 to Dzenis and Reneker,[61] which marked the foundation of a new subfield of advanced composites research.

Continuous nanofiber sheets electrospun from polymer solutions can suppress delamination in two ways. First, nanofibers themselves toughen the resin in the interlaminar region. Second, nanofiber interleaves, which are isotropic in the laminate plane, locally reduce the ply anisotropic properties mismatch and act as buffers to reduce interlaminar edge stresses, which has been proven by computational modeling. This creates a hierarchical reinforcement system in which the carbon fibers are the primary reinforcement, and the nanofibers are the secondary reinforcement in delamination-prone critical volumes.

Reinforcing laminate interfaces with continuous NF interleaves has several distinct advantages over other delamination suppression methods. Compared to discontinuous nanoparticles, electrospun NFs are more likely to bridge across interlaminar cracks.[63] During curing of laminates under pressure, individual NFs can even be oriented in the out-of-plane direction, which allows them to support peeling (mode I) stresses. Electrospun nanofiber veils also add negligible weight and thickness to the laminates, which differentiates them from other interleaf materials. Their top-down, simple, and cheap nanomanufacturing process can be used to tune nanofiber diameters and morphologies for optimal properties. Since hundreds of polymers can be electrospun into nanofibers, the proper polymer can be chosen based on the matrix material and requirements of the application. Electrospinning can also be integrated into existing laminate manufacturing methods through either direct collection onto composite plies or post-spinning application of nanofibrous mats. Finally, electrospun fiber continuity also decreases the chance of inhaling the ultrafine fibers, thus reducing or eliminating potential environmental health hazards.[61]

Figure 2.9: (left) Advanced laminated composite with nanofiber-reinforced interfacial layer. (right) In situ observation of interlaminar toughening nanomechanisms including Velcro-like crack bridging by nanofibers.[41]

In the last two decades, the number of publications with "nanofibers" and "composites" in the title or abstract has steadily risen.[85] Many of these papers describe the use of NFs as interlaminar reinforcement in laminates. Specifically, extensive research has been performed at UNL. A wide variety of polymer NFs have been studied, including polyamide-6 (PA6),[63,65,86,87] polyamide-66,[66] polyamide-6.9,[65,88] polycaprolactone (PCL),[65,87,89] and polyacrylonitrile (PAN),[90] along with core-shell NFs made of a PA6 core and PCL shell,[91] among others. Most studies concluded that modes I and II interlaminar fracture toughness can be significantly improved via NF-reinforcement. In addition, some studies have shown that electrospun NF interleaves can also provide improved delamination resistance under fatigue loading,[65] as well as increased impact energy absorption,[66,67] tensile strength, short beam shear strength, and flexural strength.[68] Although these properties differentiate interleaves made of NF sheets from previous interleaf materials that reduced in-plane properties, mechanical results on laminates are still limited.

Overall, continuous nanofiber interleaves possess high potential for commercial applications, especially in high-performance carbon/epoxy laminates. They have received substantial interest, and there are even a few companies that produce and sell electrospun nanofiber sheets in bulk to be used as interlaminar reinforcement. However, high-temperature laminates, which are even more susceptible to delamination, have not been studied with regards to nanofiber reinforcement.

2.6 HIGH-TEMPERATURE COMPOSITES

Although delamination has been extensively investigated in various conventional fiber-reinforced polymer composites, such as carbon/epoxy composites, there are still very few results for laminates made from high-temperature polymer resins. Recently, the demand for polymer matrix, fiber-reinforced composites for high temperature applications has increased dramatically. Although original structural applications in aerospace targeted service temperatures up to 120°C, attention is now being focused on usage where temperatures can reach 200-400°C.[20] Most of these applications are highly relevant to the military and defense fields. More specifically, parts on or around aircraft engines, airframe structural components in high-speed transport aircraft, and space re-entry features will need to endure quite high temperatures (350°C or above).[20] However, due to their higher curing and service temperatures, polymers suitable for these applications are susceptible to microcracking.

Since the polymer matrix is more affected by the high temperatures than the reinforcing fibers, researchers have worked to developed several polymers that can perform satisfactorily in temperatures up to 300°C, and sometimes higher.[20] These

polymers include bismaleimides (BMIs), cyanate esters (CEs), and thermoplastic and thermosetting polyimides (PIs).[20]

Low molecular weight thermoplastic PIs, cured at temperatures from 345 to 370°C, were first developed by the NASA Langley Research Center and also became good candidates for aircraft components.[1,20] Different mixtures of amorphous and crystalline thermoplastic systems, such as blends of polyetheretherketone (PEEK) and polyetherimide (PEI), are sometimes used to combine the advantages of both types.[20] However, there is a lack of manufacturing infrastructure for these thermoplastic resins. Thus, there is a very high current interest in high-temperature thermosets.

In the 1970s, BMIs and CEs were developed as easy-to-process thermosets suitable for 177°C hot-wet service.[11] They are good candidates for high-speed fighters and future high-speed civil transport with service temperatures around 180°C.[20,23] BMIs have higher modulus values and higher thermal ratings, giving them a strong position in military aircraft, such as the F-22 fighter.[11] Carbon/BMI composites have been used as skins of the inboard flaps and the strakes, which are located under the fuselage.[11] BMI resins reinforced with carbon or glass fibers also find applications in cowlings, nacelles, and thrust reversers of jet engines.[20]

Cyanate esters, on the other hand, have superior dielectric loss properties and exhibit lower moisture absorption than BMIs, making them useful in several applications, such as radomes, skins covering phase-array antennae, advanced Stealth composites, missile nose cones, and space structures.[11,20] Cyanates also cure epoxy resins so cost-effective hybrids retain an unusually high fraction of CE homopolymer properties.[11]

The family of polymers with service temperatures between 250~350°C are dominated by thermosetting polyimides (PIs).[20] These resins owe their outstanding high temperature mechanical properties and thermal-oxidative stability to aromatic heterocyclic repeat units and a minimum aliphatic content, or the presence of C-H and C=C groups that contribute to thermal-oxidative instability. Although many types of aromatic heterocyclic polymers are possible, polyimides, which possess glass transition temperatures greater than 316°C, attract the highest commercial interest. Their highly aromatic character and minimal flexible linkages provide inherent rigidity which results in high glass transition temperatures.[11] The key to the success of polyimides has been the development of several techniques to achieve a balance between their processability and the resulting performance. Both condensation type and addition type polyimides have been extensively researched and some were commercialized, mostly in the US.[20] Commercial polyimide resins mainly have applications in aircraft. A PMR-15/graphite composite is used in ducts of the F-404 engine in the US Navy's F-18 fighter, in a fire wall for the GE-90 engine, and as splitters and fairings for the F-110 engine. Avimid® N/graphite is used in variable stator vanes in a variety of military and commercial jet engines. Other applications include radomes, missile fins, jet engine nozzle flaps, fairings, cowls, inlet guide vanes, gear cases for helicopters, and heat shields.[11,20] Despite the use of polyimide resin in high-temperature composites, it has a number of limitations. In fact, PMR-15, which is the most prevalent thermosetting PI resin in the industry today, faces challenges related to reliable methods of quality control, batch-to-batch variability, and high-temperature processing. One of its ingredients, methylene dianiline (MDA), is also a known carcinogen and liver toxin, which requires strict handling regulations

imposed by the Occupational Safety and Health Administration.[92] This limits the commercialization of PMR-15.

Overall, composites made from CEs are currently the most commercially available and are being used in select applications driven by their flexibility, curing methods being similar to those of epoxies, and low moisture absorption. However, due to their high curing and hardening (annealing, or post-curing) temperatures, major challenges regarding thermal stresses and microcracking are still prevalent and need to be resolved. These challenges are common to all high-temperature thermosetting matrix composites.

2.7 MICROCRACKING AND DELAMINATION IN HIGH-TEMPERATURE COMPOSITES

Because composite laminates are composed of more than one material and cured at elevated temperatures, they experience residual stresses. Residual stresses are the result of cure shrinkage of the matrix, differences in the coefficient of thermal expansion (CTE) between the fibers and the matrix, and the difference in the expansion/shrinkage between individual plies. During and after curing, once the material falls below its stress-free temperature (when no residual stresses exist), increased thermal stresses can cause significant damage in the composite material, including microcracking and delamination. The thermal stresses increase as the temperature deviates from the stress free temperature.[24] Generally, higher cure temperatures result in higher glass transition temperatures, higher stress free temperatures, and higher residual thermal stresses. These properties correspond to increased levels of microcracking, wider and more tortuous cracks, and greater propensity to delaminate.[24] Even thermoplastic resins, although they

are generally tougher than thermosets, are susceptible to microcracking instabilities due to their higher solidification temperatures.[11]

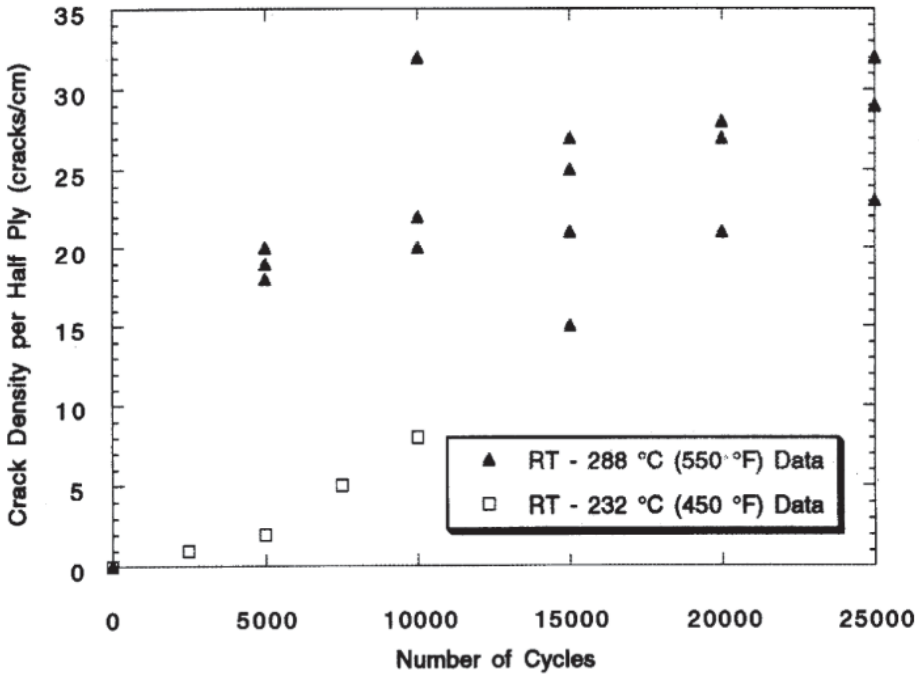

Figure 2.10: Crack density compared with accelerated thermal cycles for graphite fabric/PMR-25 polyimide laminates.[11]

Microcracking by thermomechanical cycling, especially in wet conditions, serves as one of the main factors having a negative effect on the long-term durability of high-temperature polymer matrix composites. In high-temperature applications, thermal cycling is a necessary process. This can cause microcracks in as few as 1000-5000 cycles, and cycling to higher temperatures results in a much higher concentration of microcracks. Microcracking can cause oxidation and accelerate the degradation of mechanical strength as cracks coelesce.[23] It can also cause detrimental reductions in matrix-dominated compressive strength and interlaminar fracture toughness, but fiber-dominated tensile strength is usually unaffected by the presence of microcracks.[11]

Although microcracking can occur in all resins exposed to thermal cycling, higher cure temperatures result in increased thermal stresses at cryogenic temperatures and,

therefore, greater density and size of microcracks, which can lead to delamination.[24] Microcracking in carbon/BMI composites undergoing stress-thermal cycling can be increased by higher temperature ranges, number of cycles, heating and cooling rate, and environmental humidity. Fiber-matrix thermal expansion mismatch is also exacerbated at higher curing temperatures, leading to fiber-matrix interface failure at high temperatures and matrix microcracking at lower temperatures due to residual stresses.[93] Thermal spiking can also occur when a composite is exposed to rapid increases in temperature, which can cause microcracks and increase the equilibrium moisture content. If the temperature increases are sufficient, delamination can occur due to steam pressure within the cracks.[1] Reducing moisture absorption in high temperature polyimides without causing adverse effects on other properties such as strength, toughness, and thermal-oxidative stability remains a critical challenge.[11] Although CEs exhibit lower moisture absorption and higher resistance to microcracks, they are inherently brittle, which limits their effective utilization in applications.[94] For the above reasons, it is highly critical to reduce microcracking and increase the toughness of high-temperature resins.

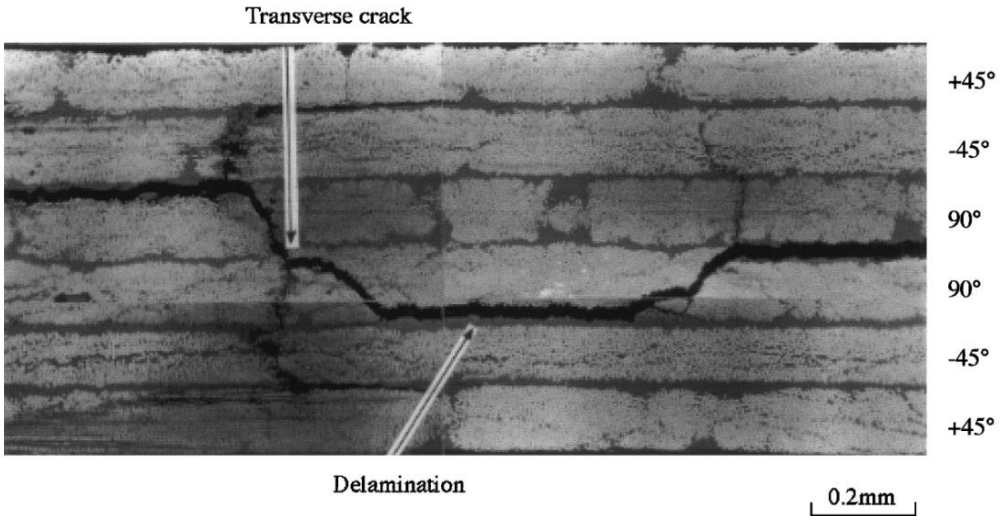

Figure 2.11: Microscopic damage in a G40-800/5260 carbon fiber/bismaleimide $[\pm 45/90]_S$ laminate (ε=1.6%).[95]

2.8 TOUGHENING OF HIGH-TEMPERATURE RESINS

Two general approaches have been explored to increase the toughness of high-temperature resins that are prone to microcracking. The first involves chemical resin modification, and the second involves physical modification using rubber, stiff, or thermoplastic particles.[25,26]

The primary chemical modification method that can improve the toughness of high-temperature resins is called copolymerization, which occurs when monomers from different polymer molecules join together in random or prescribed sequences. In a recent study, high-temperature resistant structural adhesives were prepared based on the copolymerization of 4,4'-bismaleimidediphenylmethane (BDM) and 2,2'-diallylbisphenol A (DABPA) together with a novel maleimide-capped polyetherimide containing cardo side groups (mPEI-C) as a toughening agent. Results showed increased flexural, impact, and bonding strength in this mPEI-C toughened BMI resin. In addition, the mixture maintained low moisture absorption rates. However, the mPEI-C toughening agent caused a decrease in the T_g of the BDM/DABPA,[96] which is detrimental for high-temperature applications.

The set of toughening methods using physical modification can involve the addition of elastomeric rubber particles. Although this has been shown to significantly enhance fracture toughness and impact strength, the drawback is that the rubber particles cause a degradation in high-temperature properties, and the addition of soft rubber reduces the overall yield strength and stiffness of the system.[94,97] Stiffer particles, such as glass, silica, mica, clay, aluminum hydroxide, and zirconia, have also been added to high-

temperature resins in an attempt to maintain the stiffness of the resin.[25,94] However, toughening of high temperature polymers with stiff particles has seen limited success.[94]

Table 2.2: Physical modifiers used to investigate toughening of cyanate ester resin.[25]

Modifier	Size
Alumina, Al_2O_3	~0.1 μm
Alumina, Al_2O_3	~20 nm
Carbon short-fibres	7 μm fibre diameter, 1 mm long
Glass-fibre woven-mat	10 μm fibre diameter, woven mat
Hollow glass spheres	9–13 μm diameter
Kevlar short-fibres	1 mm long
Muscovite mica	10 μm
Muscovite mica	40 μm
Muscovite mica	80 μm
PEEK powder	<200 μm
PEEK monofilament	200 μm fibre diameter
PEEK fibre	34 μm fibre diameter, 30 filaments per tow
PEEK woven-mat	300 μm monofilament diameter, twill weave
PTFE powder	6–9 μm
Silicon dioxide, SiO_2	~20 nm
Titania, TiO_2	~20 nm
Wollastonite	10 μm diameter, 50 μm long
Yttrium oxide, Y_2O_3	~20 nm

Thermoplastic particles have also been used to toughen high-temperature thermosets. This can lead to improvements in fracture toughness without significantly reducing the high-temperature properties. Polymer blending with thermoplastics that have higher glass transition temperatures can even increase the overall T_g of the system.[94] Some common thermoplastics used in blending with CEs include polyetherimide (PEI), polyether sulfone (PES), polysulfone (PSF), polyarylene ether, polytetrafluoroethylene (PTFE), PEEK, and others.[25–27,94] BMI and CE resins can also be toughened with thermoplastic PI particles or dissolved powdered amorphous thermoplastics to decrease microcracking in service.[11,28] The toughening mechanisms for these thermoplastic toughened CEs include crack bridging, crack pinning, crack path deflection, cavitation, and massive shear yielding.[94]

Although high-temperature thermosets can be toughened to an extent using rubber, stiff, or thermoplastic additives, careful consideration must be given to ensure the high-temperature properties are maintained. In addition, the discontinuous nature of particles greatly limits the reinforcing effect. Finally, as discussed in section 2.4, large particle size can lead to significant reduction of overall fiber volume fraction and load carrying capacity of composites.

2.9 HIGH-TEMPERATURE NANOFIBERS

To ensure the high-temperature properties of PIs, BMIs, CEs, and other polymers with elevated glass transition temperatures are retained, the proper toughening material must be chosen. Ceramic materials, such as alumina, mullite, silicon carbide, and silicon nitride can be produced in short nanofiber or nano-whisker form by melt spinning, chemical vapor deposition, sol-gel, and several other processes. These fibers/whiskers are generally dense, and whiskers can be defect free. They can be used for high-temperature structural applications due to their high thermo-mechanical properties such as high strength and modulus. However, their relatively low aspect ratios make it difficult to orient them and create a suboptimal reinforcing effect. Their size and discontinuity also allow them to be inhaled, which can have adverse health implications. To maximize the toughening effect and minimize the health concerns of nanomaterials that toughen high-temperature resins, fibers with high aspect ratios and controllable morphologies and configurations should be used.

Continuous electrospun nanofibers have proven successful as structural reinforcement of polymer matrices. However, for high-temperature applications, the choices of electrospinnable polymers are limited. Continuous ceramic nanofibers can be

produced by electrospinning of ceramic precursors. After calcination at high temperatures of the electrospun fibers that contain an inorganic precursors and polymer assistant material, a purely ceramic phase is obtained.[98] Electrospun ceramic NFs have all the characteristics of ceramic materials, including high mechanical, thermal, and chemical resistance, and catalytic and photocatalytic activity, but are in the form of continuous nanofibers. By carefully selecting the composite NF materials and altering the calcination conditions, more than a hundred different types of continuous ceramic NFs have been produced.[99] However, most electrospun ceramic NFs are porous, which is expected to reduce their mechanical properties.[100] The calcination process also makes it difficult to control their morphologies.[98]

A variety of electrospun metal and metal oxide nanofibers have been produced by removal of the polymeric matrix through either incineration or dissolution in selected solvents.[54,60,101–103] These metallic nanofibers have applications in electronics, photonics, and other related areas, and have much higher thermal stabilities than polymer nanofibers.[102] However, their two-step manufacturing process limits their integration with existing composite manufacturing methods. Manufacturing metallic NFs is also expensive due to high material costs.

In addition to ceramic and metallic NFs, continuous carbon nanofibers (CNFs) can be produced from several polymer precursors. This process entails first stabilizing the electrospun polymer NFs in air between 200-300°C, which prevents the NFs from melting during the subsequent carbonization step. The carbonization process occurs in an inert atmosphere (nitrogen or argon) at temperatures ranging from 800-1800°C. Although carbon materials are obtained at these temperatures by selectively eliminating the

noncarbonized elements in a gaseous form and without compromising the fibrous morphology, a graphitization process is sometimes performed at around 3000°C to further eliminate heteroatoms, grow the graphitic layers, and improve the stacking order. Polyacrylonitrile (PAN) is the most common CNF precursor because it has good spinnability and relatively high carbon yield (>50%).[51] Electrospun PAN-based CNFs were studied extensively by the Dzenis group at UNL and were even used to significantly improve the mechanical properties of epoxy resin.[104] Polyimide can also produce high carbon yield after carbonization at 1000°C. Lignin, on the other hand, only yields a carbon content of 20-40%, although it has been used to produce CNFs as thin as 200 nm in diameter. Other polymers, such as pitch, PVDF, cellulose, PVA, and PVP have also been explored for the production of CNFs.[51] The carbonization temperature has a profound effect on the physiochemical properties of the CNFs. However, higher carbonization temperatures require expensive equipment. In addition, it is important to avoid shrinkage during the thermal treatments.[51] Although several CNF designs and morphologies have been tested, further tuning of the properties, such as architecture, morphology, and composition optimization are necessary to enhance overall performance. Similar to metallic and ceramic NFs, carbon NFs must undergo thermal post-processing treatments after electrospinning. This makes it difficult to directly incorporate them as interlaminar reinforcement in traditional composite laminates.

Recently, a new class of high-temperature polymer nanofibers has been developed. This class consists of aromatic polyimides (PIs), which are a group of polymers that exhibit enhanced thermal stability, high mechanical properties, and good chemical resistance.[105] Most PI fibers must be derived from a two-step process: (1)

mixing of dianhydrides and diamines to produce the precursor polyamic acid (PAA) then (2) performing thermal/chemical imidization to obtain the final PI polymer (see **Figure 2.12**).[106] Depending on the combination of dianhydrides and diamines used to synthesize the polymer, the chemical structure of PIs can be tailored to possess a wide range of mechanical and thermal properties.[105,107] In general, electrospun PI NFs, PI composite NFs, and PI-based CNFs possess large surface-area-to-volume ratio, high mechanical properties, and enhanced thermal stability.[105] These characteristics give them great potential for several applications, including reinforcement of composites, energy storage, filtration, and biomedical engineering.[105,108]

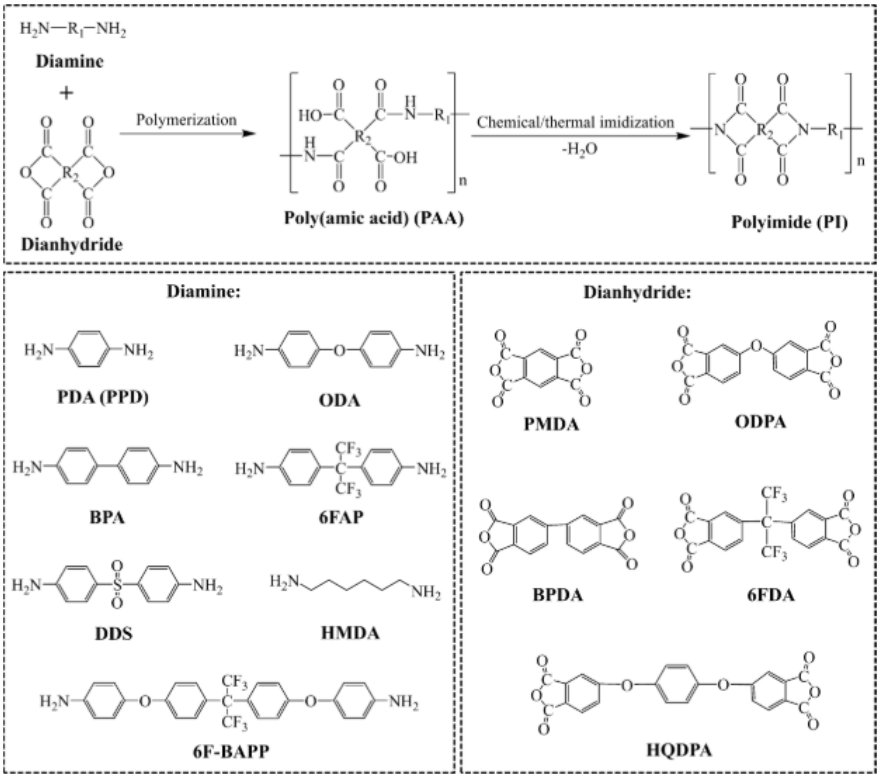

Figure 2.12: Illustration of two-step method for synthesizing polyimides and chemical structures of some commonly used diamines and dianhydrides.[105]

Several groups have investigated the mechanical properties of polyimide fibers. High-performance PI fibers with tensile strengths up to 4.0 GPa and tensile moduli up to

160 GPa were constructed using a two-step wet spinning process. However these fibers remained brittle, breaking at strains between 2-4%.[106] Several other research groups have successfully fabricated PI nanofibers with the two-step process.[109–113] However, during the imidization process, issues can arise. Specifically, localized fusion at fiber-fiber junctions can detrimentally alter the fibrous morphology and, therefore, the mechanical performance of the PI NF mats.[114] More critically, the imidization process must be completed before two-step PI nanofibers can be used to reinforce composite materials. This makes integrated fabrication of PI nanofiber-reinforced composite laminates impossible. For these reasons, there is a need for soluble PIs that retain strong high-temperature properties immediately after electrospinning and can be practically incorporated into advanced composites.

In recent years, pioneering research by our group at UNL in collaboration with the College of Polymer Science and Polymer Engineering at the University of Akron has helped develop a handful of one-step, soluble, fully-imidized polyimides.[59] Continuous nanofibers produced from these novel polyimides possess high thermal stability without the need to undergo thermal imidization after electrospinning. They have also been shown to exhibit dramatic improvements in mechanical properties as diameters decrease below several hundred nanometers,[59] similar to electrospun PAN NFs.[58] Although these one-step PI NFs have been used in our group to reinforce epoxy, they have not been used to reinforce high-temperature resins. Their high thermal stabilities make them strong candidates for high-temperature composite reinforcement, but further investigation is needed to optimize the preparation conditions and focus on practical, high-value applications.[105] The demand for nanotoughened structures in high-temperature

applications may also require the development of completely new composite material combinations.

2.10 STRUCTURAL SOURCES OF DELAMINATION

Despite the numerous studies surrounding NF-reinforcement in composites, there is still a lack of research regarding NF-toughening of composite structures that experience complex 3D stress states. Almost all results are based on modes I and II and mixed mode I/II interlaminar fracture toughness testing. Although there are limited results related to tensile, impact, flexural, and compression after impact properties, these tests were performed on 2D plates that experience relatively simple plane stress loadings. Three-dimensional composite structural elements, such as holes, curves, joints, and ply drops, can experience much more complex stress states and are especially susceptible to delamination. Nonetheless, publications describing the interlaminar reinforcement using electrospun nanofibers of delamination-prone design features in composite structures are virtually nonexistent.

It is important to distinguish between overall interlaminar stresses that arise due to direct out-of-plane loadings or special geometries, and highly localized interlaminar stresses that arise due to discontinuities and may be associated with stress singularities. However, both of these cases contribute to delamination and may even occur simultaneously to initiate failure.[33]

Overall interlaminar stresses owing to direct out-of-plane loading can include a lug fitting or rib-to-skin joint, as shown in **Figure 2.13**. The first example can be found when a rigging wire is connected to a composite yacht mast or when a bolt is fed through a composite plate. The second example may be seen in aircraft wings where the

connection may experience through-thickness loads due to the constraint between different parts and the way overall loads are carried throughout the structure, even if no external out-of-plane loads are applied. Another critical example of an out-of-plane loading is impact, which produces through-thickness shear and compression stresses.[33]

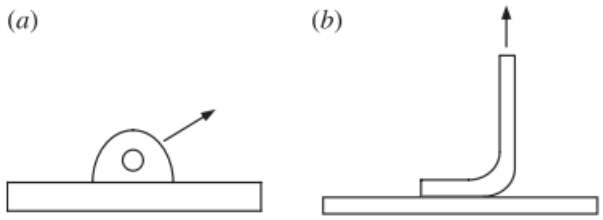

Figure 2.13: Features prone to delamination owing to direct through thickness loading: (a) lug fitting and (b) rib-to-skin joint.[33]

Overall interlaminar stresses can also be produced as an indirect result of the geometry of the structure. One example of this is a ply taper, in which the in-plane load diffuses with the change in thickness. Another example is the bending of a curved laminate, in which interlaminar normal stresses are induced. These stresses increase as the ratio of thickness to curve radius increases. Curved geometries occur in several composite structures, and bending can even be induced during tight-tolerance assembly and temperature changes.[33]

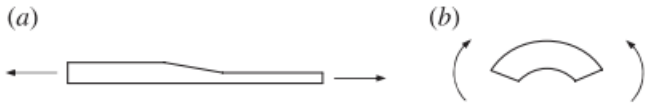

Figure 2.14: Features prone to delamination owing to geometry: (a) taper and (b) curved section in bending.[33]

Interlaminar stresses can also arise at the local level near geometrical or material discontinuities. Cracks can arise during manufacturing or impact, which cause high stress concentrations that can initiate delamination. Ply drops or material changes can also induce transverse cracks that lead to delamination. Structural joints, such as where a flange attaches to a skin, are also susceptible to delamination. Lastly, because of the

anisotropy of laminates, free edges and holes are discontinuities where delamination can initiate due to the free edge effects described previously.[33]

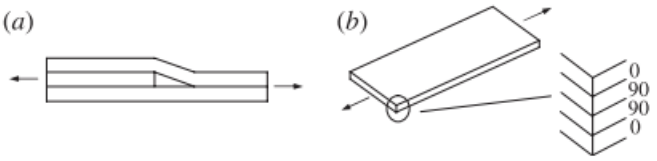

Figure 2.15: Features prone to delamination owing to discontinuities: (a) ply drop and (b) free edge.[33]

The design features that make laminates susceptible to delamination, including through-thickness loads, special geometries, and discontinuities, shall be termed *sources of delamination*. These sources of delamination occur throughout composite structures and serve as regions where failure can initiate (see **Figure 2.16**a). There is a pressing need to expand the nanofiber toughening research and development beyond the simple modes I and II fracture studies and to extend it to structural sources of delamination.

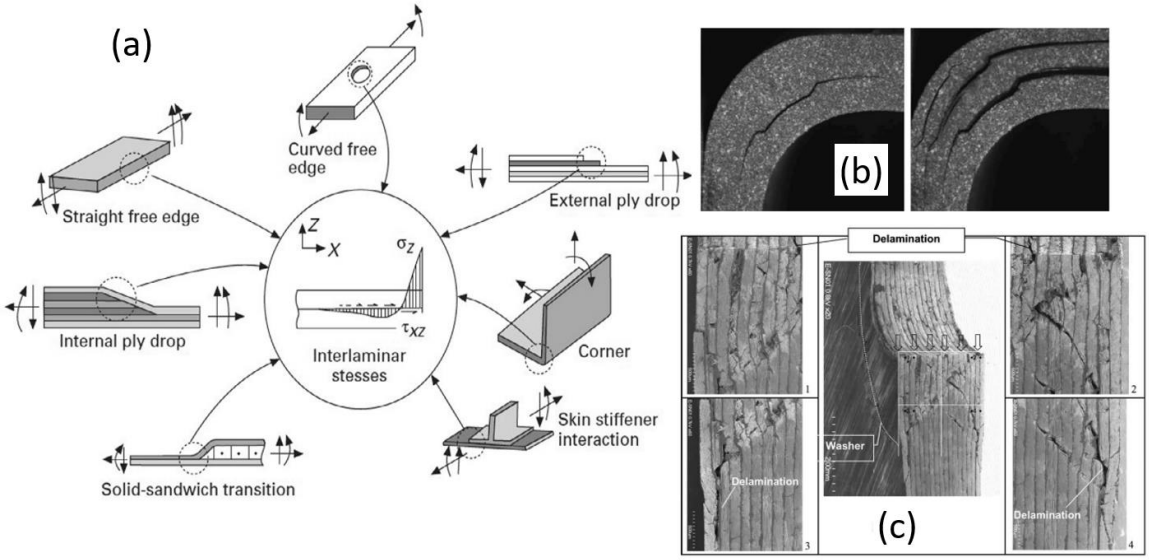

Figure 2.16: (a) Sources of delamination.[45] (b) Measured delamination in an L-shaped laminate specimen.[115] (c) SEM micrographs of through-thickness bearing damage showing noticeable delamination.[116]

2.11 TESTING METHODS FOR COMPOSITE STRUCTURES

When it comes to laminated composite structures that are especially prone to delamination, there are limited established testing methods. Mode I (ASTM D5528[117]),

mode II (ASTM D7905[118]), and mixed mode I-mode II (ASTM D6671[119]) interlaminar fracture toughness tests have been standardized, but these are only applicable to unidirectional 2D plates. As discussed above, there are several 3D structural elements that experience high interlaminar stresses and, therefore, serve as sources of delamination. However, there exist only a handful of well-defined testing methods for the interlaminar stresses these composite structures experience. Laminates with different layups, which can already be considered structural elements because their anisotropy will cause delamination to initiate at the free edge, can be tested in uniaxial tension in accordance with ASTM D3039.[120] Along with the geometric limitations, these methods are only valid for one loading configuration. L-bend laminates, for example, can be tested using several different loading configurations that will induce buckling and delamination in the curved section.

Although some standardized tested methods exist, the virtually limitless geometries found in composite structures are not entirely supported. For example, there are no standardized testing methods for composites with ply drops,[121] ply tapers,[122] or sandwich section transitions,[123] which can be prevalent in composite structures. Also, study of delamination in joints, other than the bearing strength test, is highly limited. Apart from bolted joining, alternative methods for mechanical joining composites to metals include riveting, cinching, form-locked joints, pin joints, and loop joints.[124] Although some computational models have been developed to predict failure of composite joints,[125,126] delamination remains a critical, complex issue, and safe-use of composite joints requires experimental testing.[127] With regards to pressure vessels, the pressurized ring test was proposed in 1995 but has yet to be standardized.[128] The multi-

axial composite tube test configuration is capable of producing different combinations of tensile and compressive axial loads, internal pressures, and torsional loads in a composite tube, but specimen preparation and loading fixtures are complicated and expensive.[129] Numerical models have shown that composite corners can experience 3D interlaminar stress singularities, which are more detrimental in concave corners.[130,131] However, there are no existing experimental methods for characterizing composite corner strength. Lastly, composite structural beams, such as I-beams, U-beams, or other constant-cross-section parts (likely manufactured via the pultrusion process) can be tested in simple flexure, but in many applications, composite beams experience complex, 3D stress distributions. These stress distributions can be modeled, but experimental testing is a necessary step required for industrial use. In addition to the limitations in geometries and loading configurations, there exist very few results regarding the testing of high-temperature composite structures.

2.12 SUMMARY AND TECHNICAL PROBLEM FORMULATION

Delamination in advanced composite laminates remains a critical issue impeding broader applications of composites. Ubiquitous mechanisms, such as anisotropic ply properties mismatch, make delamination a pervasive damage mode in laminates. Delamination is especially critical in composites with brittle thermoset resins, such as carbon/epoxy composites that currently dominate the advanced composites market. Next generation, high-temperature composites are even more prone to microcracking and delamination due to their higher cure temperatures and residual stresses. Novel, high-temperature-NF reinforcement has been identified as a promising approach to toughen interfaces in such composites. However, no relevant research has been performed to date.

In addition, although NF interleaves exhibited the ability to toughen conventional composites, such as carbon/epoxy, most research related to NF interleaving of composites pertained to fairly simple geometries in which the laminates experienced simple stress states. Certain design features of composite structures, which experience more complex, 3D stress states, are especially prone to delamination. Nonetheless, research regarding NF-reinforcement in composite structures possessing these design features is essentially nonexistent. CHAPTER 3 and CHAPTER 4 will describe a systematic investigation of NF-reinforcement for delamination suppression in carbon fiber-reinforced composite laminates. The experimental work will include modes I and II interlaminar fracture toughness testing to establish the fracture toughening baseline (CHAPTER 3), followed by tensile testing of multidirectional laminates with and without holes and flexure testing of unidirectional L-shaped composites to evaluate the baseline translation to complex structural elements (CHAPTER 4). Reinforcement of two different polymer matrix composite materials (epoxy and cyanate ester) using two different nanofiber materials (polyacrylonitrile and polyimide) will be studied. The cyanate ester matrix reinforced with polyimide NFs is especially applicable to high-temperature applications.

In addition to secondary interlaminar reinforcement, electrospun nanofibers can also be used as primary reinforcement of bulk polymer resins. However, challenges regarding the mechanical properties of individual NFs and their manufacturing have limited the resulting structural improvements seen to date. To further enhance the mechanical properties of nanocomposites, two approaches can be taken. The first requires controlling the configurations of electrospun NFs within the polymer matrices. In

CHAPTER 5, results of a comprehensive parametric study on axial alignment in NF sheets will provide a better understanding of how to control and optimize NF orientation. In addition, high-speed videography of the electrospinning jet instabilities will be analyzed in an attempt to better understand and minimize them and to develop future computational models. With the results of these studies, novel nanolaminated composites will be fabricated from electrospun NFs and their improvements in mechanical properties will be documented.

The second approach to enhance the properties of nanocomposites involves improving the mechanical properties of NFs themselves through the use of post-processing methods or the addition of nanoparticles. APPENDIX D will describe an exploratory study of feasibility of improving the graphitic structure of electrospun continuous CNFs that can provide enhanced and tailorable strength and stiffness.

CHAPTER 3. INTERLAMINAR FRACTURE TOUGHNESS TESTING OF ELECTROSPUN NANOFIBER-REINFORCED COMPOSITES

Delamination in composites arises due to normal (mode I), shear (mode II), or a combination of these interlaminar forces. Although linear elastic fracture mechanics (LEFM) of modes I and II failure in isotropic materials is well-established, its application to laminated composites is limited by their anisotropic and heterogeneous nature. However, LEFM can be used to analyze interlaminar fracture under mode I or mode II loadings.[132] When cracks propagate self-similarly (without deflecting) along the fiber direction between composite plies, LEFM provides a safe approximation for interlaminar fracture toughness, which is defined as the energy needed to crow the crack.[31,69,133] The fracture toughness of a composite, along with other linear elastic materials, can be characterized by one of two parameters: the critical strain energy release rate (SERR) G_C or the critical stress intensity factor (SIF) K_C.[133]

To determine mode I interlaminar fracture toughness (IFT), the double cantilever beam (DCB) test was developed, and is now standardized as ASTM D5528.[117] For mode II, the most popular method is the end-notched flexure test, which is standardized as ASTM D7905.[118] Several studies have used the DCB and ENF tests to determine modes I and II IFT of electrospun nanofiber-interleaved composites.[45,62–64,87,91,134,135] Results of these studies have shown that NF interleaves can significantly improve both modes I and II interlaminar fracture toughness. The ability of the NF interleaves to provide interlaminar toughening depends on several factors, including the amount of NFs, their compatibility with the matrix, and their diameters and morphologies.[45] Although several different composite and NF materials have been tested, the amount of material

combinations is virtually limitless. In addition, new polymer resins and NFs are continually being developed for new applications. Some of the more recent developments include those specifically applicable to high-temperature uses. However, studies on interlaminar fracture toughness of high-temperature composites, especially those reinforced with electrospun nanofiber interleaves, are extremely limited.

This chapter outlines attempts to increase the interlaminar fracture toughness of two composite materials using electrospun nanofiber interleaves. A carbon/epoxy material and a carbon/cyanate ester material are reinforced with either polyacrylonitrile (PAN) or polyimide (PI) nanofibers. Although carbon/epoxy has been extensively studied with regards to NF interleaving, results on cyanate ester matrix materials, which have high-temperature service capabilities, are limited. In addition, the PI material is a recently developed, soluble polyimide, which makes it electrospinnable without post-processing, in contrast to previous polyimides. Section 3.2 describes the results of mode I interlaminar fracture toughness testing of several different material combinations. Different amounts of NFs are used until positive results were obtained. Section 3.3 includes the results of mode II IFT testing using similar materials to those that produced positive mode I results. The material improvements seen in interlaminar fracture toughness from NF interleaving will serve as a baseline to compare to the structural improvements described in CHAPTER 4.

3.1 EXPERIMENTAL METHODS

3.1.1 Composite Materials and Manufacturing

The two composite materials used in this study were carbon/epoxy (TR50S/PMT-F3) unidirectional prepreg from Patz Materials, Inc. and carbon/cyanate ester (CE)

(T1100G/RS-3C) unidirectional prepreg from Toray Industries, Inc. The PMT-F3 is a nano-silica loaded epoxy resin, and the RS-3C is a modified cyanate ester resin. It should be noted that the PMT-F3 resin is expired according to the manufacturer recommendation, which may have significantly reduced its mechanical properties, although the prepreg remained tacky and plies were adequately bonded after curing. Plies were cut directly from the prepreg roll using a utility blade. The cure schedule for the carbon/epoxy material was 250°F for 2 hours, under 80-90 psi and -25 in. Hg vacuum pressure. The cure schedule for the carbon/CE material was 350°F for 2 hours, under approximately 100 psi and -25 in. Hg vacuum pressure.

Flat composite panels were cured using a Carver, Inc. model 2699 press-clave in combination with a Carver, Inc. model 3874 vacuum pump. **Figure 3.1** shows the schematic assembly that was placed in the press-clave, but the assembly was modified slightly. The bottom aluminum plate in the assembly was first coated with Loctite Frekote® 700-NC mold release agent spray. Once dry, the metal plate was covered with white woven peel ply cut to proper dimensions. On top of this went the composite layup, which was covered with a thin brown woven release ply. Then, another layer of peel ply was added, followed by a layer of white breather material. Since the silicone seal had a chunk missing, which would show up as a bump in the cured panel, a smaller, release sprayed, aluminum plate was placed on top of the breather. Finally, the silicone seal frame and the top aluminum plate were added before the entire configuration was placed in the press-clave and securely clamped in place. The pressurized air and vacuum tubes were connected and powered on before turning on the heat supply. The air pressure was

monitored throughout curing to ensure it stayed within 5 psi of the cure schedule requirement.

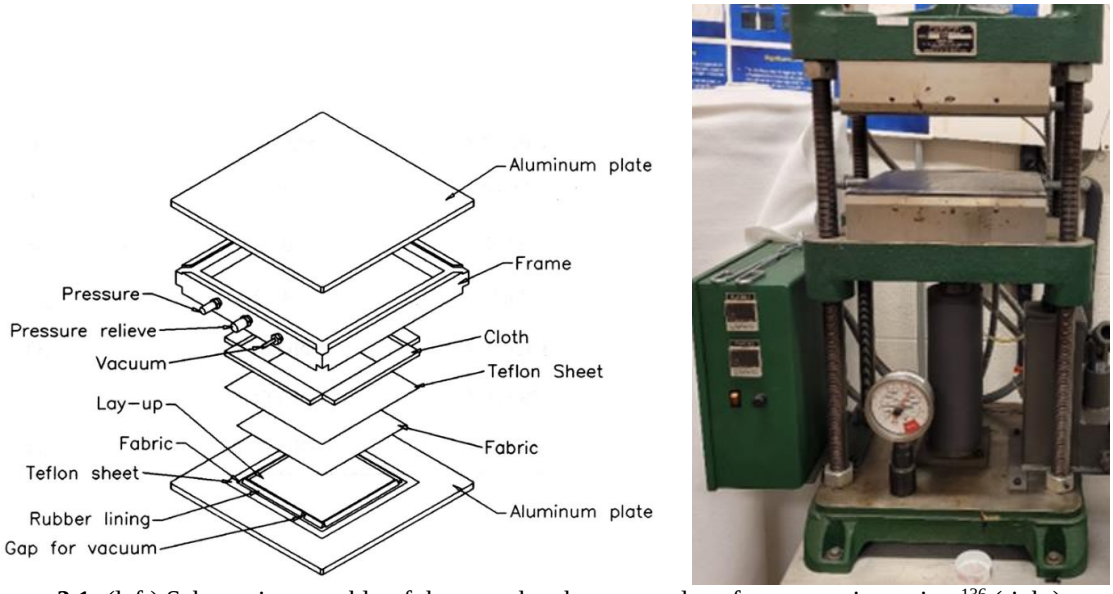

Figure 3.1: (left) Schematic assembly of the two-chamber press-clave for composite curing.[136] (right) Carver, Inc. model 2699 press-clave without the assembly inserted.

Unidirectional $[0]_4$ and $[90]_8$, along with $[\pm45]_{2S}$, rectangular panels made from the carbon/epoxy material were cured, tabbed, and cut into rectangular specimens using a Ridgid wet circular saw. All specimen dimensions were measured using a Mitutoyo Absolute Digimatic digital caliper and tested in uniaxial tension using an MTS 810 hydraulic load frame in conjunction with and Instron 8800 controller and electronics. The unidirectional specimens were tested in accordance with ASTM D3039[120] and the $[\pm45]_{2S}$ specimens were testing according to ASTM D3518.[137] The load cell had a capacity of 25 kN. To obtain strain measurements, an Instron model I3560-BIA-025M-010-ST biaxial extensometer was used. Results of these tests provided the longitudinal and transverse UD strength and moduli (E_1 and E_2), shear modulus (G_{12}), and Poisson's ratio (ν_{12}) for the carbon/epoxy material. For the carbon/CE material, on the other hand, $[90]_8$

specimens were tested to determine E_2 and ν_{12}, but E_1 and G_{12} were provided by the manufacturer.

Table 3.1: Material properties of unidirectional, orthotropic plies of both the carbon/epoxy and carbon/CE materials. All values were determined experimentally except for E_1 and G_{12} of the carbon/CE material, which was provided by the manufacturer. *Manufacturer data.

Material property	Carbon/epoxy (TR50S/PMT-F3)	Carbon/CE (T1100G/RS-3C)	Method
E_1 (GPa)	96.6±1.0	185*	ASTM D3039[120]
0° tensile strength (MPa)	1263.6±56.4	1999*	ASTM D3039[120]
E_2 (GPa)	6.69±0.02	7.61±0.15	ASTM D3039[120]
90° tensile strength (MPa)	29.5±3.8	36.2±3.7	ASTM D3039[120]
G_{12} (GPa)	3.41±0.03	4.28±0.07*	ASTM D3518[137]
In-plane shear strength (MPa)	54.1±4.1	152.5±2.0*	ASTM D3518[137]
ν_{12}	0.317±0.009	0.28	ASTM D3039[120]

Figure 3.2: (left) MTS 810 servo-hydraulic load frame with an Instron 8800 controller. (right) Instron 5966 screw-driven load frame.

Panels for mode I and mode II interlaminar fracture toughness (IFT) characterization were made from a unidirectional layup. With the carbon/epoxy material, 10-ply panels were manufactured, while 16-ply panels were manufactured with the carbon/CE material because its cured-ply thickness (CPT) was smaller. To make the pre-cracks for the IFT tests, a purple Teflon film approximately 26 microns thick and coated in Loctite Frekote 700-NC mold release agent was used.

For both IFT panels, NFs were electrospun for half of the total spin time onto each of the two plies that met at the midplane. This way, the Teflon film could easily be sandwiched between the two layers of NFs to serve as the pre-crack. This also ensured that there were equal amounts of NFs above and below the pre-crack.

3.1.2 Nanofiber Materials and Electrospinning Process

The electrospun polymer nanofiber materials were polyacrylonitrile (PAN) from Sigma Aldrich (250,000 MW) dissolved as a 9wt% solution in dimethylformamide (DMF) and polyimide (PI) (APS-C2) dissolved as a 10wt% solution in DMF. After mixing the dry polymers with the DMF solvent, the solution was heated to approximately 45°C and stirred for at least 24-48 hours until the polymer was completely dissolved.

For all NF-reinforced panels, nanofibers were collected directly onto prepreg plies, which were taped to a cardboard disk with a bolt through the center. The bolt was secured using conductive carbon tape on the surface of the disk, while the back side of the bolt was fed through a grounded loop and connected to a drill. The drill rotated the disk at approximately 180 rpm to achieve relatively uniform NF-mat thickness on the surface of the ply, although the thickness may have varied by approximately 10% between the center and edges of the ply based on preliminary studies. The carbon tape was covered

with a layer of aluminum foil. The plies were taped down to cover the aluminum foil to ensure a partially conductive path between the grounded bolt and the prepreg. Although there was still a layer of non-conductive covering on the back side of the plies (between the foil and prepreg), the electric field remained strong enough to pull the electrospinning jet towards the plies.

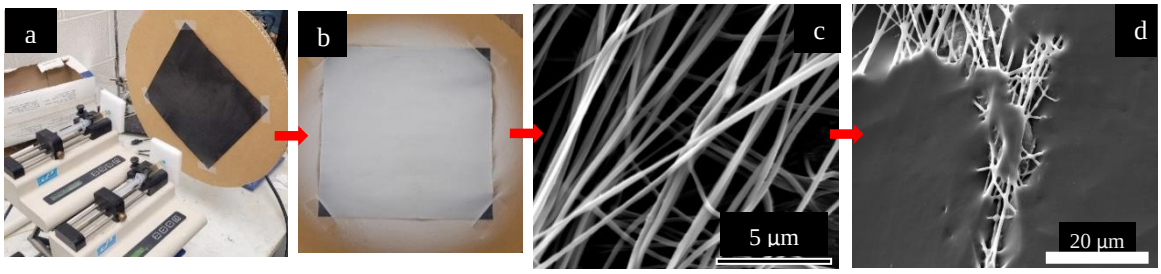

Figure 3.3: Process of electrospinning directly onto prepreg plies before curing. (a) Electrospinning setup. (b) Prepreg ply covered with nanofibers. (c) SEM image of electrospun NFs. (d) resin impregnation of the NF mat, which shows how the resin naturally wetted the NF mats after being left at room temperature for several weeks.

The electrospinning parameters used to fabricate the NF interleaves that reinforced the midplane of the mode I and II IFT specimens are shown in **Table 3.2** and **Table 3.3**, respectively. Although several different NF mats were used to reinforce the specimens, only the mats that provided improved properties are outlined in the tables below. The electrospinning parameters used for other mats can be found in **Table A.1** and **Table A.2**.

Table 3.2: Electrospinning parameters used to manufacture NF interleaves that produced positive mode I IFT results.

Prepreg material	Polymer, concentration (wt%), & solvent	Total spin time (hours)	Needle gauge	Collector distance (cm)	Applied voltage (kV)	Flow rate (mL/h)	Temp (°C)	% Relative humidity
Carbon/ epoxy	PAN 9% + DMF	1	23	16	9.5	0.22	21.7	27.0
Carbon/ CE	PI 10% + DMF	8	23	15	10.0	0.28-0.30	21.5-22.2	24.5-29.8

Table 3.3: Electrospinning parameters used to manufacture NF interleaves that produced positive mode II IFT results.

Prepreg material	Polymer, concentration (wt%), & solvent	Total spin time (hours)	Needle gauge	Collector distance (cm)	Applied voltage (kV)	Flow rate (mL/h)	Temp (°C)	% Relative humidity
Carbon/ epoxy	PAN 9% + DMF	1	23	14	10.0	0.20-0.22	21.7	23.6
Carbon/ CE	PI 10% + DMF	6	23	15	10.0	0.22-0.24	21.7	26.0-28.0

3.1.3 Specimen Preparation and Interlaminar Fracture Toughness Testing

To determine the mode I interlaminar fracture toughness (IFT), the double-cantilever beam (DCB) test, which was detailed by Carlsson[32] and standardized as ASTM D5528,[117] was used. Testing coupons were cut using a Ridgid wet circular saw from the manufactured panels based on the dimensions in **Figure 3.4**. For the carbon/epoxy material, the ASTM standard method was used, but for the carbon/CE material, the procedure from Carlsson was used because the specimens were thinner. Hinges were glued to the top and bottom sides of each specimen using MS-907 two-part epoxy adhesive from Miller-Stephenson and allowed to dry overnight. For the carbon/epoxy specimens, the hinges were positioned to produce an initial pre-crack length of approximately 50mm, while the initial pre-crack length for the carbon/CE material was approximately 35mm. One edge of each specimen was painted white and marked every 5 mm from the end of the pre-crack with a fine point marker to monitor how far the crack had propagated throughout the test. Tests were performed using an Instron 5966 screw-driven load frame with a 2kN load cell and pneumatic grips. Videos of all DCB tests were captured using a cellular phone to monitor crack growth throughout the tests.

Initially, both PAN and PI NFs were electrospun onto both prepreg materials for several different spin times. However, after several different DCB tests, it was determined that only the PMTF3-PAN1 and RS3C-PI12 specimens exhibited positive results (see **Table 3.4**).

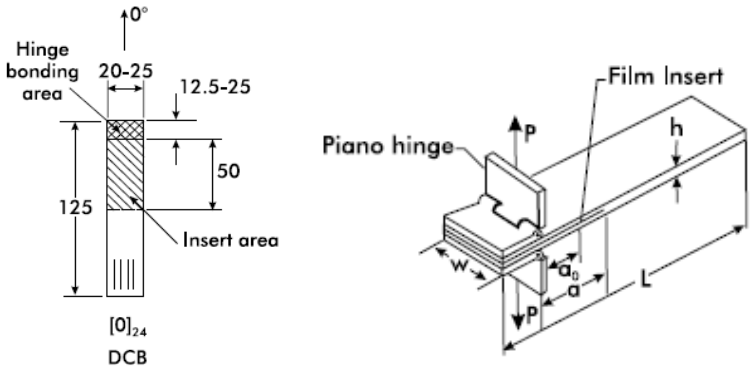

Figure 3.4: Typical dimensions, layup, and geometry for the DCB specimens.[32]

Table 3.4: Materials testing using the DCB procedure.

Material	fiber	resin	NF material	spin time (hours)	Approx. areal weight of NF mat (g/m^2)	Abbrev.	Structure/ test	results compared to pristine
Carbon/ epoxy	TR50S	PMT-F3	-	-	-	PMTF3 (pristine)	Mode I IFT	-
Carbon/ epoxy	TR50S	PMT-F3	PAN	1	0.8	PMTF3-PAN1	Mode I IFT	Significant improve-ments
Carbon/ epoxy	TR50S	PMT-F3	PAN	2	2.1	PMTF3-PAN2	Mode I IFT	Negative
Carbon/ epoxy	TR50S	PMT-F3	PAN	4	5.8	PMTF3-PAN6	Mode I IFT	Negative
Carbon/ epoxy	TR50S	PMT-F3	PAN	8	12.5	PMTF3-PAN12	Mode I IFT	Negative
Carbon/ epoxy	TR50S	PMT-F3	PI	1	0.8	PMTF3-PI1	Mode I IFT	Negative
Carbon/ epoxy	TR50S	PMT-F3	PI	2	1.9	PMTF3-PI2	Mode I IFT	Negative
Carbon/ epoxy	TR50S	PMT-F3	PI	8	9.9	PMTF3-PI10	Mode I IFT	Negative
Carbon/ CE	T1100 G	RS-3C	-	-	-	RS3C (pristine)	Mode I IFT	-
Carbon/ CE	T1100 G	RS-3C	PI	8	12.0	RS3C-PI12	Mode I IFT	Significant improve-ments

Carbon/ CE	T1100 G	RS-3C	PAN	1	0.9	RS3C-PAN1	Mode I IFT	negative
Carbon/ CE	T1100 G	RS-3C	PAN	2	1.5	RS3C-PAN2	Mode I IFT	negative
Carbon/ CE	T1100 G	RS-3C	PAN	8	7.1	RS3C-PAN7	Mode I IFT	negative

To determine the mode II IFT, the end-notched flexure test, which is also described by Carlsson,[32] but has since been standardized as ASTM D7905,[118] was used. Testing coupons were cut from the manufactured panels based on the dimensions in **Figure 3.5**. For the sake of efficiency and because the results for the IFT testing are only preliminary to the structural testing, the procedure from Carlsson was followed. The method requires a three-point bend (3PB) loading fixture. The fixture available in our lab had 1 inch diameter loading noses. Once again, one edge of each specimen was painted white and marked at 5mm increments. The locations of the loading noses on the specimens were marked to determine the length of the initial pre-crack. Specimens were tested using the MTS 810 load frame paired with the Instron 8800 controller.

Since only PAN NFs and PI NFs provided improvements in mode I IFT for the carbon/epoxy and carbon/CE material, respectively, only PAN NFs were electrospun onto the carbon/epoxy material and only PI NFs were electrospun onto the carbon/CE material for the mode II IFT testing (see **Table 3.5**).

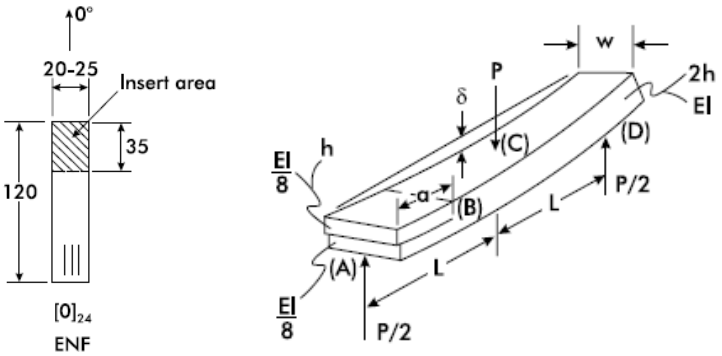

Figure 3.5: Typical dimensions, layup, and geometry for the ENF specimens.[32]

Table 3.5: Materials tested using the ENF procedure.

Material	fiber	resin	NF material	spin time (hours)	Approx. areal weight of NF mat (g/m^2)	Abbrev.	Structure/ test	results compared to pristine
Carbon/ epoxy	TR50S	PMT -F3	-	-	-	PMTF3 (pristine)	Mode II IFT	-
Carbon/ epoxy	TR50S	PMT -F3	PAN	1	0.8	PMTF3-PAN1	Mode II IFT	Slight improve-ments
Carbon/ epoxy	TR50S	PMT -F3	PAN	2	1.3	PMTF3-PAN2	Mode II IFT	Negative
Carbon/ CE	T1100 G	RS-3C	-	-	-	RS3C (pristine)	Mode II IFT	-
Carbon/ CE	T1100 G	RS-3C	PI	6	7.1	RS3C-PI7	Mode II IFT	Significant improve-ments

3.2 MODE I INTERLAMINAR FRACTURE TOUGHNESS TESTING RESULTS

Load-displacement data obtained during the mode I interlaminar fracture toughness (IFT) tests was compiled for all samples tested. Although double-cantilever beam (DCB) specimens were machined to similar dimensions, the load data was normalized by dividing it by the sample width and plotted versus crosshead displacement. Curves from all materials tested were compared to determine which materials had improved mode I IFT (see **Figure 3.6**). As it turned out, it was difficult to obtain improvements with the carbon/epoxy material. In fact, despite testing a multitude of NF interleaf areal weights with both PAN and PI NFs, only PAN1 specimens experienced increased maximum loads compared to the pristine specimens. The PAN2, PAN6, and PAN12 specimens exhibited significantly reduced max loads, while the PI1, PI2, and PI10 specimens showed no significant differences. In addition, based on when the curves become nonlinear, it appeared that the NF interleaves in the PAN1 specimens only

provided increases to the propagation fracture toughness of the material and not the initiation fracture toughness.

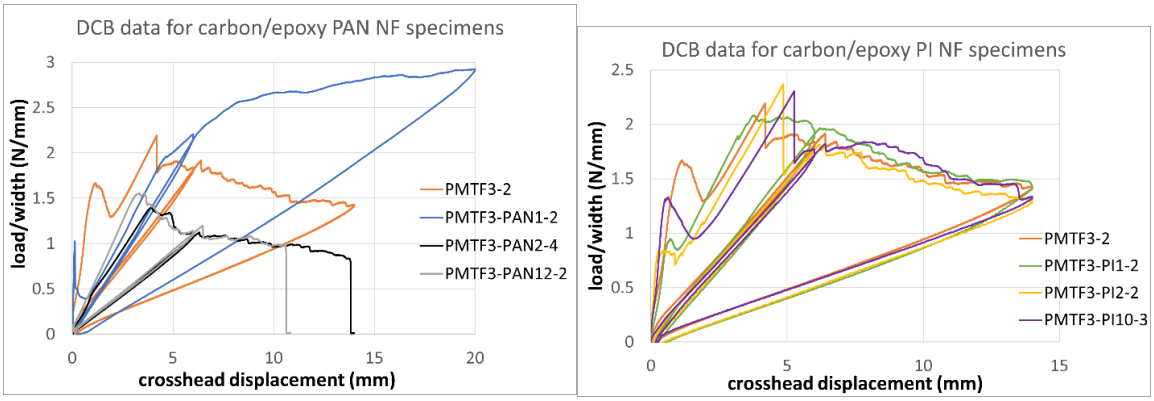

Figure 3.6: Representative curves for the DCB results of the carbon/epoxy materials.

With regards to the carbon/CE material, the PI12 DCB specimens clearly experienced higher loads, even when accounting for the sample width (see **Figure 3.7**). In contrast, all three of the PAN specimens (PAN1, PAN2, and PAN7) exhibited reduced mode I IFTs. Once again, while the PI12 specimens provided much higher load carrying capabilities, the nonlinearity of the curves for both the pristine and PI12 specimens begin at approximately the same applied load. This indicates that the NF interleaves in the PI12 specimens only provided enhanced propagation and not initiation mode I IFT.

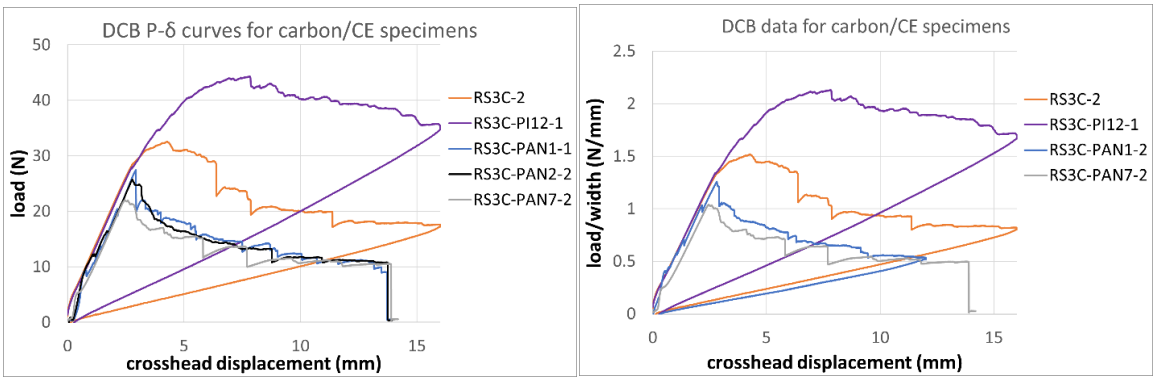

Figure 3.7: Representative curves for the DCB results on the carbon/CE materials.

3.2.1 Mode I Interlaminar Fracture Toughness Data Analysis

For modes I and II, the corresponding interlaminar fracture toughness (IFT) of composites is defined as the work needed to grow a delamination crack.[32,133] In linear elastic fracture mechanics, fracture can be characterized by one of two parameters: the critical strain energy release rate G_C or the critical stress intensity factor K_C. In the case of self-similar (without deflecting) crack growth through an isotropic, homogeneous, linear elastic, and brittle material, it is straight-forward to use either value as a single parameter to characterize fracture.[133] However, the anisotropy and fiber-matrix interaction in FRCs makes the relationship between energy release rate and stress intensity factor slightly more complex, although they can still be safely used to characterize fracture within the interlaminar regions of laminated composites.

The fracture toughness of composites is closely related to the fracture toughness of the matrix material because the crack propagates around and between the fibers.[32,133] However, because of the influence of the fibers, the fracture toughness of the matrix material is rarely the same as that of the composite.[133]

There are three methods that can be used to compute the mode I critical strain energy release rate G_{IC} of unidirectional composites: (1) modified beam theory (MBT), (2) the compliance calibration (CC) method, and (3) the modified compliance calibration (MCC) method.[117] Another method involves computing the difference in area beneath the loading and unloading sequences of the load-displacement curve. Although this "area method" is a very direct approach for determining G_{IC} and only requires the assumption that interlaminar crack propagation is the only source of energy change, while MBT and the CC method require an additional assumption about the load, deflection, and center

crack length,[138] this method is outdated and not recommended because it will not yield an initiation value of G_{IC} or a delamination resistance curve.[139,140]

The other methods were established through extensive research over the last several decades. The CC method was first developed by Berry in 1963 as the "cleavage technique."[141] A beam theory approach was first developed by Williams in 1988,[142] and modified a year later by Hashemi.[143] The MCC method was first proposed by Kageyama in 1990.[144] Although the CC method was a revolutionary analysis, it relies on purely empirical curve-fitting, making MBT and the MCC methods preferred,[145] even though the G_{IC} values determined by all three methods differed by not more than 3.1% in ASTM round robin testing.[117] Overall, MBT is recommended as it yielded the most repeated values of G_{IC} for 80% of specimens tested during ASTM round robin testing, and it typically gives more conservative results.[117] Consequently, the MBT method was used to compute the G_{IC} for all DCB specimens in this work.

The beam theory expression for a perfectly built-in (clamped at the crack front) double cantilever beam is shown in **Equation 3.1**, where P is the load, δ is the crosshead displacement, w is the specimen width, and a is the crack length.

$$G_I = \frac{3P\delta}{2wa}$$

Equation 3.1 [32,117]

However, this expression will overestimate G_I because the beam is not perfectly built-in, which means rotation may occur at the delamination front. One technique for correcting for this rotation is to assume that the DCB contains a slightly longer delamination crack, $a + |\Delta|$. This gives us **Equation 3.2**, where Δ is the x-intercept of the plot between the

crack length a and the cube root of the compliance $C^{1/3}$, as shown in **Figure 3.8**. The compliance, C, is the ratio of the load point displacement to the applied load, δ/P.

$$G_I = \frac{3P\delta}{2w(a + |\Delta|)}$$

Equation 3.2 [32,117]

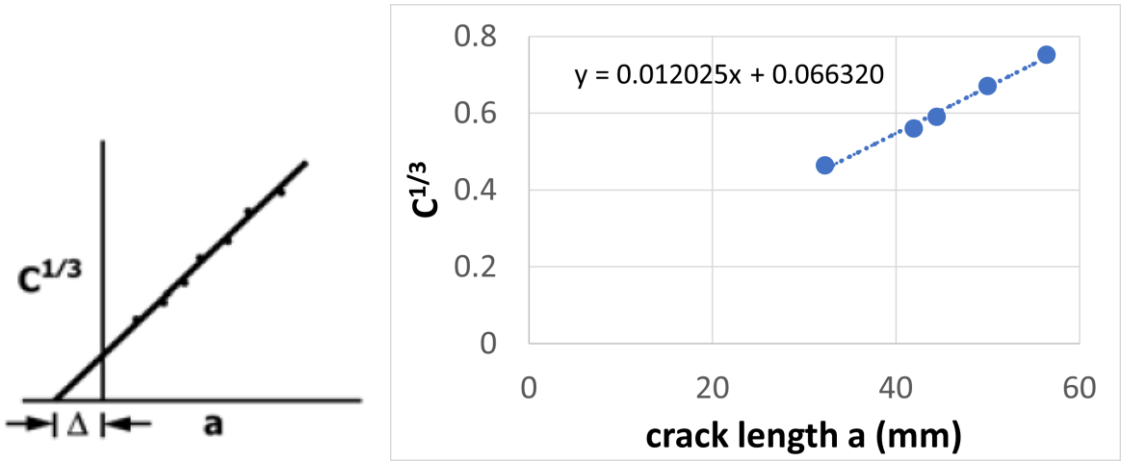

Figure 3.8: Example (left) and measured (right) plot of the crack length vs. the 1/3 power of the compliance. The measured plot came from the DCB data on the RS3C-PI12-1 specimen.

Using this MBT equation, five distinct G_I values were determined from each DCB specimen made from the PMTF3 pristine, PMTF3-PAN1, RS3C pristine, and the RS3C-PI12 materials, starting from mode I crack initiation. These 5 data points were used to compile a mode I crack resistance curve (R-curve) for each specimen (see **Figure 3.9**). To determine the crack length a, the videos obtained during the tests were analyzed. The corresponding load and displacement values were determined by matching the time stamps from the video and the raw data.

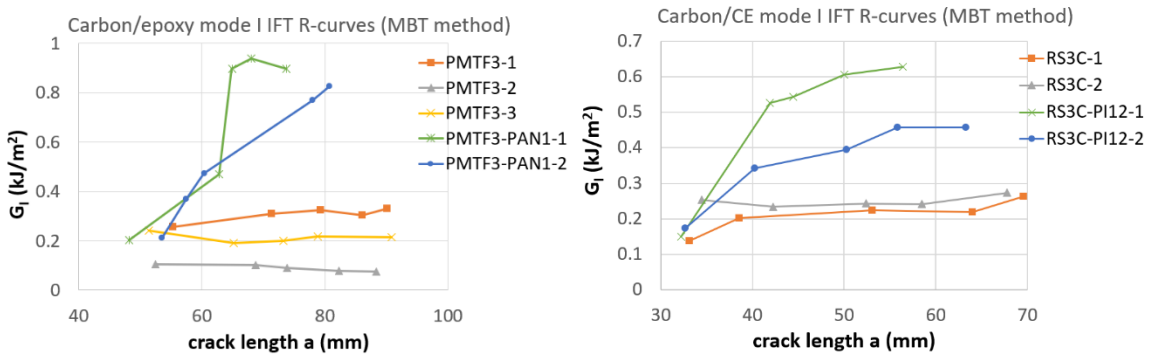

Figure 3.9: Mode I interlaminar crack resistance curves.

Although the initiation G_I values were relatively similar for all specimens, the PMTF3-PAN1 and RS3C-PI12 specimens exhibited significantly increasing G_I values as the mode I crack grew. In contrast, both the pristine carbon/epoxy and pristine carbon/CE specimens showed relatively constant G_I values with crack length. **Figure 3.10** shows the comparison between the initiation G_I (or G_{IC}) and the maximum G_I, of which the NF-reinforced specimens exhibited drastically improved values. The initiation G_{IC} was measured just before the mode I crack propagated past the Teflon pre-crack, while the maximum G_I could have occurred anytime throughout the test (i.e., during initiation or propagation). For the NF-reinforced specimens with improved G_I values, the G_I values typically increased with the crack length, so most maximum G_I values occurred at the maximum crosshead displacement. Explanation of these results will be provided in the following section.

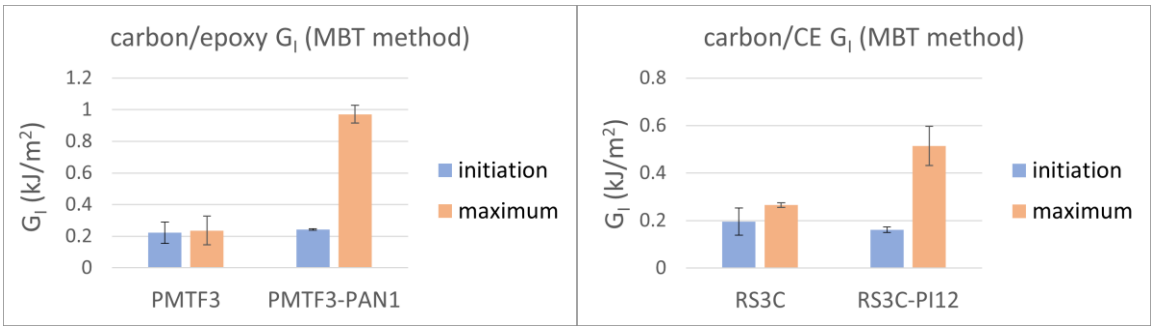

Figure 3.10: Mode I strain energy release rates.

Once the strain energy release rates were computed, **Equation 3.3** was used to compute the stress intensity factors K_I, where $S_{11} = \frac{1}{E_1}$, $S_{22} = \frac{1}{E_2}$, $S_{12} = \frac{-\nu_{12}}{E_1}$, and $S_{66} = \frac{1}{G_{12}}$. Results were charted in **Figure 3.11**. Although the improvements seen in the NF-reinforced specimens compared to the pristine specimens for the K_I values were more modest than those for the G_I values, it is still obvious that the NF interleaves were able to considerably increase the maximum stress intensity factors of both the carbon/epoxy and carbon/CE materials.

$$G_I = K_I^2 \left(\frac{S_{11}S_{22}}{2}\right)^{1/2} \left[\left(\frac{S_{22}}{S_{11}}\right)^{1/2} + \frac{2S_{12} + S_{66}}{2S_{11}}\right]^{1/2}$$

Equation 3.3 [146]

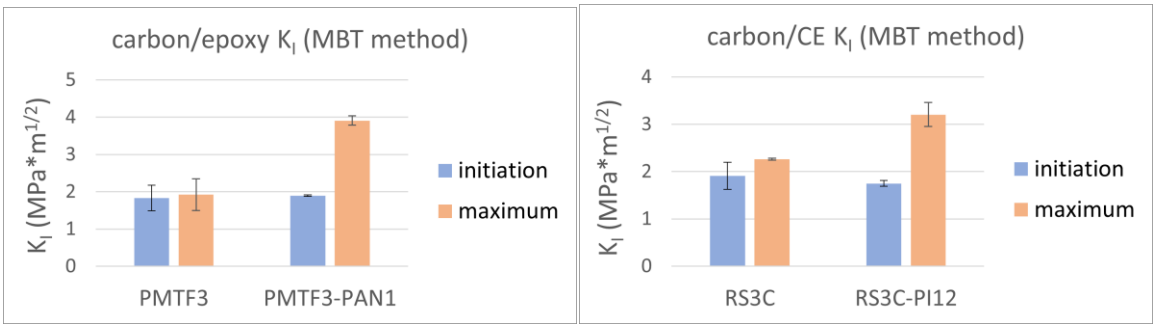

Figure 3.11: Mode I critical stress intensity factors.

3.2.2 Discussion of Mode I Interlaminar Fracture Toughness Testing Results

Based on the curves obtained from the DCB tests, the thickness of the NF interleaves plays a critical role in mode I IFT. Both not enough and too many nanofibers added to the interlaminar region can cause decreased interlaminar properties.[64,147] Specifically, one study found that specimens reinforced with NF interleaves over 10 g/m^2 exhibited decreased fracture toughness.[64] However, NF mats with areal weights up to 25 g/m^2 have been used to increase mode I IFT. In addition, areal weights as low as 1.5 g/m^2 have provided improved properties. Nanofiber wettability is a critical factor of

interlaminar toughening.[148] If there are too many NFs, it can lead to improper wetting compaction, which impedes the interface bonding.[147] The VARTM process may result in better resin impregnation, while prepreg manufacturing is more prone to create voids that weaken the interface if the NF mat is not porous enough.[45] However, based on **Figure 3.12**, both PAN and PI NFs showed adequate wettability with both PMT-F3 epoxy and RS-3C cyanate ester resins. The PAN and PI NF mats were electrospun directly onto the carbon/epoxy prepreg for 30 minutes and 4 hours, respectively, while the PAN and PI NF mats were spun onto the carbon/CE prepreg for 30 minutes and 3 hours, respectively. These NF-covered prepregs, which were leftover sections obtained before curing the panels, were left to sit at room temperature for several weeks. Both PAN and PI NFs show good wettability with both types of resin, even at room temperature and with no added pressure. During curing, the increased temperature and pressure would allow the resin to fully impregnate the NF interleaves, which is evident in **Figure 3.12**e-g, in which the NF interlayer has fewer voids than the unreinforced interlayers. Even though the PMT-F3 resin is expired, it was able to adequately infuse through even the PI10 NF mat.

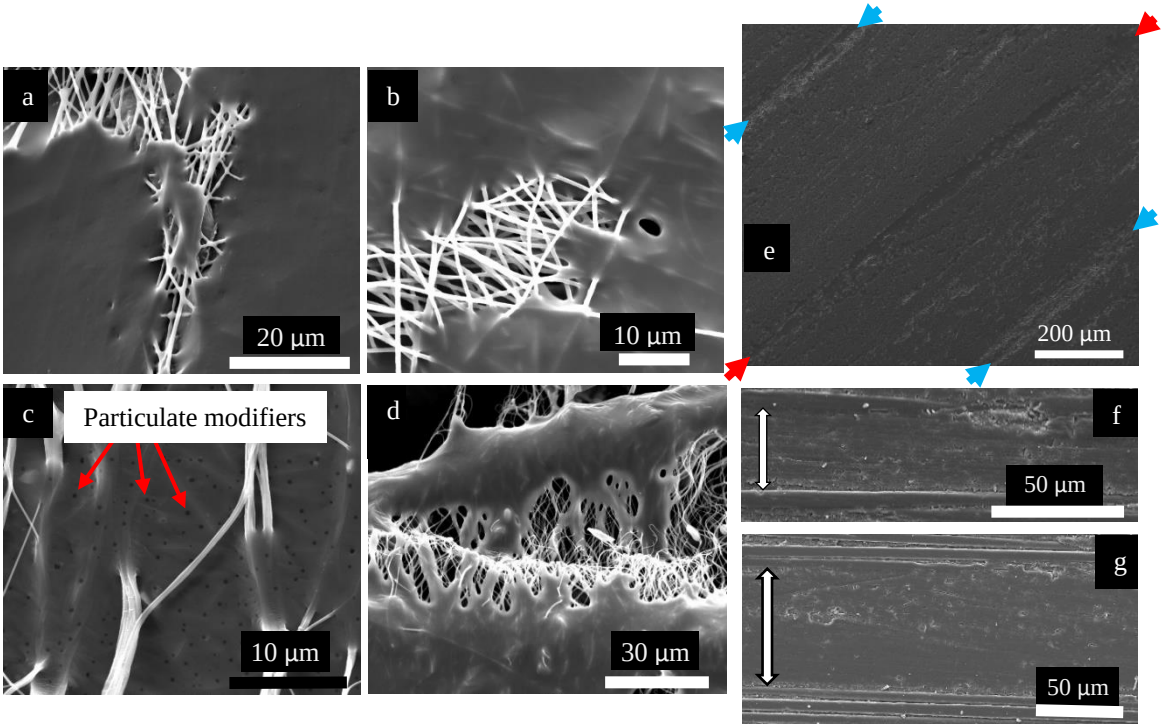

Figure 3.12: SEM images showing the wettability of (a) PAN NFs with epoxy, (b) PI NFs with epoxy, (c) PAN NFs with epoxy, and (d) PI NFs with CE resin. The black dots in (c) are the particulate modifiers that were added by the manufacturer to increase the toughness of the CE resin. (e) cross-section of a DCB PMTF3-PAN1 specimen. The red arrows indicate the NF-reinforced interlayer while the blue arrows indicate the pristine interlaminar regions. (f) cross-section of a DCB pristine PMTF3 specimen. (g) cross-section of a DCB PMTF3-PI10 specimen. In (f) and (g), the double-sided arrows represent the approximate thickness of the interlaminar region at the midplane.

One of the main advantages of nanofiber interleaves compared to other delamination suppression methods is that they add much less weight and thickness to the composite laminate. Based on **Figure 3.13**, even the RS3C-PI12 NF-reinforced interlayer was only 28.5 ± 3.4 microns thick in the cured laminate, which is relatively similar to the thicknesses of the unreinforced interlaminar regions in the carbon/epoxy and carbon/CE specimens. This accounts for only 1.34% of the total 16-ply laminate thickness. In addition, the areal weight of 12 g/m^2 is only about 8.9% of the areal weight of a single ply of the carbon/CE composite material, which has an areal weight of 135 g/m^2.[149] This makes the weight of the NF interleaf only about 0.56% of the 16-ply laminate. As shown in **Figure 3.13**c and d, the thickness of the interlaminar region of the pristine specimens

is comparable to that of the RS3C-PI12 specimen. The areal weight of the carbon/epoxy composite material is 124 g/m^2, but its cured-ply thickness (CPT) is much larger. The CPT of the carbon/CE material is around 0.127mm, while the CPT of the carbon/epoxy material is around 0.380mm. According to the manufacturer (Patz Materials and Technologies), this large CPT was likely due to the fact that the resin was well past its shelf life, preventing its flowing during the thermal curing schedule. This caused a 10-ply layup made from the carbon/epoxy material to be almost twice as thick as a 16-ply layup made from the carbon/CE material. Thus, a NF interleaf with an areal weight of 12 g/m^2 would account for an even smaller percentage of the overall thickness of a 10-ply carbon/epoxy laminate. In practice, only the PMTF3-PAN1 specimens experienced increased mode I IFT, which means the NF weight and thickness fraction of the entire material was negligible.

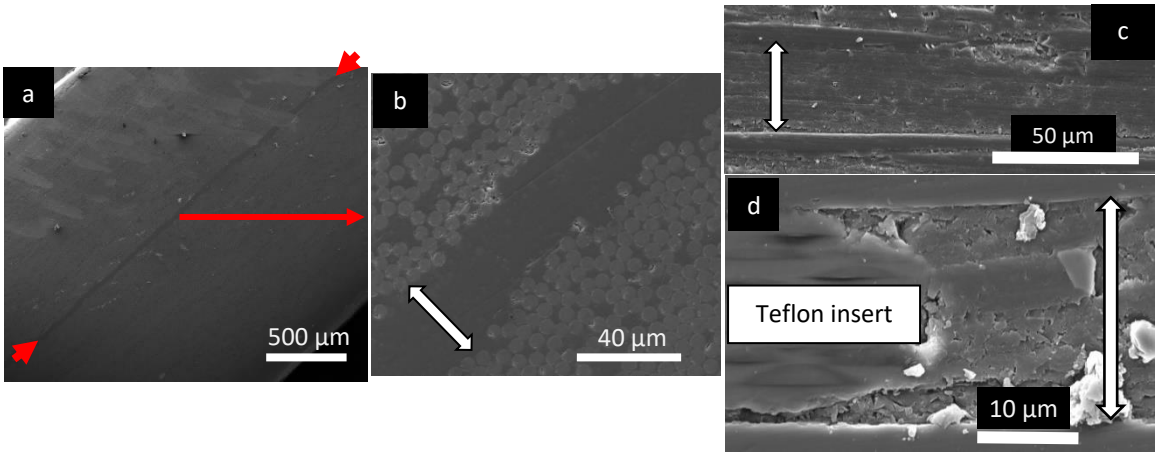

Figure 3.13: (a and b) SEM micrographs of the RS3C-PI12 DCB specimen cross-section. Mode I crack propagation would have occurred into the page. (c and d) Cross-sections of pristine (c) PMTF3 and (d) RS3C DCB specimens. Crack propagation would have occurred from left to right. All double-sided arrows represent the thickness of the interlaminar region at the midplane.

One of the primary toughening mechanisms that has been observed in mode I IFT testing is fiber bridging across the crack. This can occur at two scales. At the macroscale, the bridging of the primary reinforcing fibers (most commonly carbon or glass) occurs,

while at the microscale, the nanofibers are able to bridge the interlaminar crack. During mode I failure, loading of the NFs is less optimal (compared to mode II) and highly dependent upon the presence of a carbon fiber bridging zone.[45,63] As the crack propagates, bridging carbon fibers are torn through the NF modified layer, which assists effective load transfer to the NFs and thus high mode I IFT values.[63] Carbon fiber bridging was highly evident in the DCB specimens tested. **Figure 3.14** shows that the carbon/epoxy pristine and PAN1 specimens experienced significant CF bridging, while the PI1 specimen experienced much less. The CF bridging in the PAN1 specimens also occurred much closer to the crack front compared to that of the pristine specimen. In **Figure 3.15**, the carbon/CE pristine and PI12 specimens show some CF bridging, while the PAN7 specimens shows none. These observations help explain the differences in mode I IFT.

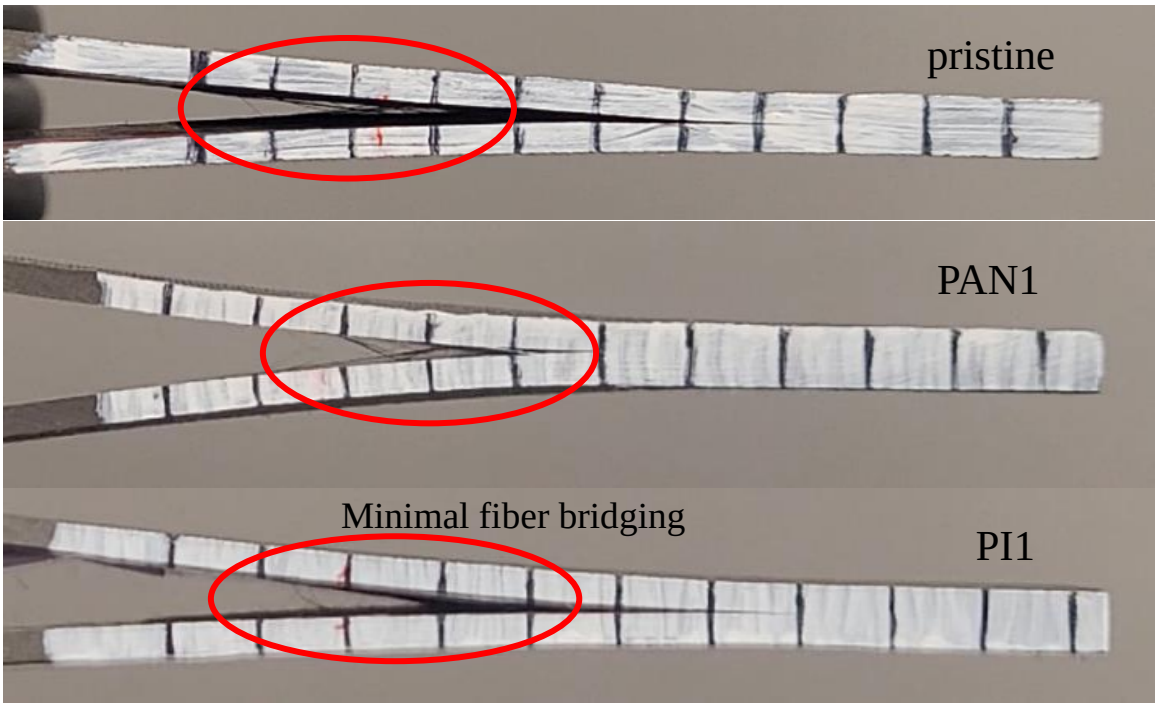

Figure 3.14: Carbon/epoxy mode I crack propagation.

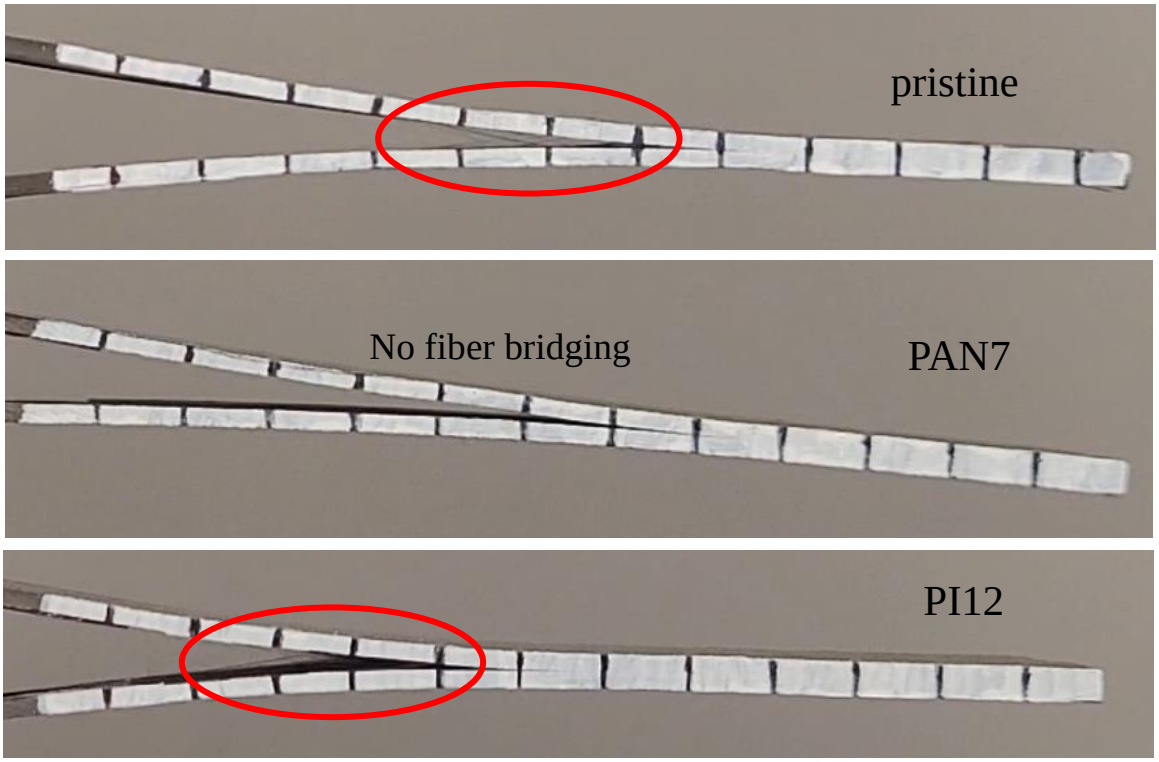

Figure 3.15: Carbon/CE mode I crack propagation.

SEM investigation of the mode I fracture surfaces shows that the PMTF3-PAN1 specimens experienced more CF breakage than did the PMTF3 specimens (see **Figure 3.16**). A similar trend is evident on the fracture surface of the RS3C and RS3C-PI12 DCB specimens (see **Figure 3.17**). There is some fiber breakage, but the surface is smooth for the most part, meaning the crack propagated longitudinally through the resin-rich interlayer over the surfaces of the carbon fibers. On the PAN1 surface, there is much more fiber breakage compared to the pristine specimen, and the surface is rougher, signifying fiber bridging and a more tortuous crack path. This is the reason for the increased mode I IFT. With respect to the carbon/CE material, the pristine specimen shows significant hackle patterns, characteristic of matrix failure, while the PI12 specimen shows carbon fiber breakage, which would have occurred during carbon fiber bridging and is the primary mechanism of increased mode I IFT.

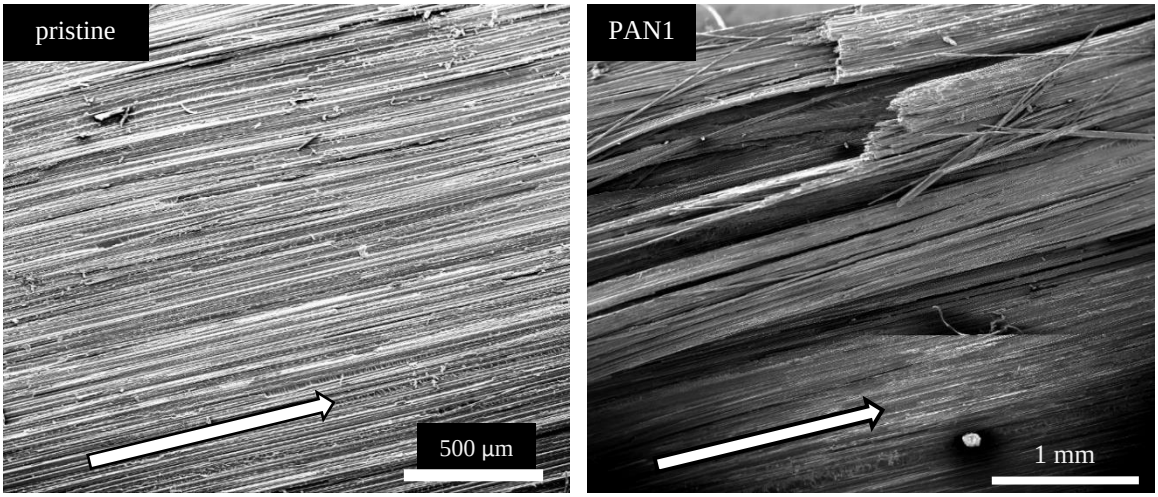

Figure 3.16: SEM micrographs of the mode I interlaminar fracture surface of carbon/epoxy pristine and PAN1 specimens. The crack propagation followed the direction of the arrows.

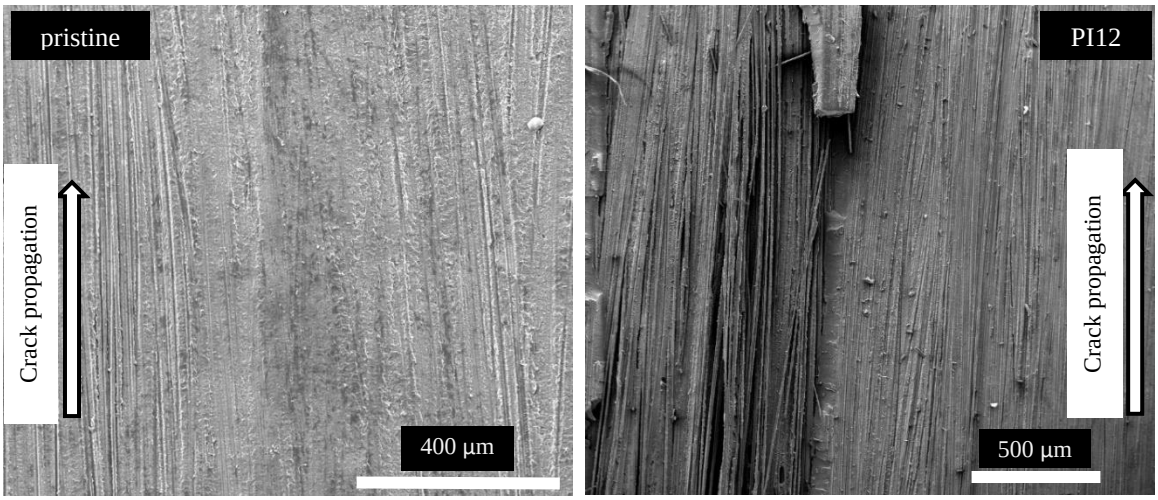

Figure 3.17: SEM micrographs of the mode I interlaminar fracture surfaces of carbon/CE pristine and PI12 specimens.

Near the interlaminar microcrack front, nanofiber bridging can occur, which has the ability to greatly increase the mode I IFT of the material. Whenever the crack sporadically crosses the NF-reinforced interlaminar region, the NFs have the opportunity to bridge across it.[45,87] This causes the NFs to be strained, and their large plastic deformation increases the energy needed to grow the crack. [64,87,134] In **Figure 3.18**, there is evidence of PI NF bridging in addition to particulate toughening (from the manufacturer) of the CE resin matrix. Although the NF bridging mechanism can provide

significant interlaminar toughening, its effectiveness depends on proper load transfer to the NFs, which is highly dependent on NF-matrix adhesion.[63] In **Figure 3.19** and **Figure 3.20**, the debonded PAN NFs and nanofiber indents are clear signs of suboptimal NF-matrix adhesion.

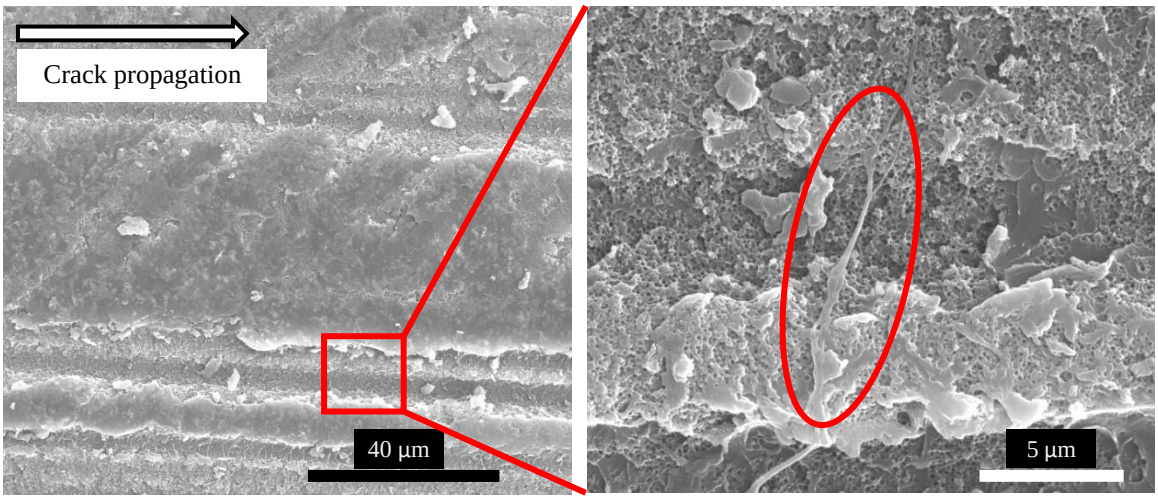

Figure 3.18: SEM micrographs of the mode I interlaminar fracture surface of a RS-3C-PI12 specimen.

Fracture toughness of NF-interleaved laminates is highly dependent upon the NF and matrix materials used, along with the manufacturing process. Choosing the proper polymer nanofiber material is also a critical factor. The toughening effect depends on proper load transfer to the NFs, which requires compatibility between the nanofiber and matrix materials. [63,148] NF-matrix adhesion is crucial because the NFs are subject to normal forces during mode I fracture.[64] Developing an optimum, repeatable, and reliable interleaving process in which the resin and NFs have a good bond is considered crucial.[45] Nanofiber debonding from the matrix can cause significant decreases in mode I IFT.[150] This is the main reason for the poor results obtained for the PMTF3-PAN2, PMTF3-PAN6, and PMTF3-PAN12 specimens. Although the epoxy resin was able to adequately infiltrate the NF interleaves, the adhesion between the resin and the PAN NFs was suboptimal, which caused the mode I crack to initiate before reaching loads comparable

to those reached by the pristine PMTF3 specimens. Evidence of poor NF-matrix adhesion, which was even present in the PMTF3-PAN1 specimens, can be seen in **Figure 3.19** and **Figure 3.20**.

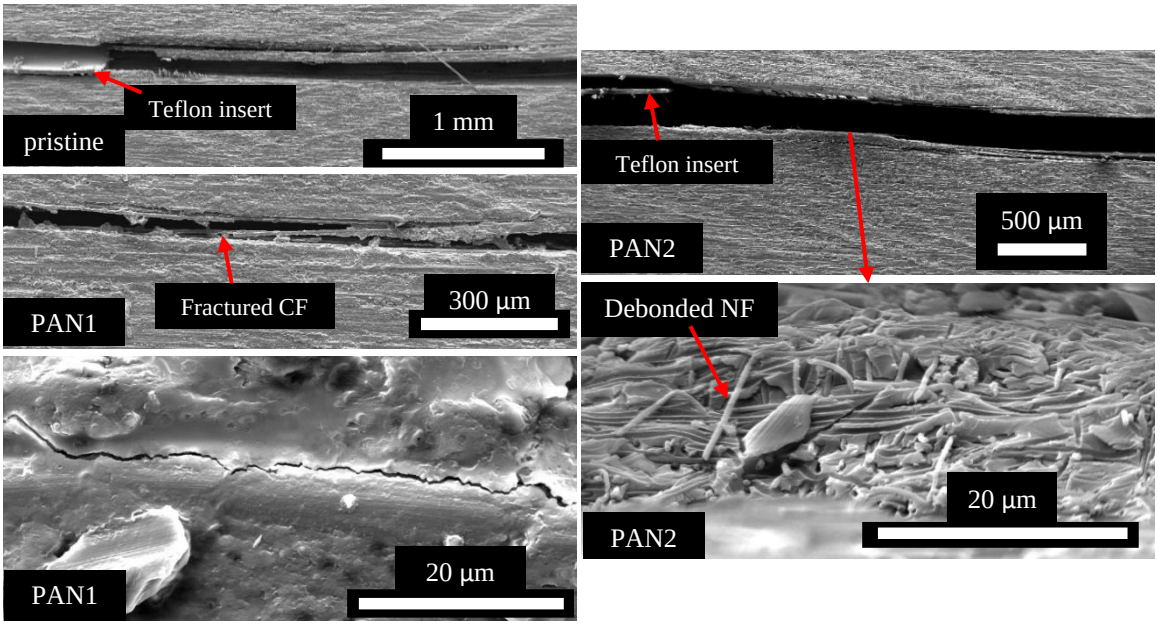

Figure 3.19: SEM images showing the mode I interlaminar crack paths and fracture surfaces of carbon/epoxy specimens. Crack propagation occurred from left to right.

One of the possible reasons for the poor adhesion between the PAN NFs and the epoxy resin is the fact that the resin is expired. Although the laminates made with the PMTF3 epoxy matrix cured adequately, the resin was several years past its storage life. Because crosslinking in thermosetting resins progresses over time, thermoset matrix prepregs have both a shelf life and an out life. The shelf life, typically around 2 years, is defined as the amount of time that the resin can be stored at low temperatures, usually below 0°C (32°F), before the amount of crosslinking makes it no longer considered within specification.[151] The out life, roughly between 10 days and 6 months, is defined as the amount of time the resin can be at room temperature before crosslinking impacts its properties. Although it is commonly accepted that expired prepregs have diminished properties, one investigation of the effect of aging on polymer matrix prepregs found that

Toray T700G-12k/2510 epoxy prepreg could be recycled to make short fiber composites with no loss in modulus and actually a slight increase in strength with age.[152] Another study concluded that excessively aged scrap carbon/epoxy prepreg retained a surprising amount of strength and stiffness.[151] However, Grunenfelder et al. found that when the out life of 21 days for an out-of-autoclave (OOA) curing carbon/epoxy prepreg was surpassed, the void content began to increase due to increased resin viscosity and earlier gelation over the cure cycle. The decreased resin flow rate as out time increased led to inadequate fiber impregnation.[153]

According to the manufacturer (Patz Materials & Technologies), the shelf life for the PMTF3 epoxy resin when stored below 10°F (-12°C) is 2 years, and the out life is 6 months.[154] The prepreg was manufactured in 2009, so it had long passed its shelf life, but the out life has not been reached. One of the ways to test the properties of the cured resin is to perform 90° tensile tests, in which failure is dominated by resin fracture. The manufacturer values for 90° tensile strength and modulus were 55.8 MPa and 11.1 GPa, respectively.[154] Meanwhile, the measured 90° tensile strength and modulus values were 29.5±3.8 MPa and 6.69±0.02 GPa, respectively. These are much lower than the manufacturer values, indicating that the resin properties had substantially diminished since manufacturing. This may have negatively impacted its ability to bond to the electrospun nanofibers.

The poor bonding between the PAN NFs and the expired epoxy resin is shown in **Figure 3.20**. Although both brittle matrix fracture and NF failure mechanisms are evident in the PMTF3-PAN1 specimen, the figure also shows indents of NFs in the polymer

matrix and debonded NFs, which are signs of poor NF-matrix adhesion. However, as the crack propagated, both NF and carbon fiber bridging caused an increase in G_{IC}.

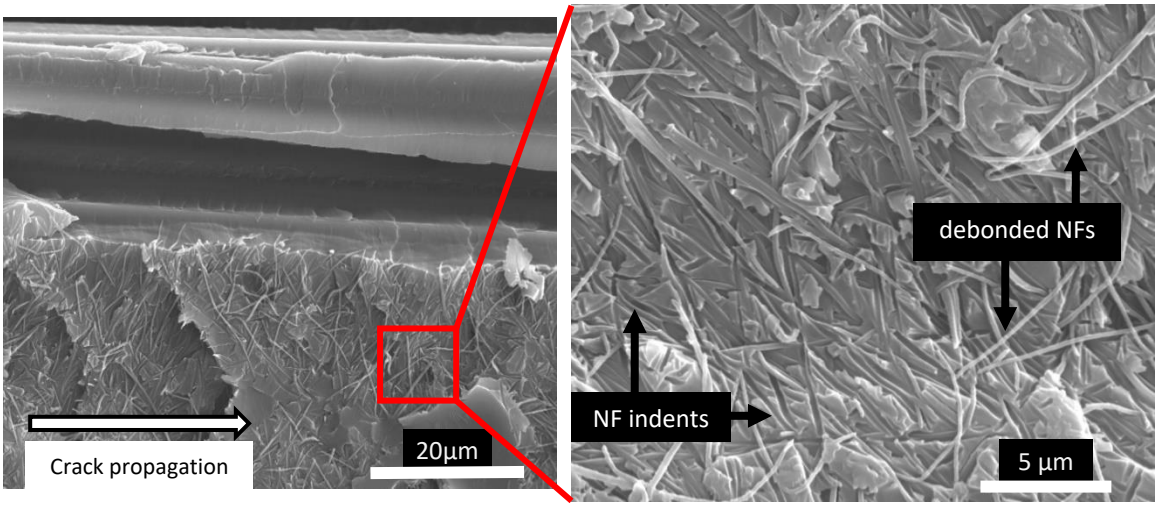

Figure 3.20: SEM micrographs of the mode I interlaminar fracture surface for a PMTF3-PAN1 specimen.

Because interlaminar fracture toughness is defined as the energy needed to grow an interlaminar crack, another primary toughening mechanism in IFT testing is crack deflection. Although interlaminar cracks are generally macroscopically self-similar, they can become crooked and tortuous if the interlaminar region is effectively toughened, especially in an anisotropic manner. In addition to leading to carbon fiber bridging when cracks propagate into the plies (intralaminar fracture), a more tortuous interlaminar crack path requires the crack to break more matrix material, and also more nanofibers, increasing the energy it needs to extend.[90] This is arguably the most effective mechanism to hinder crack propagation.[45] **Figure 3.19** shows a crooked microcrack path in a PMTF3-PAN1 specimen, which would have contributed to its increase G_I values. Meanwhile, the interlaminar crack propagated more self-similarly in the pristine specimens. Although the PAN2 crack path is not perfectly self-similar, the debonding of NFs led to decreased G_{IC}. The PAN1 crack path was very tortuous, evidenced by the fractured carbon fiber, which indicates propagation into the ply. This can occur when the

high toughening effect in the interlayer forces the crack to propagate inside the ply, which is called intralaminar fracture.[56] Although the NFs can only act as crack deflection/stopping zones in the NF-reinforced interlaminar regions, the plies are much less resin-rich than the interlaminar regions, which can make crack propagation require even more energy and can increase the amount of carbon fiber bridging.[64,87] In addition to observing the crack path from the side of DCB specimens, another method for determining how tortuous the crack path was is to investigate the fracture surface using microscopy. A rougher fracture surface confirms that the NFs were able to avert the microcracks, making their paths more tortuous.[90]

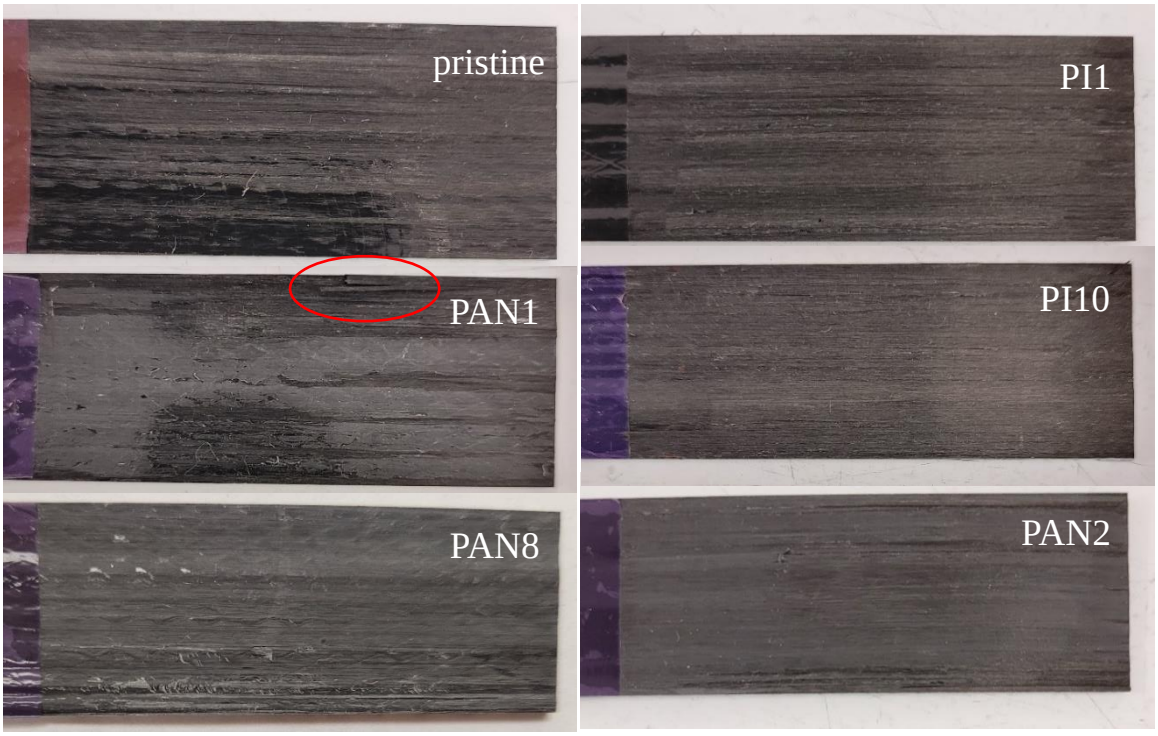

Figure 3.21: Carbon/epoxy DCB fracture surfaces. Crack propagation occurred from left to right.

Looking at the fracture surfaces of the DCB specimens provides insight into how the mode I cracks propagated. At first glance, one can notice the obvious difference in surface roughness. In **Figure 3.21**, the PI1, PI10, and PAN2 specimens show relatively smooth fracture surfaces. Although the pristine, PAN1, and PAN8 specimens possess

rougher surfaces, only the PAN1 specimen surface shows signs of carbon fiber fracture, which occurred during carbon fiber bridging and served to significantly increase the energy needed to grow the crack.

In **Figure 3.22**, although the PAN7 and PI12 specimens exhibit rougher surfaces than the pristine and PAN1 specimens, only the PI12 specimen does not show the striped pattern of alternating stable (slow) and unstable (fast) crack growth. In addition, the PI12 specimen shows signs of carbon fiber breakage and a shiny, resin-rich surface, meaning the mode I crack propagated both through and around the NF-reinforced interlayer. The pristine and PAN1 surfaces are comparatively smooth, while the PI12 and PAN7 surfaces are rougher. Although the crack path may have been more tortuous through the PAN7 specimen, the specimen showed no carbon fiber bridging during testing, while the PI12 specimen did. Also, even if NF bridging occurred, the PAN NFs would have become cyclized during the high-temperature curing cycle of the CE resin, making them brittle. Overall, the fracture surface of the PI12 specimen is the roughest and possesses many fractured carbon fibers, which are the reasons for the increased G_I values.

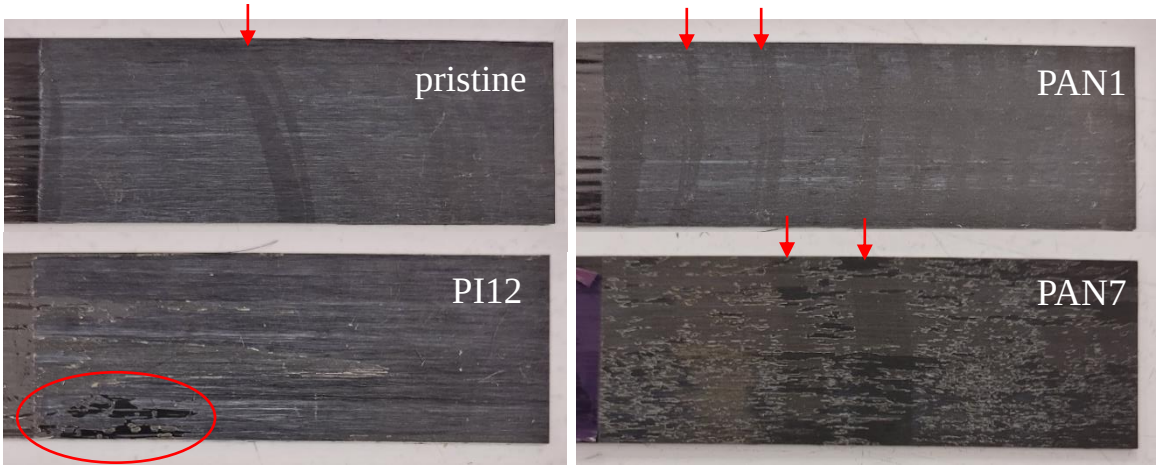

Figure 3.22: Carbon/CE mode I interlaminar fracture surfaces. Crack propagation occurred from left to right. The arrows indicate striping patterns due to alternating stable and unstable crack growth. A matrix dominated failure zone is outlined in the PI12 specimen.

One important thing to note is that even the specimens that exhibited significantly increased maximum G_I values, the initiation G_{IC} values showed little change between the pristine and NF-reinforced specimens. This is primarily due to the bluntness of the pre-crack tip, or the end of the Teflon insert, as shown in **Figure 3.23**. The tip of the Teflon insert was almost completely perpendicular to the crack propagation direction, which means NF bridging could not occur. Also, carbon fiber bridging had not occurred yet either, which was the primary mode I toughening mechanism. However, almost immediately, the toughening effect from the NF interleaves was made evident because no unstable crack growth or consequent drop in load occurred as they did in the pristine specimens (see **Figure 3.24**). During the testing of the PMTF3 pristine specimen, significant unstable crack growth was observed. At 1:54 in the video obtained during the test, the crack had only opened to the end of the Teflon pre-crack, but at 1:55, it had "jumped" by over 10 mm. This "jump" is called unstable crack growth, which is represented by the large drop in load on the load/width vs. displacement curve. Unstable crack growth was also evident in the PMTF3-PI2 and PMTF3-PI10 specimens. However, the PMTF3-PAN1 specimens never experienced this crack "jump," and crack propagation was stable throughout the tests.

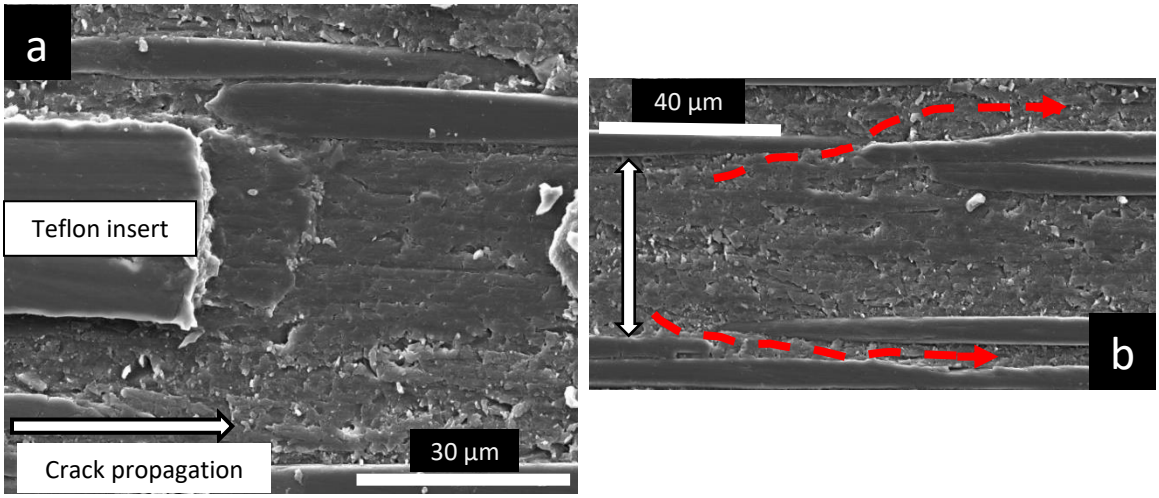

Figure 3.23: Cross-section of a PMTF3-PAN1 DCB specimen. The double-sided arrow represents the thickness of the NF-reinforced interlaminar region. The red dashed arrows in (b) represent potential crack paths that would lead to carbon fiber bridging.

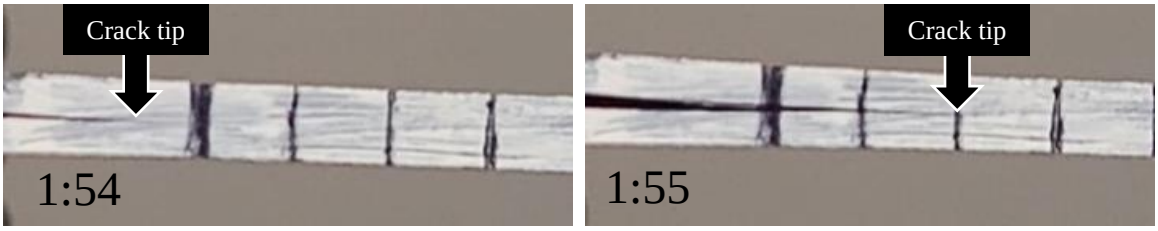

Figure 3.24: Unstable mode I crack propagation in a pristine carbon/epoxy specimen.

Further evidence of the nanotoughening near the edge of the pre-crack is shown in **Figure 3.25** and **Figure 3.26**. The pristine PMTF3 specimen shows significant hackle patterning characteristic of brittle matrix failure just past the edge of the pre-crack, while the PMTF3-PAN1 specimen shows very little or no hackle patterning near the edge of the pre-crack. The PAN1 specimen also possesses both rough and smooth surfaces, indicating that the crack propagated both through and around the NF-reinforced region.

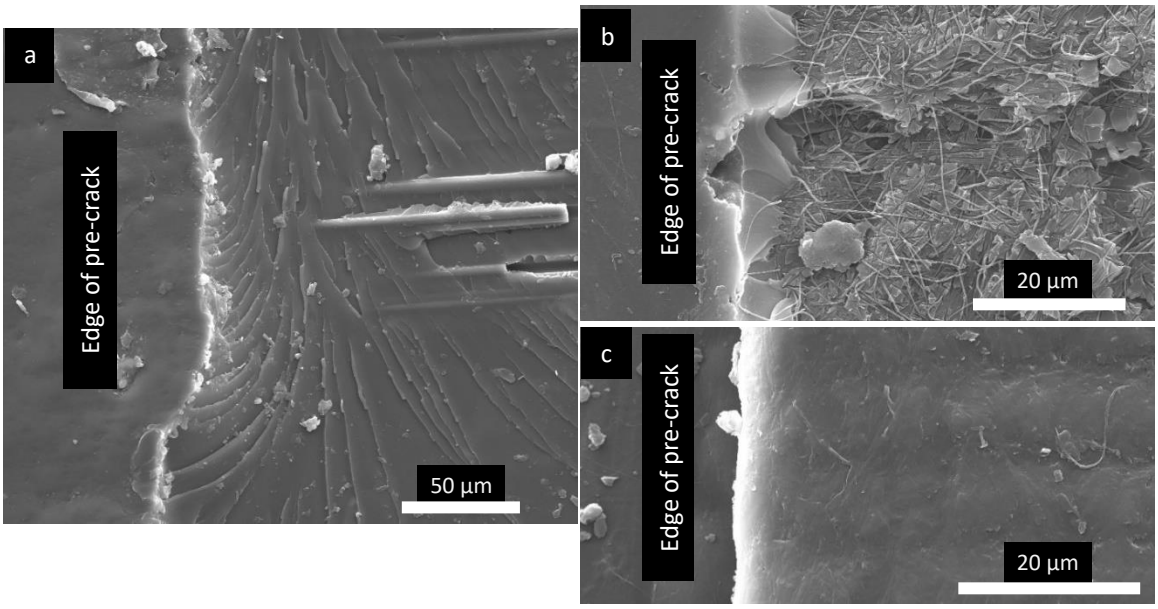

Figure 3.25: Mode I interlaminar fracture surface of (a) pristine and (b & c) PAN1 carbon/epoxy specimens. Crack propagation occurred from left to right.

Meanwhile, the pristine RS3C specimen exhibits a small region of uniformly self-similar crack propagation before the path becomes more tortuous. There are also some voids present. On the other hand, the RS3C-PI12 specimen exhibits multiple failure mechanisms, similar to the PMTF3-PAN1 specimen, in which the crack passed both through and around the NF-reinforced interlayer. In addition, there is evidence of fractured carbon fibers immediately past the pre-crack tip and both smooth resin and rough, jagged regions. This indicates that multiple failure mechanisms occurred.

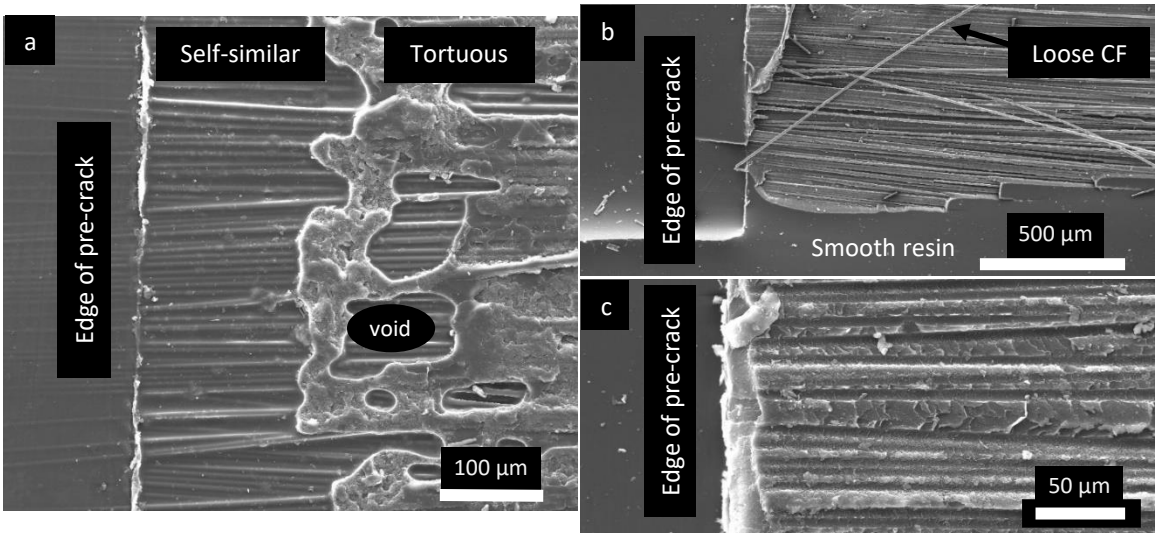

Figure 3.26: Mode I interlaminar fracture surface of (a) pristine and (b & c) PI12 carbon/CE specimens. Crack propagation occurred from left to right.

It has been shown that some NFs can dissolve in resins at elevated curing temperatures, which can be detrimental to nanofiber morphology and can eliminate the ability of NFs to bridge interlaminar cracks.[64] To determine if fiber morphology was preserved during high temperature curing of CE resin, PI NFs were electrospun onto a section of a carbon/CE ply, which was subsequently cured in an oven uncovered. **Figure 3.27** shows that the nanofiber mat was impregnated extremely well with the CE resin and the fibrous morphology of the nanofiber mat was maintained, which allowed for NF bridging to occur.

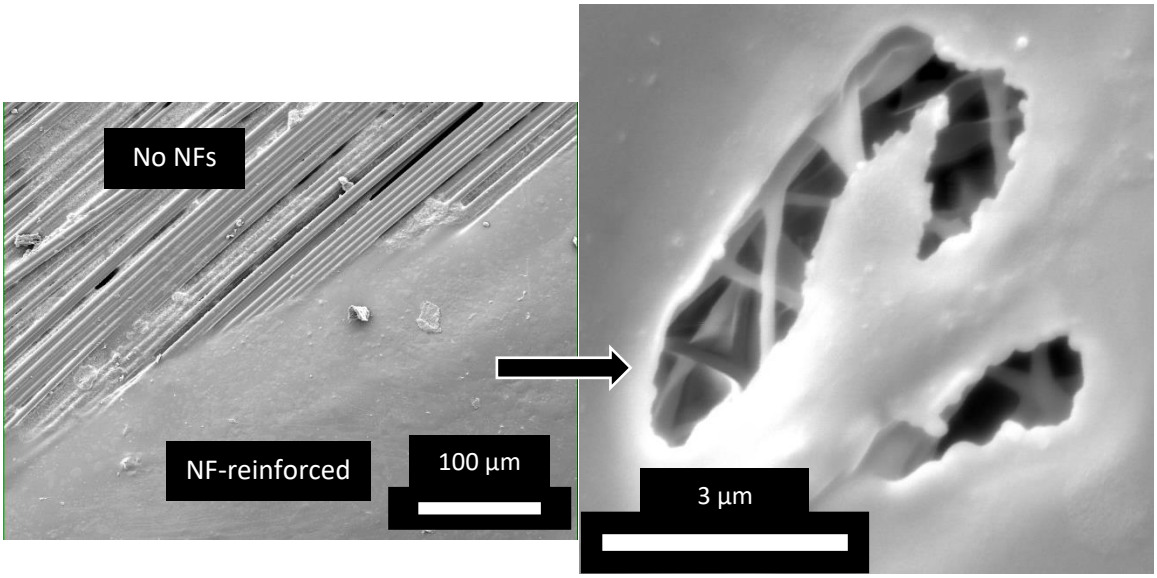

Figure 3.27: Cured carbon/CE ply surfaces covered partially by PI NFs. The plies were cured in an oven without any added pressure.

In addition to morphology, nanofiber diameter can also play a role in delamination resistance. Because fiber diameter affects the properties of individual nanofibers, along with NF mats, it also can influence the toughening effect of nanofiber interleaves. Electrospun nanofibers have been shown to exhibit simultaneous increases in strength and toughness, but only at ultrafine diameters (i.e. ≤ 400 nm).[58] With effective load transfer to ultra-tough NFs, they have the ability to greatly increase composite fracture toughness.[63] In addition, smaller nanofiber diameters typically lead to more significant improvements due to higher surface area per volume, which leads to better fiber-matrix bonding.[150] However, electrospun, crosslinked SBS fibers with diameters up to 2 µm have been used to increase the G_{IC} of glass/epoxy composites.[155] In contrast, large nanofibers with ribbon-like morphologies have been shown to decrease IFT compared to that of pristine specimens, mainly due to the large ribbon-ribbon interfaces that allow the crack to propagate relatively easily.[134] Although there were no observed ribbon-like morphologies in this work, relatively large nanofiber diameter may have

contributed to the poor results obtained from the PMTF3-PAN12 specimens, which had an average NF diameter of 810±110 nm, while the PMTF3-PAN1 specimens had an average NF diameter of 249±48 nm. The RS3C-PI12 specimens had a similar average nanofiber diameter of 253±57 nm. This difference may have played a role in the difference in final mode I IFT, because the smaller nanofibers may have significantly enhanced mechanical properties,[58] along with smaller pore size and higher specific surface area.

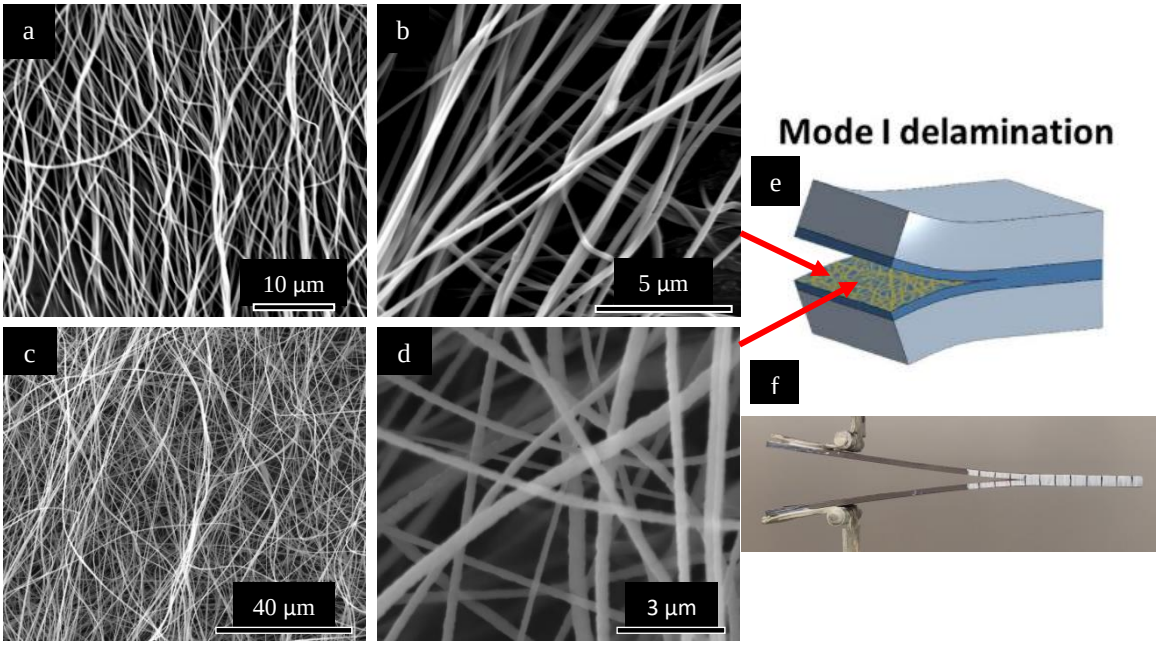

Figure 3.28: SEM micrographs of the (a & b) PMTF3-PAN1 and (c & d) RS3C-PI12 NF mats. (e) schematic of mode I crack growth through the NF-reinforced interlaminar region.[91] (f) DCB experimental setup.

Another factor that can influence the toughening effect of NF interleaves is their thermal stability.[148] In addition to dissolving or melting in the resin matrix, polymer nanofibers can undergo chemical changes during heating. One relevant example of this is the cyclization reaction of polyacrylonitrile, which is initiated at around 180°C.[156] PAN fibers do not melt (unless heated quickly), but rather they go through a series of thermal degradations. At around 180°C, PAN turns into a rigid, crosslinked structure and releases

energy. This process if called cyclization and is shown in **Figure 3.29**. During the cyclization process, PAN turns from white to yellowish, then to brown and, finally, black in color. It also experiences mass loss due to the release of gases.[157] During thermal heating above 180°C, PAN fibers experience both physical and chemical shrinkage. The physical shrinkage can be described as the release of the stresses that were frozen during spinning, which causes entropic shrinkage in the molecular chains. Chemical shrinkage is that which occurs due to the cyclization of nitrile groups leading to imperfect ladder polymer formation.[156] Cyclization can also decrease the tensile strength and Young's modulus of PAN fibers. As the reaction progresses, polar C≡N groups are converted to C=N groups. The absence of polar forces between molecules causes a decrease in the strength of the fibers. In addition, due to the intermolecular crosslinking, the fibers experience a reduced strain at failure, making them much more brittle.[156]

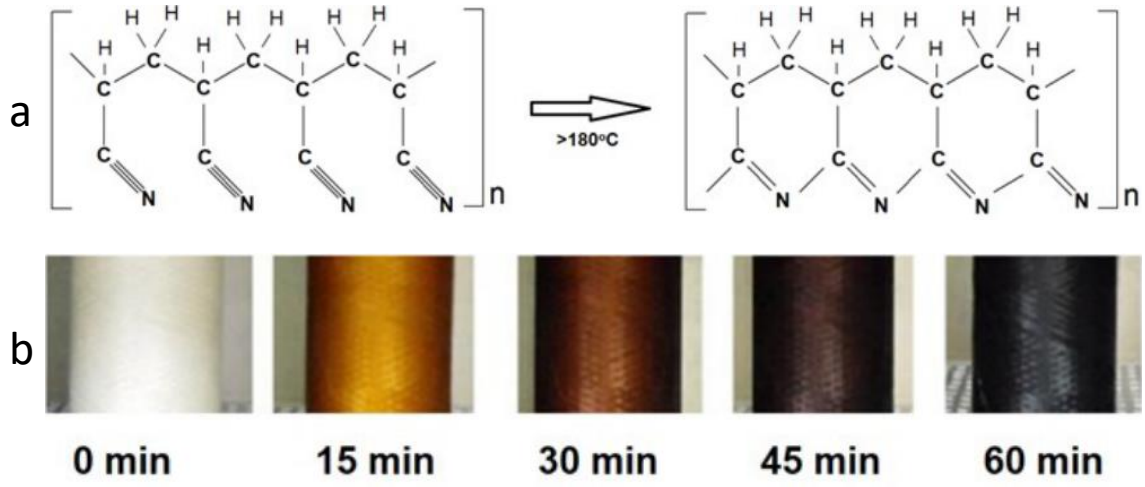

Figure 3.29: (a) PAN cyclization reaction.[157] (b) Heating of PAN-co-PS fibers in isothermal conditions at 190°C in air.[157]

Thermal cyclization of the PAN NFs reinforcing the carbon/CE material may have contributed to the poor mode I IFT. The cure temperature of the carbon/CE specimens was 350°F (177°C), which is right around the threshold at which the

cyclization reaction begins. To examine the thermal effects on the NFs, PI and PAN NF mats were each placed between two pieces of glass and covered with a 200g weight before being baked in an oven at 350°F (177°C) for two hours. As shown in **Figure 3.30**, the PAN mat became yellowish in color and broke with very little deformation. In contrast, the PI mat remained white (see **Figure 3.31**) and experienced a qualitatively higher failure strain when pulled apart by hand. The brittleness of the PAN NFs, in addition to reduced tensile strength and modulus that arise during cyclization, may have been responsible for the significantly reduced mode I IFT experienced by the RS3C-PAN specimens.

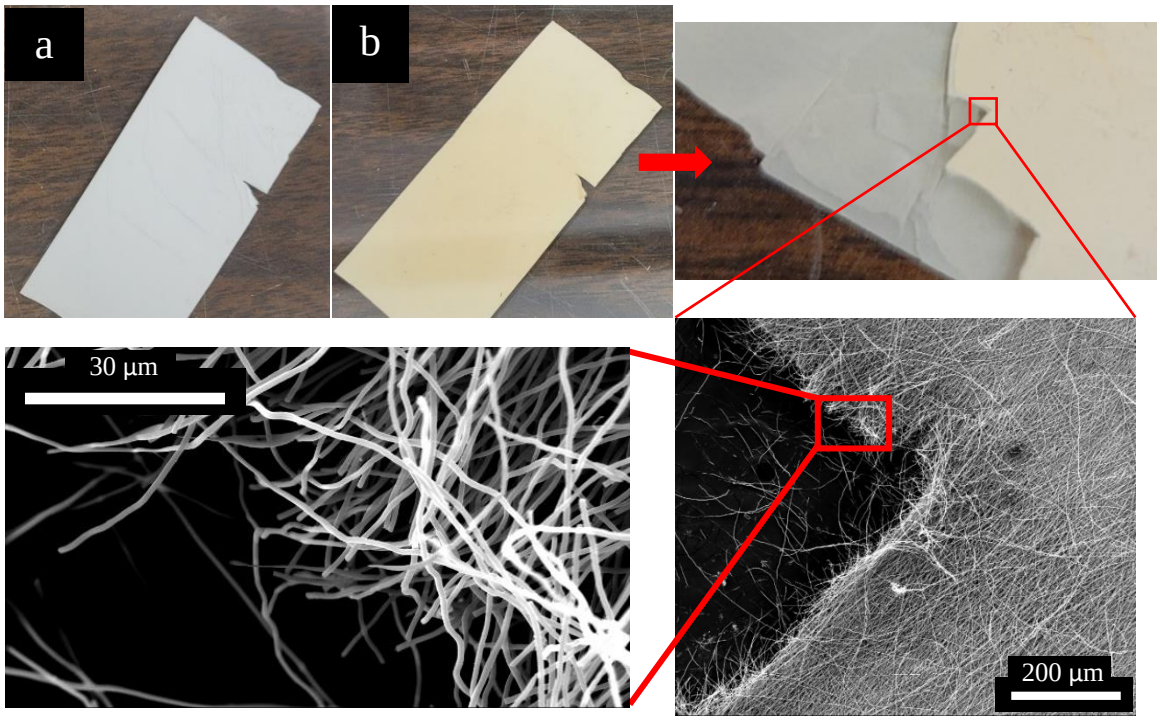

Figure 3.30: A PAN nanofiber mat (a) before and (b) after baking in oven at 350°F for 2 hours and being fractured in tension by hand.

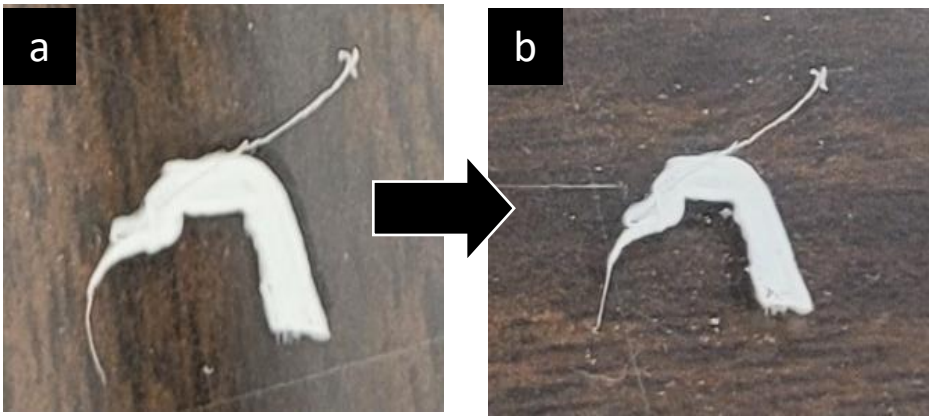

Figure 3.31: Section of a PI NF mat (a) before and (b) after baking in an oven at 350°F for 2 hours between two glass plates.

3.3 MODE II INTERLAMINAR FRACTURE TOUGHNESS TESTING RESULTS

Since only PAN NFs improved mode I IFT in the carbon/epoxy material and only PI NFs improved mode I IFT in the carbon/CE material, the same material combinations were used for the mode II IFT testing: carbon/epoxy + PAN NFs and carbon/CE + PI NFs. During the ENF tests, load-displacement data was obtained, along with a video to monitor crack propagation through the specimens, although mode II crack propagation is unstable during ENF tests, meaning the crack propagated rapidly. For this reason, only one value of G_{II} (G_{IIC} occurs at the maximum load) can be obtained from each ENF specimen.[32] From the raw data, the flexural stress σ_f in the outer (lower) fibers at the midpoint of the span was determined using **Equation 3.4**, where P is the applied load, L is the support span, w is the width of the ENF specimen, and $2h$ is the specimen thickness, and plotted versus the crosshead displacement (see **Figure 3.32**).

$$\sigma_f = \frac{3PL}{2w(2h)^2}$$

Equation 3.4 [158]

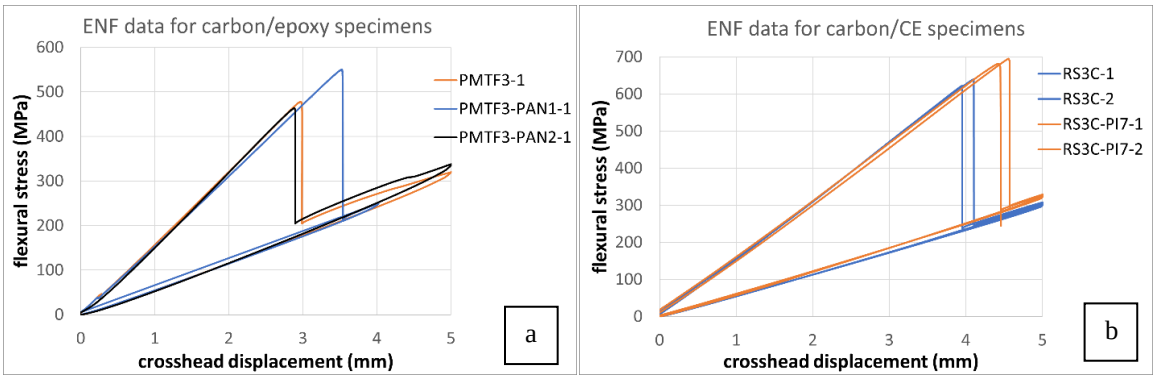

Figure 3.32: (a) Carbon/epoxy representative and (b) carbon/CE stress-displacement curves from the ENF tests.

Based on the stress-displacement curves, it is clear that the PMTF3-PAN1 and RS3C-PI7 specimens exhibited increased mode II IFT compared to the respective pristine specimens. However, further data analysis is needed to determine the actual G_{IIC} and K_{IIC} values.

3.3.1 Mode II Interlaminar Fracture Toughness Data Analysis

In the ENF test, the measured G_{IIC} is believed to represent the critical strain energy release rate for crack propagation from the film insert. The load is introduced by flexural forces to produce a crack from the insert. The crack then extends as a result of shear forces at the crack tip.[139] Standardization of a mode II IFT test was a difficult process, due to several factors. First, the ENF-test is essentially unstable and thus allows only determination of initiation values but not of crack resistance curves. Second, friction may play a significant role in fracture, which resulted in the questioning of whether mode II data were valid as material data.[139]

There are three methods that can be used to compute the mode II critical strain energy release rate G_{IIC}: modified beam theory (MBT) with and without E_1 and the compliance calibration (CC) method.[32,118] The MBT was first proposed by Carlsson et al.[159] with and without knowing E_1.[32] The CC method, which is outlined in ASTM

D7905,[118] was also proposed by Carlsson et al,[160] and it requires that specimens be tested with three distinct crack lengths.[118] Then, a set of compliance values is obtained, and the data is fit to a third order polynomial in crack length.[32] Although the CC method typically provides more conservative and accurate results,[161] Davies et al. found that for a carbon/epoxy material, the coefficient of variation was 21% using the CC method while it was only 14% using the MBT method. This was explained by the fact that the rate of change in the ENF specimen compliance with crack length is relatively small, and the experimental determination of compliance requires accurate measurements of crack length, load, and displacement, while the MBT method only requires the measured crack length and load.[162]

For the sake of efficiency, the MBT approach using the E_1 values in **Table 3.1** was used (see **Equation 3.5**).

$$G_{IIC} = \frac{9a^2P^2}{16w^2h^3E_1}\left[1 + 0.2\left(\frac{h}{a}\right)^2\frac{E_1}{G_{13}}\right]$$

Equation 3.5 [32]

Here, a is the crack length, P is the applied load, w is the specimen width, h is half the specimen thickness, E_1 is Young's modulus in the fiber direction, and G_{13} is the in-plane shear modulus since $G_{13} \approx G_{12}$ for unidirectional specimens.[32] Since crack propagation was unstable, the crack length was determined from the location of the end of the Teflon insert, making it equal to the initial pre-crack length. This equation was used to compute the average critical strain energy release rates for all specimens. The PMTF3-PAN1 specimens showed increased G_{IIC} values compared to the pristine PMTF3 specimens, while the PAN2 specimens showed reduced G_{IIC} values. At the same time, the RS3C-PI7

specimens showed noticeably increased G_{IIC} values compared to the pristine RS3C specimens.

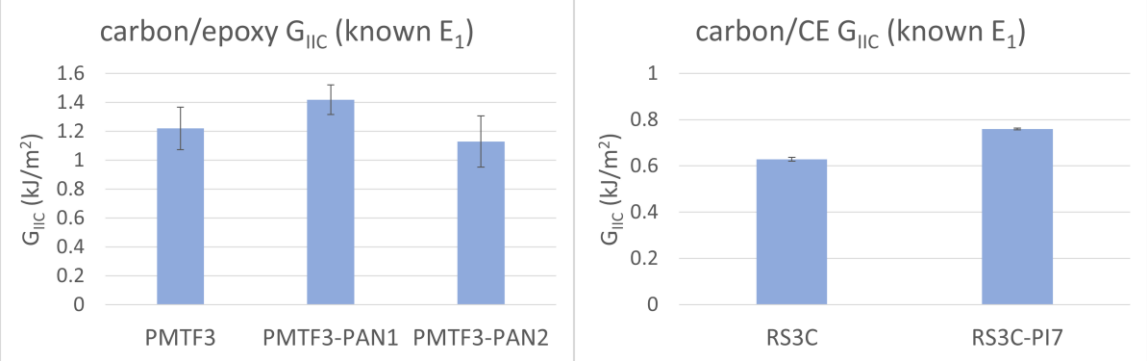

Figure 3.33: Mode II critical strain energy release rates.

Once the mode II strain energy release rates were computed, **Equation 3.6** was used to compute the mode II critical stress intensity factors K_{IIC}, where $S_{11} = \frac{1}{E_1}$, $S_{22} = \frac{1}{E_2}$, $S_{12} = \frac{-\nu_{12}}{E_1}$, and $S_{66} = \frac{1}{G_{12}}$. Results were charted in **Figure 3.34**. Similar to the results from the mode I IFT tests, the improvements in K_{IIC} values were more modest than those seen for the G_{IIC} values.

$$G_{IIC} = K_{IIC}^2 \frac{S_{11}}{\sqrt{2}} \left[\left(\frac{S_{22}}{S_{11}} \right)^{1/2} + \frac{2S_{12} + S_{66}}{2S_{66}} \right]^{1/2}$$

Equation 3.6 [146]

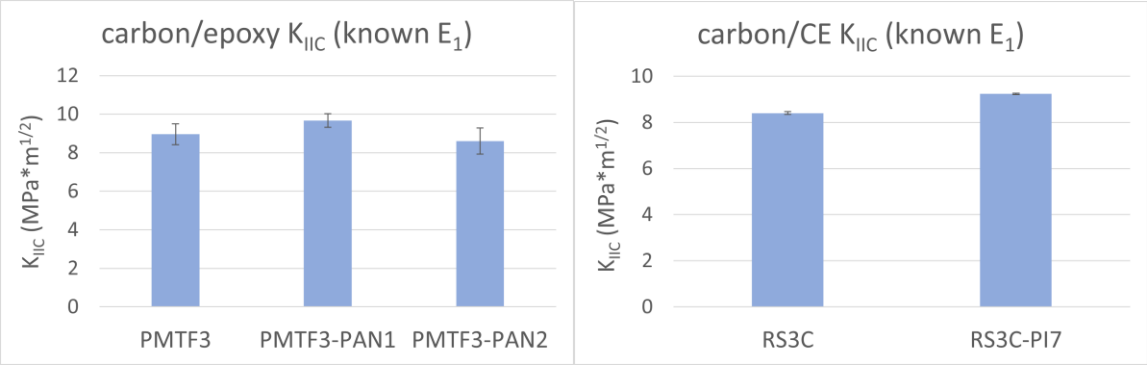

Figure 3.34: Mode II critical stress intensity factors.

3.3.2 Discussion of Mode II Interlaminar Fracture Toughness Testing Results

Mode II interlaminar fracture toughness in NF-interleaved laminates depends on similar factors to those on which mode I IFT depends, namely, NF interleaf thickness and morphology, NF-matrix compatibility, NF bridging, and crack deflection.

According to the literature, mode II interlaminar fracture properties can drop when the nanolayer reaches a certain thickness. There is a threshold value on the amount of nanoreinforcement after which the compliance of the random polymeric NF mat overcomes its strengthening effect.[45] Based on one study, NF mat areal densities of 5-10 g/m^2 seem to be ideal for both modes I and II, and IFT values seem to level off after 10 g/m^2.[64] However, results have been positive with NF interleaf areal weights from 3-22 g/m^2.[45] Looking at the results of the carbon/epoxy ENF tests, the thickness of the NF interleaves in the PAN2 specimens, which had an areal weight of only 1.3 g/m^2, led to decreased G_{IIC} values compared to the pristine PMTF3 specimens. In contrast, the PAN1 specimens, which were reinforced with a NF interleaf with an areal weight of 0.8 g/m^2, exhibited increased G_{IIC} values. It is interesting that a difference of only 0.5 g/m^2 in NF interleaf areal weight led to different results. However, it was already observed that the poor adhesion between the epoxy resin and the PAN NFs may have played a significant role in limiting the interlaminar fracture toughness. It seems as if the interleaf areal weight threshold for the poor NF-matrix bonding to have a negative effect is right around 1.0 g/m^2, above which IFT values are decreased. In contrast, the PI NF mat that reinforced the carbon/CE material had an areal weight of 7 g/m^2. However, significant mode I IFT improvements were seen with a PI NF interleaf of 12 g/m^2. Consequently, an optimal areal weight of PI NF interleaves in the carbon/CE material for both modes I and II toughening should be between 7 and 12 g/m^2.

Like in all composites, toughening during mode II interlaminar fracture critically depends on effective load transfer to the reinforcing component(s).[63] In this case, the reinforcement is the nanofiber interleaf. Although, compared to that during mode I, NF-matrix adhesion during mode II fracture is less crucial because the shear adhesion strength of all NFs is relatively high due to the high specific surface area.[64] In addition, increases in mode II IFT are typically higher than those of mode I IFT due to the optimal, in-plane loading of the NF veil.[63] Nonetheless, since smaller fiber diameters lead to more surface area per volume, they also enhance the NF-matrix bonding.[56,150] In addition, thinner nanofibers have been shown to have improved mechanical properties.[58] Increases in mode II IFT values have been shown with NF diameters from 50 all the way up to 2000 nm, although most studies had diameters between 150 and 500 nm.[45] For these reasons, it is important that the nanofibers are not too large. In the PMTF3-PAN1 specimens, the average PAN nanofiber diameter was 224±37 nm, while in the RS3C-PI7 specimens, the average PI nanofiber diameter was 182±50 nm. These diameters are plenty small enough to provide adequate toughening in the interlaminar region, so long as the NF-matrix adhesion is sufficient.

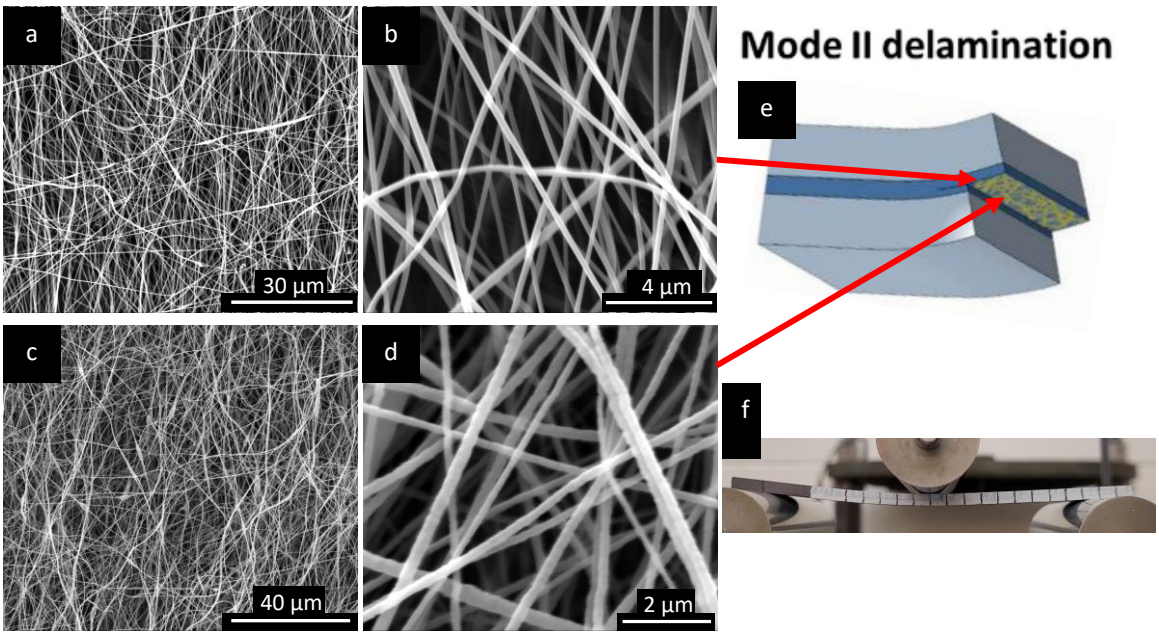

Figure 3.35: SEM micrographs of the (a and b) PMTF3-PAN1 and (c and d) RS3C-PI6 NF mats. (e) schematic of mode II crack growth through the NF-reinforced interlaminar region.[91] (f) ENF experimental setup.

Investigation of the mode II fracture surfaces is a crucial step in understanding the failure and toughening mechanisms. With the naked eye, the fracture surface of the PMTF3-PAN2 specimen looks slightly smoother than those of the pristine and PAN1 carbon/epoxy specimens. Since ENF testing provides only an initiation value for mode II IFT, the fracture surface just ahead of the pre-crack tip can provide valuable insights. The SEM images in **Figure 3.36** and **Figure 3.37** attempt to examine this region. In **Figure 3.36**, shear hackle patterns, along with smooth carbon fiber surfaces can be seen on the pristine PMTF3 ENF specimen fracture surface. These characteristics indicate brittle matrix failure and CF-matrix debonding. In the PAN1 specimens however, the fracture surfaces are rougher and there are fewer shear hackle patterns, which indicates a more tortuous crack path.

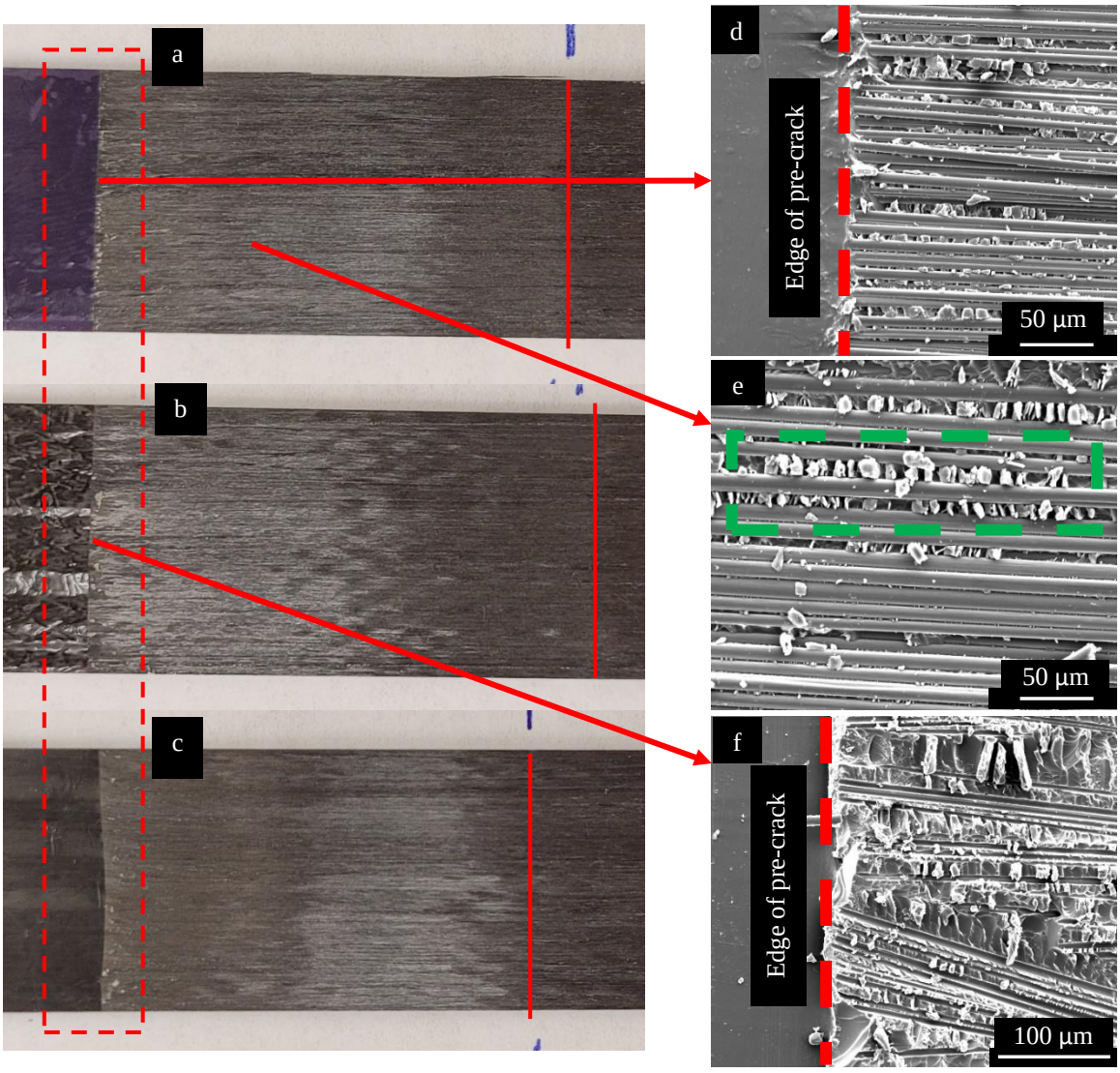

Figure 3.36: Mode II interlaminar fracture surfaces for the carbon/epoxy material. (a, d, and e) pristine, (b and f) PAN1, (c) PAN2. The red box outlines the end of the pre-crack, while the red lines show the approximate location where the cracks terminated after the drastic drop in load. The green box indicates a shear hackle pattern.

Similarly, the pristine RS3C ENF specimen fracture surface is smoother than that of the PI7 specimen. It also shows more shear hackle patterns than that of the RS3C-PI7 specimen, which includes evidence of CF failure (see **Figure 3.37**). Typically, in pristine specimens, hackle patterns are more dense and common, while in NF-reinforced specimens, hackle patterns are locally altered or replaced by a more complex structure or enlarged in size.[148]

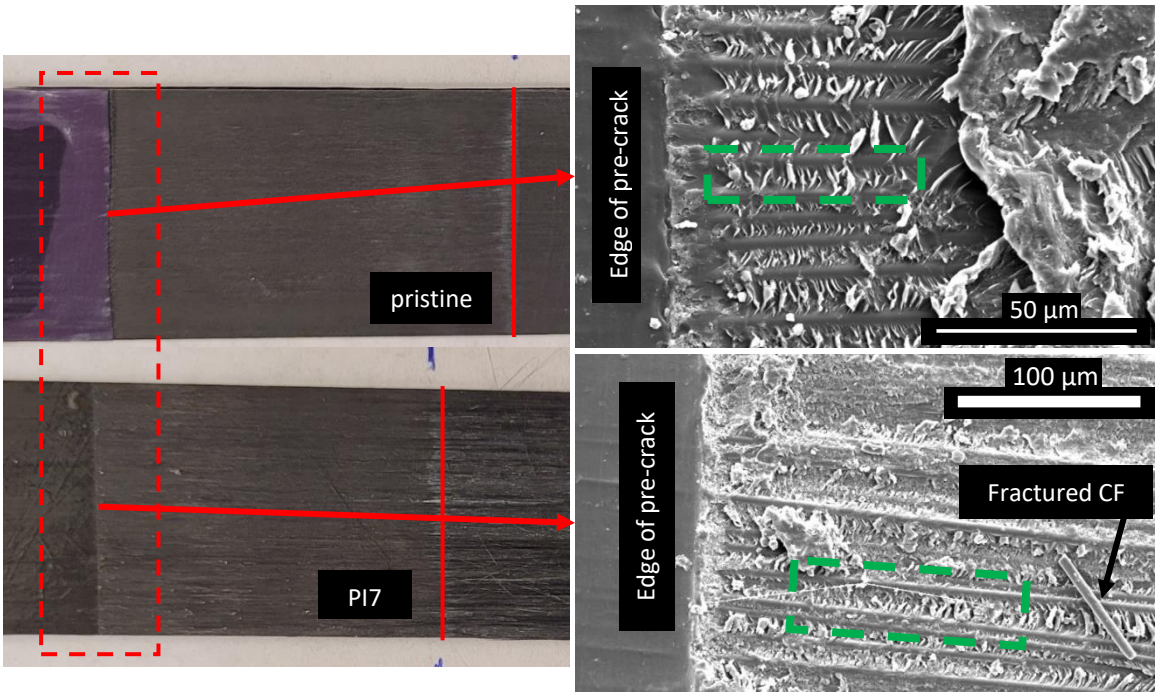

Figure 3.37: Mode II interlaminar fracture surfaces of the carbon/CE material. The red box outlines the end of the pre-crack, while the red lines show the approximate location where the cracks terminated after the drastic drop in load. The green boxes show shear hackle patterns between carbon fibers.

During mode II fracture, carbon fibers have much less opportunity to bridge the interlaminar crack. This gives priority to nanofiber bridging as a toughening mechanism.[45,63] One of the reasons NFs can provide effective toughening is their ability to experience large plastic deformation, which can occur when NFs bridge interlaminar cracks.[64,87,134] However, adequate NF-matrix adhesion is necessary to avoid NF debonding or pullout. **Figure 3.38** shows the rough fracture surface of a PMTF3-PAN1 ENF specimen. There is clear evidence of NF bridging and necking, but the NF debonding and pullout are signs of suboptimal NF-matrix bonding, which limited the mechanical improvements.

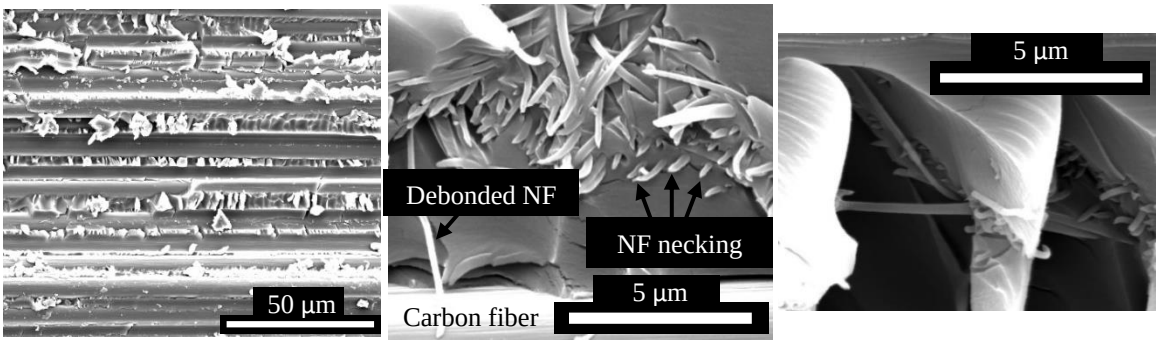

Figure 3.38: Mode II interlaminar fracture surface of a PMTF3-PAN1 specimen. The crack propagation direction was from left to right.

In the RS3C-PI7 ENF specimens, nanofiber bridging was also present. **Figure 3.39** shows evidence of NF necking right near the end of the pre-crack. In addition, the fracture surface shows very little NF pullout, which indicates very strong NF-matrix adhesion. The rough surfaces between hackle patterns are signs of matrix toughening, which can also serve to increase mode II IFT.[45] Although NF bridging can play an important role in mode II IFT, it relies on the crack passing through the interlaminar region. The amount of these interlaminar crossings can depend on numerous parameters such as the delamination mode, the nanofibrous veil areal density, reinforcing ply architecture, interleaving method, and mechanical properties of the nanofibers.[87] More interlaminar crossings means more opportunity for NF bridging, but it also means that the crack must follow a more tortuous crack path, which requires more energy.

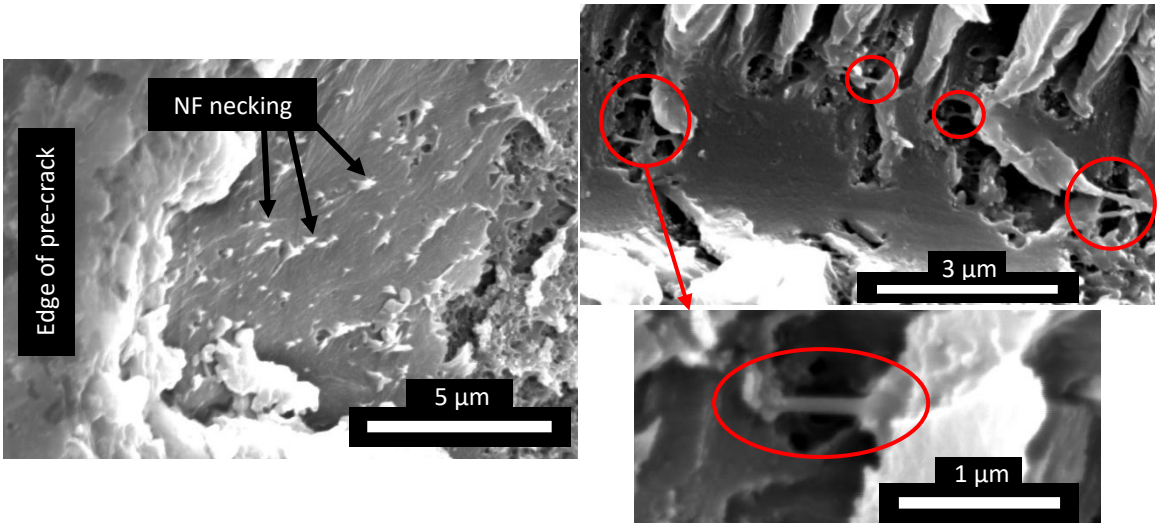

Figure 3.39: Mode II interlaminar fracture surface of a RS3C-PI7 specimen. The crack propagation direction was from left to right.

Delamination resistance in composites can occur when the crack path is deflected or modified, which requires more energy. Toughening at the interlaminar level can occur when the NF-toughening at the resin level forces the crack into the intralaminar region.[64,87,134] In fact, in mode II fracture, crack path modification is one of the primary toughening mechanisms.[45] In **Figure 3.40**, SEM micrographs show that the paths of the mode II interlaminar cracks were more tortuous in the PMTF3-PAN1 and PMTF3-PAN2 specimens compared to the pristine PMTF3 specimen, in which the crack path propagated in an almost perfectly self-similar manner. However, the PAN2 specimen exhibited large shear hackle patterns, which are characteristic of brittle, untoughened matrix failure.

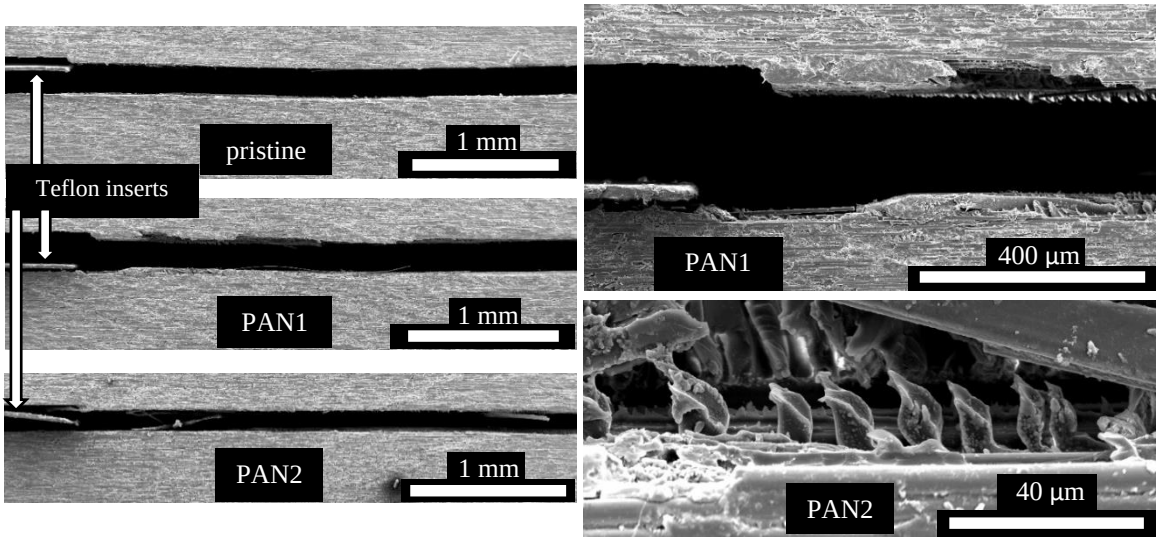

Figure 3.40: Mode II interlaminar crack paths of carbon/epoxy specimens.

In **Figure 3.41**, SEM images show that the mode II crack path of the RS3C-PI7 specimen was slightly more crooked and tortuous than that of the pristine RS3C specimen. In addition, although CF bridging rarely occurs during mode II interlaminar fracture, the PI7 specimen possesses a bundle of fractured CFs, which would have required more energy to break than the CE resin. These mechanisms contributed to the increased G_{IIC} values compared to those of the pristine specimens.

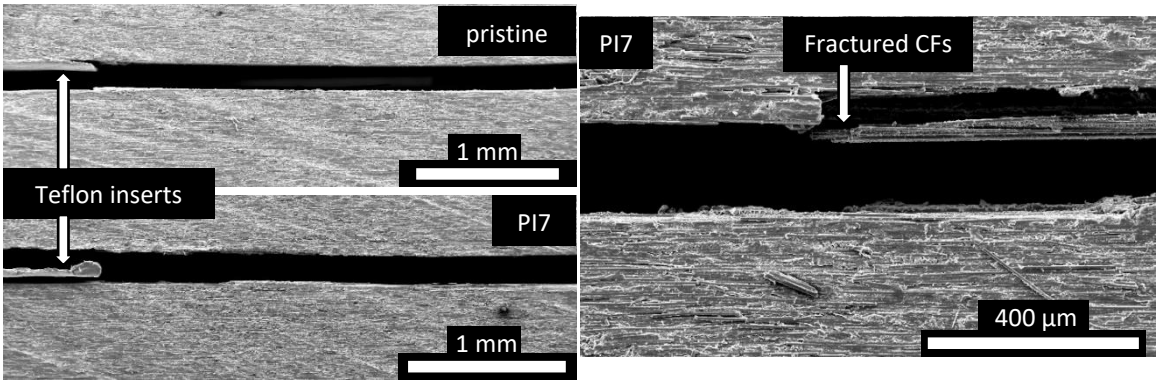

Figure 3.41: SEM micrographs showing the mode II crack paths of carbon/CE specimens. Crack propagation occurred from left to right.

3.4 SUMMARY OF INTERLAMINAR FRACTURE TOUGHNESS TESTING RESULTS

Results of the interlaminar fracture toughness testing were promising. Increases in maximum G_I of 294% and 102% were obtained for the PMTF3-PAN1 and RS3C-PI12 specimens, respectively, compared to the pristine PMTF3 and RS3C specimens. However, the initiation G_{IC} values for both the carbon/epoxy and carbon/CE materials showed little change with the addition of the NF interleaves. For mode II, the PMTF3-PAN1 and RS3C-PI7 specimens experienced increases of 15% and 21% in G_{IIC}, respectively, compared to the corresponding pristine specimens. This is interesting to note because typically increases in mode II IFT are higher than those in mode I IFT due to more optimal, in-plane loading of the NF interleaf during mode II fracture.[63]

Table 3.6: Carbon (or graphite)/epoxy mode I IFT results.

Material	Initiation G_{IC} (kJ/m^2)	Max G_I (kJ/m^2)	Percent increase in max from pristine (%)	Initiation K_{IC} (MPa*m$^{1/2}$)	Max K_I (MPa*m$^{1/2}$)	Percent increase in max from pristine (%)	Ref.
TR50S/ PMTF3	0.201	0.223	-	1.835	1.923	-	-
PMTF3-PAN1	0.207	0.881	294	1.896	3.910	103	-
T-300/5208 graphite/epoxy	0.087	-	-	-	-	-	[163]
AS-1/3502 graphite/epoxy	0.140	-	-	-	-	-	[163]
AS-4/3502 graphite/epoxy	0.161	-	-	-	-	-	[163]
AS-4/3501-6 graphite/epoxy	0.254	-	-	-	-	-	[163]
T-300/F-185 graphite/epoxy	1.880	-	-	-	-	-	[163]
HTA-12000/ Toho 113 carbon/epoxy	0.130	-	-	-	-	-	[162]
AS-4/BP907 carbon/epoxy	0.400	-	-	-	-	-	[117]
AS-4/3501-6 graphite/epoxy	0.085	-	-	-	-	-	[117]

Examination of the mode I IFT results from this study show that the obtained G_{IC} values are comparable to those of similar materials in other studies. However, the polysulfone and PEEK matrix composites in **Table 3.7** show much higher G_{IC} values, but this is because they are thermoplastic polymers. Although, it is promising that the RS3C-PI12 specimens exhibit maximum G_I values similar to the G_{IC} values of the AS-1/ polysulfone material.

Table 3.7: Carbon/CE and other high-temperature mode I IFT results. *Thermoplastic matrix.

Material	Initiation G_{IC} (kJ/m^2)	Max G_I (kJ/m^2)	Percent increase in max from pristine (%)	Initiation K_{IC} (MPa*m$^{1/2}$)	Max K_I (MPa*m$^{1/2}$)	Percent increase in max from pristine (%)	Ref.
T1100G/ RS3C	0.196	0.268	-	1.910	2.260	-	-
RS3C-PI12	0.161	0.543	102	1.750	3.205	42	-
T-300/ V387A graphite/ bismaleimide	0.072	-	-	-	-	-	163
AS-1/ polysulfone*	0.585	-	-	-	-	-	163
AS-4/PEEK*	2.89	-	-	-	-	-	163
AS-4/PEEK*	0.983	-	-	-	-	-	117

Although most studies on NF interleaving in mode I IFT tests compare the initiation G_{IC} values between pristine and NF-reinforced materials, with improvements between -58 and 340%,[45] the materials in this study showed either minor improvements or negative results in G_{IC} for the NF-reinforced materials. In addition, previous studies have compared the G_{IR} values, or the propagation mode I IFT, with improvements between -68 and 322%.[45] The G_{IR} value is defined as the steady-state mode I IFT reached when the crack resistance curve (R-curve) begins to plateau, corresponding to an equilibrium number of bridged fibers per unit crack area.[32] However, the R-curves of the NF-reinforced specimens in this study did not reach a steady state value, mainly due to increasing carbon fiber bridging as the crack grew. According to Suo et al., such R-

curves do not represent true material behavior because they depend on specimen thickness, and fiber bridging can increase as the crack grows.[164] Therefore, some authors adopted the initiation G_{IC} value associated with the initial crack propagation from the Teflon insert as the conservative estimate of fracture toughness.[32,117,140] However, the bluntness of the pre-crack tip established with the Teflon insert is not representative of the sharpness of an actual interlaminar microcrack. For this reason, it is relevant to examine both the G_{IC} and maximum G_I values.

Table 3.8: Carbon/epoxy mode II IFT results, along with values from the literature. **350°F dry and 270°F wet service capability.

Material	G_{IIC} (kJ/m^2)	Percent improvement from pristine (%)	K_{IIC} (MPa*m$^{1/2}$)	Percent improvement from pristine (%)	Ref.
TR50S/PMTF3	1.220	-	8.717	-	-
PMTF3-PAN1	1.418	16.2	9.429	8.2	-
HTA-12000/ Toho 113 carbon/epoxy	0.620	-	-	-	162
T-300/BP907 carbon/epoxy	1.49	-	-	-	161
IM7/977-3 Graphite/epoxy**	0.620	-	-	-	118
G40-800/5276 Carbon/epoxy	1.99	-	-	-	118

Although mode I delamination has received considerable attention in the literature, there is increased interest in mode II delamination because of its apparent relationship to impact damage tolerance of laminates.[163] Because of the inherent instability of mode II crack propagation through linear elastic materials during the ENF test, only a single value of G_{II} can be obtained, which is defined as G_{IIC}.[165] This means that no mode II crack resistance curve can be obtained from an ENF test. The 4-point bending ENF test, on the other hand, can be used to obtain a mode II R-curve that relates the mode II IFT to the crack length.[166,167] This was attempted with a few PMTF3 pristine specimens to include in this work, but crack growth remained unstable during all tests.

The mode II IFT values for both the pristine PMTF3 and PMTF3-PAN1 specimens were comparable to those for other materials in the literature. The PAN1 material exhibited a 16.2% increase in G_{IIC} compared to the pristine material. At the same time, the RS3C-PI7 material exhibited a 20.7% increase in G_{IIC} values compared to pristine RS3C material. Although the G_{IIC} values for both carbon/CE materials are much lower than that of the AS-4/PEEK material, PEEK is a thermoplastic matrix, so it is expected to have a much higher fracture toughness than those of thermosetting matrices.

Table 3.9: Carbon/CE mode II IFT results, along with another value of a high-temperature matrix composite from the literature. *Thermoplastic matrix.

Material	G_{IIC} (kJ/m^2)	Percent improvement from pristine (%)	K_{IIC} (MPa*m$^{1/2}$)	Percent improvement from pristine (%)	Ref.
T1100G/ RS3C	0.629	-	8.40	-	-
RS3C-PI7	0.759	20.7	9.23	9.9	-
AS-4/ PEEK*	2.68	-	-	-	[161]

3.5 CONCLUSIONS

Modes I and II interlaminar fracture toughness studies have been performed on novel composite material combinations. The propagation mode I and critical mode II interlaminar fracture toughnesses were increased significantly with the addition of PAN nanofibers in carbon/epoxy material and PI nanofibers in carbon/CE material. Although PAN nanofibers have been used to reinforce carbon/epoxy prepreg during mode I IFT testing before,[168] results were negative. This may be explained by the fact that the epoxy resin had a curing temperature of 175°C, which caused the cyclization of the PAN NFs, similar to what was witnessed in this work when PAN NFs were used to reinforce the carbon/CE material. On the other hand, the carbon/CE material reinforced with polyimide

nanofibers is the first of its kind, and due to the high-temperature stability of cyanate esters and polyimides, it is applicable to high-temperature uses.

Despite the fact that the epoxy and CE resins used in this work were already toughened by the manufacturers, the addition of electrospun nanofiber interleaves to the interlaminar region further increased the fracture toughness of the laminated composite material. This was achieved with very little material optimization, leaving room for further improvements in the future. During mode I fracture, crack deflection, which led to extensive carbon fiber bridging, was the primary reason for increased propagation fracture toughness. Nanofiber bridging and resin toughening were also prominent toughening mechanisms, although they played more of a role in mode II interlaminar fracture. Improvements were slightly limited by the suboptimal adhesion between the PAN nanofibers and the epoxy matrix, evidenced by pulled out and debonded nanofibers on the fracture surfaces, but the PI nanofibers showed excellent adhesion to the CE matrix.

The results of this interlaminar fracture toughness study supplement a crucial step towards commercial application of NF-interleaved composite laminates. Two new materials with enhanced delamination resistance, which is a highly advantageous property for composites, were explored and demonstrated. These materials will be examined further with respect to structural properties in the next chapter. Notably, one of them has the potential to be used specifically for high-temperature applications, which are increasing and may be highly critical in the future of polymer matrix composite materials.

CHAPTER 4. NANOFIBER REINFORCEMENT OF COMPOSITE STRUCTURES

Despite the amount of studies surrounding nanofiber-reinforcement in composite laminates,[45] there is still a lack of research regarding NF-toughening of composite structures that experience complex 3D stress states. Modes I and II interlaminar fracture toughness have been extensively studied, but tensile, bending, impact, and compression after impact tests are more limited. Also, these tests have mostly been performed with cross-ply or unidirectional layups, although some quasi-isotropic layups were tested under impact.[45] Modes I (G_{IC}) and II (G_{IIC}) interlaminar fracture toughnesses can be considered material properties, but structural applications of NF-reinforced laminates require a deeper understanding of how composite structures respond to loadings. Due to the limitless variety of layups and geometries of laminated composite structures, the amount of mechanical testing configurations is similarly endless. In composite structures, delamination can be induced by through thickness loadings, special geometries, or discontinuities. These design features, such as holes, curves, corners, and ply drops and tapers, serve as prominent sources of delamination.[33]

Several research groups have investigated delamination in some of these structural elements, such as L-bend laminates[115,169–174], open-hole laminates,[175–180] composite tubes[181–184], beams[185,186], and plates with holes subject to bearing loads[116,127] and under impact.[187] These studies examined different loading configurations, all of which induced delamination. However, cases of nanoreinforcement in these structural elements are extremely limited. Two studies have examined nanofiber-reinforcement in open-hole tensile specimens.[89,188] Although less delamination was observed in the NF-reinforced specimens, increases in open-hole tensile strength were modest (<10%). With

respect to L-bend laminates, stitching,[189] aligned CNTs,[190] graphene oxide,[191] and Kenaf short fibers[191] have been used to suppress delamination. Nonetheless, publications describing the interlaminar toughening of 3D composite structures through the use of continuous NF interleaves are virtually nonexistent.

In this chapter, electrospun nanofibers are used to reinforce the interlaminar regions of composite structural elements, starting from the simplest form (a laminated plate loaded in tension), and progressing to a curved beam (L-bend). In between, the tensile properties of open-hole laminates are also examined. The same composite and nanofiber materials used in the interlaminar fracture toughness tests are used for this study, also. Positive results will demonstrate a translation of material delamination resistance to the structural performance of certain delamination prone design features.

4.1 EXPERIMENTAL METHODS

4.1.1 Materials

The composite materials used in this chapter were the same as those used in CHAPTER 3: carbon/epoxy (TR50S/PMT-F3) unidirectional prepreg from Patz Materials, Inc. and carbon/cyanate ester (CE) (T1100G/RS-3C) unidirectional prepreg from Toray Industries, Inc. In addition, the same polyacrylonitrile (PAN) and polyimide (PI) nanofiber materials used in CHAPTER 3 were used in this chapter.

To determine the layup that would induce the highest interlaminar shear stress, the material properties found in **Table 3.1** were used. Via orthotropic mechanical analysis, the relationship between $\eta_{xy,x}$ and the ply orientation with respect to the loading axis was determined for both the carbon/epoxy and carbon/CE materials. From these relationships, it was determined that the maximum mismatch of $\eta_{xy,x}$ and, therefore,

maximum interlaminar shear stress τ_{xz}, in the carbon/epoxy material occurred between plies oriented at 12° and -12°, while the maximum $\eta_{xy,x}$ mismatch in the carbon/CE material occurred between plies oriented at +10° and -10°. However, for consistency, laminates were fabricated with +12° and -12° plies for both materials. It should be noted that these values and the plots in **Figure 4.1** were obtained based on the E_1, E_2, G_{12} and ν_{12} values of the pristine materials. The NF-reinforced materials could have different properties.

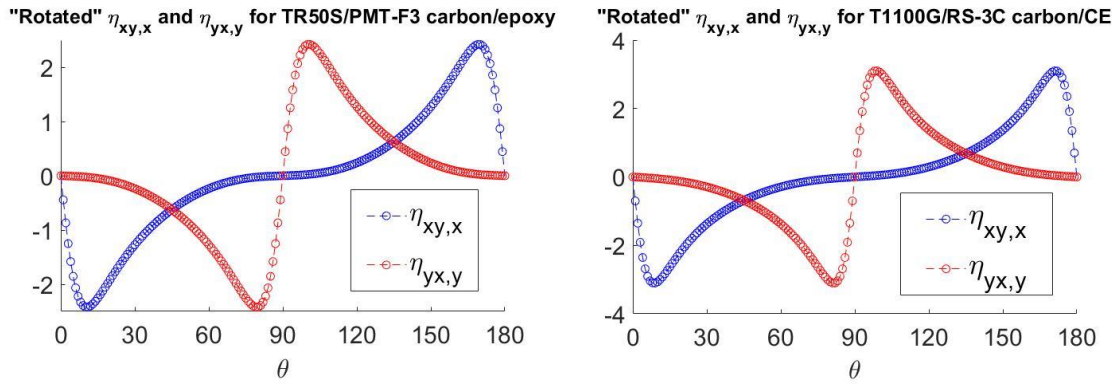

Figure 4.1: Rotated coefficients of mutual influence (extension-shear coupling) for unidirectional plies of the (left) carbon/epoxy and (right) carbon/CE materials.

4.1.2 Electrospinning Parameters

The electrospinning parameters used to fabricate the NF interleaves that reinforced the laminate and open-hole tensile specimens at the ±12° interfaces are shown in **Table 4.1**. Two PAN NF mats were electrospun for 1 hour each (using the same apparatus described in CHAPTER 3) onto 12° and -12° prepreg plies, respectively. The same process was repeated for PI NFs onto the carbon/CE prepreg material, but the spin time was 6 hours this time. In both materials, the NF interleaves reinforced both ±12° interfaces. The electrospinning parameters used to fabricate the NF interleaves that reinforced the L-bend are shown in **Table 4.2**. In the L-bend specimens, PAN NF interleaves were placed between every 2 plies in the 8-ply carbon/epoxy material and PI

NF interleaves were placed between every 4 plies in the 16-ply carbon/CE material. Nanotoughened L-bend panels were designed this way because the maximum interlaminar tensile stress in the bend occurs in the middle third of the thickness.[192] Nanofiber interleaves were strategically placed in the center and on each side of this region to support these interlaminar stresses.

Table 4.1: Electrospinning parameters used to fabricate the NF interleaves for the laminate and open-hole tensile specimens.

Prepreg material	Polymer, concentration (wt%), & solvent	Spin time (hours)	Needle gauge & amount	Collector distance (cm)	Applied voltage (kV)	Flow rate (mL/h)	Temp (°C)	% Relative humidity
Carbon/ epoxy	PAN 9% + DMF	1	23 - 2	15	8.0-9.5	0.16-0.18	21.6	24.2-25.0
Carbon/ CE	PI 10% + DMF	6	23 - 2	15	11.0	0.19-0.20	21.4	26.0-27.6

Table 4.2: Electrospinning parameters used to fabricate the NF interleaves for the L-bend specimens.

Prepreg material	Polymer, concentration (wt%), & solvent	Spin time (hours)	Needle gauge	Collector distance (cm)	Applied voltage (kV)	Flow rate (mL/h)	Temp (°C)	% Relative humidity
Carbon/ epoxy	PAN 9% + DMF	1	23	16	9.5	0.24	21.5	25.7
Carbon/ CE	PI 10% + DMF	8	23	15	11.0	0.18-0.19	21.5	27.5-28.5

4.1.3 Laminate Specimen Manufacturing and Testing

A $[\pm 12/0]_S$ layup was manufactured with the carbon/epoxy material, and a $[12_2/-12_2/0]_S$ layup was manufactured with the carbon/CE material. Both pristine and NF-reinforced panels were cured using the same methods as those used to cure the interlaminar fracture toughness panels.

The laminate specimen preparation included sanding and cleaning the region one inch from each end of the panel and 1-inch tabs made from a short fiberglass material (approximately 1/16” thick). The tabs were bonded to both sides of the panel using MS-907 epoxy and allowed to dry for 24 hours.

Laminate specimens were gripped by the tabs and tested in tension at a loading rate of 2mm/min, in accordance with ASTM D3039.[120] To obtain strain measurements, an Instron biaxial extensometer was used.

4.1.4 Open-Hole Tension Specimen Manufacturing and Testing

From the same panels from which the laminate specimens were cut, open-hole tension test specimens were cut according to Configuration A from ASTM D5766.[180] However, specimen widths were decreased to 18mm instead of the 36mm recommended in the ASTM to ensure that specimens would fail before maxing out the 25kN load cell. It should be noted that this changed the ratio of specimen width to hole diameter from the recommended 6:1 to 3:1, which will significantly affect the resulting open-hole tensile strengths since they were computed based on the specimen cross-sectional area disregarding the hole. For drilling of the centrally located holes, a 6mm diameter 3-flute carbide end mill drill bit was used. The specimens were sandwiched between two aluminum plates during drilling, and a feed rate of 0.0015” per revolution was used to minimize the damage and/or delamination induced near the hole edge during drilling. The drill bit was rotated at around 2000 rpm.

Open hole tensile specimens were tested at a loading rate of 2mm/min. The Instron biaxial extensometer was mounted so the hole was approximately centered in the longitudinal gage length and used to obtain strain measurements.

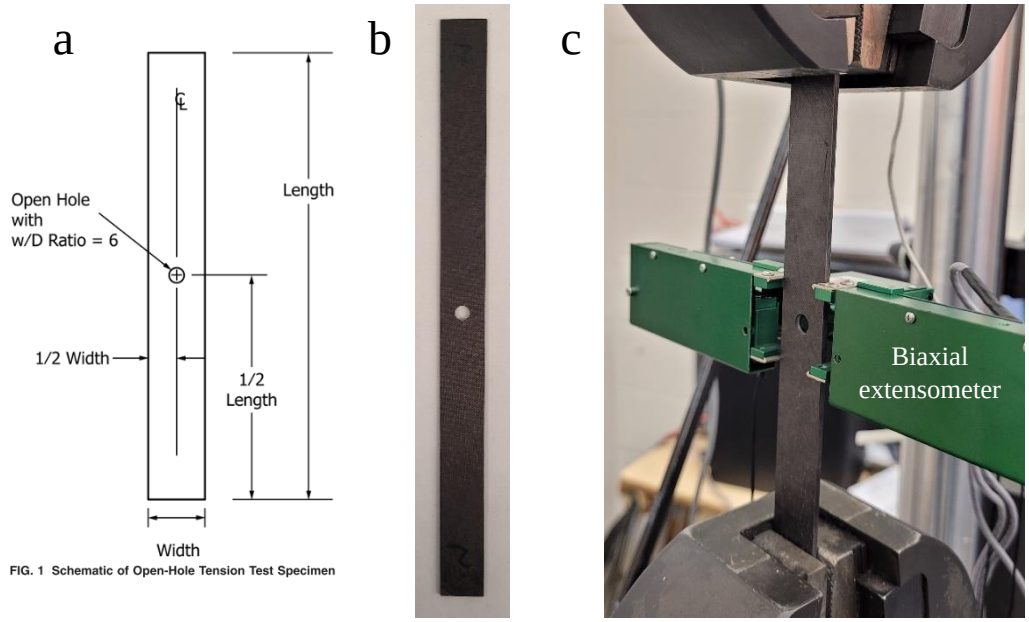

Figure 4.2: (a) Schematic of open-hole tension test specimen.[180] (b) Untested open-hole tensile specimen. (c) Open-hole tensile testing setup.

4.1.5 L-bend Specimen Manufacturing and Testing

The L-bend composites were manufactured with either 8 UD plies of carbon/epoxy or 16 UD plies of carbon/CE. All plies were cut to 6” x 8”, with the fiber direction along the 8” dimension. The nanofiber-reinforced, carbon/epoxy panels included electrospun PAN NF interleaves (spun directly on a prepreg ply for 1 hour each) every 2 plies, while the carbon/CE material was reinforced with electrospun PI NF interleaves (spun directly on a prepreg ply for 8 hours each) every 4 plies. This ensured that both materials had three total nanofiber-reinforced interfaces that were equally spaced. At the bend, the thickness of the carbon/epoxy pristine and PAN NF-reinforced specimens were 2.95±0.06mm and 2.98±0.05mm, respectively, while the thickness of the carbon/CE pristine and PI NF-reinforced specimens were 2.39±0.13mm and 2.51±0.04mm, respectively.

For the curing, a method similar to the vacuum bag molding process was used. First, the male corner of a 12” long aluminum angle with 6” legs was routed to a curve

with a ¼” outer radius and sanded to ensure a smooth surface. AT200Y® vacuum bag flex tape from AirTech Advanced Materials Corp. was placed around the edges while including four “tucks,” or sections of overlapping, extra tape to ensure the air has ample room to flow underneath the vacuum bag. The aluminum surface was covered with ToolTec® from AirTech, which was coated with a small amount of Loctite® Frekote 700-NC mold release agent. Once the release agent dried, the prepreg plies, including those covered with NFs for the NF-reinforced panels, were laid up by hand directly on the ToolTec. The layup was covered with a layer of thin brown woven release ply, then a white woven peel ply, which was secured in place with FlashBreaker® 1 shrink tape from AirTech. The white breather material came next, and it was secured by sticking it to the edges of the flex tape. Three layers of breather material were taped beneath a high temp 3/8” resin infusion connector (RIC), which was also taped in place. One small breather piece was used to connect the breather underneath the RIC to the large breather on top of the layup. Lastly, the vacuum bagging film (KM 1300® (.002") from AirTech) was firmly stuck to the flex tape to ensure there were no leaks.

A razor blade was used to poke a small hole in the vacuum bag in the center of the RIC. Then, a 3/8” nylon tube with a pointed end was fed through the hole and secured with the RIC. The nylon tube was connected to a vacuum valve, which was connected to a 3/8” polyurethane (PU) vacuum tube. The PU tube was connected to an MTI® model YTP 500 vacuum. Once the vacuum was turned on, the vacuum bag was checked for leaks by listening for them. Any leaks were sealed with more flex tape. The entire L-bend configuration was placed in a Thermo Scientific HERATherm® oven. Once the oven reached the respective cure temperature (250°F for carbon/epoxy and 350°F for

carbon/CE), the heat was left on for 2h20min (20 min more than the recommended amount) to give the composite ample time to reach the air temperature in the oven. After the heat was turned off, the vacuum was left on for at least twelve hours to ensure the pressure on the layup was sustained until it reached room temperature.

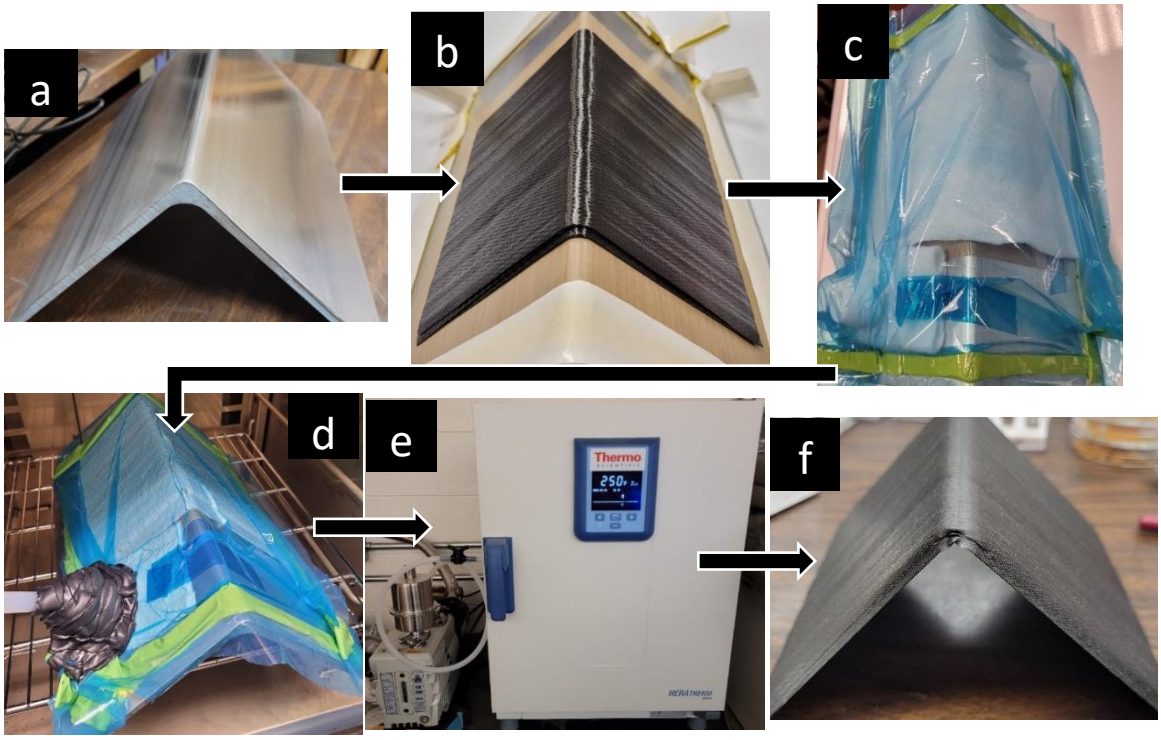

Figure 4.3: Chronological manufacturing procedure for L-bend panels: (a) aluminum angle, (b) composite layup, (c) vacuum-bagged layup, (d) sealed and vacuum pressurized layup, (e) Thermo Scientific HERATherm oven and MTI vacuum, (f) cured panel.

The unidirectional L-bend specimens were cut using a Ridgid wet saw to the dimensions outlined in the standard curved beam strength test (ASTM D6415).[193] The testing parameters also followed those recommended in the ASTM, but the loading noses in the four-point bend (4PB) fixture used had 1 inch diameters. The lower and upper spans between the loading noses were approximately 100 mm and 75 mm, respectively. Specimens were testing at a loading rate between 0.5 and 4.0 mm/min.

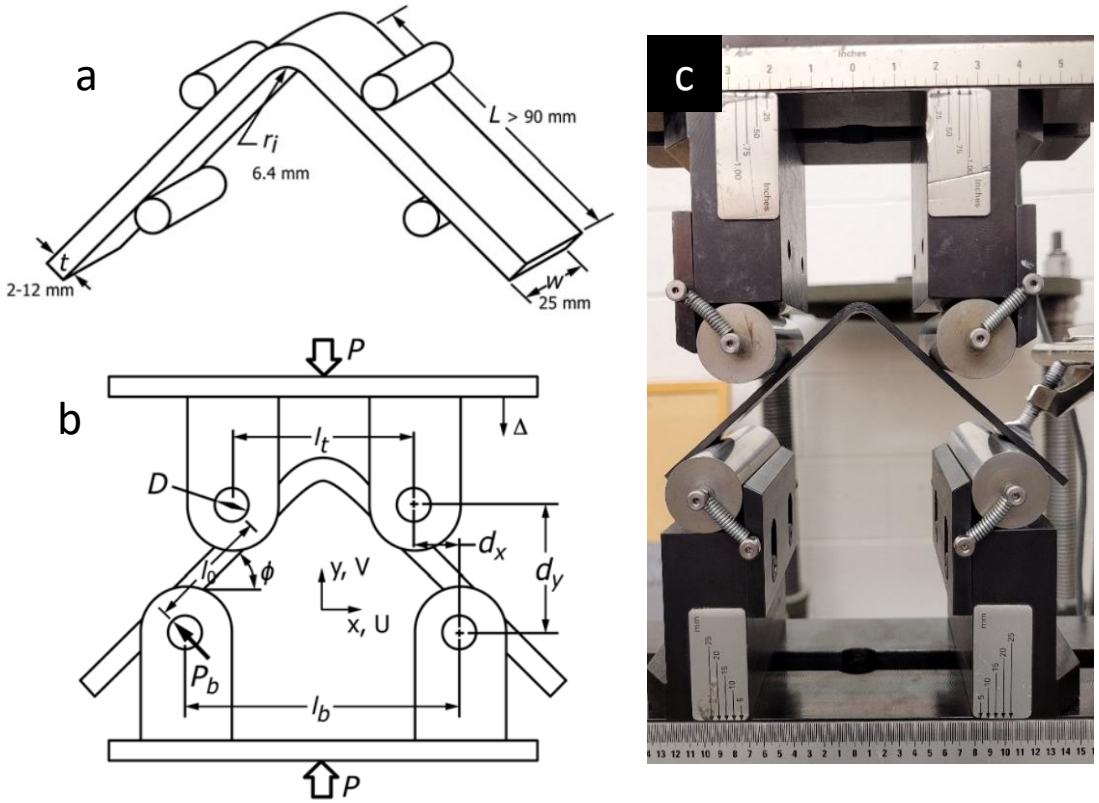

Figure 4.4: (a) Curved beam strength test specimen geometry (SI units).[193] (b) curved beam in four-point bending.[193] (c) Experimental setup for curved beam strength test.

4.1.6 X-Ray Computed Tomography

X-ray computed tomography (CT) was performed on one untested and one tested open-hole and L-bend specimen made from each material. The x-ray CT scans were obtained with a Nikon XT H 225 ST at 467 µA and a voltage of 140 kV. Porosity analysis was performed on untested open-hole and untested and tested L-bend specimens using the tools on myVGL 3D visualization software.

4.1.7 DMA Testing

To determine the effects of the NF interleaves on the viscoelastic properties of the carbon/CE laminates, dynamic mechanical analysis (DMA) was performed. Two specimens each were cut from four already manufactured carbon/CE panels: L-bend RS3C pristine, DCB RS3C-PAN7, DCB RS3C-PI12, and L-bend RS3C-PI8. These

specimens will be called pristine, PAN7, PI12, and PI8-3layers, respectively. One specimen from each panel was tested after initial curing while the second was post-cured in an oven at 450°F for 2 hours according to the manufacturer's (Toray) recommendation to increase the expected T_g from 375°F to 490°F before DMA testing. All specimens were tested at 1 Hz with a 3-point bending fixture using a Mettler Toledo DMA 1 STARe system and heated from room temperature at 3°C/min. Data was analyzed to compare the storage moduli, damping coefficients $\tan\delta$, and glass transition temperatures of the 8 different materials.

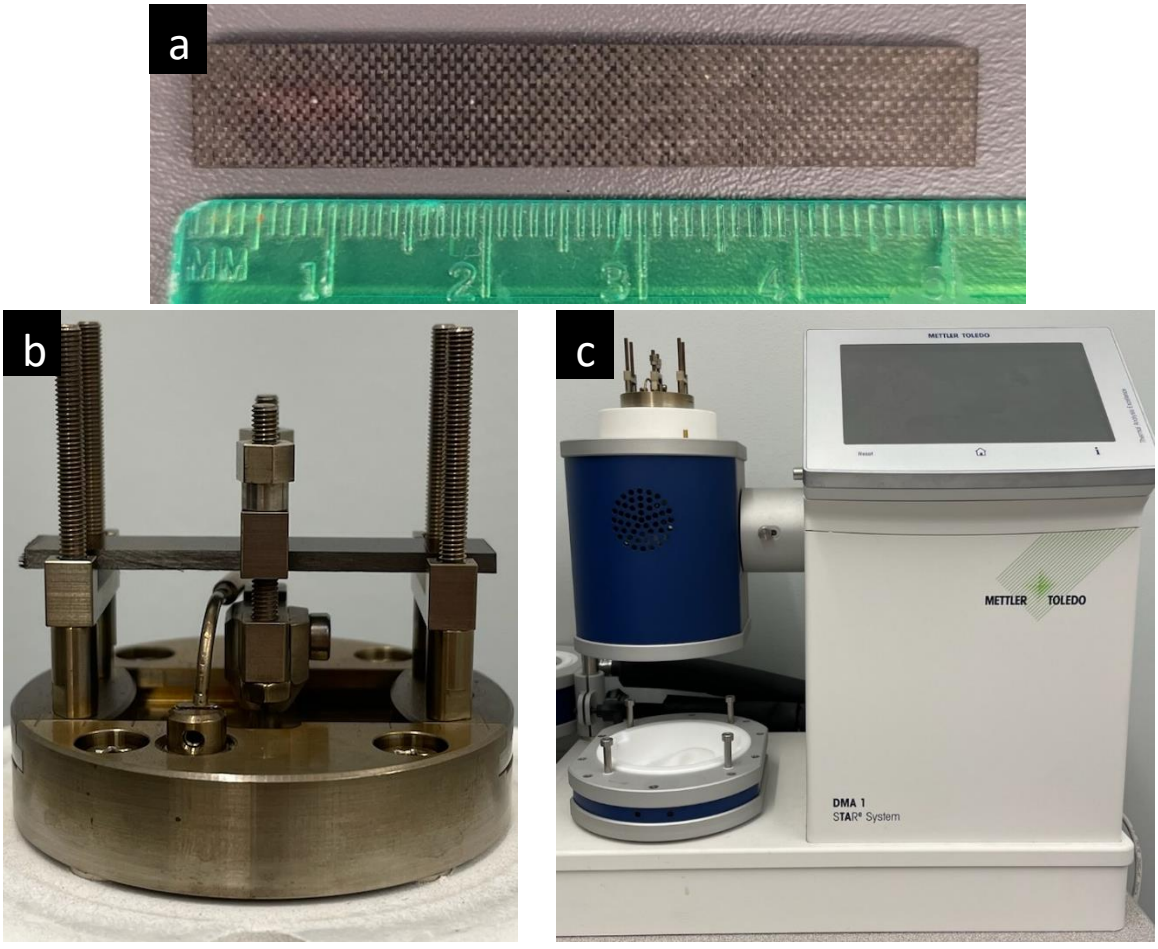

Figure 4.5: (a) Representative DMA specimen. (b) DMA specimen loaded in 3PB fixture. (c) Mettler Toledo DMA 1 STARe system.

4.1.8 List of Materials and Structures Tested

In this chapter, composite structural elements were reinforced with NF interleaves with areal weights similar to those that produced positive results during the modes I and II IFT testing. For the carbon/epoxy material, it was determined that the optimal areal weight of PAN NF interleaves was around 1 g/m^2 for both modes I and II. Thus, the carbon/epoxy material was reinforced with similar amounts of nanofibers for this study, although actual areal weights ended up being slightly lower than 1 g/m^2 (see **Table 4.3**).

Table 4.3: List of materials and structures tested with the carbon/epoxy material.

material	fiber	resin	NF material	spin time of each NF mat (h)	Approx. areal weight of each NF mat (g/m^2)	Abbrev.	Structure/ test	Results compared to pristine
Carbon/ epoxy	TR50S	PMT-F3	-	-	-	PMTF3	$[\pm12/0]_S$ laminate in tension	-
Carbon/ epoxy	TR50S	PMT-F3	PAN	1	0.7	PMTF3-PAN1	$[\pm12/0]_S$ laminate in tension	Slight improvements
Carbon/ epoxy	TR50S	PMT-F3	-	-	-	PMTF3	$[\pm12/0]_S$ laminate with hole in tension	-
Carbon/ epoxy	TR50S	PMT-F3	PAN	1	0.7	PMTF3-PAN1	$[\pm12/0]_S$ laminate with hole in tension	Very small improvements
Carbon/ epoxy	TR50S	PMT-F3	-	-	-	PMTF3	UD L-bend in 4PB	-
Carbon/ epoxy	TR50S	PMT-F3	PAN	1	0.9	PMTF3-PAN1	UD L-bend in 4PB	Negative

From the interlaminar fracture toughness study, it was determined that modes I and II IFT in the carbon/CE material could be increased with NF interleaves having areal weights between 7-12 g/m^2. Although spin times were the same as in the IFT study (8 and 6 hours for modes I and II, respectively), actual interleaf areal weights ended up being around 6.2 and 7.9 g/m^2 for the laminates (and open hole specimens) and L-bend

panels, respectively (see **Table 4.4**). Based on the layups and loading configurations, the laminates and open-hole tensile specimens should experience more shear interlaminar stresses, while the L-bend specimens should experience more tensile interlaminar stresses.

Table 4.4: List of materials and structures tested with carbon/CE material.

material	fiber	resin	NF material	spin time of each NF mat (h)	Approx. areal weight of each NF mat (g/m^2)	Abbrev.	Structure/ test	Results compared to pristine
Carbon/ CE	T1100G	RS-3C	-	-	-	RS3C	$[12_2/-12_2/0]_S$ laminate in tension	-
Carbon/ CE	T1100G	RS-3C	PI	6	6.2	RS3C-PI6	$[12_2/-12_2/0]_S$ laminate in tension	Significant improvements
Carbon/ CE	T1100G	RS-3C	-	-		RS3C	$[12_2/-12_2/0]_S$ laminate with hole in tension	-
Carbon/ CE	T1100G	RS-3C	PI	6	6.2	RS3C-PI6	$[12_2/-12_2/0]_S$ laminate with hole in tension	Significant improvements
Carbon/ CE	T1100G	RS-3C	-	-		RS3C	UD L-bend in 4PB	-
Carbon/ CE	T1100G	RS-3C	PI	8	7.9	RS3C-PI8	UD L-bend in 4PB	Significant improvements

4.2 RESULTS OF MULTIDIRECTIONAL LAMINATE TESTING

Because of its mechanisms, delamination can initiate at the free edge during in-plane loading, which can cause laminates to fail at tensile loads lower than those predicted by classical lamination theory.[33] However, electrospun NF interleaves have been shown to provide improved tensile strength of laminated composites,[68] which differentiates NF interleaves from previous interleaf materials.

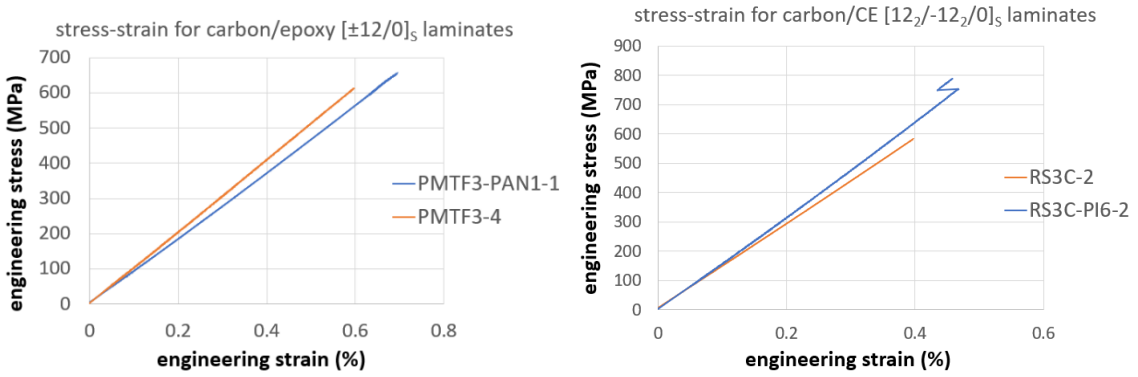

Figure 4.6: Representative stress-strain curves for the laminate tensile tests. The sharp drop in strain in the PI6 curve is due to the extensometer edges slipping.

Based on the raw data from the laminate tensile tests, the PMTF3-PAN1 specimens exhibited slightly increased tensile strength and failure strain, in combination with slightly decreased modulus, compared to the pristine PMTF3 specimens. The RS3C-PI6 specimens, on the other hand, exhibited significantly higher strengths and failure strains, along with slightly enhanced modulus. However, the minor improvements obtained with the carbon/epoxy material were anticipated since the mode II IFT improvements were also modest. Similarly, the significant enhancements in the NF-reinforced carbon/CE laminates were akin to the enhancements seen in mode II IFT.

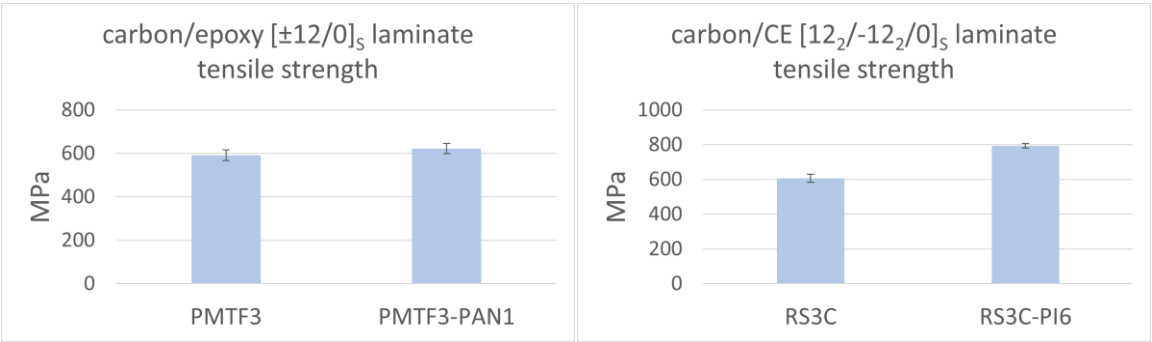

Figure 4.7: Laminate tensile strength results.

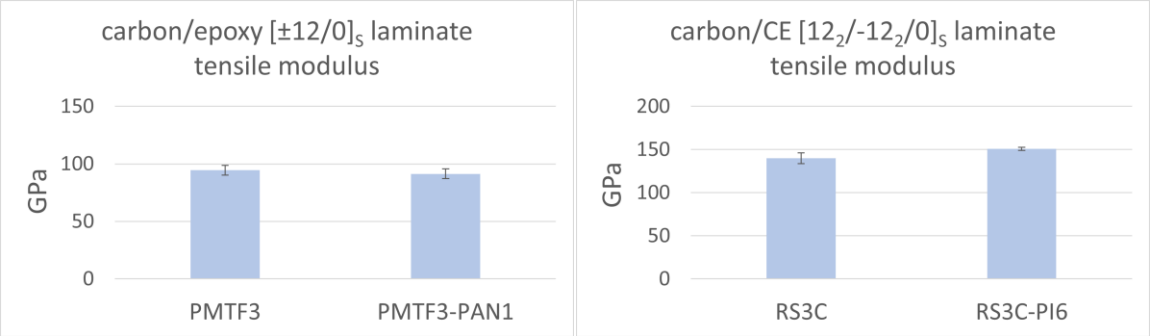

Figure 4.8: Laminate tensile modulus results.

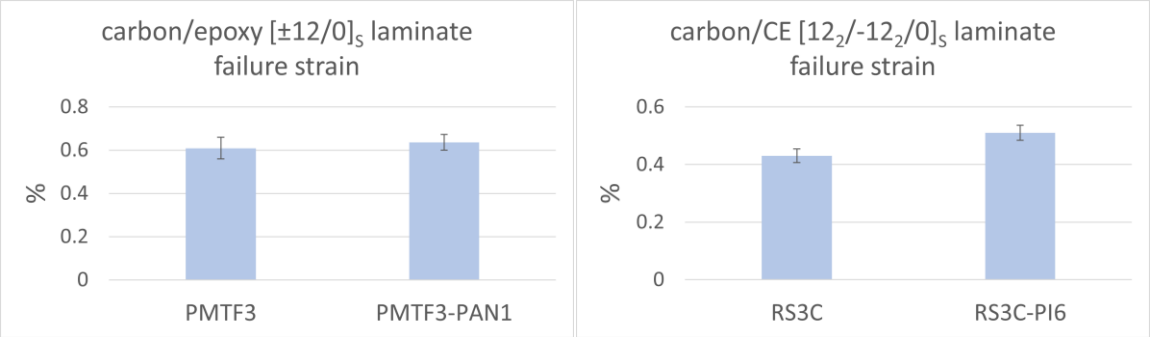

Figure 4.9: Laminate failure strain results.

4.2.1 Discussion of Laminate Tensile Testing Results

Composite laminates can undergo several different failure modes, including matrix cracking, fiber failure, and fiber debonding/pullout. However, due to their anisotropy, delamination of adjacent plies is also a critical failure mechanism and can even arise during in-plane loading. Due to its prominence and ability to cause catastrophic failure, delamination and methods of suppressing it have been extensively studied. Of these delamination suppression methods, the toughening of interlaminar regions with electrospun nanofiber veils is arguably the most effective. However, studies on tensile properties of laminates reinforced with electrospun NFs are somewhat limited. In addition, most of these studies have been performed on cross-ply[89,188,194–196] or [±45°][89] laminates. Since laminate properties can be tailored for countless different applications based on their layup, they can be considered structural elements. However,

the endless number of layup variations makes it challenging to determine how different laminates reinforced with NF interleaves will respond to structural loads. For this reason, it is vital to examine the mechanical performance of a multitude of laminated composite structures reinforced with electrospun nanofiber interleaves.

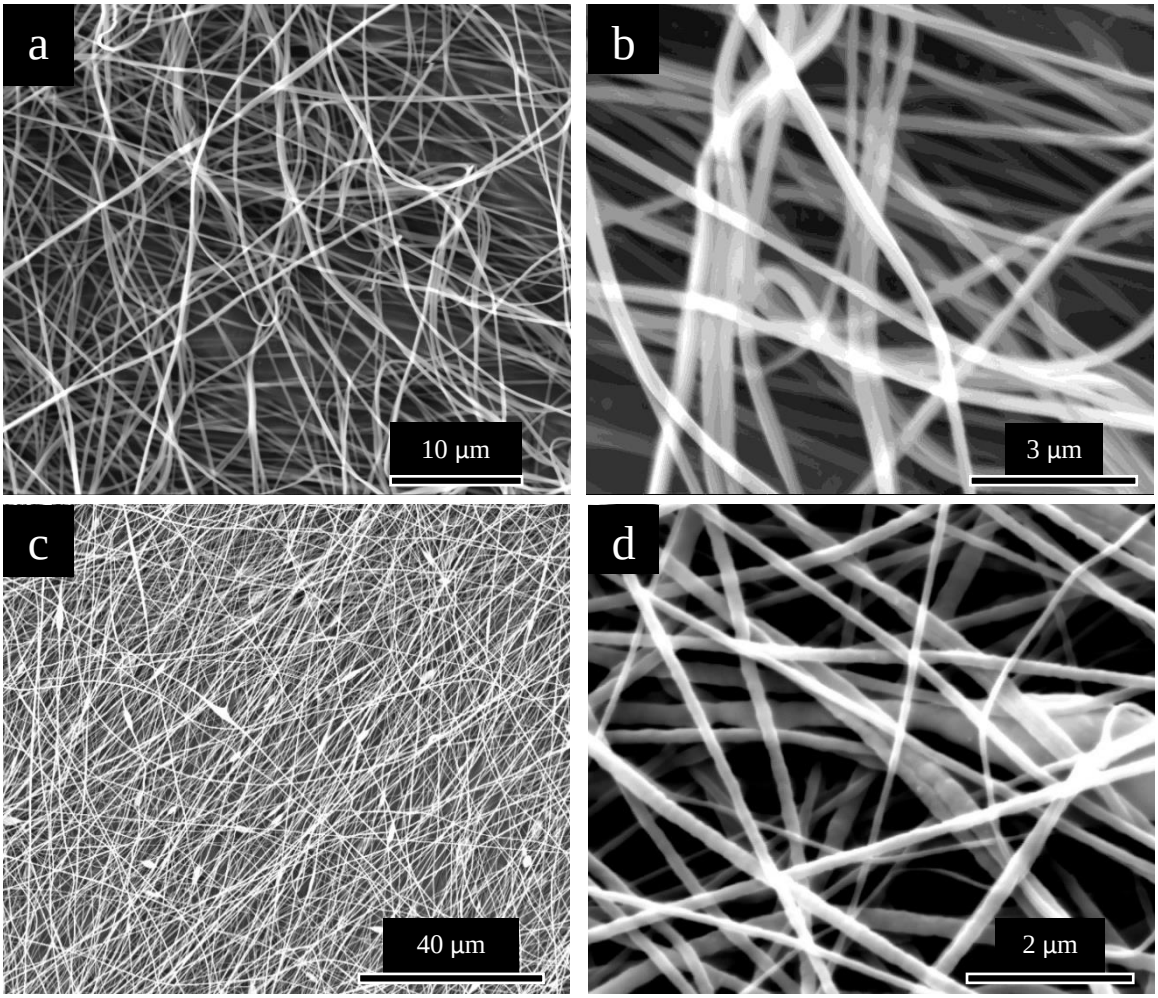

Figure 4.10: Representative SEM images of (a & b) the PMTF3-PAN1 and (c & d) the RS3C-PI6.

The factors that influence the toughening effect of NF interleaves in laminates subject to tensile loads are the same as those when the laminates are subject to modes I and II interlaminar fracture. To achieve adequate load transfer to the nanofibers, the NF-matrix adhesion must be sufficient, and the resin must be able to fully impregnate the NF mat. This depends on both the diameters of the NFs and the thickness of the NF mats.

The average PAN NF diameter was 241±42 nm, while the average PI NF diameter was 163±45 nm. Since the NF diameter distributions of the NF interleaves reinforcing the laminate specimens were similar to those of the NF interleaves that reinforced the DCB and ENF specimens in the previous chapter, the degree of resin impregnation should be similar. In addition, the areal weights of the NF interleaves were similar to those from the interlaminar fracture toughness study. To investigate the quality of resin impregnation in the NF-reinforced interlayers, the ±12° interfaces of both pristine and NF-reinforced specimens were examined in the SEM (see **Figure 4.11**). Although the ±12° interlaminar regions of the NF-reinforced specimens are thicker than those of the pristine specimens, the NF interleaves seem to be adequately infused with resin.

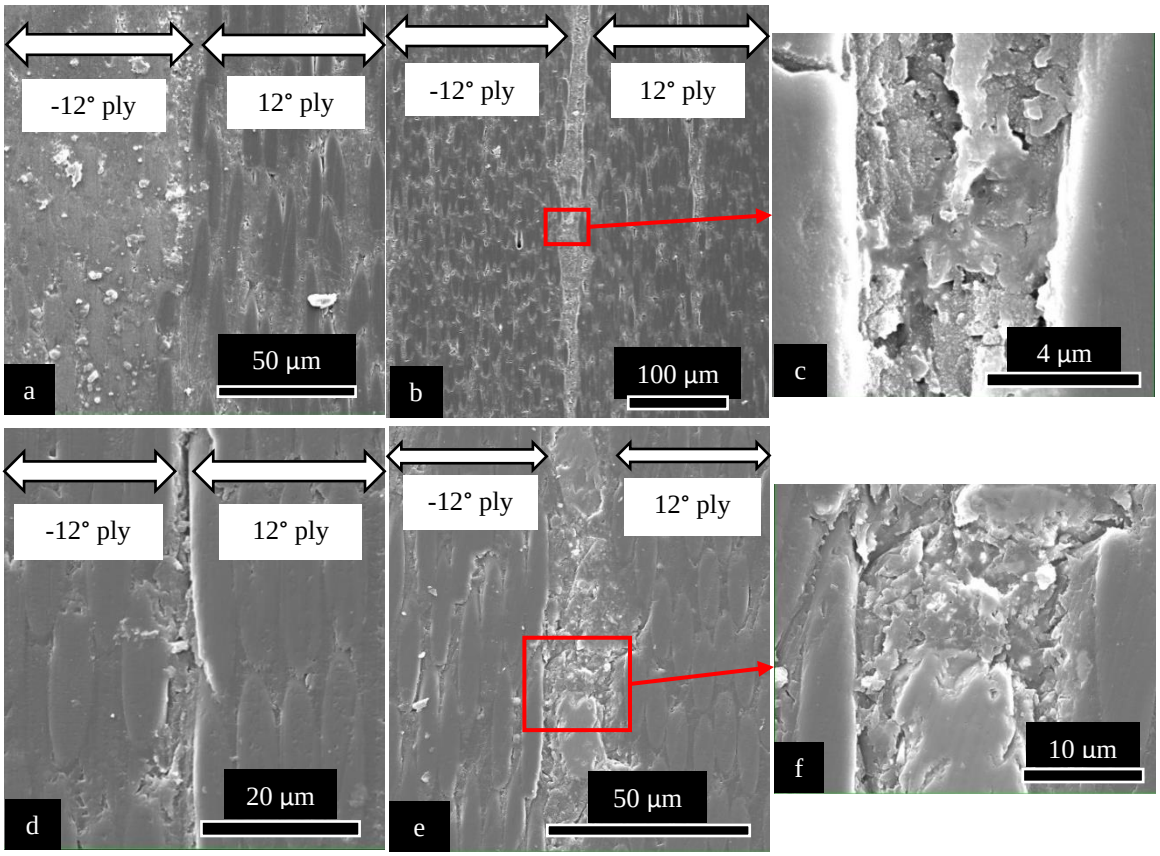

Figure 4.11: SEM micrographs of ±12° interfaces in untested laminate specimens: (a) pristine PMTF3, (b & c) PMTF3-PAN1, (d) pristine RS3C, and (e & f) RS3C-PI6.

Depending on the material and layup, composite laminates can experience a multitude of failure modes when tested in uniaxial tension. These failure modes can be described by a distinct failure code, as defined in ASTM D3039 (see **Figure 4.12**).[120] Although matrix cracks serve as an intermediate failure mode and are not the direct cause of ultimate failure, they can cause ply-by-ply failure, internal and edge delaminations, and facilitate fiber breakage. Delamination can also lead to ultimate failure by separating subsequent plies.[148] Composite laminates will find the lowest energy route to shedding load, and sometimes this occurs by delamination and splitting rather than fiber fracture.[33] In laminates, delamination initiates at the free edge and causes tensile specimens to failure before the expected loads predicted by CLT.[197] This makes the role of delamination in in-plane failure extremely important, but it has been studied much less than its effect on failure due to through-thickness loadings.

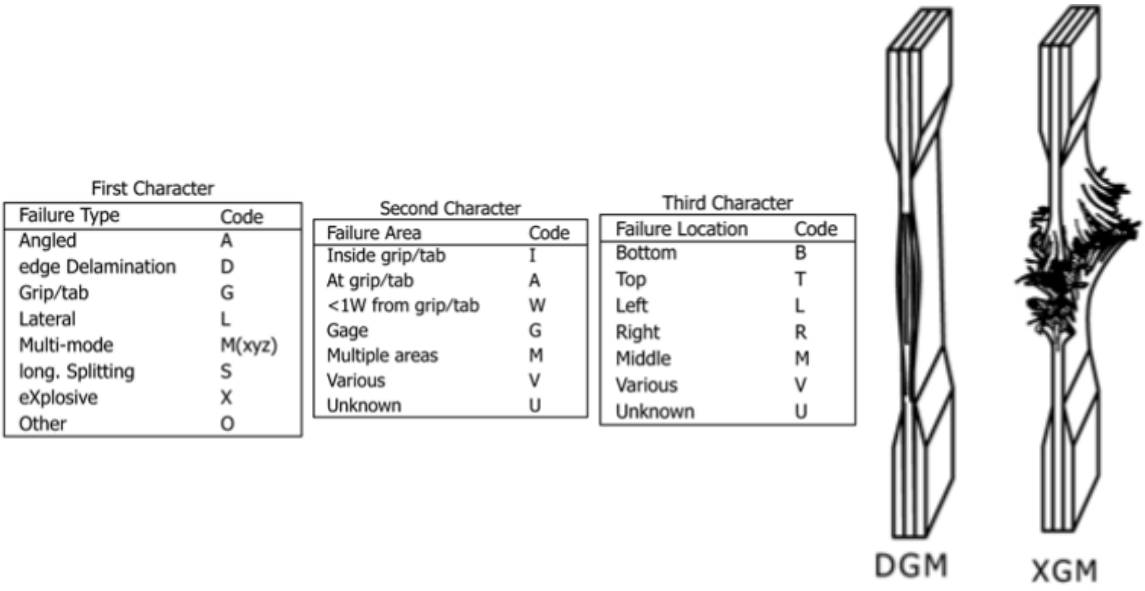

Figure 4.12: Laminate tensile test failure codes and examples of two common failure modes.[120]

The failure modes of the carbon/epoxy $[\pm 12/0]_S$ laminates are shown in **Figure 4.13**. Common failure modes for both the pristine and PAN1 specimens were AGM and DGM, although some experienced local LGM failure where the fiber failure in the central

0° plies dominated. Although all specimens exhibited some degree of edge delamination, one pristine specimen “fanned out” much more than the others.

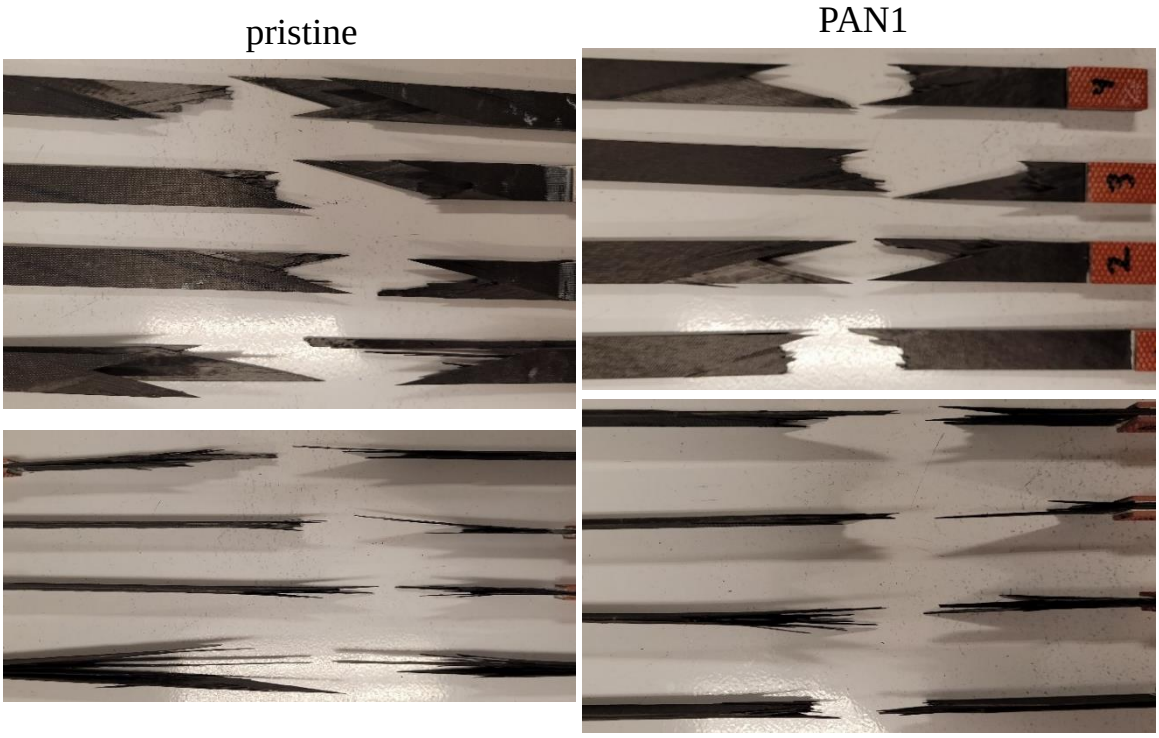

Figure 4.13: Failure modes of the carbon/epoxy $[\pm 12/0]_S$ pristine and PAN1 laminate specimens.

The failure modes of the $[12_2/\text{-}12_2/0]_S$ carbon/CE laminates are shown in **Figure 4.14**. The prominent failure modes include DGM and XGM, although some specimens show SGM from the failure of the 0° plies. Once again, delamination was present in all specimens, but extensive fanning out can be seen in all the pristine specimens, while one of the PI6 specimens shows less than average.

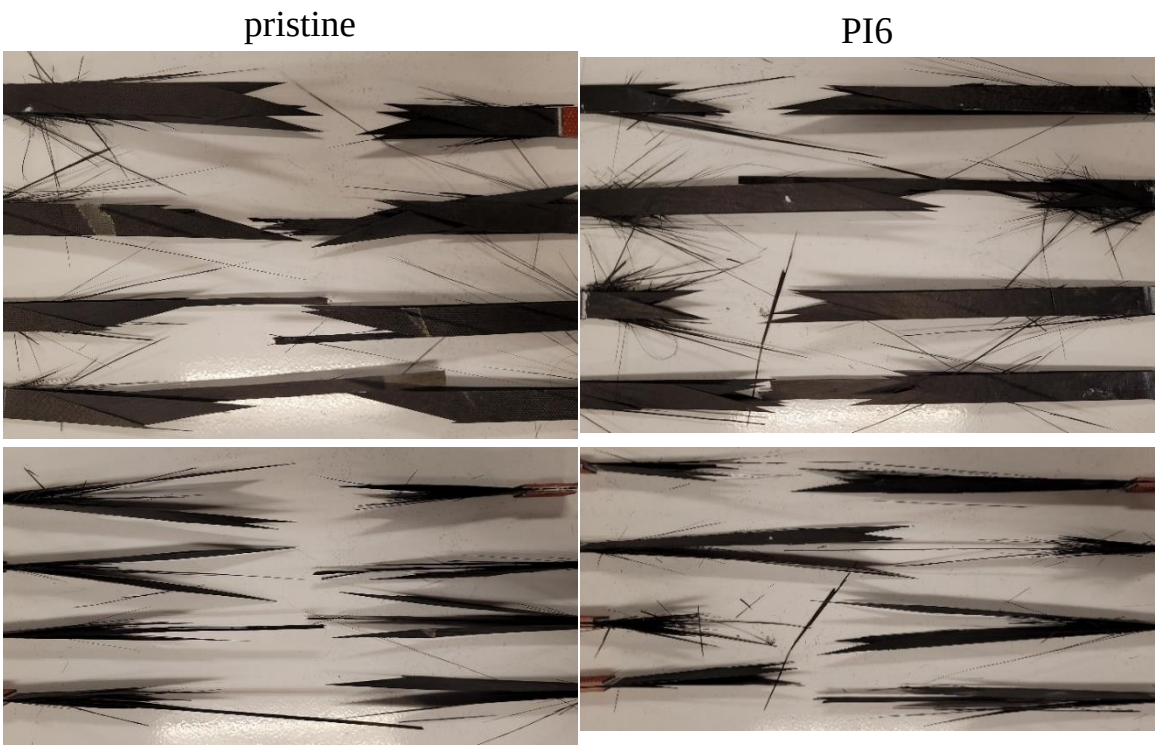

Figure 4.14: Failure modes of the carbon/CE $[12_2/-12_2/0]_S$ pristine and PI6 laminate specimens.

In the angle-ply laminates, the NF interleaves reinforced the ±12° interfaces since that is where the coefficient of mutual influence mismatch was maximized. However, delamination also occurred at the 0°/12° interfaces. Overall, the carbon/epoxy specimens showed less edge delamination than did the carbon/CE specimens. This was expected based on the photos of the failed specimens in **Figure 4.13** and **Figure 4.14**. In the carbon/epoxy specimens, the angled failure modes and less fanning out of the outer plies indicate that matrix cracking in the ±12° plies may have played a more substantial role in failure than delamination did. This would help explain the limited mechanical improvements obtained with the PAN1 specimens.

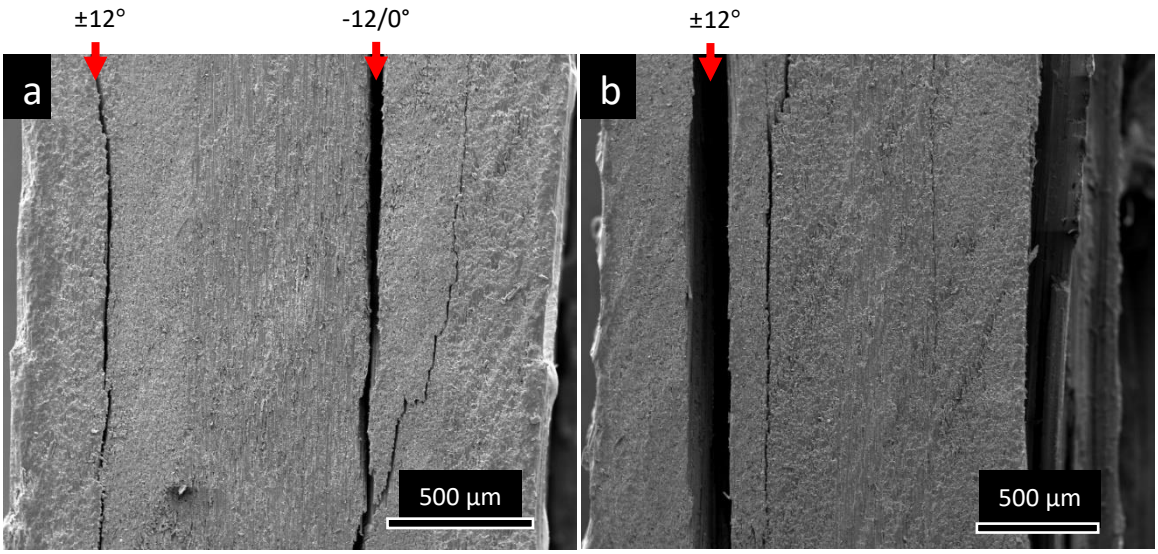

Figure 4.15: Edges of failed carbon/epoxy $[\pm 12/0]_S$ laminate specimens: (a) pristine and (b) PAN1. Crack propagation occurred in the downward direction.

In the carbon/CE specimens, failure was much more explosive, and the outer plies delaminated significantly. Although the PI NFs were intended to suppress delamination at the ±12° interfaces, the SEM images in **Figure 4.16** show that a PI6 laminate specimen exhibited delamination at both ±12° interfaces, along with both -12°/0° interfaces. Meanwhile, the pristine specimens only experienced delamination at the -12°/0° interfaces. However, the NF-reinforced specimen failed at a much higher strength, so it can be inferred that delamination at the ±12° interfaces would have occurred in the pristine specimen had it not failed at the lower strength level. These images also may imply that delamination between the 0° and -12° plies is more detrimental to the overall strength of the laminate. Investigation of delamination onset location and corresponding load point may find these hypotheses true, but this is beyond the scope of this dissertation. It should also be noted that these images only represent one edge on one side of one tested specimen for each material. In addition, the presence of delamination at the

edge does not provide information on delamination propagation rate with the load increase.

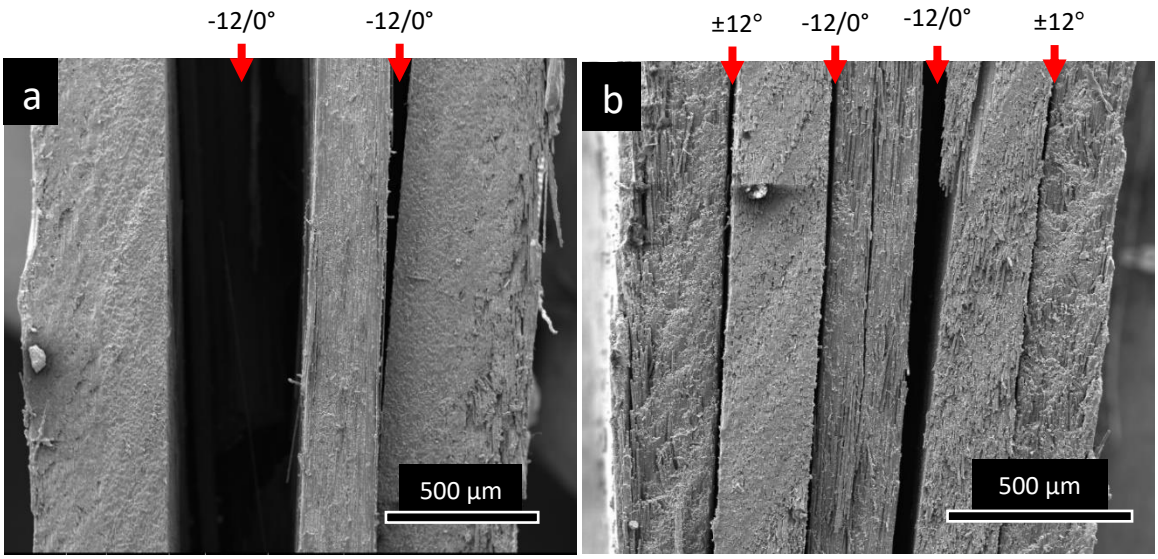

Figure 4.16: Edges of failed carbon/CE $[12_2/-12_2/0]_S$ laminate specimens: (a) pristine and (b) PI6. Crack propagation occurred in the downward direction.

The primary role of nanofiber interleaves in laminates subject to tensile loads is to suppress delamination. Electrospun nanofibers have the ability to minimize the formation of delamination cracks between plies and help transfer the load from the resin to the fibers. In addition, they can reinforce the matrix interlayer to slow the growth of damage.[45] Nanofiber bridging across interlaminar and transverse cracks can also occur, which can contribute to enhanced toughness.[87] This leads to NF pullout and breakage in the resin rich area, absorbing energy and increasing tensile properties. In NF-reinforced specimens, the type of the fracture in the resin rich regions is expected to be tougher rather than more brittle like it is in pristine specimens.[68] To determine the toughening mechanisms in the laminate specimens, SEM images were obtained of the fracture surfaces at the ±12° interfaces.

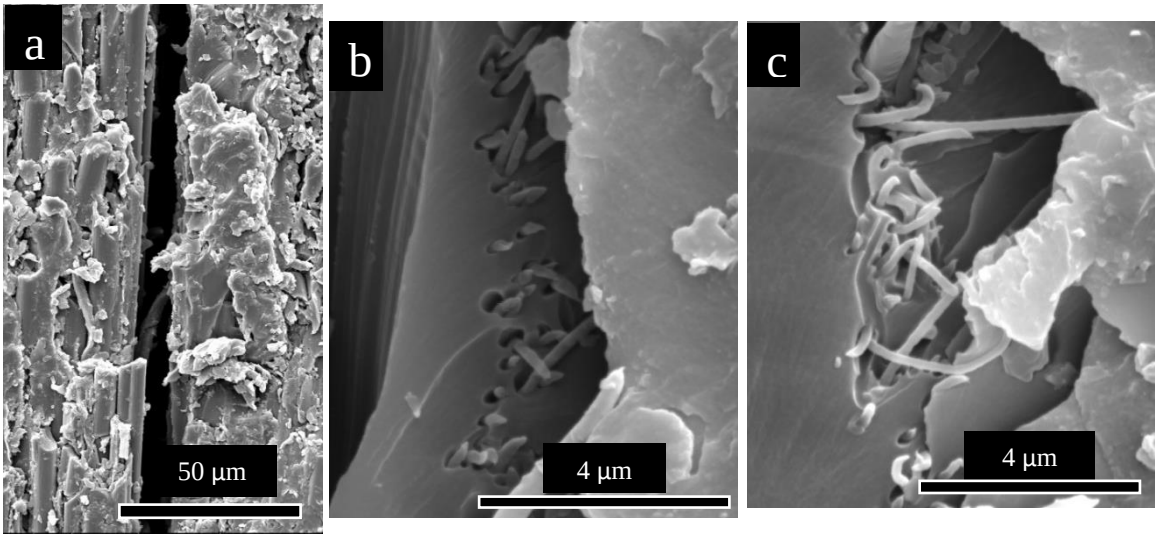

Figure 4.17: (a) Interlaminar crack at a ±12° interface in a failed PMTF3-PAN1 laminate specimen. (b & c) Fracture surfaces near the PMTF3-PAN1 interlaminar region.

In the PMTF3-PAN1 specimens, it is clear that NF bridging occurred within the brittle, resin-rich interlaminar region, as shown in **Figure 4.17**. However, the voids surrounding the failed PAN NFs are present evidence of NF pullout and poor NF-matrix adhesion. This may be the reason why the PAN1 specimens exhibited limited improvements in tensile strength and failure strain, along with decreases in tensile modulus, compared to the pristine specimens. In contrast, the RS3C-PI6 specimens display porous and bumpy fracture surfaces characteristic of tougher resin failure (see **Figure 4.18**). There is also no evidence of NF pullout or debonding, indicating excellent NF-matrix adhesion. The rough fracture surface is also a sign of a tortuous, energy-intensive crack path. These mechanisms contributed to the substantial enhancements in tensile properties compared to the pristine specimens.

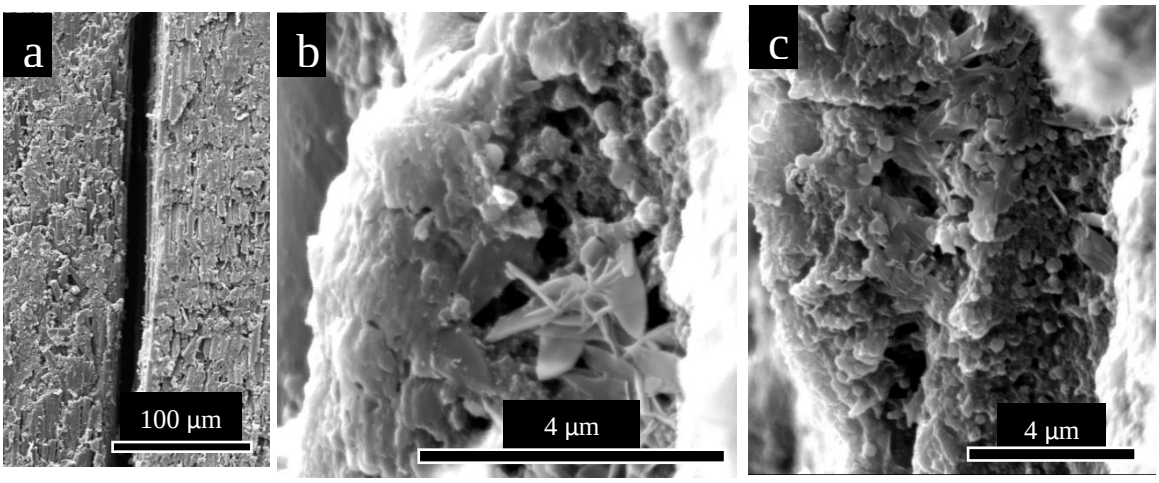

Figure 4.18: (a) Interlaminar crack at a ±12° interface in a failed RS3C-PI6 laminate specimen. (b & c) Fracture surfaces near the PI6 interlaminar region.

4.3 OPEN-HOLE TENSILE TESTING RESULTS

It is well known that delamination plays a vital role in the in-plane failure of composite laminates. This phenomenon becomes even more critical when there are sites of stress concentrations, such as holes.[33] However, many structural applications, such as bearing joints and fasteners, require notched plates. This has generated significant research surrounding failure of open-hole laminates,[175–179,187,198–205] but publications regarding their NF reinforcement are limited.[89,188] Therefore, further investigation of the effect of NF interleaves on the structural performance of notched or holed laminates is needed.

Overall, the results of the open-hole tensile testing in this study were positive. The representative stress-strain curves are shown in **Figure 4.19**. The PMTF3-PAN1 specimens showed modest improvements, while the RS3C-PI6 specimens showed substantial improvements compared to their respective pristine specimens.

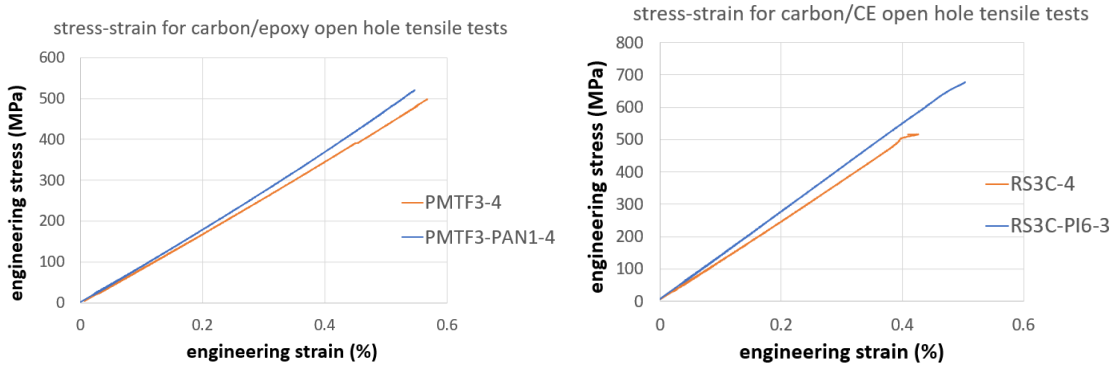

Figure 4.19: Representative stress-strain curves for the open-hole tensile tests.

Open-hole tensile strength was computed by dividing the load by the total cross-sectional area of the specimens, disregarding the missing material at the hole. Both of the NF-reinforced materials showed increases in open-hole tensile strength compared to the respective pristine material. The PMTF3-PAN1 specimens showed modest improvements, but the RS3C-PI6 specimens showed significant enhancements. Values and percent improvements are tabulated in **Table 4.11**.

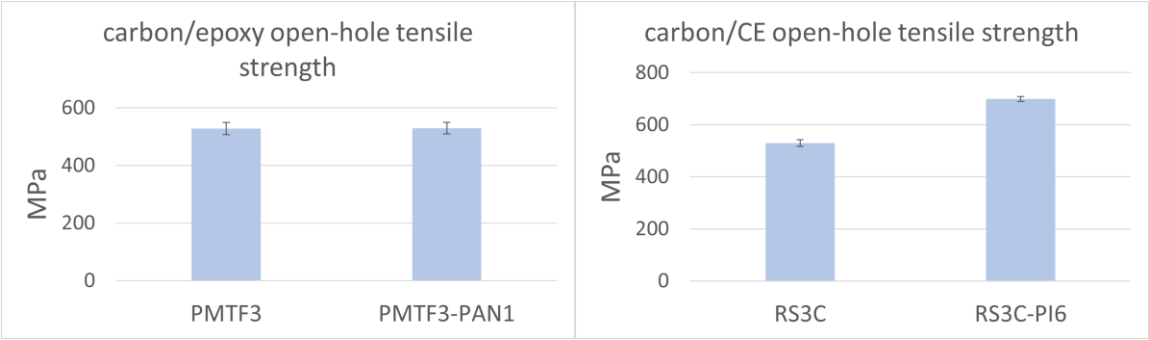

Figure 4.20: Open-hole tensile strength results.

With respect to tensile modulus, the nanofiber interleaves also had a positive effect on performance. Improvements were slightly greater than those seen in open-hole tensile strength for the PMTF3-PAN1 specimens, while they were smaller than the strength improvements for the RS3C-PI6 specimens. In contrast, the PAN1 specimens exhibited very slightly reduced average failure strains, while the PI6 specimens, once again, showed significant improvements.

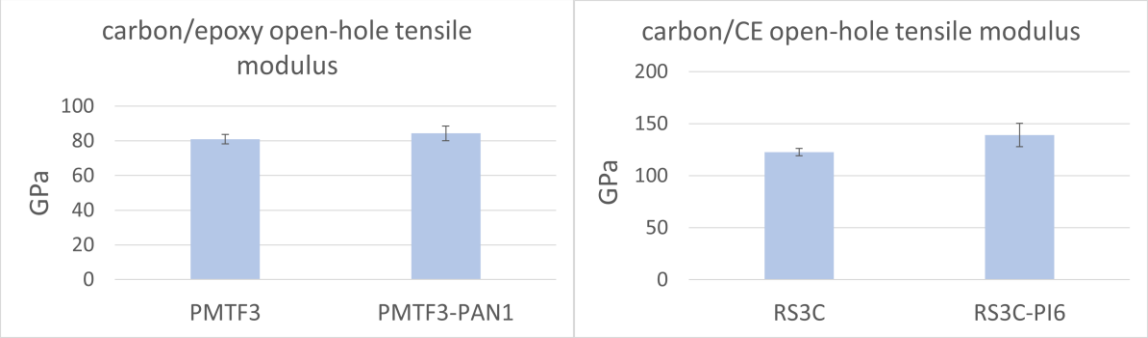

Figure 4.21: Open-hole tensile modulus results.

Due to extensometer slippage at higher deformations, some failure strain values were approximated based on the measured strength and modulus values. This method provided safe estimates of failure strains because the stress-strain curves were fairly linear. However, if toughness (or energy to failure), which can be equated to the area under the stress-strain curve, was estimated by assuming the curves were perfectly linear, the error would be magnified. For this reason, toughness values were not computed. However, the combination of increased strength, modulus, and failure strain (seen in the RS3C-PI6 specimens) would have led to tremendous increases in toughness.

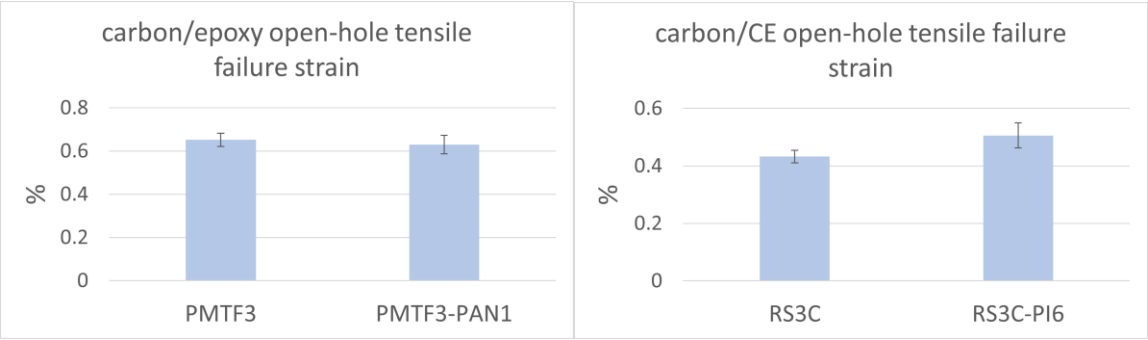

Figure 4.22: Open-hole tensile failure strain results.

4.3.1 Discussion of Open-Hole Tensile Testing Results

Similar to unnotched laminate, open-hole tensile specimens can undergo a multitude of different failure modes. For a test to be valid, failure should occur near the hole and not at some obvious defect.[180] The same set of failure codes that are used for

typical laminate tensile testing apply to open-hole tensile testing (see **Figure 4.12**).[120] However, since the hole acts as a considerable defect and stress concentration site, failure is almost always initiated near the hole, which would be considered the middle (M) location. **Figure 4.23** shows some common failure modes for open-hole tensile specimens. Typically, cross-ply specimens fail in LGM mode, quasi-isotropic and zero-dominated specimens fail in MGM mode, and angled plies failed in AGM mode. Meanwhile, zero-dominated specimens often exhibit more LGM failure modes than quasi-isotropic ones.[175]

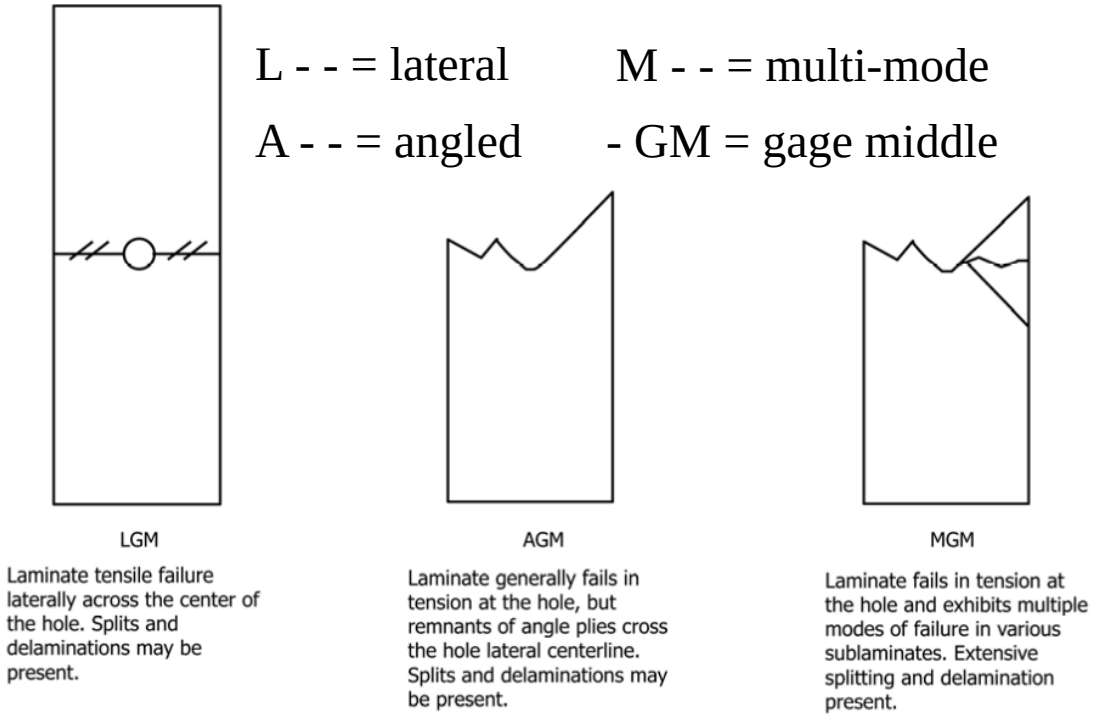

Figure 4.23: Acceptable open-hole tensile failure modes.[180]

The carbon/epoxy open-hole specimens mainly experienced multi-mode failure, as shown in **Figure 4.24**. Angled matrix cracking is prominent in the ±12° plies, but some specimens failed in a lateral manner, indicating more dominant fiber failure in the ±12° plies. There is a combination of matrix and fiber failure modes in all specimens. Although a couple specimens failed in an LGM mode, most failed in either an AGM or

MGM mode. It is noteworthy that failure of the ±12° plies occurred almost simultaneously with complete failure. This aligns with other results, where ultimate failure occurred almost instantaneously, with subtle warnings of fiber failure and catastrophic delamination.[175]

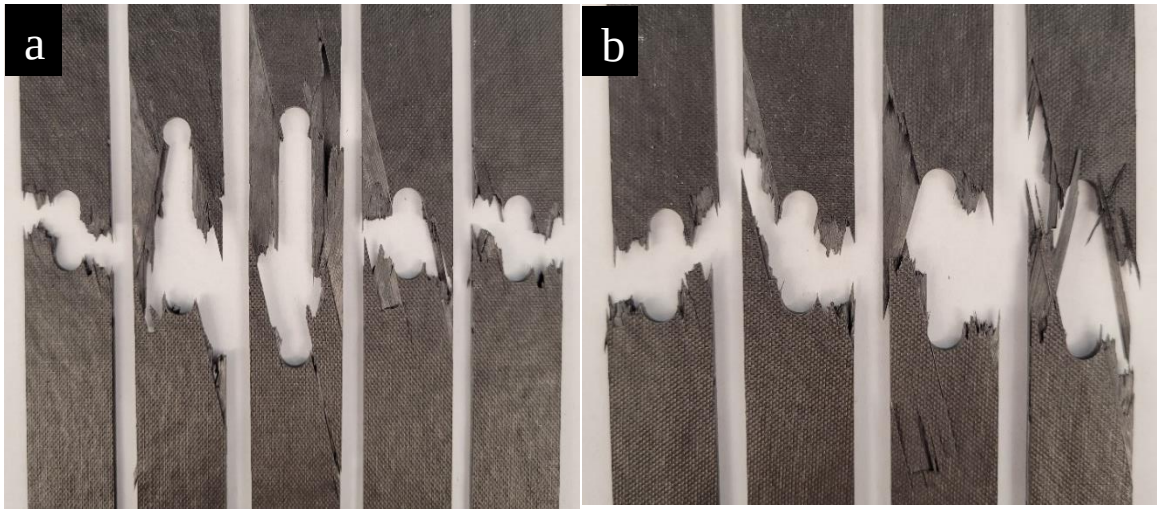

Figure 4.24: Failed carbon/epoxy open-hole tension specimens: (a) PMTF3 pristine and (b) PMTF3-PAN1.

On the other hand, the carbon/CE specimens were only tested until the ±12° plies failed, which caused a clear drop in the load, but most of the 0° fibers were left intact. Matrix failure is the primary failure mode, but there is also some fiber failure in the PI6 specimens. The PI6 specimens also experienced more explosive failure than the pristine specimens. This is not a surprise because they experienced higher loads.

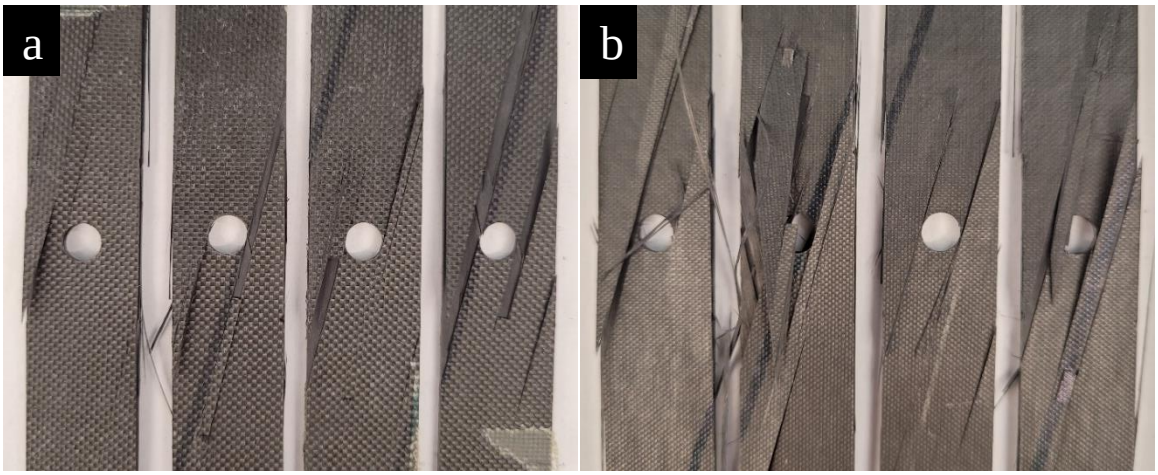

Figure 4.25: Failed carbon/CE open-hole tension specimens: (a) RS3C pristine and (b) RS3C-PI6.

Composite laminates, especially those with holes, experience failure in a sequential manner. In general, failure can be dominated by delamination, which has been shown to initiate at the hole and spread to the sides.[33] Initially, matrix failure occurs around the hole, which leads to extensive delamination and fiber-matrix debonding.[178] The size of the localized delaminations at the hole edge begin on the order of the ply thickness, but they quickly join up and allow damage to propagate across the width and along the length of the specimen.[33,201] This behavior is similar to that which occurs globally in unnotched laminates.[33]

According to Hallett et al., for a generic quasi-isotropic laminate, damage can be divided into four separate stages, according to its location in the specimen, occurring in the following order: (1) isolated damage at the hole and specimen free edge, (2) interconnected damage at the hole (inner delamination regions) and localized damage at the free edge resulting from full width matrix cracks, (3) damage across the width of the specimen in a ‘‘zone of influence” of the hole, (i.e. the outer delamination regions, bounded by + and -45° cracks emanating from the hole), and (4) final catastrophic failure.[176] Also, in studies on delamination onset, it was seen to occur earlier for a smaller

hole diameter or increased ply thickness, due to the increased ratio of ply thickness to hole diameter.[33,201,202] In all cases, however, the critical factor controlling strength is the relative propensity to delaminate.[33]

This is promising news for NF-reinforcement, since its primary goal is to suppress delamination. Nonetheless, it should be noted that this work did not specifically examine the onset of delamination or the failure sequence, which would have required continuous monitoring. Delamination onset[202] and the effect of hole size on failure mechanisms[177] in laminates with holes has been studied before, but only with quasi-isotropic layups. During the open-hole tensile tests in this work, it is possible that delamination initiated at the straight free edges and not at the hole edges since the layup was designed to maximize the shear interlaminar stress τ_{xz} at the straight edges. The stress distribution around the hole is more complex, however, and the layups used in this work have not studied before, making it difficult to determine whether the holes served as additional sources of delamination or just as stress concentrations where interlaminar cracks were allowed to propagate. Future research could investigate the effects of hole size on the location of delamination initiation with layups that have not been previously studied.

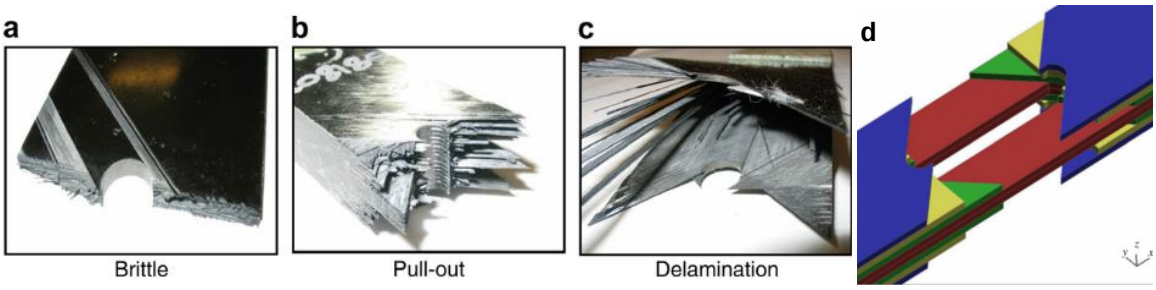

Figure 4.26: Different failure mechanisms observed in open-hole tensile specimens: (a) brittle, (b) pull-out, and (c) delamination.[176] (d) Schematic of outer 45/90/-45 plies separating from the 0° plies and pulling out in a notched quasi-isotropic laminate.[33]

Although the NF interleaves in this study were meant to suppress delamination, it still occurred in all specimens (see **Figure 4.27**), although it seems to be more prevalent

in the carbon/CE specimens. The carbon/CE open-hole specimens were not tested to complete failure because once the ±12° plies failed, the extensometer edges slipped and could no longer accurately measure the strain. However, delamination still played a prominent role in the failure of the ±12° plies, and all subsequent plies of different orientations were debonded to an extent. Nonetheless, the NF-reinforced specimens, especially the RS3C-PI6 specimens, typically experienced higher loads than the pristine specimens, meaning higher interlaminar stresses were needed to induce delamination. Although the onset of delamination was not directly observed, there were not many cracking sounds heard before ultimate delamination of the ±12° plies (or ultimate failure of the carbon/epoxy specimens). This indirect evidence of the delay in delamination onset is one reason for the increased properties

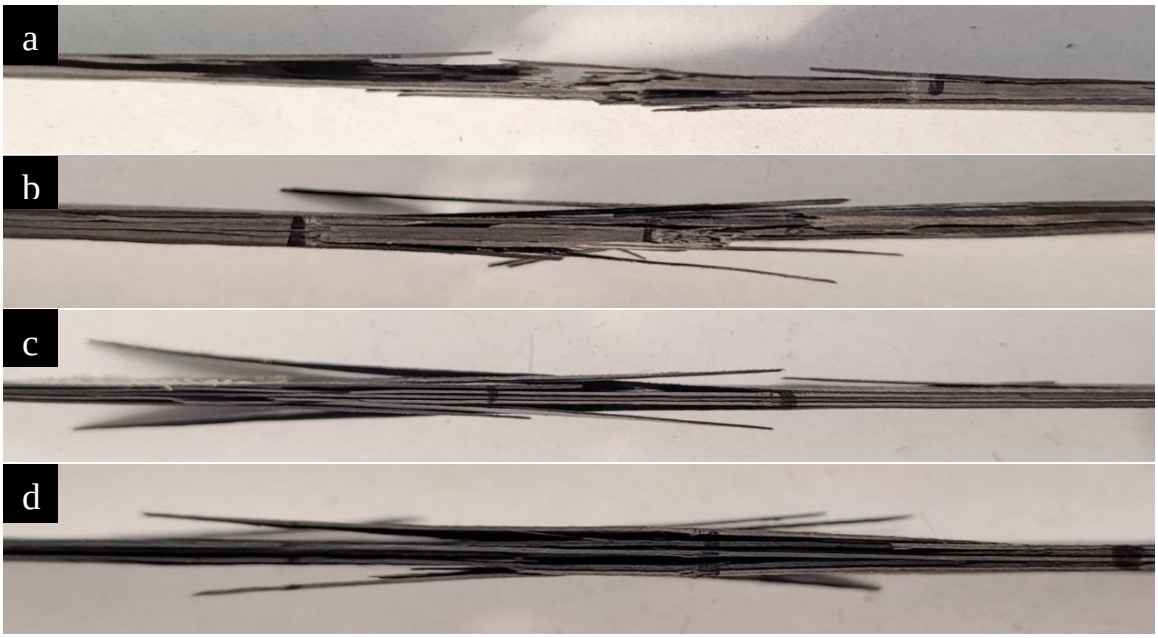

Figure 4.27: Edge delamination in failed open-hole tensile specimens: (a) PMTF3 pristine, (b) PMTF3-PAN1, (c) RS3C pristine, (d) RS3C-PI6.

Since edge delamination can also occur at the hole edges, they were examined in the SEM. **Figure 4.28** shows the hole edges in failed carbon/epoxy specimens. Delamination is present in both the pristine and PAN1 specimens, but the PAN1

specimen seems to have experienced more ply pullout failure. It is also noteworthy that the delamination cracks appear to subside at a certain distance from the sides of the holes. The ±12° interface shows signs of NF failure, but the poor NF-matrix adhesion between PAN and epoxy seen before limited the property improvements.

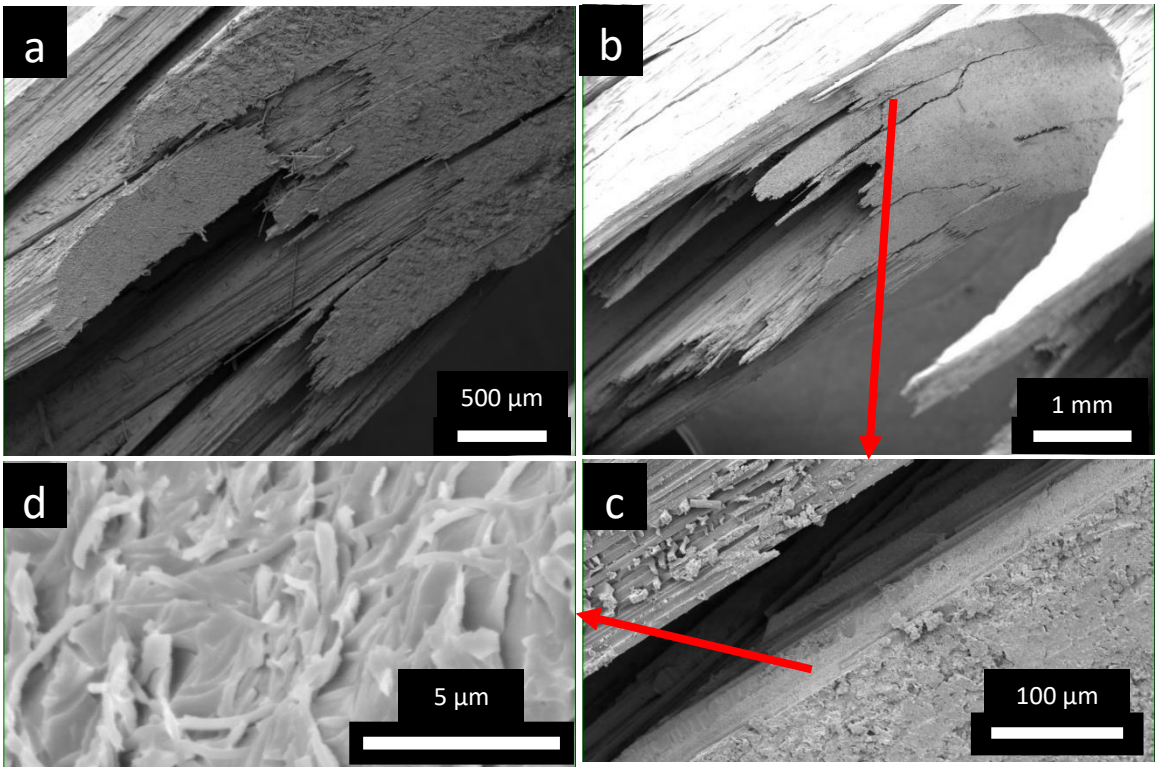

Figure 4.28: Hole edges in failed carbon/epoxy open-hole tensile specimens: (a) pristine and (b, c, & d) PAN1. Figure (d) shows some fractured NFs.

Figure 4.29 shows the hole edges of failed carbon/CE specimens. The pristine specimen exhibits clear delamination at both ±12° interfaces, while the PI6 specimen shows some much less prominent interlaminar cracking. The PI6 shows more fractured carbon fibers, indicating a more explosive failure mode, which occurred at a higher load. The PI6 specimen may have also experienced some ply pullout near the hole. Once again, the primary mechanisms that increased delamination suppression in the carbon/CE specimens reinforced with PI NFs are matrix toughening and NF bridging.

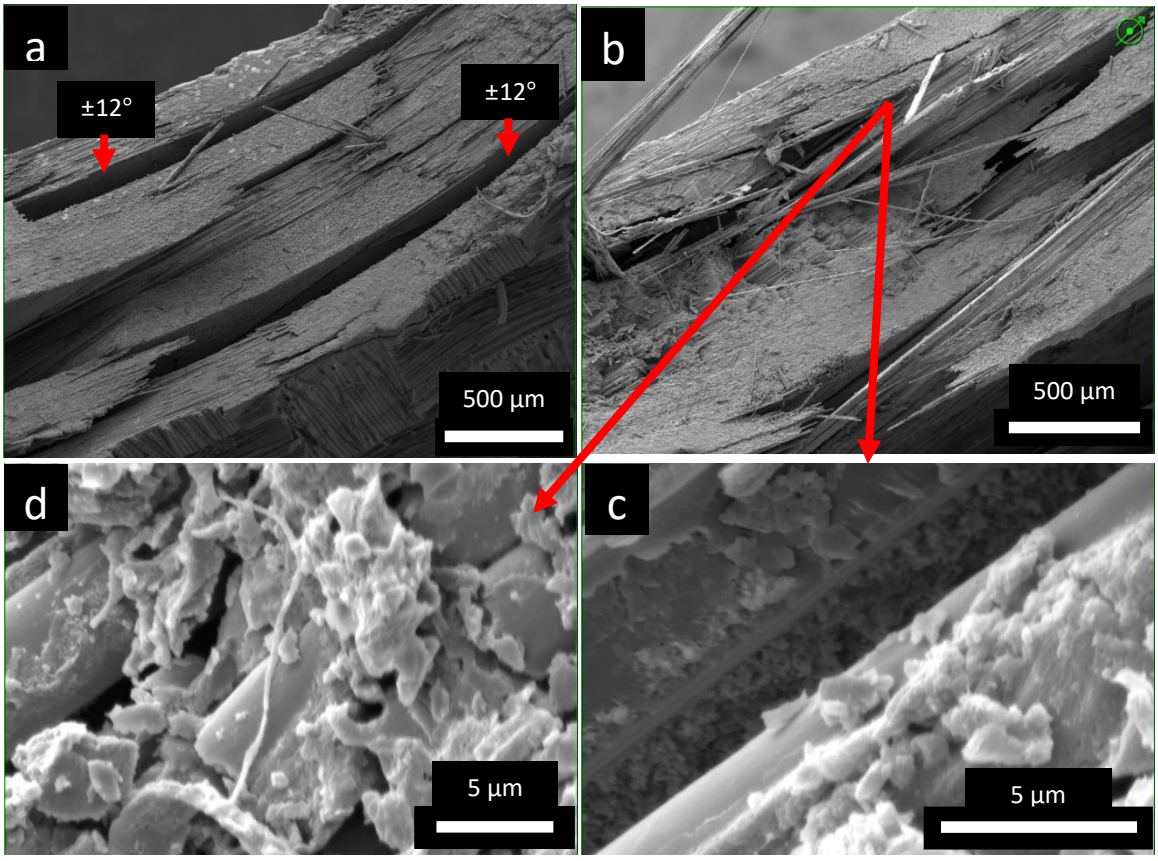

Figure 4.29: Hole edges in failed carbon/CE open-hole tensile specimens: (a) pristine and (b, c, & d) PI6. Figures (c) and (d) show signs of matrix toughening and NF bridging.

SEM investigation of delamination at the straight external edges was also performed on tested specimens. Although both the pristine and PAN1 carbon/epoxy specimens exhibit multiple interlaminar cracks, the pristine specimen shows three, while the PAN1 specimen shows four (see **Figure 4.30**). However, in the pristine specimen, both ±12° interfaces are delaminated, while only one is cracked in the PAN1 specimen. Interestingly, the PAN1 specimen also shows an interlaminar crack near the midplane, through the two centrally located 0° plies. This crack may have occurred due to the fact that one ±12° interface did not delaminate or have initiated from a defect after curing. To alleviate the global stress, the crack propagated longitudinally and somewhat transversely before failure.

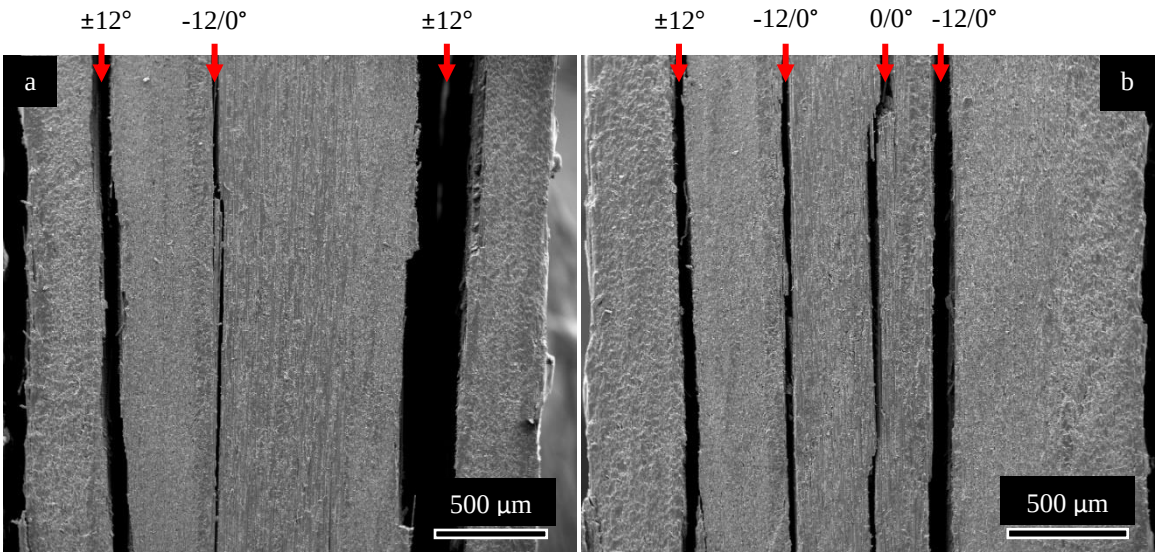

Figure 4.30: Edges of failed carbon/epoxy open-hole tensile specimens: (a) pristine and (b) PAN1. Crack propagation occurred in the downward direction.

Both the carbon/CE pristine and PI6 specimens show significant edge delamination. Similar to the carbon/epoxy specimens, the NF-reinforced specimen has delaminated at one more interface than the pristine specimen (see **Figure 4.31**). However, this is assumed to have occurred due to the higher loads, and therefore higher interlaminar stresses that the PI6 specimens experienced during the tensile tests.

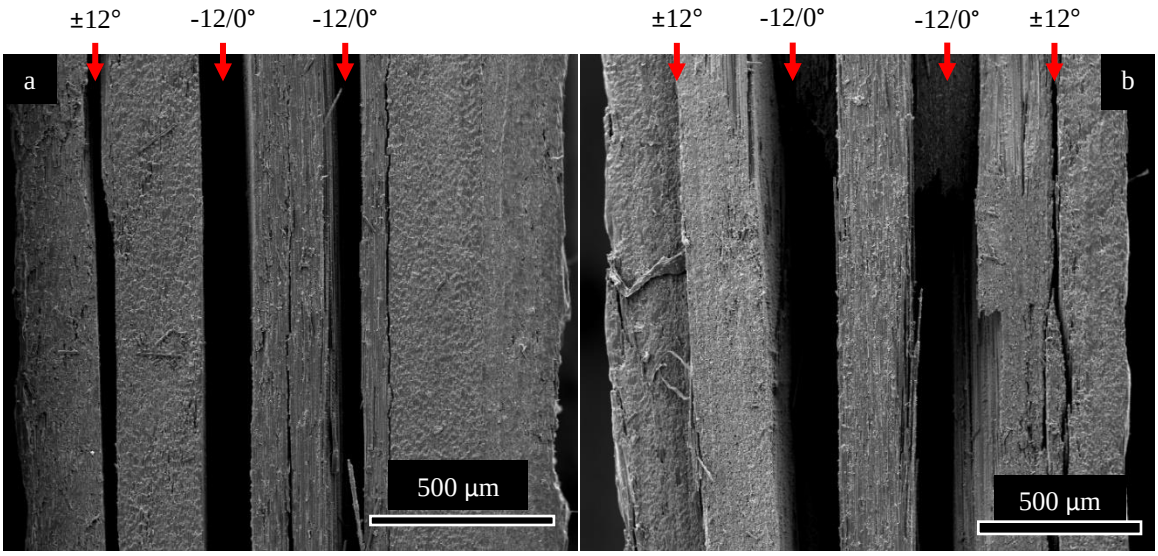

Figure 4.31: Edges of failed carbon/CE open-hole tensile specimens. (a) pristine and (b) PI6. Crack propagation occurred in the downward direction.

Looking at the ±12° interlaminar fracture surfaces of the carbon/epoxy specimens, shear hackle patterns were prominent in both the pristine and PAN1 specimens (see **Figure 4.32**). However, delamination provided opportunity for PAN NFs to bridge the cracks, which would have contributed to the slightly increased strength. Still, as seen before, the loose NFs on the fracture surface are signs of poor NF-matrix adhesion.

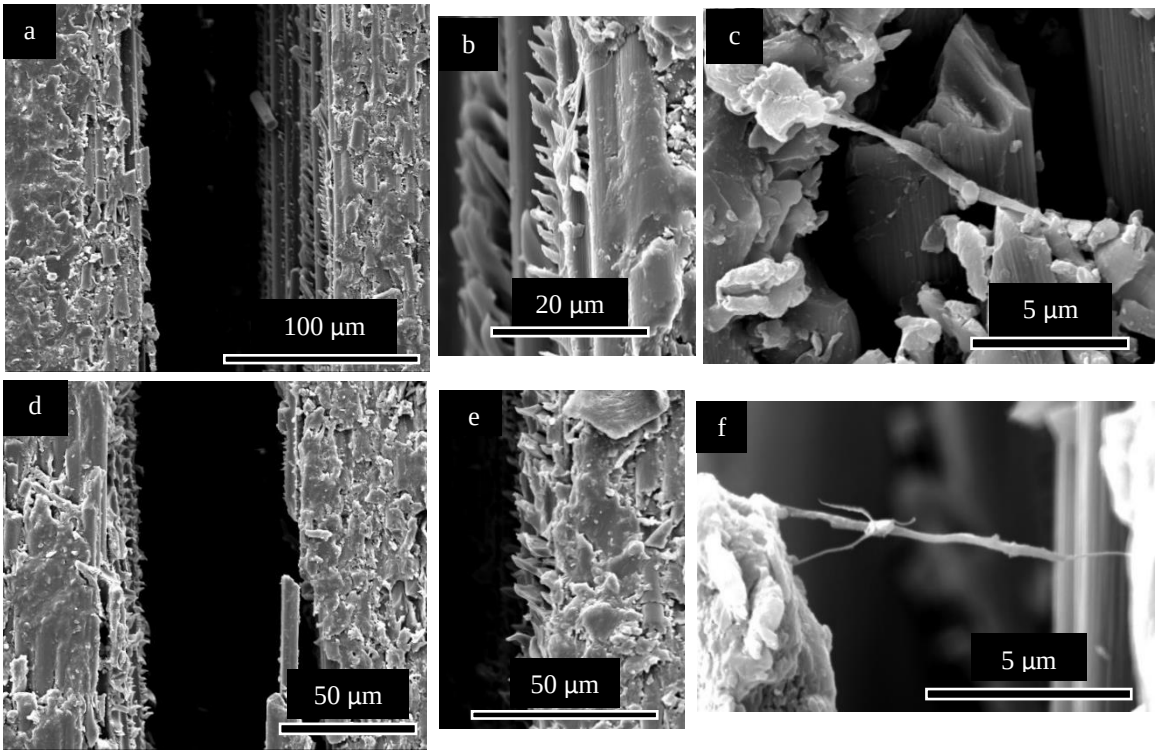

Figure 4.32: SEM images of interlaminar cracks at ±12° interfaces of tested carbon/epoxy open-hole tensile specimens: (a & b) pristine and (c, d, e, & f) PAN1.

Although the carbon/CE specimens show less shear hackle patterning than the carbon/epoxy ones, there is still evidence of NF bridging in the PI6 specimens (see **Figure 4.33**). In addition, the fracture surfaces in the PI6 specimens are rough and bumpy in many areas, which is a sign of resin toughening and a more tortuous, energy-intensive crack path. Although some of the resin toughening may come from the particulate modifiers added by the manufacturer, the bumpy surfaces were much more prevalent in

the NF-reinforced specimens, meaning the NFs played a significant additional toughening role.

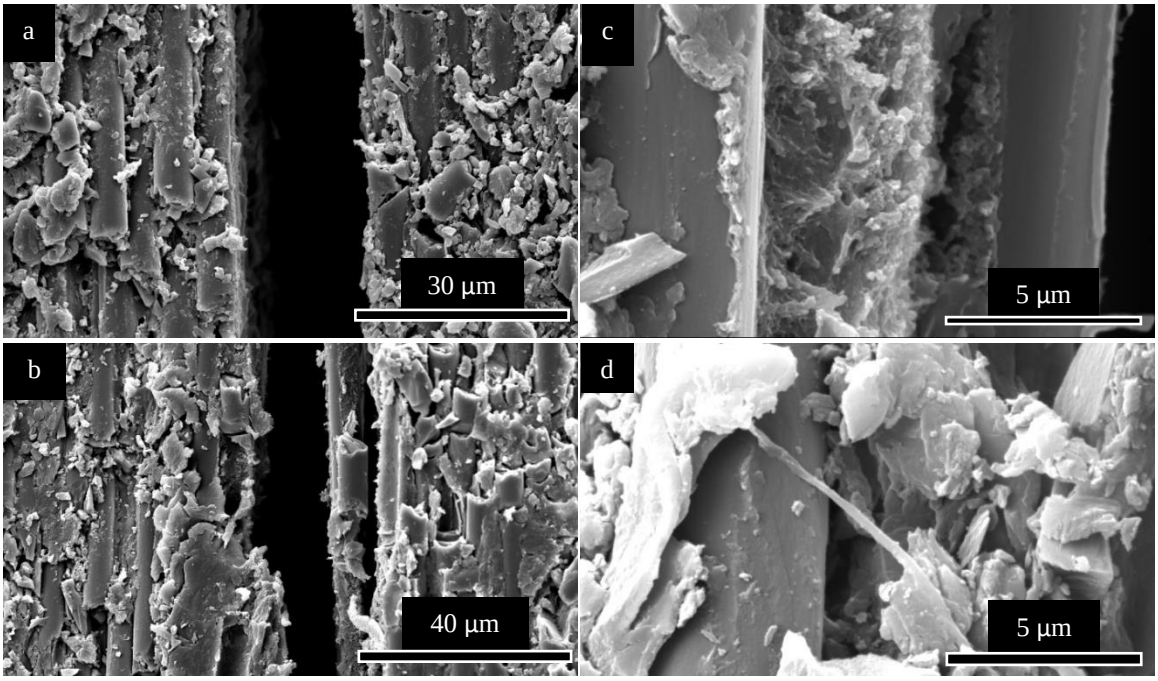

Figure 4.33: SEM images of interlaminar cracks at ±12° interfaces of tested carbon/CE open-hole tensile specimens: (a) pristine and (b, c, & d) PI6.

Although edge delamination and fracture surfaces can be examined via SEM, internal damage requires the use of other characterization techniques. X-ray computed tomography, (X-ray CT) can be used to visualize voids, defects, cracking, and delamination inside the volume of a composite. X-ray CT scans are usually in greyscale, where shade corresponds to material density.

X-ray CT scans were performed on both untested and tested open-hole specimens made from all four materials. **Figure 4.34** shows the difference between tested and untested carbon/epoxy specimens. Both specimens show small internal voids before testing. The failure modes are easy to identify in these images. Angled matrix cracking is prevalent, along with delamination that could have initiated at the hole or straight edge. However, delaminations propagated along the length of the pristine specimen on both

sides of the hole, while they only grew significantly on the left side of the hole in the PAN1 specimen. With respect to failure codes, the pristine specimen exhibits an AGM failure mode on both sides of the hole, while the PAN1 specimen exhibits an AGM mode on the left side and an LGM mode on the right side of the hole. The LGM mode requires more carbon fiber failure, which could be a reason for the small improvements in average tensile strength and modulus.

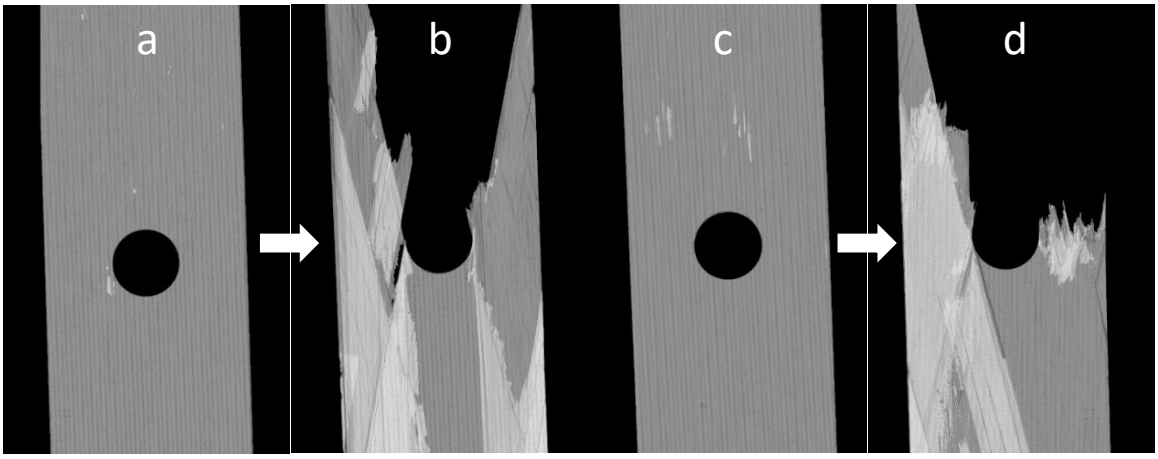

Figure 4.34: X-ray CT scans of carbon/epoxy open-hole tensile specimens. (a) untested and (b) tested PMTF3 pristine. (c) untested and (d) tested PMTF3-PAN1.

Further examination of the carbon/epoxy specimens (**Figure 4.35**) showed that the pristine specimen had more internal defects around the hole after curing than the PAN1 specimen did. Also, it seems like those defects may have contributed to the initiation of delamination around the hole in the pristine specimen. In contrast, one side of the PAN1 specimen failed in a lateral manner, indicating mostly fiber failure, which is the desired failure mode due to the high strength and modulus of carbon fibers.

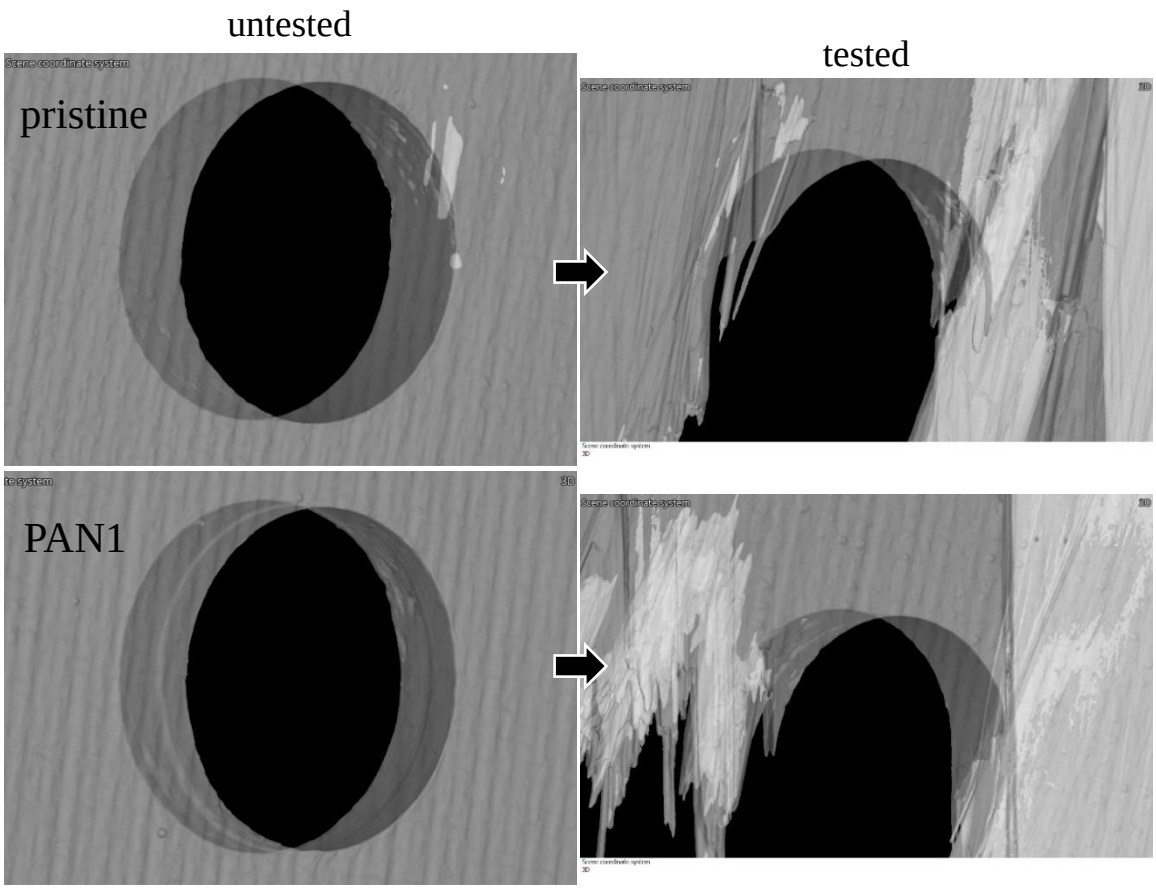

Figure 4.35: X-ray CT scans of carbon/epoxy open-hole tensile specimens.

X-ray CT scans of the carbon/CE specimens showed almost no defects before testing. After testing, the pristine and PI6 specimens showed similar combinations of failure modes, including matrix cracking, fiber failure, and delamination (see **Figure 4.36**). However, the PI6 specimen showed slightly more extensive delamination, especially towards the center line of the coupon, although this crack propagation was likely induced by higher interlaminar stresses compared to those in the pristine specimen. It is unclear whether delamination initiated at the outside edges or the edges of the holes, as both are sites of interlaminar stress singularities.

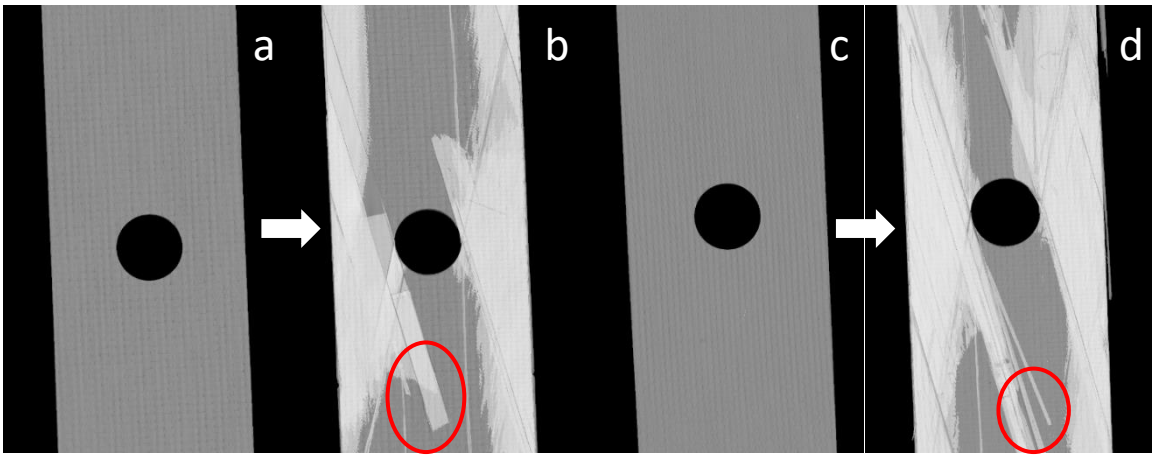

Figure 4.36: X-ray CT scans of carbon/CE open-hole tensile specimens. (a) untested and (b) tested RS3C pristine. (c) untested and (d) tested RS3C-PI6. Carbon fiber failure is outlined in red.

The zoomed in views of the X-ray CT scans of the carbon/CE specimens (**Figure 4.37**) show some surface defects on the hole edge in both untested specimens. However, these defects do not look to have propagated into the specimen very much, which means that they probably came about during the drilling of the holes. Although delamination formation during drilling of composites is a well-known issue,[206,207] care was taken in regard to drill tooling and parameters to minimize detrimental damage around the hole. Although some damage was caused, results of hole drilling were satisfactory for this study. It is noteworthy that the delaminations in the carbon/CE specimens did not propagate to the center line just above and below the holes. Instead, they propagated from the sides of the holes along the ±12° orientation of the fibers. This is not surprising because the sides of the holes serve as stress concentration sites.[204,205]

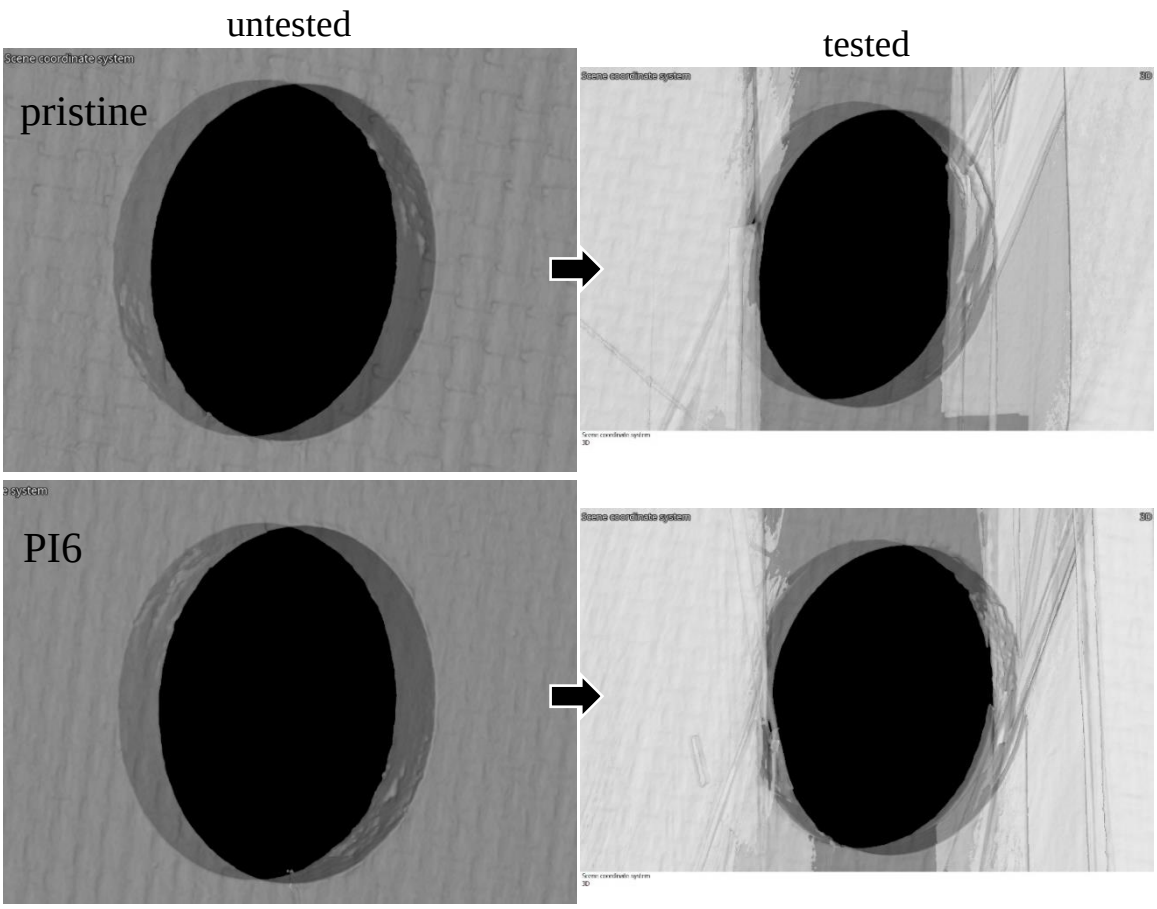

Figure 4.37: X-ray CT scans of carbon/CE open-hole tensile specimens.

Although the X-ray CT scans can provide qualitative comparisons of the damage with visual examination, porosity analysis can be used to give a quantitative comparison. Porosity analysis was performed on all four untested specimens. Results are summarized in **Table 4.5**. One surprising thing to notice is that the NF-reinforced specimens had higher defect volume ratios than the pristine specimens. In fact, the PMTF3-PAN1 specimen had over three times the percentage of defects after curing and drilling than the PMTF3 pristine specimen, but it still exhibited slightly increased strength and modulus. Even more intriguing is the fact that the untested RS3C-PI6 specimen exhibited over 17 times the percentage of defects compared to the untested RS3C pristine specimen but was able to withstand significantly higher stresses and strains before failure of the ±12° plies.

Table 4.5: Porosity results from the x-ray CT data of untested open-hole laminate specimens.

specimen	defect volume	material volume	defect volume ratio
	mm^3	mm^3	%
PMTF3 pristine	0.211528	1597.69	0.0132
PMTF3-PAN1	0.657229	1431.84	0.0459
RS3C pristine	0.109331	896.677	0.0122
RS3C-PI6	1.92585	921.604	0.2085

4.4 RESULTS OF L-BEND TESTING

The third and final composite structural element that was tested was the curved beam, or L-bend. Since one of the advantages of composites is monolithic construction, bends and curves are quite prevalent in load bearing structural parts.[172] Generally, interlaminar stresses are developed when curved composite laminates are subjected to flexural loading in the plane of curvature or tensile loading applied on each end of the bend, resulting in delamination (see **Figure 4.38**).[208] One example of this is an L-shaped laminate, which can experience interlaminar stresses from any combination of its three sources: through-thickness loadings, geometries, and discontinuities.[33,209] Most often, interlaminar radial stresses are induced from the bending of the curved laminate.[209] In general, the resistance to delamination and other strength characteristics of L-bend laminates are affected by the type of resin & reinforcement, stacking sequence, manufacturing process, fabrication quality, aging, and geometric configurations.[172,173]

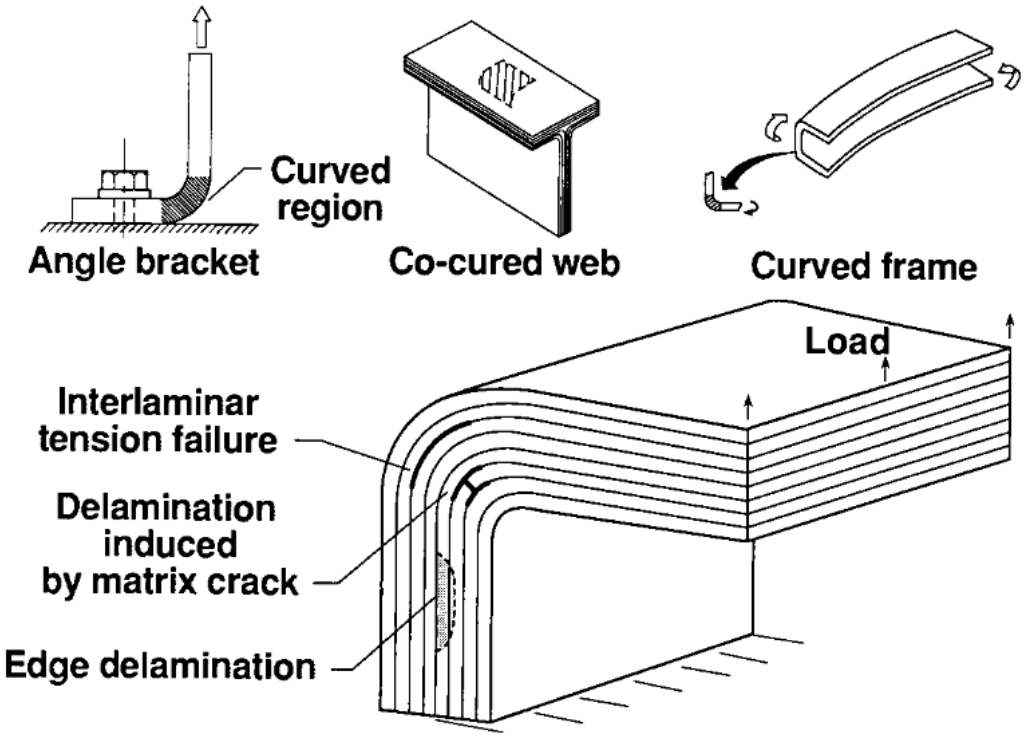

Figure 4.38: Curved laminate configurations and failure modes.[209]

To induce interlaminar stresses in curved composites, several testing methods have been developed. Although not on a L-bend beam, Hiel proposed a tensile test on a 180° bend to determine the interlaminar tensile strength around the bend in 1991.[210] Only a year later, Martin proposed the first testing configuration on a 90° bend.[209] The next year, a slightly modified method was used by him and Jackson.[211] Over the years, a few other configurations were used.[115,172,173] However, there is now a standardized method for testing the interlaminar strength of L-bend laminates (ASTM D6415),[193] which is what was used for this dissertation.

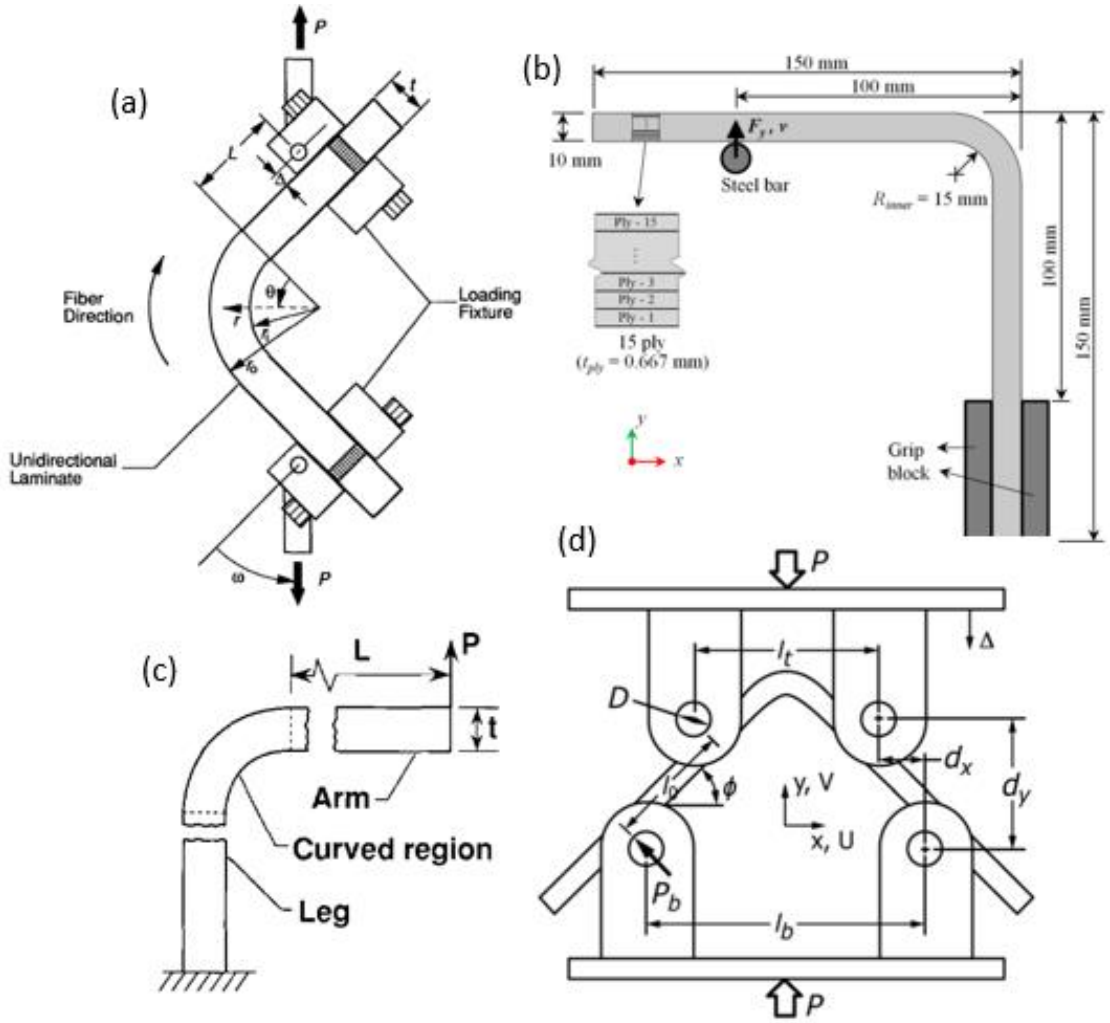

Figure 4.39: Different L-bend loading configurations that induce delamination at the curve. (a) ref. [211] (b) ref. [172] (c) ref. [209] (d) ref. [193].

4.4.1 L-bend Data Analysis

Although ASTM D6415 can be applied to composite laminates consisting of layers of fabric or unidirectional plies, a unidirectional layup in which fibers run continuously along the legs and around the bend is most suitable for the measurement of the interlaminar tensile strength (ILTS).[193] For this reason, a unidirectional layup was used in this study. Also, for comparison screening of ILTS, a specimen thickness of 4.2±0.2mm is suggested.[193] However, due to limited material, the thicknesses of the carbon/epoxy and carbon/CE specimens were only 2.954±0.064mm and 2.398±0.133mm,

respectively. This may have affected the accuracy of the obtained ILTS values, but it still allows for a one-to-one comparison between the pristine and NF-reinforced specimens.

The stress state in a curved beam during four-point bending is complex. Circumferential tensile and compressive stresses are produced along the inner and outer surfaces, respectively. The radial tensile stress ranges from zero at the inner and outer surfaces to a maximum in the central third of the thickness.[193] Thus, failure was carefully observed to ensure that a delamination was produced across the width before failure data were obtained. Because stresses are nonuniform and the critical stress state occurs in a small region, the measured curved beam and interlaminar strengths are extremely sensitive to architectural characteristics, reinforcement volume, and void content. Hence, the results may reflect manufacturing quality as much as material properties.[193] Since all specimens were manufactured using the same methods, these factors are assumed to have a minor effect on the results.

To compute the curved beam strength (CBS) in moment per unit width corresponding to the initial delamination, **Equation 4.1** was used, in combination with **Equation 4.2** and **Equation 4.3**. Here, the applied moment on the curved section of the specimen is the product of the force exerted by one of the cylindrical loading bars, P_b, and the distance, l_0, between two bars along a leg. The bar force and distance from the total force, P, at the first force drop (corresponding to the initial delamination) and the geometries of the loading fixture and test specimen, where φ is the angle in degrees of the loading arm from horizontal, d_x is the horizontal distance between the centerlines of two top and bottom adjacent rollers $(l_b - l_t)/2$, D is the diameter of the cylindrical loading bars, and t is the specimen thickness was used to calculate the CBS (see **Figure**

4.4). To calculate φ during loading, the vertical distance, d_y, between the cylindrical loading bars was calculated by subtracting the vertical displacement, Δ, of the loading fixture from the initial value of d_y. The vertical displacement, Δ, was obtained from the linear variable deformation transformer (LVDT) displacement output during the test. The initial value of d_y was calculated from the initial angle, φ_i, and the loading geometry. The initial angle, φ_i, is half the overall angle between the loading arms of the specimen prior to testing.[193] See **Figure 4.40** for the average curved beam strengths of the four materials tested.

$$CBS = \frac{M}{w} = \frac{P_b l_0}{w} = \left(\frac{P}{2w\cos\varphi}\right)\left(\frac{d_x}{\cos\varphi} + (D+t)\tan\varphi\right)$$

Equation 4.1 [193]

$$d_y = d_x \tan\varphi_i + \frac{D+t}{\cos\varphi_i} - \Delta$$

Equation 4.2 [193]

$$\varphi = \sin^{-1}\left(\frac{-d_x(D+t) + d_y\sqrt{d_x^2 + d_y^2 - D^2 - 2Dt - t^2}}{d_x^2 + d_y^2}\right)$$

Equation 4.3 [193]

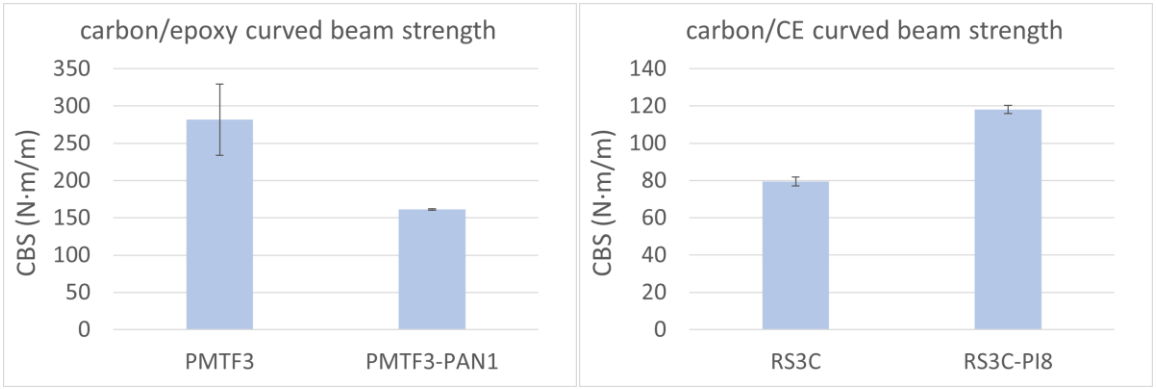

Figure 4.40: Curved beam strengths of the L-bend specimens.

To compute the radial stress in the curve, **Equation 4.4**, developed by Lekhnitskii[192] for the stresses in a curved beam segment with cylindrical anisotropy,

along with **Equation 4.5** and **Equation 4.6**, were used, where $\kappa = \sqrt{\frac{E_\theta}{E_r}}$, $\rho = \frac{r_i}{r_o}$, and E_θ and E_r can be approximated by E_1 and E_2, respectively. The maximum radial stress, or ILTS, determined using **Equation 4.4** ("measured") was compared to that found with **Equation 4.7** ("computed"), which is an approximate simple calculation useful for verifying the stress calculated in **Equation 4.4**. The measured radial stress is plotted against the crosshead displacement in **Figure 4.42**, while example load-displacement curves are shown in **Figure 4.41**. The accuracy of **Equation 4.7** decreases as the E_θ/E_r ratio increases or the r_i/r_o ratio (ρ) decreases. For the suggested geometry to determine interlaminar strength, an E_θ/E_r ratio of less than 20 should produce an error of less than 2%.[193] While the E_θ/E_r (or E_1/E_2) ratio for the TR50S/PMT-F3 carbon/epoxy material is about 14.4, the E_θ/E_r ratio for the T1100G/RS-3C carbon/CE material is about 24.3. In addition, these are properties of the pristine materials. The NF-reinforced materials could have slightly different E_1 and E_2 values. These facts should be considered when regarding the "computed" values of interlaminar tensile strength.

$$\sigma_r = -\frac{CBS}{r_o^2 g}\left[1 - \frac{1-\rho^{\kappa+1}}{1-\rho^{2\kappa}}\left(\frac{r_m}{r_o}\right)^{\kappa-1} - \frac{1-\rho^{\kappa-1}}{1-\rho^{2\kappa}}\rho^{\kappa+1}\left(\frac{r_o}{r_m}\right)^{\kappa+1}\right]$$

Equation 4.4 [193]

$$g = \frac{1-\rho^2}{2} - \frac{\kappa}{\kappa+1}\frac{(1-\rho^{\kappa+1})^2}{1-\rho^{2\kappa}} + \frac{\kappa\rho^2}{\kappa-1}\frac{(1-\rho^{\kappa-1})^2}{1-\rho^{2\kappa}}$$

Equation 4.5 [193]

$$r_m = \left[\frac{(1-\rho^{\kappa-1})(\kappa+1)(\rho r_o)^{\kappa+1}}{(1-\rho^{\kappa+1})(\kappa-1)r_o^{-(\kappa-1)}}\right]^{\frac{1}{2\kappa}}$$

Equation 4.6 [193]

$$\sigma_r^{max} = \frac{3 \cdot CBS}{2t\sqrt{r_i r_o}}$$

Equation 4.7 [193]

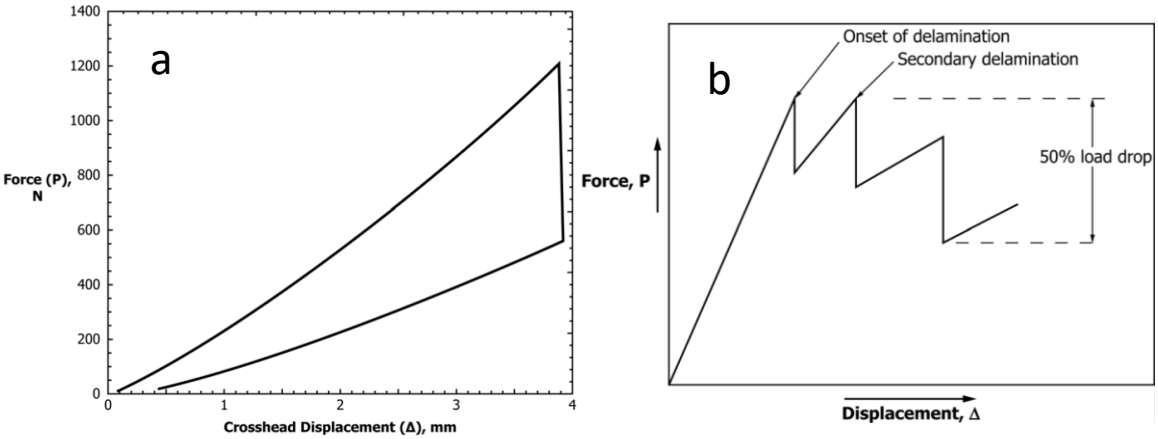

Figure 4.41: Typical load-displacement responses for (a) unidirectional and (b) multidirectional specimens.[193]

It is typical for unidirectional L-bend specimens to exhibit a large drop in load (>50%) at the initial delamination, while multidirectional specimens commonly exhibit secondary and subsequent delaminations that cause the load to drop in steps (see **Figure 4.41**). The specimens in this study were unidirectional, but they exhibited failure characteristics similar to multidirectional specimens (see **Figure 4.42**). This may have something to do with the toughening of the epoxy and CE resins. It could also be partially explained by the loading configuration and specimen geometries. During the DCB test, mode I delamination growth is stable, while during the ENF test, mode II crack propagation is unstable. The curves obtained during the L-bend tests are reminiscent of stable crack growth, with a few points of unstable growth, as shown by the sharp decreases in interlaminar tensile stress, which were larger in the carbon/epoxy specimens.

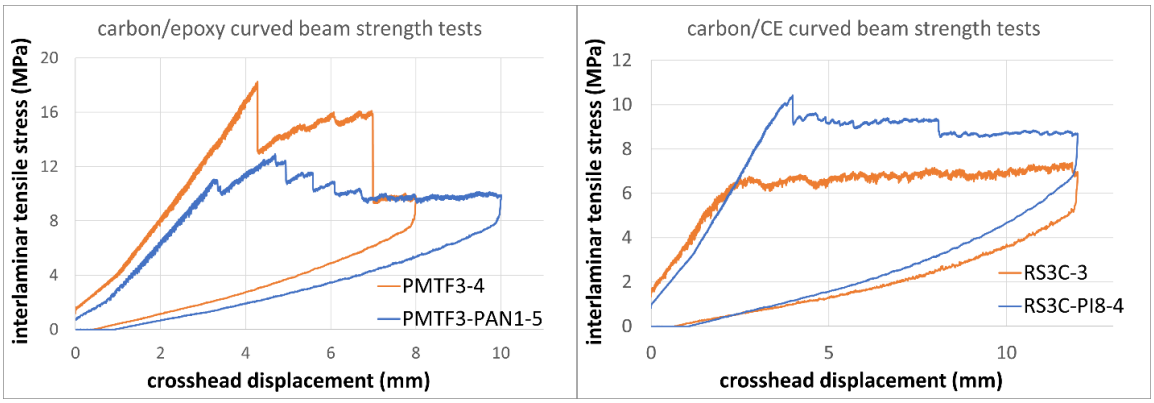

Figure 4.42: Representative interlaminar tensile stress-displacement curves for the L-bend tests.

The interlaminar tensile stresses that corresponded to the initial delaminations were determined from the curves. These values will be termed the "measured" ILTSs, while the "computed" ILTSs were determined with **Equation 4.7**. Comparison of both values for the four materials tested is shown in **Figure 4.43**.

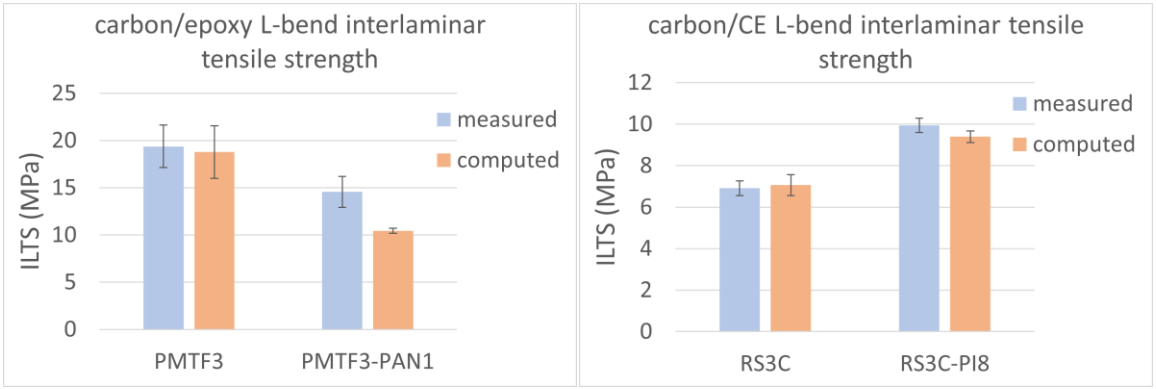

Figure 4.43: Interlaminar tensile strengths determined from the L-bend tests.

4.4.2 Discussion of L-bend Testing Results

Since both the curved beam strength and interlaminar tensile strength of L-bend specimens depend on their propensity to delaminate, delamination suppression techniques can be used to provide performance enhancements. Stitching was proposed by Cox in 1996, but his work is purely theoretical.[189] More recently, aligned CNTs were found to improve L-bend specimen deflection by 26% compared to the baseline specimens, but improvements in strength were negligible.[190] Another group used kenaf short fibers and

graphene oxide (GO) to reinforce glass/epoxy laminates.[191] However, only the kenaf fibers provided increased CBS and ILTS, while the addition of GO led to decreased mechanical performance due to extensive fiber pullout and poor fiber-matrix bonding. These results indicate the importance of the compatibility of the secondary reinforcement with the matrix. As before, the toughening effect of NF interleaves in L-bend composites depends on several factors, including the amount and size of the NFs and the NF-matrix adhesion. In addition, since the L-bend panels were manufactured using a different process than the other panels studied in this dissertation, which were all flat plates, the amount of resin impregnation and void content may be different.

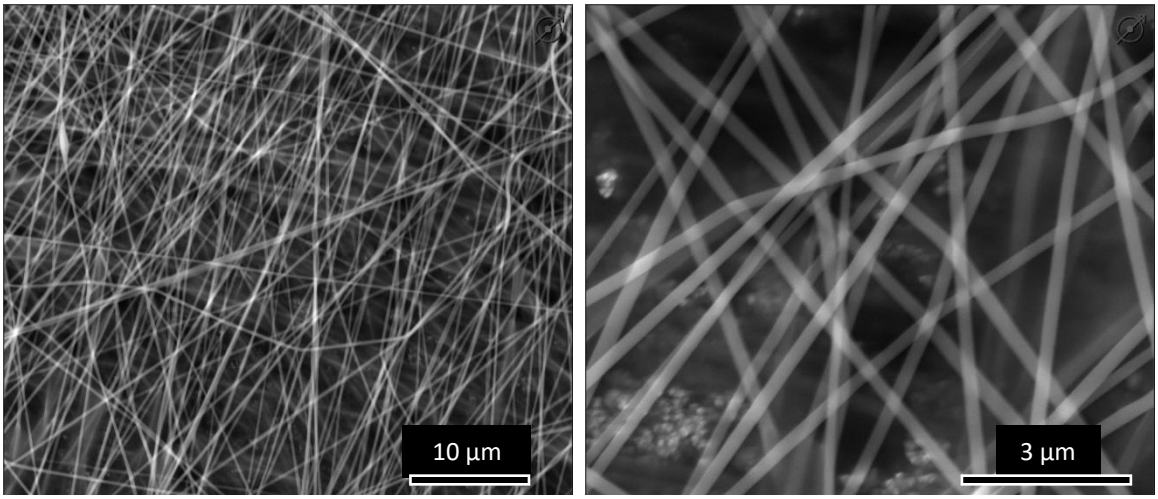

Figure 4.44: SEM micrographs of a PAN1 NF mat that was used to reinforce the interfaces between every 2 plies in the carbon/epoxy L-bend specimens.

Based on the results of the interlaminar fracture toughness testing, the range of areal weights of NF interleaves that should provide interlaminar toughening are known. However, since the CBS tests induce interlaminar normal stresses, the mode I data should be most relevant. Since a PAN NF interleaf areal weight of around 1 g/m^2 was used to enhance the mode I IFT of the carbon/epoxy material, the areal weight of the three PAN NF interleaves used to reinforce the carbon/epoxy L-bend specimens was approximately

0.9 g/m^2. With respect to the carbon/CE material, a PI NF interleaf with an areal weight of around 12 g/m^2 produced improved mode I IFT. Thus, the three PI NF interleaves were electrospun for the same 8 hours as the DCB interleaf, but their areal weights ended up being approximately 7.9 g/m^2. Consequently, it can be safely assumed that the thickness of the NF interleaves used to reinforce the L-bend specimens was satisfactory. In addition, the diameter distributions of the nanofibers were similar to those in the laminate interleaves (PAN1 average NF diameter: 232±38 nm, PI8 average NF diameter: 189±45 nm), so resin impregnation and NF-matrix adhesion should have been similar.

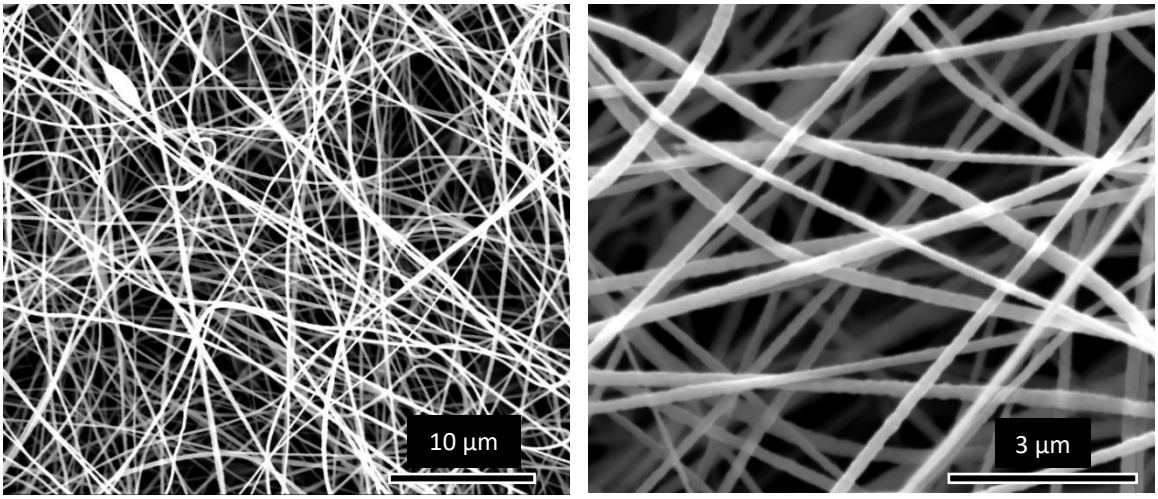

Figure 4.45: SEM micrographs of a PI8 NF mat that was used to reinforce the interfaces between every 4 plies in the carbon/CE L-bend specimens.

During the CBS tests, videos were obtained of the specimen edges at the curved section. These were used to determine when delamination was initiated, for computing the CBS and ILTS. Comparison of the pristine and NF-reinforced specimens' edges at the same displacements show similar amounts of delamination and buckling. To observe a difference, further investigation is needed.

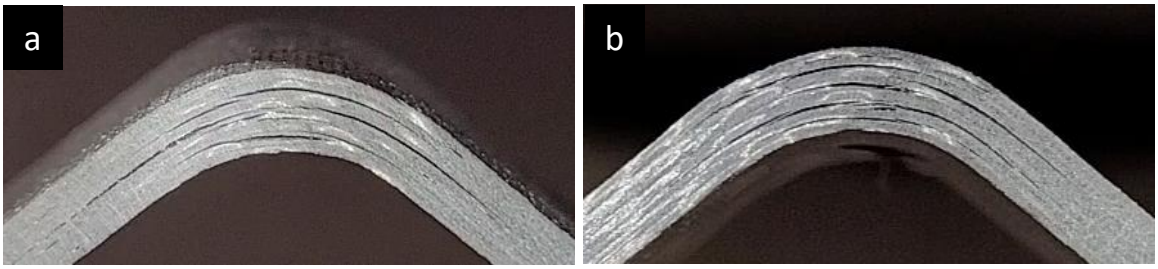

Figure 4.46: Edge view of delamination in carbon/epoxy L-bend specimens during testing when crosshead displacement was at 8 mm: (a) pristine (8mm) and (b) PAN1 (12mm). The value in parentheses indicates the maximum crosshead displacement during the test on that specimen.

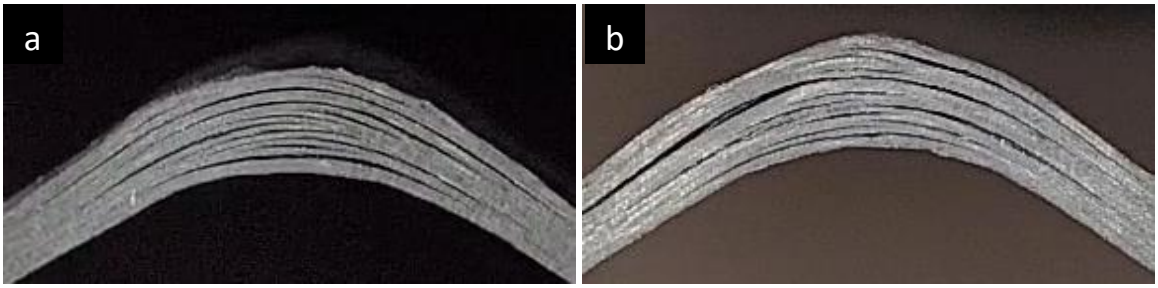

Figure 4.47: Edge view of delamination in carbon/CE L-bend specimens during testing when crosshead displacement was at 12 mm: (a) pristine and (b) PI8. Both specimens were tested to 12mm displacement.

In the SEM, comparisons are easier to see. Although the PMTF3 pristine (tested to 8mm crosshead displacement) and PAN1 (tested to 12mm crosshead displacement) specimens showed similar amounts of delamination, void content, and transverse cracking, the PAN1 specimen showed slightly more delamination, but this is because it was tested to a higher crosshead displacement. The PAN specimen also showed signs of NF bridging across interlaminar cracks, which is typically a toughening mechanism. However, most NFs do not look to be strained or broken, which may mean that they were easily pulled out from the matrix. This is a sign of poor NF-matrix bonding and would explain the decreased mechanical properties compared to those of the pristine specimens. In addition, during the mode I IFT tests, the primary toughening mechanism was carbon fiber bridging, which increased as the mode I crack grew. However, during the L-bend tests, the interlaminar cracks were not able to propagate any appreciable distance since they remained primarily in the curved region.

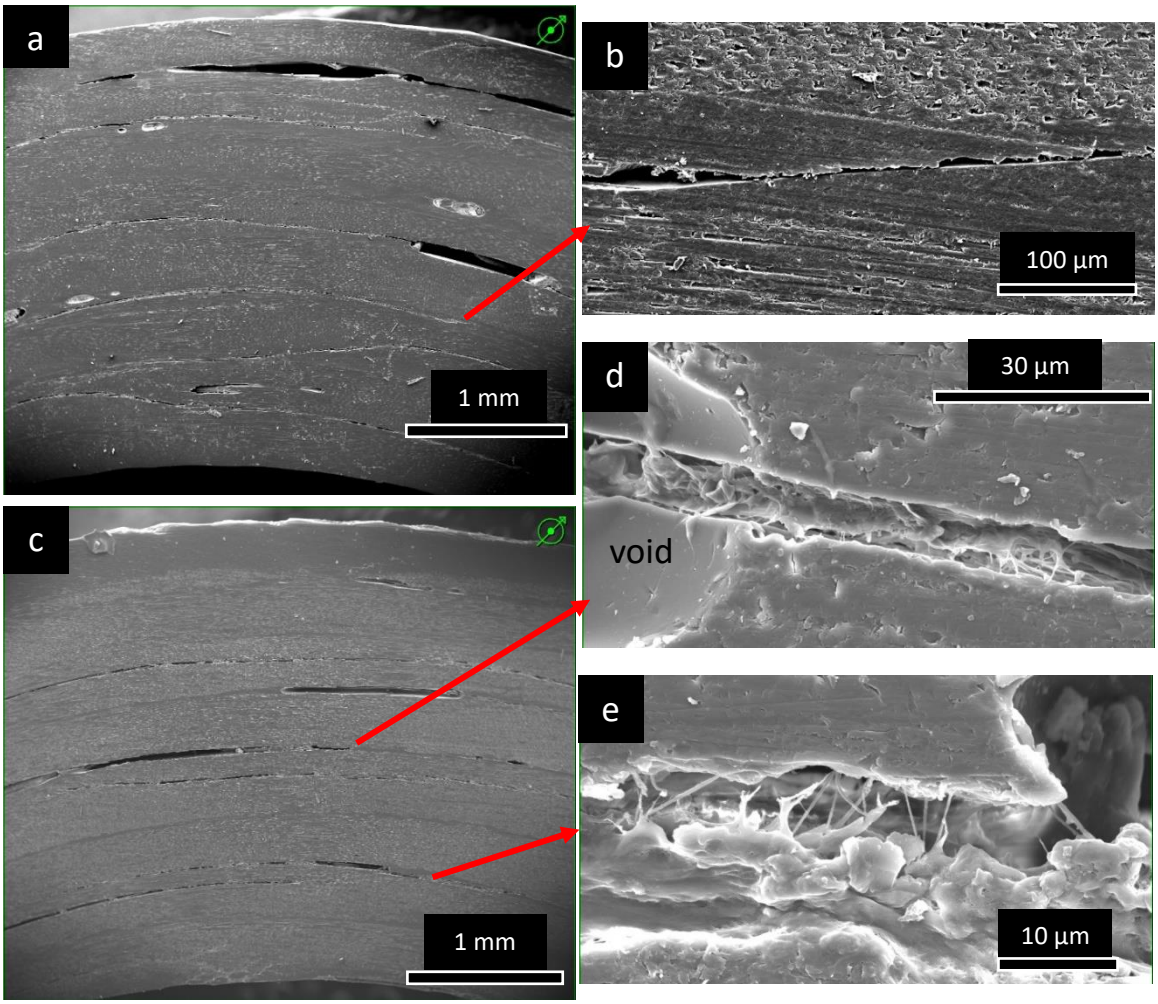

Figure 4.48: SEM images of the curved edge of tested carbon/epoxy L-bend specimens: (a & b) PMTF3 pristine and (c, d, & e) PMTF3-PAN1. Image (b) shows a transverse crack that has propagated through the resin-rich interlaminar region, which would be a great candidate for NF-reinforcement. Image (d) shows an interlaminar crack that initiated at a large void and has propagated through the NF reinforced interlaminar region. Image (e) shows evidence of NF bridging across an interlaminar crack.

In **Figure 4.49**, the RS3C-PI8 (tested to 12mm crosshead displacement) specimen showed more delamination than the RS3C pristine (tested to 10mm crosshead displacement) specimen because it was tested to a higher crosshead displacement. It also experienced higher ultimate radial stresses during the test. However, delamination initiated at a higher interlaminar tensile stress than it did in the pristine specimen. Nanofiber bridging was also noticeable in both the untested and tested PI8 specimens. In

addition, the PI NFs show less NF pullout and, thus, better NF-matrix adhesion compared to the PAN NFs in the PMTF3-PAN1 L-bend specimens.

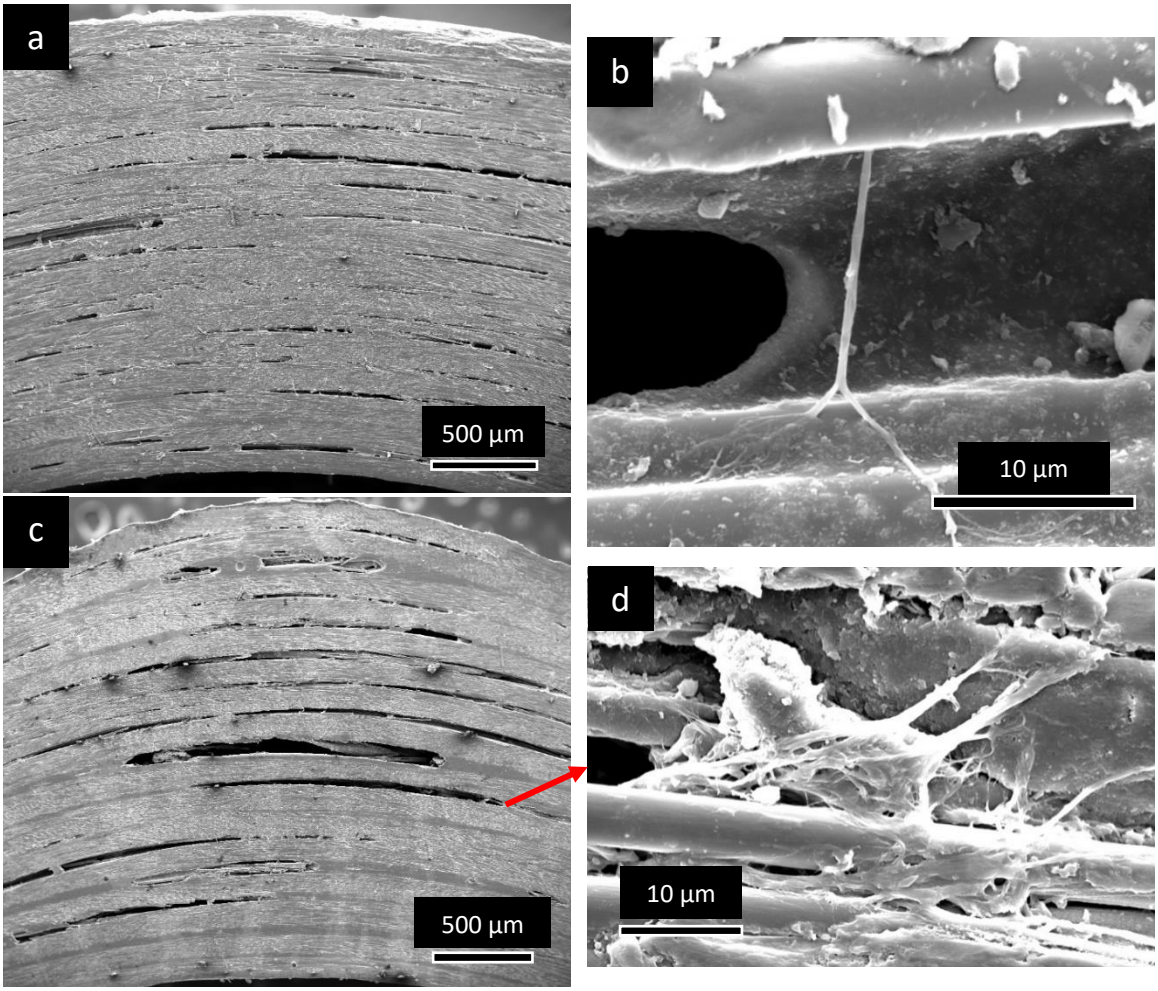

Figure 4.49: SEM images of the edges of carbon/CE L-bend specimens. (a) RS3C pristine specimen, (b) untested RS3C-PI8 specimen, and (c & d) tested RS3C-PI8 specimen. Figures (b) and (d) show clear evidence of nanofiber bridging in both the untested and tested RS3C-PI8 specimens.

Since the results for the PAN1 carbon/epoxy material were significantly worse than those for the pristine carbon/epoxy material, X-ray CT was performed on both untested and tested L-bend specimens of all four materials to investigate internal defects that could have developed during curing or testing.

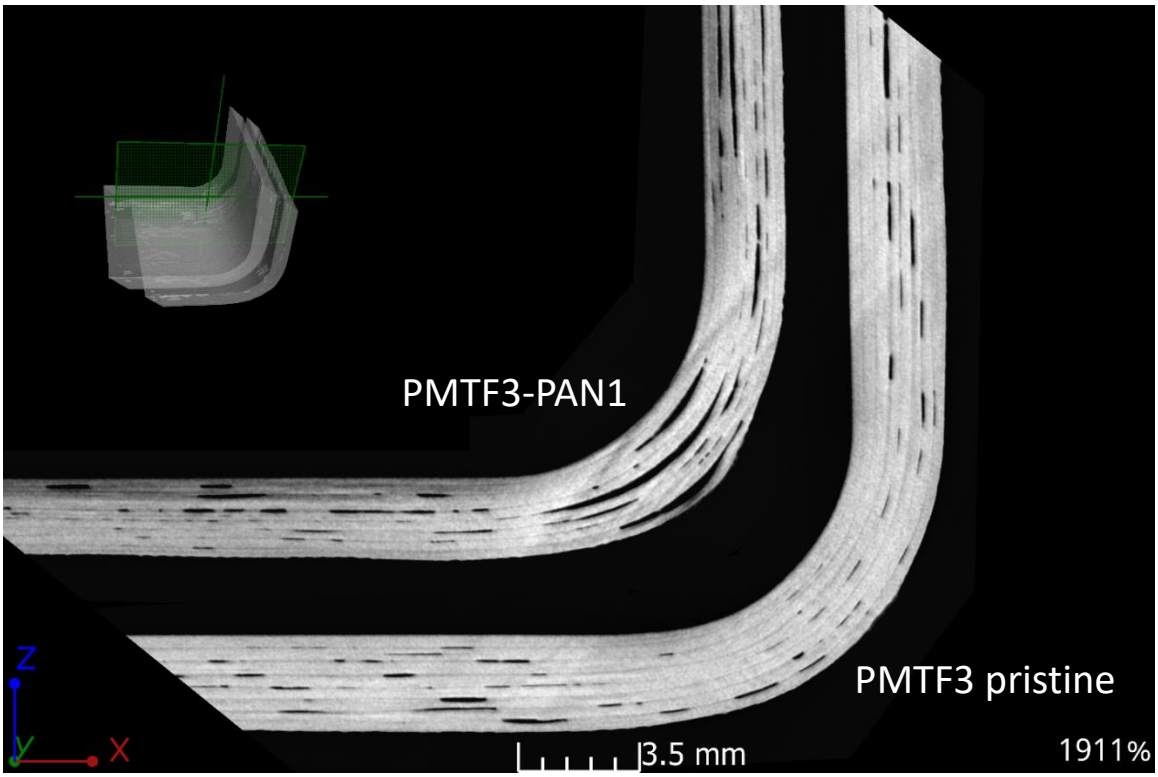

Figure 4.50: X-ray CT scan of untested carbon/epoxy L-bend specimens.

In **Figure 4.50**, the PAN1 specimen shows significantly more initial delamination in the curved region compared to the pristine specimen. This may have contributed to the decreases in CBS and ILTS. In contrast, the PI8 specimen actually looks to have less initial delamination in the curved region compared to the pristine specimen in **Figure 4.51**. However, each of these figures are only representative of one slice of the cross-section of the specimen. Porosity analysis is required for quantitative comparison of the defect volumes in the specimens.

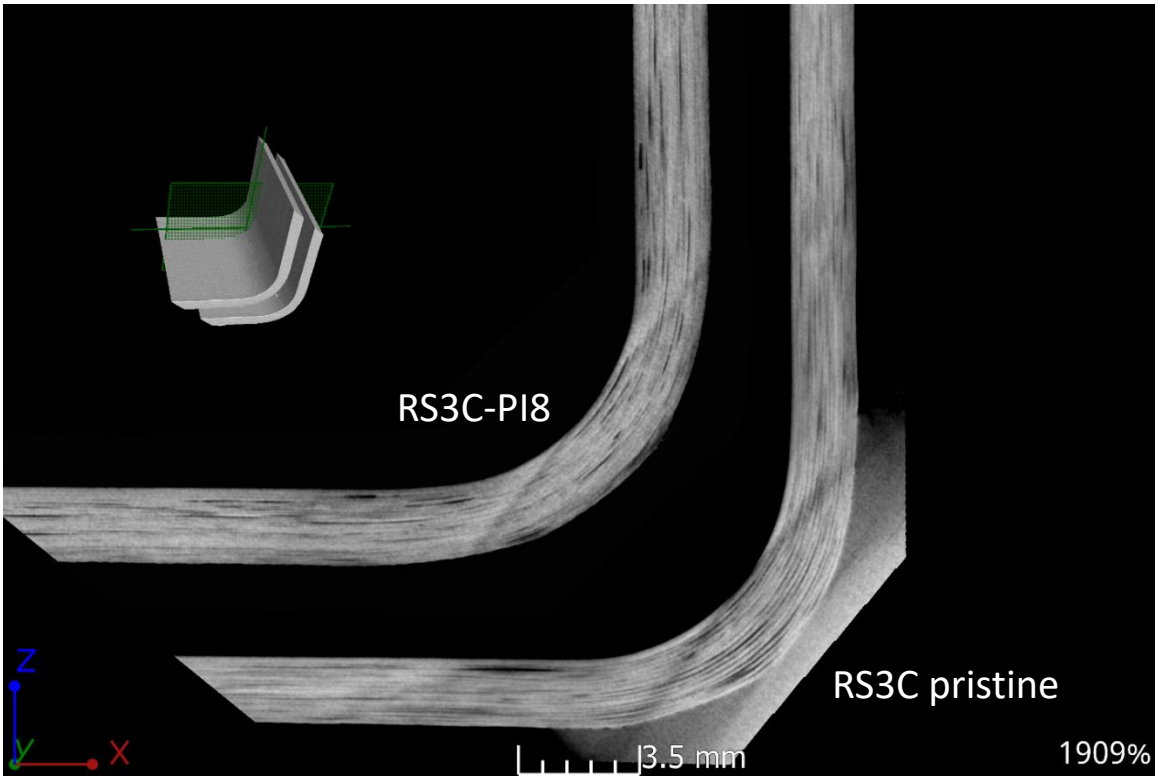

Figure 4.51: X-ray CT scan of untested carbon/CE L-bend specimens.

When manufacturing L-bend laminates under vacuum bag pressure, tooling material can play a crucial role in the properties of the cured part. One study concluded that in woven glass prepreg, the use of a fiberglass edge breather, a PTFE release film, and an aluminum intensifier can have significant effects on final void content.[212] With optimal parameters, the minimum void content achieved was 3.85% in the bend region. Based on the porosity results for the untested L-bend specimens tabulated in **Table 4.6**, all specimens possessed much lower defect volume ratios than this, indicating the effectiveness of the manufacturing process used in this work.

Comparing the materials, the PMTF3-PAN1 specimens had a slightly lower defect percentage than the PMTF3 pristine specimens. This means the decrease in properties was not due to inadequate resin impregnation but rather due to the poor NF-matrix adhesion. The RS3C-PI8 specimen, on the other hand, had a defect volume ratio

more than double that of the RS3C pristine specimen but still exhibited improved properties.

Table 4.6: Porosity results for untested L-bend specimens.

specimen	defect volume	material volume	defect volume ratio
	mm^3	mm^3	%
PMTF3 pristine	11.3307	2667.34	0.4230
PMTF3-PAN1	7.95291	2411.73	0.3287
RS3C pristine	4.92169	1936.54	0.2535
RS3C-PI8	10.6414	1900.78	0.5567

The porosity results for the tested L-bend specimens are shown in **Table 4.7**. Even though the PMTF3-PAN1 specimen was tested to a higher displacement than the PMTF3 pristine specimen, it still had a lower defect volume ratio. This means that the NF interleaves did not increase the size or number of voids compared to the pristine specimen, but rather that the poor PAN NF-epoxy adhesion was to blame for the decreases in CBS and ILTS experienced by the PAN1 specimens compared to the PMTF3 pristine specimens. Meanwhile, the RS3C pristine and PI8 specimens had very similar defect volume ratios, meaning they probably delaminated to a similar extent, although the PI8 specimen withstood higher loads.

Table 4.7: Porosity results for tested L-bend specimens.

specimen	defect volume	material volume	defect volume ratio	max displacement
	mm^3	mm^3	%	mm
PMTF3 pristine #3	5.48727	3640.82	0.1505	8
PMTF3-PAN1 #4	2.61921	3532.18	0.0741	12

RS3C pristine #3	1.57398	2464.06	0.0638	12
RS3C-PI8 #3	1.74089	2681.65	0.0649	12

4.5 DMTA TESTING AND DISCUSSION OF RESULTS

Due to the heterogenous nature of composites, after curing at elevated temperatures, they are left with residual stresses, which can cause matrix cracking. The higher the curing temperature, the more susceptible the composite is to microcracking. During service, thermal stresses can be magnified by thermal cycling, and, sometimes, working temperatures are close to the glass transition temperature (T_g). Although carbon fibers are not affected by high temperatures, the matrix is highly susceptible.[6] These harsh thermal environments can lead to degradation, matrix cracking, and, therefore, reduced mechanical properties, especially strength and stiffness.[6,213]

Thermal and viscoelastic properties of polymer matrix composites have been extensively studied. One of the main approaches to this is to perform dynamic mechanical thermal analysis (DMTA). Four of the main viscoelastic properties of polymers are the storage modulus E', the loss modulus E'', the damping ratio $\tan\delta = E''/E'$, and the glass transition temperature T_g. Viscous materials have high damping, are soft, and exhibit viscoelastic behavior, which give them a higher loss modulus. Elastic materials have high stiffness, are hard, and exhibit more brittle, elastic behavior, which give them a higher storage modulus. Thus, the damping ratio is effectively the ratio of viscous behavior to elastic behavior of a material, and polymers can be a mixture of both.[214] The storage modulus also gives information about the amount of rigidity in a material, and can be defined as the material's ability to store elastic energy.[215] Most thermoset resins are more elastic than viscous, which is desirable for applications that

require high strength and stiffness. The change from brittle to highly elastic, rubbery behavior is called the glass transition, and the temperature range over which it occurs is called the glass transition temperature, or T_g. There are three common definitions that can be used as the T_g of a material: the E' onset, the peak E'', and the peak $\tan\delta$ temperatures. The peak E'' and peak $\tan\delta$ temperatures can be determined straight forwardly, as they are the temperatures that correspond to the maximum E'' and $\tan\delta$ values, respectively. However, the E' onset temperature can be found by determining the intersection of the tangent lines of two sections of the E' curve, as shown in **Figure 4.52**. Nonetheless, the E' onset temperature is the lowest of the three, which means it indicates the point at which the elastic properties begin to decline drastically. Thus, it approximates the upper threshold of service temperatures, making it the most conservative and common value used for safety-critical structural applications.[214]

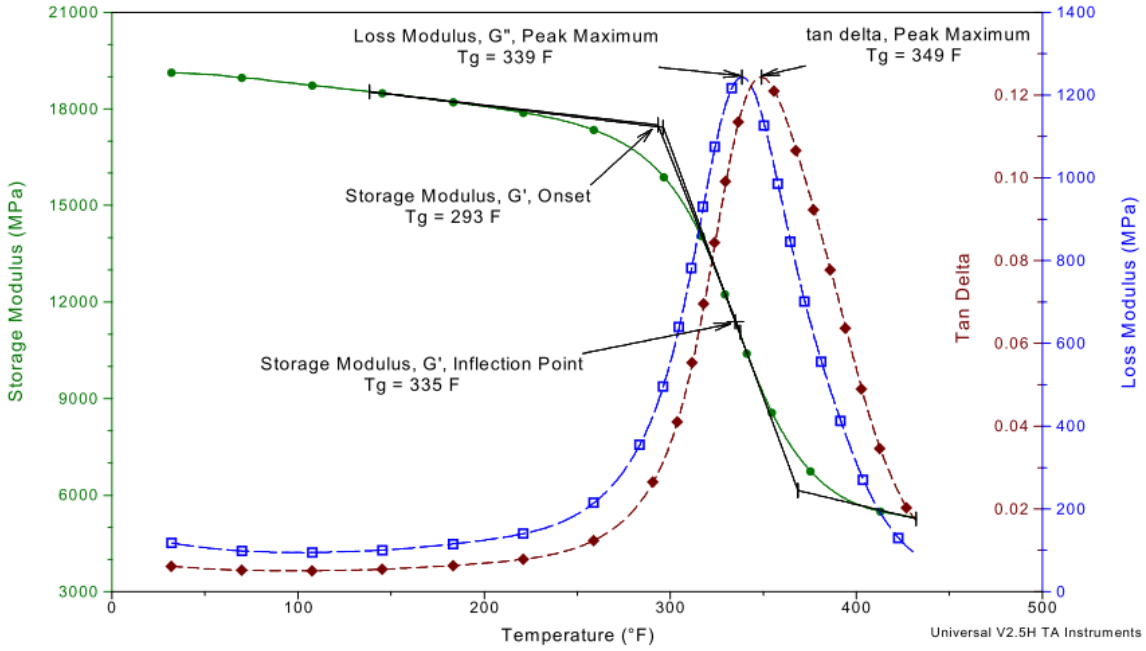

Figure 4.52: Some definitions of glass transition temperature from DMA.[214]

Several factors can influence the thermal properties, particularly the storage moduli and glass transition temperatures, of polymer matrix composites, such as post curing,[216] catalyst composition,[216] thermal degradation,[216,217] crosslink density,[216,217] and thermal aging.[217] However, there has been limited research performed on the thermal effects of electrospun NFs in polymer matrices. One study determined that P(St-coGMA) NF-reinforced epoxy nanocomposites can show increased T_g, decreased $\tan\delta$, and significantly increased E' due to the inherent cross-linked fiber structure and the surface chemistry of the electrospun NFs, which caused cross-linked NF-matrix interfacial bonding.[218] Another group concluded that PAN NFs in a PMMA matrix did not affect the T_g but significantly increased the storage modulus in the glassy and glass-rubbery transitional states because the PAN NFs help reduce the matrix mobility and deformation above the T_g.[219] Also, the presence of cellulose NFs in epoxy has been shown to enhance the storage modulus in the glassy state.[220] Lastly, cellulose NFs in a PVA matrix increased the storage modulus, especially in the melting zone due to limited chain mobility within the matrix.[221] Although there have been a handful of studies regarding the thermal properties of polymer nanocomposites, results have varied and research on NF-reinforced laminates is even more scarce.

Limited work has been performed to investigate the thermal properties of NF-interleaves composite laminates. One study concluded that the coefficient of thermal expansion (CTE) of a carbon/epoxy material can change around the glass transition temperature due to relaxation of the molecular orientation in both the carbon fibers and the reinforcing carbonized PAN nanofibers (T_g of PAN is 105°C) around those temperatures.[222] Two other groups determined that an epoxy matrix laminate reinforced

with PCL nanofibers was able to maintain its T_g, which gave confidence that the composites would retain its structural capacity at elevated temperatures.[6,168] The PCL nanofibers maintained their fibrous phase in the matrix, while the addition of PVA nanofibers to carbon/epoxy caused a slight increase in T_g due to the higher T_g of PVA.[223] These results are promising, but more research into the performance at elevated temperatures of nanofiber-interleaved composites is necessary to expand their safe use.[64]

Three-point bending DMA tests were performed on eight different materials, all made with 16 UD plies of the carbon/CE material: pristine RS3C, RS3C-PAN7 (NF interleaf at the midplane), RS3C-PI12 (NF interleaf at the midplane), RS3C-PI8 (with three total interleaves, one every 4 plies), and the same 4 materials that had been post-cured at 450°F for two hours. From the DMA data, the storage modulus E' was plotted as a function of sample temperature. Based on the results shown in **Figure 4.53**, both PAN and PI NF interleaves reduced the storage modulus of the composite. Although the addition of thermoplastic NFs to a thermoset matrix-composite may have led to a decrease in the material's ability to store elastic energy, the reason for this significant reduction in storage modulus is unclear and requires more investigation. However, this decrease in stiffness was not realized in the previous tests, in which the PI NF-reinforced carbon/CE multidirectional laminates with and without holes exhibited increased tensile modulus compared to the pristine carbon/CE specimens.

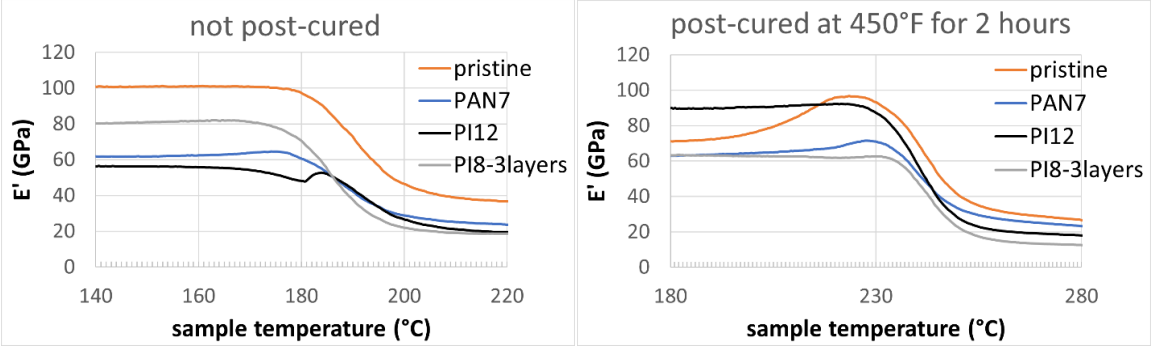

Figure 4.53: Storage modulus data from the DMA testing.

Based on **Figure 4.54**, the addition of PAN NFs to the carbon/CE material caused a very slight decrease in the damping ratio of specimens that were and were not post-cured. The addition of PI NFs, on the other hand, led to an increase in the damping ratio for both types of specimens. In addition, the more PI NFs that were added, the higher the damping ratio became. This is noteworthy because the damping ratio is the ratio of viscous behavior to elastic behavior. This means that the addition of thermoplastic PI nanofibers increases the material's ability to absorb energy. These are very promising results since increased energy absorption can lead to increased material toughness.

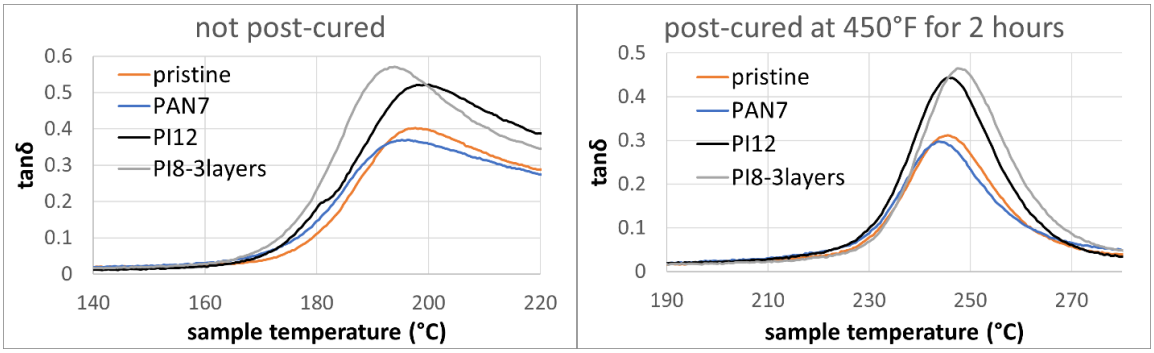

Figure 4.54: Damping ratio results from DMA tests.

With respect to the glass transition temperature, the addition of NFs did not have any significant effect. Although the T_g of all tested specimens was reduced slightly compared to the manufacturer's value, it is unclear which definition of T_g they used.

Table 4.8: DMA results for specimens that were not post cured. *It is unclear which definition was used.

	T_g (°C) (E' onset)	T_g (°C) (peak tan δ)	Max damping ratio (tan δ)	E' at 30°C (GPa)	E' at 220°C (GPa)
manufacturer value	191*	-	-	-	-
pristine	181.2	197.7	0.402	102.3	36.7
PAN7	180.4	196.3	0.369	65.7	23.8
PI12	183.7	200.0	0.521	56.6	19.6
PI8-3layers	179.5	193.9	0.571	82.1	18.6

Table 4.9: DMA results for specimens that were post cured at 450°F for 2 hours. *It is unclear which definition was used.

	T_g (°C) (E' onset)	T_g (°C) (peak tan δ)	Max damping ratio (tan δ)	E' at 30°C (GPa)	E' at 220°C (GPa)
manufacturer value	254*	-	-	-	-
pristine	239.4	245.5	0.312	75.8	27.0
PAN7	236.1	244.0	0.297	58.8	23.4
PI12	232.4	245.6	0.443	92.0	18.0
PI8-3layers	236.5	247.7	0.465	63.9	12.6

4.6 CONCLUSIONS

In this chapter, the NF-reinforcement of composite structures was examined. Multidirectional laminates with and without holes were reinforced with NF interleaves at two delamination prone interfaces and tested in tension. Unidirectional L-bend specimens were also reinforced with NF interleaves (three equidistant apart) and tested in 4-point bending to determine their curved beam and interlaminar tensile strengths. Results are tabulated in **Table 4.10**, **Table 4.11**, and **Table 4.12**.

Table 4.10: Results of laminate tensile testing.

Material	Tensile strength		Tensile modulus		Failure strain	
	Value (MPa)	Percent improvement from pristine (%)	Value (GPa)	Percent improvement from pristine (%)	Value (%)	Percent improvement from pristine (%)
PMTF3 pristine	590±25	-	94.5±4.3	-	0.609 ±0.050	-
PMTF3-PAN1	622±23	5.3	91.4±4.1	-3.3	0.636 ±0.037	4.4
RS3C pristine	606±23	-	139.7±6.3	-	0.430 ±0.024	-
RS3C-PI6	793±14	30.8	150.9±1.8	8.0	0.510 ±0.026	18.7

Table 4.11: Results of open-hole tensile testing.

Material	Open-hole tensile strength		Open-hole tensile modulus		Failure strain	
	Value (MPa)	Percent improvement from pristine (%)	Value (GPa)	Percent improvement from pristine (%)	Value (%)	Percent improvement from pristine (%)
PMTF3 pristine	528±21	-	81.0 ±2.7	-	0.652 ±0.031	-
PMTF3-PAN1	529±20	0.26	84.3 ±4.3	4.1	0.630 ±0.043	-3.5
RS3C pristine	529±13	-	122.6 ±3.5	-	0.432 ±0.022	-
RS3C-PI6	699±9	32.1	139.2 ±11.2	13.5	0.506 ±0.044	17.0

Table 4.12: Results of L-bend testing.

Material	Curved Beam Strength		Interlaminar Tensile Strength, "measured"	
	Value (N·m/m)	Percent improvement from pristine (%)	Value (MPa)	Percent improvement from pristine (%)
PMTF3 pristine	281.6±47.9		19.37±2.25	-
PMTF3-PAN1	161.1±1.0	-42.8	14.56±1.63	-24.9
RS3C pristine	79.4±2.4		6.92±0.35	-
RS3C-PI8	118.0±2.2	48.6	9.95±0.35	43.8

Based on the results of the mechanical testing, the addition of continuous NF interleaves provided significant enhancements to most structural properties. However, the

improvements were more consistent and substantial for the carbon/CE material reinforced with PI nanofibers compared to those for the PAN NF-reinforced carbon/epoxy.

The data obtained in this study proves for the first time that material improvements, such as modes I and II interlaminar fracture toughness, based on NF-reinforcement in laminates can be translated to the properties of structural volumes. Continuous nanofiber reinforcement of curved structures had not been studied up to now. In addition, the combination of T1100G/RS-3C carbon fiber/cyanate ester and APS-C2 polyimide nanofibers represents a new advanced composite material that is especially useful for high-temperature applications.

The manufacturing methods used in this chapter can also be used as a guide for fabricating NF-reinforced composite structures. Construction of the NF-reinforced L-bend panels provided a proof-of-concept that was the first of its kind. The methodologies developed in this study can be replicated with slight modification for other composite structures and to optimize structural performance. Lastly, the new data obtained in this study could prove valuable for developing complex, 3D computational models of NF-reinforced structures, which is a crucial step towards their practical commercial application.

CHAPTER 5. ELECTROSPINNING OF ALIGNED NANOFIBER CONFIGURATIONS FOR LAMINATED NANOCOMPOSITES

Continuous nanofibers can exhibit extraordinary mechanical properties.[46,51–54,58,224] They have several applications, but one of the most promising is the reinforcement of composites. In addition to secondary reinforcement in composite laminates, continuous nanofibers can be used as primary reinforcement in bulk nanocomposites.[56] However, most nanocomposites studied to date have only been reinforced with random or partially aligned nanofibers. In order to mimic the high fiber volume fractions and controllable load-carrying capabilities of advanced composite laminates, near perfect nanofiber alignment and the ability to stack oriented nanofiber plies within polymer matrices are needed. However, most electrospinning methods used to collect continuous aligned NFs limit both the amount and the alignment of the obtained NFs. Further study is needed to optimize nanofabrication techniques to produce laminated nanocomposites reinforced with highly aligned, continuous nanofibers.

5.1 REVIEW AND IDENTICATION OF TECHNICAL PROBLEM

5.1.1 Polymer Matrix Nanocomposites

Polymer nanocomposites are defined as multi-phase, polymer matrix materials in which at least one component has at least one nanoscale dimension.[225,226] They offer great potential in the field of advanced materials for numerous multi-functional applications due to their unique property combinations and design possibilities.[227,228] With the transition from microparticles to nanoparticles, dramatic improvements in physical properties can result. Nanoscale materials have large surface-area-to-volume ratios, and many important physical and chemical interactions are governed by surfaces and surface

properties. For these reasons, a nanostructured material can have significantly different properties from a macroscale material of the same composition.[225]

To gain a better understanding of the characteristics that produce the unique properties of nanomaterials, several powerful characterization techniques have been developed, including x-ray diffraction, scanning and transmission electron microscopy, and atomic force microscopy. Fabrication methods of nanocomposites present new challenges encompassing the uniform dispersion of nanofillers in their polymer matrices.[228] Other challenges include poor alignment of the nanoreinforcing material, low reinforcement volume fraction, and inadequate bonding and load transfer at interfaces.[41] However, by conquering these difficulties and understanding the mechanisms responsible for the enhanced properties, polymer matrix nanocomposites can be designed and optimized for a wide range of applications.[227]

5.1.2 Bulk Nanofiber-Reinforced Composites

Currently, there is significant enthusiasm regarding one-dimensional (1D) nanomaterials, such as fibers or whiskers, and their use as reinforcement in nanocomposites. Due to their extraordinary mechanical properties, carbon nanotubes (CNTs) present an exciting way to reinforce bulk polymers. Most notably, several groups have used aligned CNTs to reinforce epoxy matrices, and CNT volume fractions have ranged from 0.04-50%, which is relatively high for nanocomposites.[229–233] In addition, epoxy has been reinforced with large CNT fibers,[234] yarns, and braids.[235] Almost all of these CNT/epoxy composites exhibited significant increases in tensile strength and modulus. However, their properties did not reach values expected by the rule of mixtures, mainly due to suboptimal load transfer between the epoxy and the CNTs.[234,236,237] In

addition, obtaining aligned CNTs requires complicated fabrication methods. The discontinuous nature of CNTs also makes them a health hazard.[57] Other challenges facing the use of CNT-reinforced nanocomposites are homogeneous dispersion, degassing of the resin, and wettability.[238]

On the other hand, composites reinforced with continuous fibers can show improved mechanical properties compared to those reinforced with particles, whiskers, or short fibers because the reinforcing effect depends on aspect ratio. Fiber ends in discontinuous fiber reinforced composites cause stress concentrations and act as defects. In addition, matrix-to-fiber load transfer is also reduced in such composites.[56]

Continuous electrospun polymer NFs have been shown to significantly improve the mechanical properties of polymer resins.[56,60,218,239–243] Several polymers, including nylon, polyacrylonitrile (PAN), and polyimide (PI) have been utilized based on their desired mechanical properties useful for structural applications. Continuous nanofibers can provide an excellent reinforcing effect due to their high surface-area-to-volume ratio, high (infinite) aspect ratio, and compatibility with polymer matrices.[60] These characteristics enable effective stress transfer from the polymer matrix to the reinforcing NFs, which is the most important aspect of structural composites.[60,225,227] In addition, their size-dependent mechanical properties, which can be attributed to their high molecular orientation and low defect density, provide substantial improvements in several mechanical properties, including strength, modulus, failure strain, and toughness at ultrafine diameters.[60] Another intriguing property of nanoscale fibers is their optical transparency, which is caused by their ultrafine diameters being smaller than the

wavelength of visible light. This allows for the production of optically transparent nanofiber-reinforced composites.[60]

Table 5.1: Electrospun nylon nanofiber-reinforced composites.[60]

Nanofibers	Diameter (nm)	Matrix	Properties: value of matrix/value of composites; % absolute increased properties
Nylon-4,6	30–200	Epoxy	Transparent; Young's modulus: 2.5/91 MPa; fracture stress: 1.82/2.4 MPa
Gr-nylon-6 (Gr 0.01 wt%)	300–500	PMMA	Transparent; tensile strength: 56%; modulus: 113%; toughness: 250%
Nylon-6	200–400	PMMA	Transparent; bending strength: 12%; bending modulus: 30%; tensile strength: 20%; tensile modulus: 32%
Nylon-6	200–400	PMMA	Transparent; tensile strength and modulus: >20%
Nylon-6	134	PVA	Tensile failure stress: 34/740 MPa; tensile failure strain: 340%/490%
Nylon-6	100–600	BIS-GMA/TEGDMA	Flexural strength: 36%; elastic modulus: 26%; work of fracture: 42%
Nylon-6/silica nanocrystal	250	BIS-GMA/TEGDMA	Flexural strength: 23%; elastic modulus: 25%; work of fracture: 98%
Nylon-6,6	150	Epoxy	Mechanical energy absorbing capability: 23.2%; maximum stress: 6.5%
Nylon-6,6	75–250	Epoxy/carbon	Impact force: 900/2100 N; impact energy: 0.46/1.8 J; impact damage growth rate: 0.115/0.105 $mm^2\ N^{-1}$
Nylon-6,6	150–300	Carbon/epoxy	Fracture toughness: 156% (mode I) and 69% (mode II)
Nylon-6	(A) 150 (B) 230	Glass fiber/epoxy	(A) Stress: 550/581 MPa, shear modulus: 4.0/4.7 GPa (B) Stress: 550/611 MPa, shear modulus: 4.0/4.7 GP; G_{IC}: 1264/1447 J m^{-2}
Nylon-6,6	150	Glass/epoxy	Energy release rate G_I: 4.5%; G_{II}: 68%
Nylon-6	800	PCL	Young's modulus: 352/530 MPa; stress at break: 15.9/18.1 MPa; strain at break: 467%/601%
Nylon-6	800	PLA	Modulus: 2.4/6.6 GPa; stress at break: 48/46 MPa; strain at break: 3.6%/1.7%
Nylon-6	220	Melamine-formaldehyde	(A) Stress: 47.5/74.5 MPa; strain: 76.2%/2.85%; modulus: 0.37/2.88 GPa; toughness: 21.8/1.0 J g^{-1} (B) Stress: 47.5/77.9 MPa; strain: 76.2%/38.4%; modulus: 0.37/0.85 GPa; toughness: 21.8/17.6 J g^{-1}
Nylon-6	150–300	TPU	Transparent; stress: 42.27/82.98 MPa; strain: 672.9%/876.0%; modulus: 27.1/51.9 MPa; toughness: 108.47/274.83 J g^{-1}
Nylon-6,6	200–350	Polyethylene	Tensile strength: 27.74/32.56 MPa; elongation: 1184%/1341%; toughness: 249.36/315.07 MJ m^{-3}
Nylon-6,6	150	Gr-epoxy	Mechanical energy absorbing capability: 23.2%; G_{IC}: 5%
Nylon-6,6/GNPs	90–150	Aramid/epoxy	Elongation at break: 19.9%/34.48%; toughness: 68%
Nylon-6	200–400	PMMA	Transparent; tensile strength: 27.5/54.4 MPa; modulus: 0.61/1.12 GPa; toughness: 0.7/2.1 MJ m^{-3}
Nylon-6,6	300	Cyclic butylene terephthalate	Transparent; stress: 25/44 MPa
Nylon-6	100	Protein	Tensile strength: 0.024/0.136 MPa; elastic modulus: 1.57/1.8 GPa

The critical factors that determine the mechanical properties of NF-reinforced composite are the mechanical properties of the matrix and fibers, the diameters of the fibers, the aspect ratio of the fibers, the fiber volume fraction (VF), the alignment/configuration of the fibers within the matrix, and the interfacial interaction between the fibers and polymer matrix.[60] Because continuous electrospun polymer nanofibers have desirable properties with regard to all of these factors, they have great potential to serve as bulk reinforcement of polymer matrices. However, the mechanical properties and practical usage of nanofiber-reinforced polymers have been limited by several factors, including the relatively low mechanical properties of generic as-spun

NFs, the lack of ability to control the configuration of NFs within the matrix, and the sometimes-poor NF-matrix adhesion, among others.[56] Improving any or all of these characteristics could drastically improve the mechanical properties of the nanocomposites. The list of challenges to conquer also includes (1) understanding the influence of fiber aspect ratio and diameter on the effectiveness of the reinforcement; (2) how to fabricate electrospun NF-reinforced composites at a large scale and apply them to practical applications; (3) how to decrease the cost of composite fabrications; and (4) discerning the mechanism and developing theories of electrospun nanofibers effect on composites.[60] In addition, NF-reinforced nanocomposites suitable for use in high-temperature environments have not been sufficiently studied.

5.1.3 Aligned Nanofiber-Reinforced Composites

Although several groups have investigated NF-reinforced polymer resins, most nanocomposites have been reinforced with either random or partially oriented NF mats. Consequently, although results have been positive, mechanical improvements were limited due to low fiber volume fraction (VF). In order to further enhance properties, higher VF is required. It is trivial that continuous aligned fibers allow for the highest volume fraction, which is why they are used in traditional composite laminates. During manufacturing of laminates, fiber alignment is carefully controlled, which produces optimal VF and controlled anisotropy. To mimic these characteristics and increase the properties of NF-reinforced nanocomposites, high alignment of continuous nanofibers is essential.

In an attempt to further improve the structural properties of nanofiber-reinforced composites, a handful of researchers have incorporated aligned NFs into polymer

matrices.[60,220,244] Results of these studies showed that the addition of uniaxially aligned nanofibers to polymer matrices can significantly increase the mechanical properties in the longitudinal direction compared to those of random NF composites of neat resins. Thus, polyamide-6 matrix nanocomposites reinforced with aligned polyimide NFs (50wt% fiber content) exhibited ~700% and ~500% increases in longitudinal tensile strength and modulus, respectively, compared to neat PA-6 resin.[244] However, studies that involve the stacking of aligned nanofiber sheets with different orientations are virtually nonexistent. Much like traditional laminated composites, the load-carrying capabilities of nanocomposites should be balanced along several directions to increase their structural applications. Maintaining proper fiber alignment and volume fraction during mass fabrication of nanoreinforced plies remains a critical manufacturing challenge for continuous nanofiber reinforced composites.

With different modifications to the basic electrospinning process, a multitude of methods can be used to produce aligned continuous nanofibers.[245,246] However, many of these methods can only be used to create small batches of aligned nanofibers, in which the thickness and/or the deposition area of the NF mat are limited due to residual charge build-up and restricted collector geometries. Other methods, which can produce larger and thicker aligned mats, have not been able to consistently yield high orientation. This is largely due to the instability of the bending electrospinning jet and the physics of the electrospinning process in general.[48,247] Further investigation of the relationships between processing parameters and the degree of fiber alignment is needed to optimize NF orientation in thick mats that cover large areas.

After aligned NFs are collected, they must be transferred to a suitable substrate for resin infusion and curing. When doing this, their orientations can be adversely affected. For this reason, maintaining maximum fiber alignment, and thus volume fraction, during manufacturing and within the polymer matrix, especially for nanocomposites of larger sizes, requires further investigation. In addition, toughening and failure mechanisms of these nanolaminates must be thoroughly studied to understand the effectiveness of the reinforcement and how it can be improved.

5.1.4 Summary and Problem Formulation

Continuous electrospun nanofibers can exhibit highly desirable mechanical properties and, therefore, possess great potential to be used as primary reinforcement of polymer matrices. Although several polymer matrix nanofiber-reinforced nanocomposites have been manufactured and characterized, mechanical improvements have been limited by the lack of nanofiber orientation and low fiber volume fractions. To mimic the high volume fractions and controllable load-carrying capabilities of conventional composite laminates, improved nanofiber alignment is needed. This will enable the manufacturing of nanolaminated composites with significantly enhanced mechanical properties.

In this chapter, a systematic study of continuous nanofiber alignment during electrospinning onto a rotating cylinder is presented. Relationships between several electrospinning parameters and the degree of alignment, along with nanofiber diameters, are determined. The optimized process parameters are used to fabricate UD nanofiber sheets. Laminated nanocomposites are manufactured from carbon nanofibers in an epoxy matrix and from both PAN and PI nanofibers in a high-temperature cyanate ester matrix. Mechanical testing of these “nanolaminates” are used to compare their tensile properties

to those of the two neat resin materials. Lastly, high-speed video of the electrospinning jet is obtained to gain a better understanding of its mechanisms. Results of these studies can be used to optimize NF alignment, construct novel nanocomposites reinforced with continuous aligned NFs, and eventually develop a more accurate computational model of electrospinning process.

5.2 EXPERIMENTAL METHODS

5.2.1 Materials

The three primary subjects in this chapter are (1) the alignment investigation, (2) the CNF/epoxy nanocomposite investigation, and (3) the CE matrix nanocomposite investigation, and they will be referred to as such.

(1) For the alignment investigation, a polymer solution was created by mixing polyacrylonitrile (PAN, 150,000MW) from Pfaltz & Bauer and dimethylformamide (DMF) from Sigma Aldrich. The solution was mixed as a 10wt% PAN solution and stirred for at least 24 hours at 45°C to completely dissolve the PAN.

(2) For the CNF/epoxy nanocomposite investigation, the polymer solution used to electrospin nanofibers was made from PAN (150,000MW) from Pfaltz & Bauer and DMF from Sigma Aldrich. The matrix for the nanocomposites was an EPON 828 epoxy resin mixed with a Jeffamine D-400 catalyst at a weight ratio of 5:3, respectively. The mixture was stirred at 70 rpm at room temperature for 30 min before infusion.

(3) For the CE matrix nanocomposite investigation, the polymers used to electrospin nanofibers were made from PAN (150,000MW) from Sigma Aldrich and polyimide (PI) APS-C2 obtained from the University of Akron. Both polymers were dissolved in DMF from Sigma Aldrich and stirred at 40°C for at least 24 hours until the

polymer was completely dissolved. The PAN solution was 9wt% PAN and the PI solution was 10wt% PI. The polymer matrix for the nanocomposites was a cyanate ester resin (AroCy® L-10 from Huntsman Corporation) mixed with a catalyst of Co^{3+} acetylacetonate (AcAc) (100-200 ppm) and a co-catalyst of nonylphenol (1-2 PHR). The resin mixture was stirred at room temperature for 30 min before infusion.

5.2.2 Electrospinning

Electrospinning of all aligned nanofiber mats was performed using an E-SPIN Nanotech Super ES-2 Nanofiber Unit. Nanofibers were collected onto a grounded 8.25cm diameter aluminum cylinder, which was coated in aluminum foil and rotated during collection. The foil was covered with clear, heavy duty packing tape around its circumference except for a section in the center, which served as the substrate. To make it easier to remove the NFs from the substrate for nanocomposite manufacturing, this region was covered with MS-122AD PTFE release agent dry lubricant spray from Miller Stephenson and wiped away with a cotton rag after drying. Needles were fed through a 1.5” diameter aluminum disk electrode to stabilize the electric field between the needle and collector. The remaining parameters used for each investigation are listed in **Table 5.2**, **Table 5.3**, and **Table 5.4**.

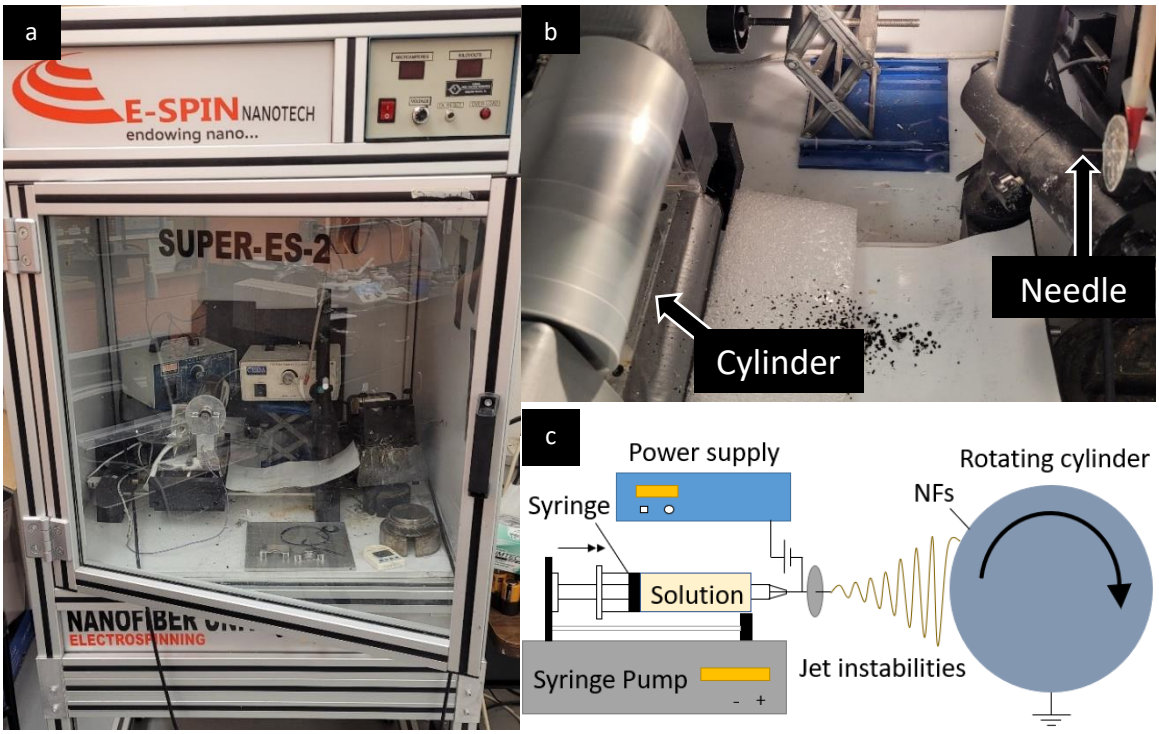

Figure 5.1: (a) E-SPIN nanofiber unit used to electrospin aligned nanofibers. (b) Experimental setup for electrospinning aligned NFs. (c) Schematic of electrospinning setup using a rotating cylinder collector.

Table 5.2: The electrospinning parameters used for the study on nanofiber alignment using the rotating cylinder method. *The flow rates were varied for the voltage study to produce continuous electrospinning.

Type of Parameter	Parameter	Our study
Process	Applied Voltage	varied
	Substrate speed (RPM)	varied
	Substrate width	varied
	Spin time	varied
	Collector type	Rotating cylinder
	Collector distance	18 cm
	Needle gauge	23 gauge (0.337 mm ID)
	Flow rate	0.340 mL/h *
Solution	Polymer type	Polyacrylonitrile (PAN)
	Polymer concentration	varied
	Solvent type	Dimethylformamide (DMF)
Environmental	Temperature	22.7 ± 1.2 °C
	Relative Humidity	34 ± 6 % RH

For all CNF mats except the ones used to reinforce the final unidirectional nanocomposite, the spin time was 2.75 hours, and the substrate surface speed was 19.4 m/s. In an attempt to increase the fiber VF of the unidirectional specimens, the spin time

was decreased to 1 hour, and the substrate speed was increased to 38.0 m/s. The other electrospinning parameters remained the same. With this change, the VF of the UD nanocomposites were increased from 10% to 22%, but both materials were tested for comparison.

Table 5.3: Electrospinning parameters used to fabricate aligned PAN NFs for the CNF/epoxy nanocomposites. *These mats were used to reinforce the UD-22%-Si nanocomposite.

Polymer, concentration (wt%), & solvent	Spin time (hours)	Needle gauge	Substrate surface speed (m/s)	Collector distance (cm)	Applied voltage (kV)	Flow rate (mL/h)	Temp (°C)	% Relative humidity
PAN 10% + DMF	2.75	23	19.4	18	9.0	0.340	22-24	40-50
PAN 10% + DMF*	1	23	38.0	18	9.0	0.340	22-24	40-50

Table 5.4: Electrospinning parameters used to fabricate aligned NFs for the CE matrix nanocomposites.

Polymer, concentration (wt%), & solvent	Spin time (hours)	Needle gauge	Substrate surface speed (m/s)	Collector distance (cm)	Applied voltage (kV)	Flow rate (mL/h)	Temp (°C)	% Relative humidity
PAN 9% + DMF	2.75	23	19.4	21	10.5	0.16-0.22	23-25	22-25
PI 10% + DMF	2.75	20	19.4	18	18.0	0.400	23-25	35-40

The alignment investigation was divided into five separate studies, based on five different electrospinning parameters: the substrate speed, spin time, substrate width, solution concentration, and applied voltage.

Substrate Speed Study

For the first study, the rotation speed of the cylinder was recorded in rotations per minute (RPM) using a Monarch PLT200 RPM sensor and incrementally increased from 0 to 8720 RPM (RPM values shown in **Table C.1**). The rotational speed slightly varied in

time, but the errors were less than 3% at each RPM. At each speed, the solution was electrospun for 1 minute onto an approximately 50mm wide substrate.

Spin Time Study

For the second study, the 10wt% PAN solution was electrospun onto the cylinder spinning at a rate of approximately 8800 RPM (the maximum) for several different spin times: 15, 30, 45, 60, 75, 90, and 105 minutes.

Substrate Width Study

For the next study, the same 10wt% PAN solution was electrospun onto the same cylinder, but the width of the section not covered with packaging tape was varied. This experiment was performed with the drum rotating at approximately 8800 RPM. The substrate widths tested were 4, 10, 20, 30, 40, 50, and 60 mm. Nanofibers were also collected with the drum rotating at 3300 RPM onto substrates with widths of 10, 30, and 50mm. Spin times with all substrate widths were 5 minutes.

Solution Concentration Study

The next study involved changing the concentrations of PAN in the solutions. While holding the substrate width at 50 mm and the rotational speed at 8800 RPM, solutions of 8wt%, 9wt%, 10wt%, 11wt%, and 12wt% PAN were electrospun for 5 minutes each.

Voltage Study

For the fifth and final study, the applied voltage was varied at 1.0 kV intervals from 7.0 to 12.0 kV. The spin time was held at 5 min, and all mats were electrospun onto a 50 mm wide substrate. The cylinder was rotated at 8800 RPM, and the solution concentration was 10wt% PAN. However, the flow rate in this study was slightly

changed to produce continuous electrospinning. The flow rates used at each voltage can be found in **Table C.4**.

5.2.3 Orientation and Diameter Analysis

After electrospinning, sections of all nanofiber mats on the aluminum foil substrate were carefully cut out with a scissors, sputter coated in gold using a Cressington 106 Auto Sputter Coater, and examined with an FEI Quanta 200 Environmental scanning electron microscope (SEM). Image analysis was performed on 16-bit SEM images using FIJI image analysis software. The directionality analysis tool, using Fourier components and 181 bins from the angles of 0 through 180 degrees (θ dimension in polar coordinates), was used to determine nanofiber orientation distributions. The measuring tool was used to determine fiber diameter distributions.

The degree of alignment was determined in two ways. The first used the standard deviation of the Gaussian curve that was fit to the directionality histograms, also called the "dispersion." Smaller standard deviation indicates higher degree of alignment. The second method took the directionality histogram data and used it to determine two different orientation parameters f_p and g_p, which were first defined by Gadu-Maria and Parsi[248] and used again by Liu and Dzenis[249] to quantify fiber orientation. The dispersion values were plotted in Excel and fit with different equation types to determine relationships between the parameters tested and the degree of nanofiber alignment, as well as average fiber diameter in some studies. The orientation parameters f_p and g_p, as shown in **Equation 5.1**, were plotted in MATLAB.

$$f_p = 2\langle cos^2\phi \rangle - 1$$
$$g_p = (8\langle cos^4\phi \rangle - 3)/5$$
such that
$$\langle cos^m\phi \rangle = \int_0^\pi cos^m\phi \Psi(\phi) d\phi\,, \quad m = 2,4$$
$$P(\phi_1 \leq \phi \leq \phi_2) = \int_{\phi_1}^{\phi_1} \Psi(\phi) d\phi$$

Equation 5.1 [248]

Here, ϕ is the orientation angle of the fiber, as defined in **Figure 5.2**. Both f_p and g_p values vary between zero and one, where perfect fiber alignment equates to a value of one, and a perfectly random orientation distribution equates to a value of zero.

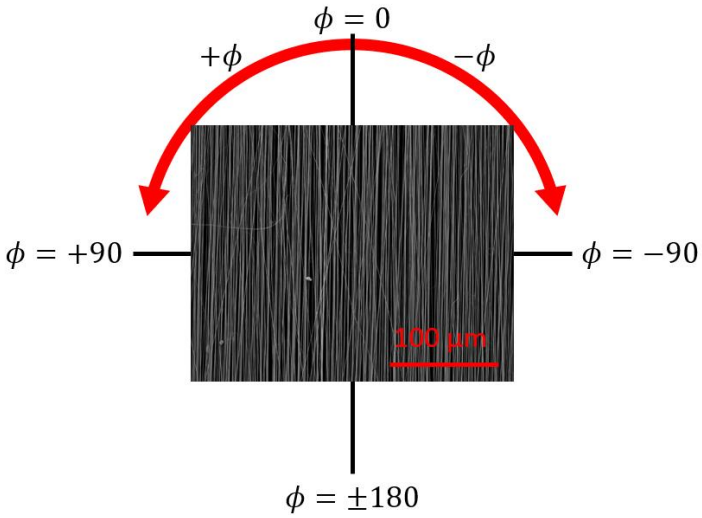

Figure 5.2: Definition of fiber orientation angle ϕ.

5.2.4 Nanocomposite Manufacturing

For a complete description of the nanocomposite manufacturing methods, see APPENDIX B.

5.2.5 Specimen Preparation and Testing

After the composites were cured, rectangular pieces were cut out using a razor blade and a hammer. Dogbone-shaped specimens were created using a Dremel tool to sand down the edges. Dogbone specimens were also made from the extra neat resin in the

cured film. The cross-sectional areas and other relevant dimensions of the dogbone specimens were measured with calipers.

All dogbone specimens were tested in uniaxial tension at 0.5 mm/min using a BOSE ElectroForce load frame, equipped with a 225N load cell. To measure axial strain values during the tests, two different methods were used. For the CNF/epoxy specimens, digital image correlation (DIC) was performed using an ARAMIS two-camera system, which required the specimens to be spray painted with a white and black speckle pattern. The average axial strain across the width of the specimen in the region where it failed was used.

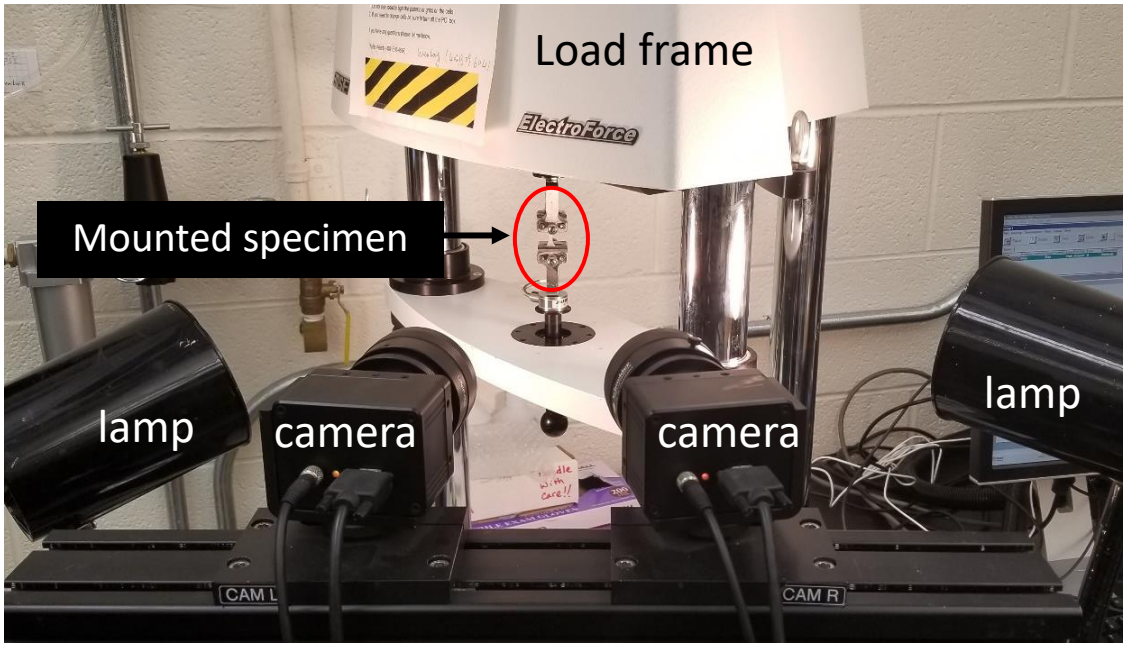

Figure 5.3: Experimental setup for tensile testing of CNF/epoxy nanolaminates with digital image correlation data collection.

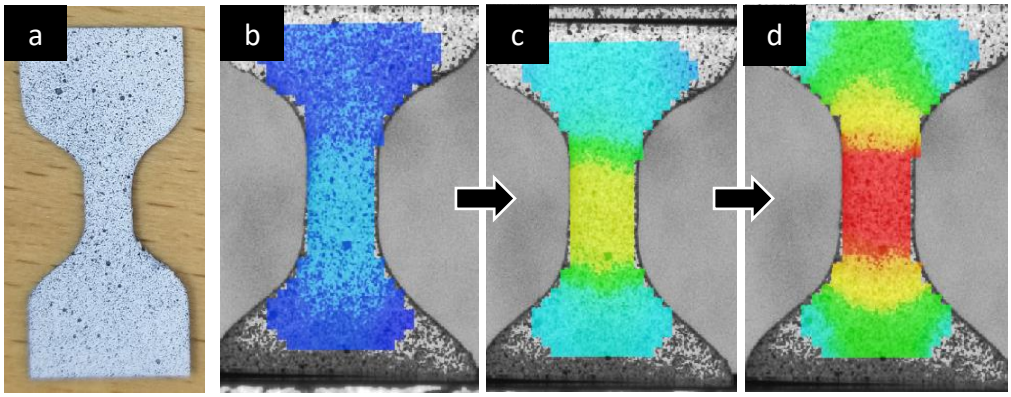

Figure 5.4: (a) CNF/epoxy nanolaminate speckled dogbone specimen. (b-d) Digital image correlation axial strain data throughout a tensile test of a CNF/epoxy nanolaminate.

For the CE matrix specimens, the quotient of the crosshead displacement and original distance between the grips was determined as the average strain. However, the cross-sectional area of the dogbone specimens varied along the gauge length (in the x direction). To account for this variable cross-sectional area $A(x)$, the width $w(x)$ of each specimen along the gauge length was estimated to determine a strain correction coefficient (SCC), which could be multiplied by the original strain values to obtain the maximum strain values, which occurred in the middle sections of the dogbone specimens where $w(x) = w_{min}$. To determine the SCC, the width of the dogbone specimens were approximated, as shown in **Figure 5.5**. Thus, since $\varepsilon = \frac{\delta}{L}$ and $\delta = \frac{P}{Et}\int_0^L \frac{dx}{w(x)}$, $\delta_{max} = \varepsilon_{max}L = \frac{PL}{Etw_{min}}$, where t is the specimen thickness. Therefore,

$$SCC = \frac{\delta_{max}}{\delta} = \frac{L/w_{min}}{\int_o^L \frac{dx}{w(x)}}$$

Equation 5.2

To find the denominator in **Equation 5.1**, the function $\frac{w(x)}{2}$ was determined, as shown in **Figure 5.5**.

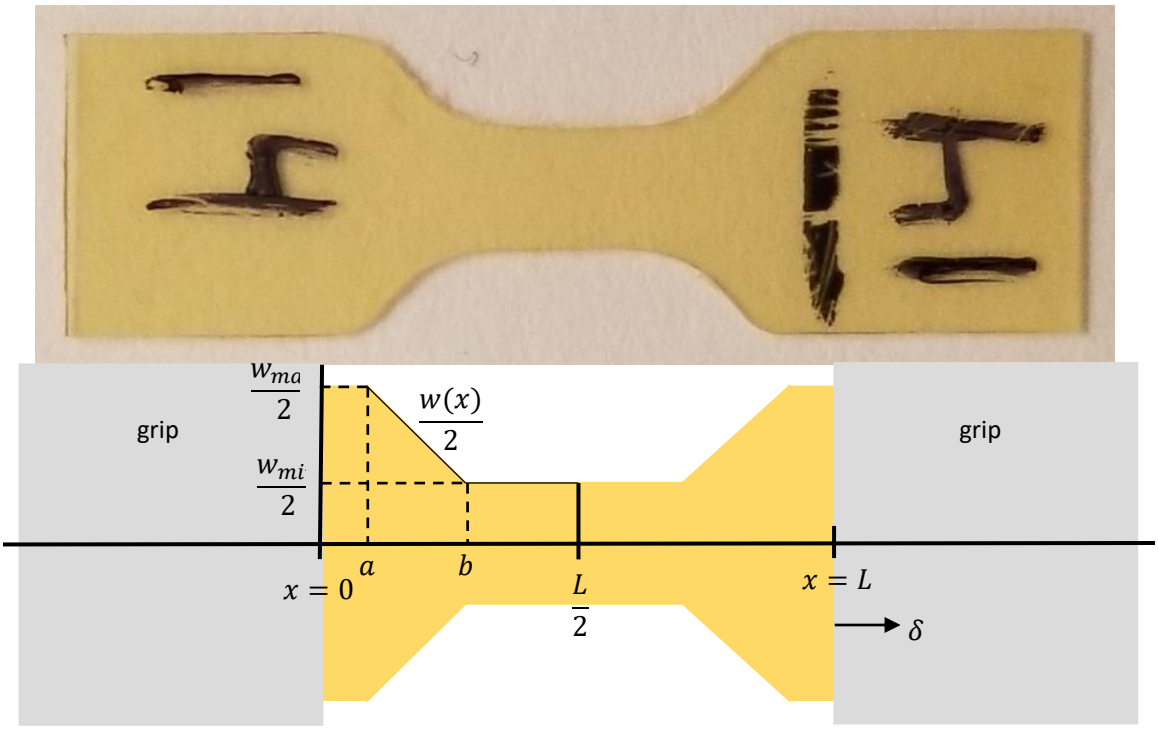

Figure 5.5: (top) Actual shape of a dogbone specimen and (bottom) the estimated shape, which was used to determine the approximate width of the specimen over the gauge length L.

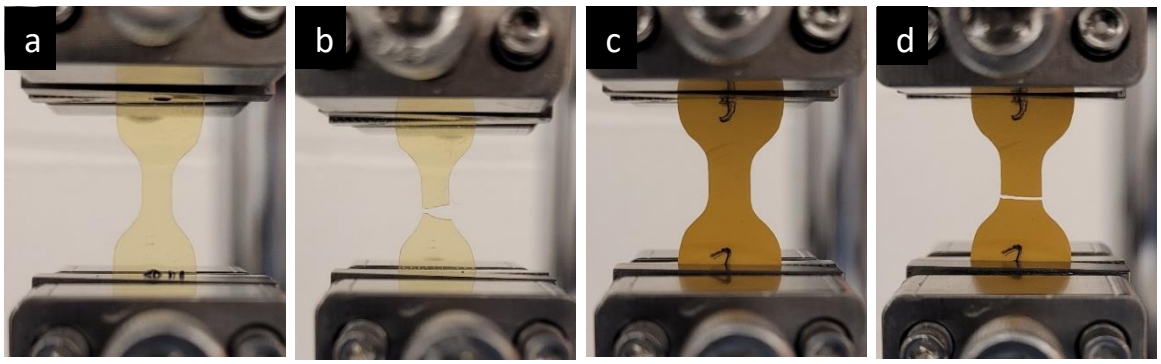

Figure 5.6: (a & b) Neat AroCy-L10 CE resin specimens before and after failure. (c & d) PAN-CP-6% nanolaminate specimen before and after failure.

Table 5.5: List of materials tested.

Material	NF material	Matrix	Spin time of 1 layer (h)	Layup	Volume fraction (%)	Abbreviation
Neat epoxy resin	-	EPON 828	-	-	-	EPON828 (neat resin)
CNF/epoxy	Carbonized PAN	EPON 828	2.75	$[0_4]$, carbonized without silicon wafers	10	UD-10%-noSi

CNF/epoxy	Carbonized PAN	EPON 828	2.75	$[0_2]$	10	UD-10%-Si
CNF/epoxy	Carbonized PAN	EPON 828	1	$[0_{12}]$	22	UD-22%-Si
CNF/epoxy	Carbonized PAN	EPON 828	2.75	$[0_2/90_2]_S$	19	CP-19%-Si
Neat CE resin	-	AroCy-L10	-	-	-	AroCy-L10 (neat resin)
PI NF/CE	PI	AroCy-L10	2.75	$[0_4/90_4]$	30	PI-CP-30%
PI NF/CE	PI	AroCy-L10	2.75	$[45_4/-45_4]$	30	PI-45-30%
PAN NF/CE	PAN	AroCy-L10	2.75	$[0_4/90_4]$	6	PAN-CP-6%
PAN NF/CE	PAN	AroCy-L10	2.75	$[0_4/90_4]$	12	PAN-CP-12%
PAN NF/CE	PAN	AroCy-L10	2.75	$[45_4/-45_4]$	20	PAN-45-20%

5.2.6 High-Speed Video Observation

To visualize polymer jet whipping instabilities, high-speed videos were obtained during electrospinning. The camera used was a Redlake MotionXtra HG-100K. The video was recorded with an exposure time of 997 μs at 1000 frames/second. The polymer jet was illuminated with a halogen quartz lamp. The experimental setup is shown in **Figure 5.7**. In addition, videos were obtained using the Super SloMo video function on a Samsung Galaxy S8+ cell phone, which is capable of capturing short high-speed videos at 480 frames/second.

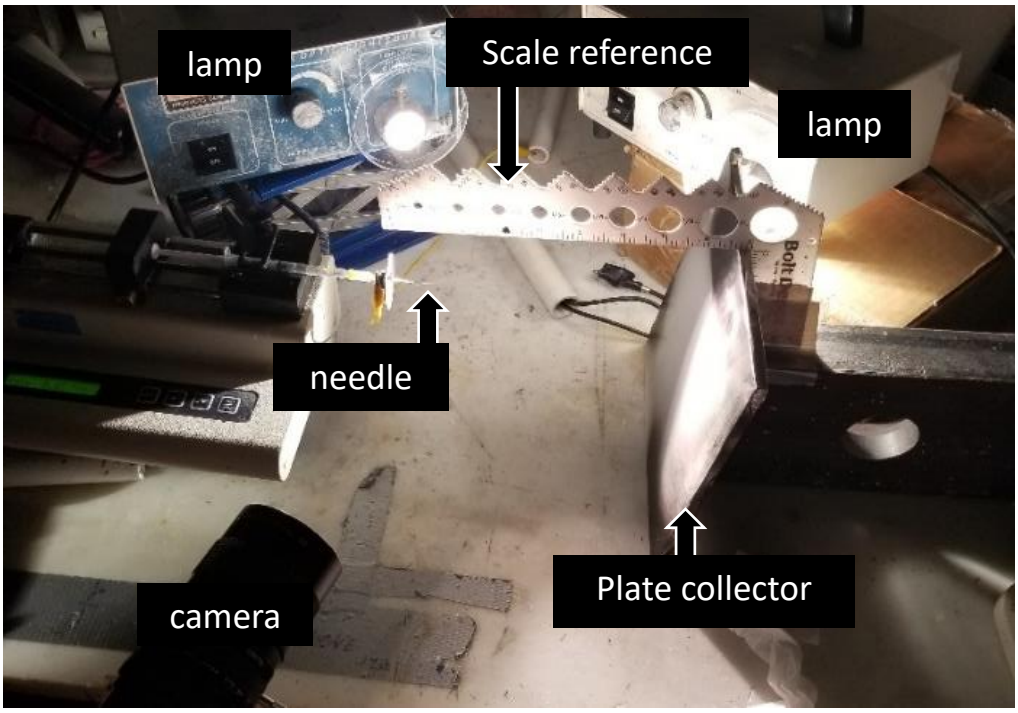

Figure 5.7: Experimental setup for capturing high-speed video of the electrospinning process.

5.3 RESULTS OF THE NANOFIBER ALIGNMENT INVESTIGATION

Although there are several methods that can be used to obtain continuous aligned nanofibers, electrospinning onto a rotating collector (e.g. mandrel, cylinder, wire drum, cone, frame, etc.) is the only one that can potentially be used for mass production of aligned nanofiber sheets.[50,246,250,251] It has been shown that the fiber alignment increases with increasing collector surface speed, but some studies have determined that there is a threshold at which the degree of alignment begins to decrease due to fiber fracture and turbulent air flow around the collector.[246,252–255] There is also a minimum threshold speed, which can vary from system to system, at which the onset of fiber alignment occurs.[256] Other researchers have reported that orientation is optimized when the linear velocity of the rotating surface matches that of the depositing jet.[50,257,258]

In addition to fiber alignment, rotational speed can also have a significant impact on fiber diameter. Reductions in diameters between 15 and 40% compared to those

obtained from conventional electrospinning have been achieved with collector speeds ranging from 5-15 m/s.[252] Rotating collectors can also be used to fabricate crossed fiber arrays by spinning in multiple directions on the same substrate.[259,260] However, the rotating collector method has its limitations. Brittle materials are more likely than flexible or elastic materials to break at lower speeds. The method is also relatively time- and energy-intensive and needs manipulation. Also, the obtained orientation has generally been poor up to know, and it decreases with increased spin time and mat thickness, but the reasons are not fully understood.[246] Nonetheless, the simplicity of the rotating collector method, along with its critical ability to produce aligned mats over large areas,[245] give it potential for nanocomposite applications. Still, more research is needed to understand the mechanisms of NF orientation (or lack thereof) to maximize fiber alignment, which could lead to the development of next-generation nanolaminates with outstanding properties.

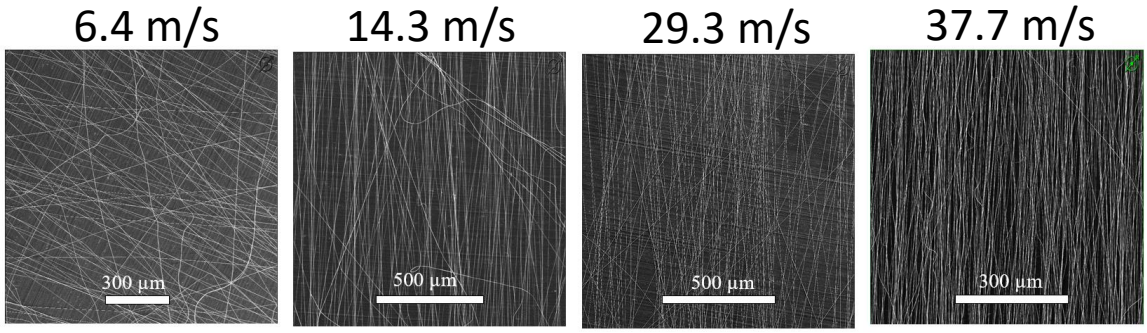

Figure 5.8: SEM images of NF mats spun with different substrate speeds.

Based on initial qualitative comparison of SEM images of the aligned mats, it was clear that fiber orientation increased with substrate speed (see **Figure 5.8**). To obtain a quantitative comparison, though, image analysis was required. Directionality histograms with bin widths of only 1 degree, like those shown in **Figure 5.9**, along with standard deviations of their fitted Gaussian curves, which will be called “dispersion” values, were

obtained. After the orientation parameters f_p and g_p were determined from the histogram data, they, in addition to the dispersion values, were plotted.

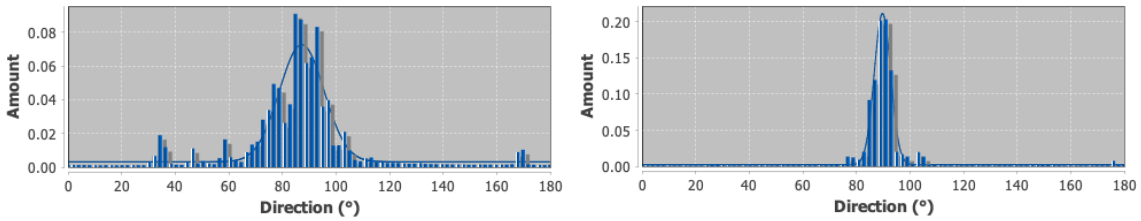

Figure 5.9: Directionality histograms obtained with Fiji and used to determine the dispersion values: (left) 6.4 m/s and (right) 37.7 m/s.

The directionality histograms show narrower Gaussian curve peaks as the substrate speed increases. This relationship corresponds to decreased dispersion values with increased surface speeds. Also, the orientation parameters both increase towards values of 1 as the substrate speed increases (see **Figure 5.10** and **Table C.1**). However, even at the maximum speed of 37.7 m/s, fiber alignment is not perfect. Nonetheless, comparing the degree of alignment of the electrospun NF mats to that of a carbon fiber preform (see **Figure 5.11**), the nanofiber mats collected onto substrates traveling over 20 m/s exhibited higher orientation with respect to the orientation parameters, even though their dispersion values were slightly higher. This is a particularly encouraging result.

Another noteworthy result is that, in our study, the degree of fiber alignment never decreased, even at high substrate speeds. This differs from the findings of other studies, in which fiber alignment decreased at higher speeds due to fiber fracture and turbulent air flow around the cylinder.[252] Although the slopes of the f_p and g_p curves begin to shrink at substrate speeds above around 15 m/s, they remain relatively linear up to the maximum speed of 37.7 m/s.

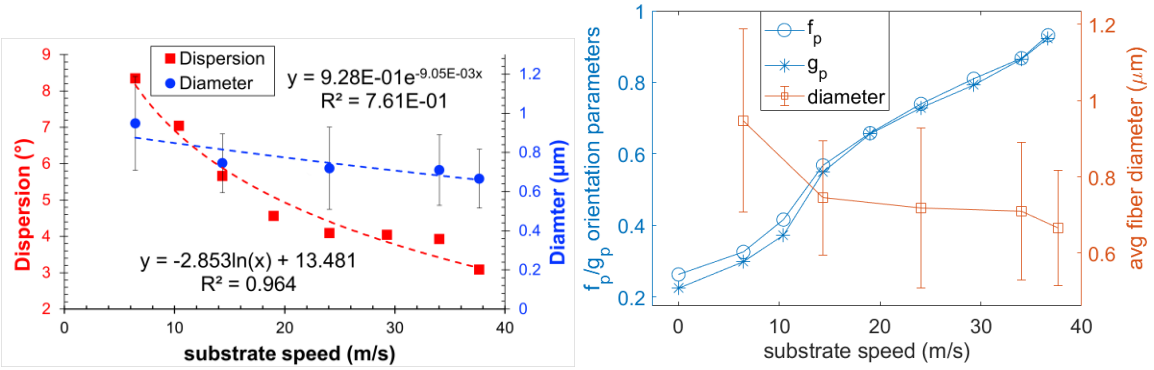

Figure 5.10: Results of the substrate speed study.

As expected, average fiber diameters are shown to decrease as rotational speeds increase. This is due to the mechanical drawing forces the drum imparts on the electrospun fibers.[246,252] Since electrospun NFs are known to exhibit improved mechanical properties at smaller diameters,[56,261,262] being able to obtain thinner and more aligned fibers simultaneously is one of the primary advantages of the rotating collector method.

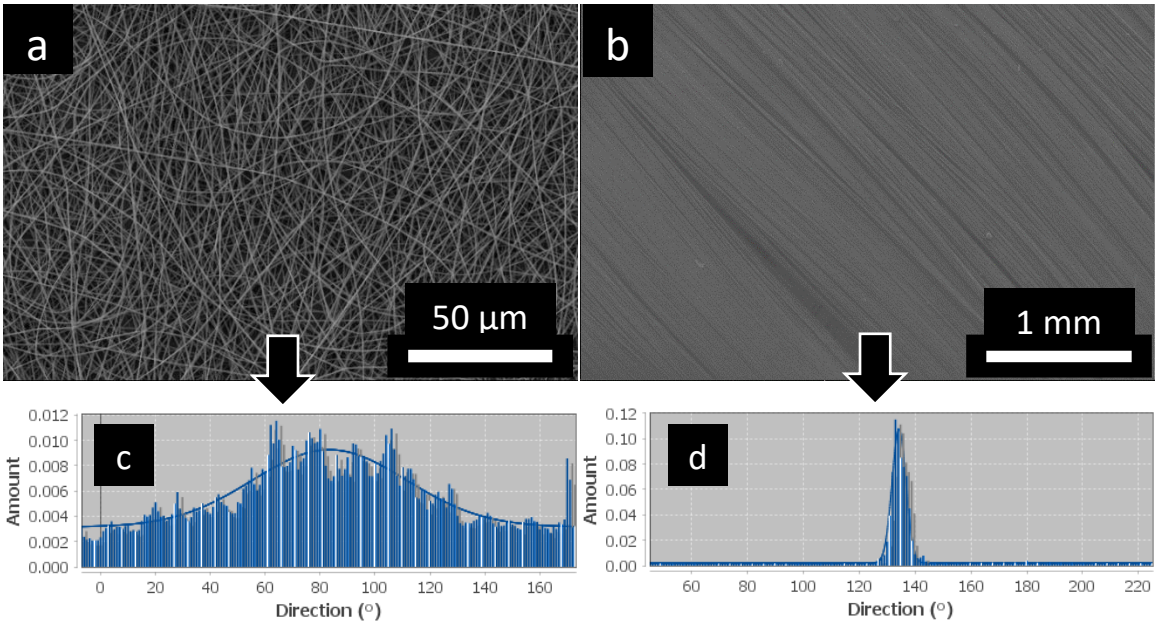

Figure 5.11: (a) A "random" PAN nanofiber mat electrospun onto a stationary collector. (b) SEM image of a unidirectional carbon fiber preform manufactured by Sigmatex. Directionality histograms corresponding to the SEM images of the (c) PAN NF mat and the (d) CF preform. The dispersion values obtained from (c) and (d) are 28.06° and 2.52°, respectively. The f_p and g_p values for the PAN NF mat are 0.2628 and 0.2241, respectively. The f_p and g_p values for the CF mat are 0.6764 and 0.6725, respectively.

The plots of the dispersion values from all parametric studies include equations that relate the electrospinning parameter studied to both the dispersion values and the average fiber diameters. These equations are meant to provide quantitative relationships based on basic logical analysis of the physics of the electrospinning process, but by no means should be accepted as governing laws. This was not one of the primary objectives of this work, mainly because the exact dependencies of fiber orientation and diameter on processing parameters can vary drastically from system to system. A comprehensive review of electrospinning parameters and their effect on fiber morphology can be found in [49].

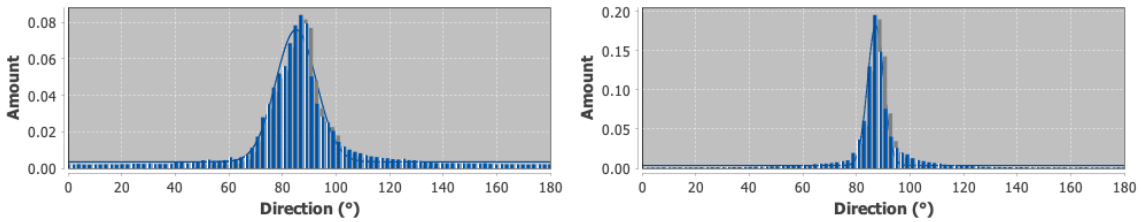

Figure 5.12: Directionality histograms obtained from NF mats spun for (left) 60 min and (right) 30 min.

Another critical property of electrospinning is spin time. For nanocomposites, thicker aligned mats are needed to make it easier to increase the fiber VF. However, as previously mentioned, most methods for developing orientation in NF mats are limited by the amount of NFs that can be collected before orientation decreases substantially. Although the reasons for this are not fully understood, one possible explanation is the buildup of residual charge from the collected fibers, which alters the electric field and causes alignment to get worse over time.[249,263] The collected fibers, although very small, may also induce more turbulent air flow around the rotating collector, which can also inhibit fiber alignment.[252] This relationship is quantified in **Figure 5.13**, in which both the dispersion values and the orientation parameters appear to depend linearly on the spin

time. One meaningful thing to notice is that relatively high alignment was maintained at a substrate speed of 37.7 m/s for spin times all the way up to 2 hours.

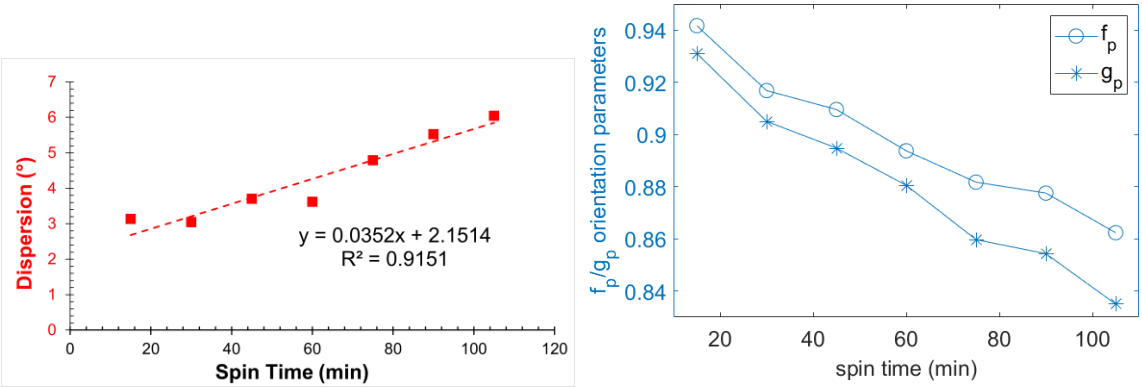

Figure 5.13: Results of the spin time study.

Although highly aligned NFs have been fabricated by collecting onto rotating disks,[251,264] this significantly limits the size of the obtained mats (substrate widths were 1 cm or less). For nanocomposite applications, aligned nanofiber sheets must be much wider. By spinning onto a rotating drum, the widths of the aligned mats are only limited by the length of the drum and the deposition area of the electrospinning jet, although some apparatuses allow for shifting of the drum so NFs can be deposited onto the entire surface. The results of the substrate width study, as shown in **Figure 5.14**, indicate an inverse relationship between substrate width and the degree of alignment. In addition, both the dispersion values and orientation parameters depend linearly on substrate width. However, even on a substrate as wide as 60 mm, relatively high alignment was retained at a drum speed of 8800 RPM.

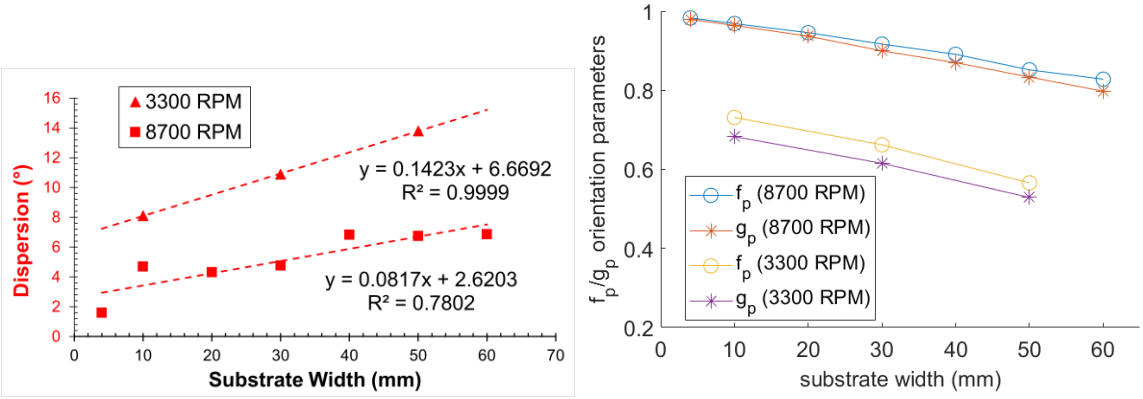

Figure 5.14: Results of the substrate width study.

It is well known that there exists a threshold voltage above which the electrostatic charges in the polymer solution can overcome surface tension and begin the electrospinning process.[49,245] This critical value depends highly on the type and concentration of the polymer. Beyond the critical value, the applied voltage can have varying effects on fiber diameters. Reneker and Chun concluded that applied voltage has little effect on fiber diameter.[265] In contrast, Yuan et al. found that diameters decreased with increasing voltage due to the increased electrostatic repulsive forces in the charged jet, which favored the thinning of fibers.[266] On the other hand, fiber diameters have been shown to increase with applied voltage due to longer jet length.[267,268] It is clear that the relationship between the applied voltage and fiber diameters depends on other factors, such as the polymer solution concentration and the distance between the tip and the collector.[269] However, one consensus that is more widely accepted is that increasing voltages can cause the formation of beads or beaded fibers due to decreased Taylor cone size and increased jet velocity.[49,270–272]

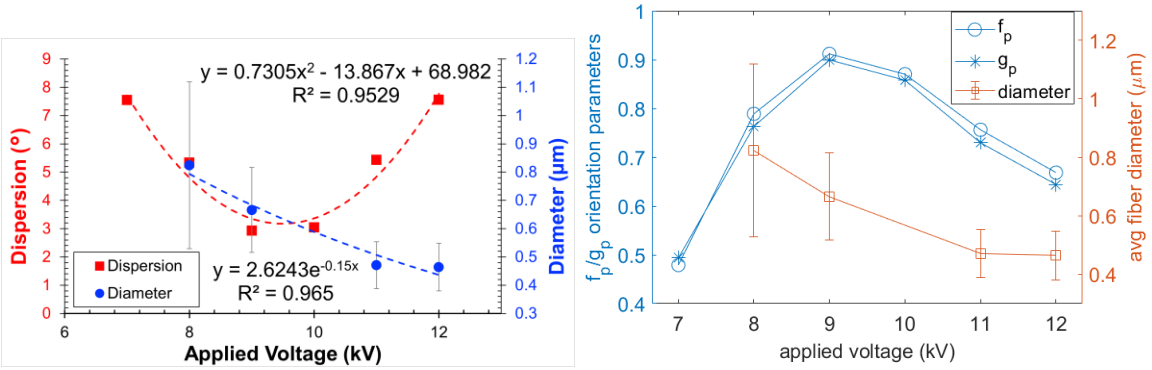

Figure 5.15: Results of the voltage study.

In this study, diameters are shown to decrease almost linearly with increasing applied voltage (see **Figure 5.15**). The relationship between applied voltage and dispersion values, on the other hand, is relatively quadratic. The plot of the orientation parameters shows a similar relationship, in which orientation is maximized around 9-10 kV and decreases above and below those values.

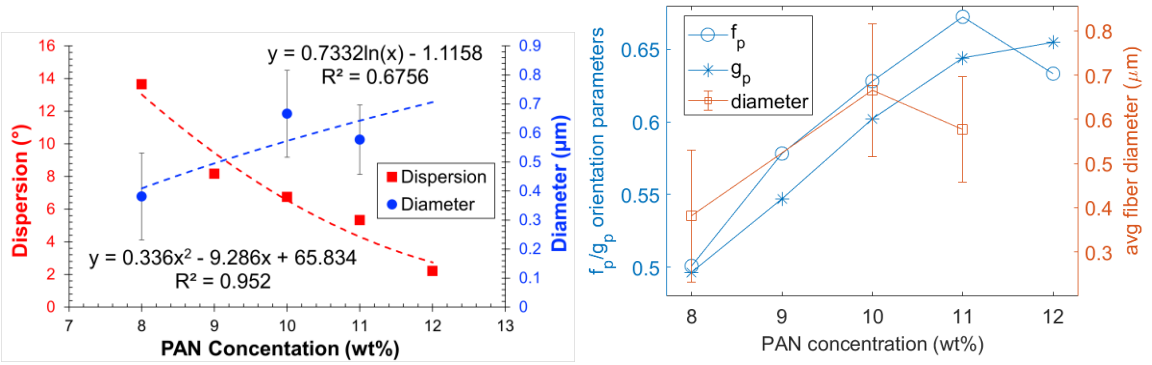

Figure 5.16: Results of the polymer concentration study.

The final parameter studied was the polymer solution concentration. The polymer concentration has a direct effect on the viscosity and charge density of the solution, which can indirectly affect the nanofiber morphology. If the concentration is too low, the electric field and higher surface tension can cause the entangled polymer chains to break before reaching the collector.[49] This can result in electrospraying instead of electrospinning.[273] Increasing the concentration will eventually allow for electrospinning

of smooth, uniform nanofibers. However, as the concentration is increased further, fiber diameters will increase.[49,273] If the concentration becomes too high, beading and/or ribbon-shaped microfibers can be produced.[49,274] In our study, no beading or ribbon-like morphologies were observed, likely because the range of concentrations tested was relatively narrow. However, fiber diameters did tend to increase with increasing polymer solution concentration. With respect to alignment, the higher PAN concentrations caused it to increase in general. This is evidenced from the decrease in dispersion values and increase in orientation parameters (other than f_p from 11 to 12wt%). However, it is theorized that increasing PAN concentrations further would eventually cause the degree of alignment to decrease.

5.4 ANALYSIS OF THE CNF/EPOXY NANOCOMPOSITE FABRICATION AND MECHANICAL CHARACTERIZATION

Using some of the knowledge obtained from the alignment investigation, laminated nanocomposites reinforced with stacks of aligned nanofiber mats could be manufactured. The first nanolaminate was made from carbon nanofibers (CNFs) in an epoxy matrix. The CNFs were produced from as-spun PAN precursor fibers. Once the aligned PAN nanofibers were collected onto a rotating cylinder, they needed to be stabilized and carbonized, which can have a significant effect on fiber diameter and morphology.[275] **Figure 5.17** shows how the diameters and alignment of the electrospun NFs change during stabilization and carbonization. The NFs become wrinkled due to shrinkage, which also decreases the degree of alignment. This was reinforced quantitatively by determining the dispersion values and orientation parameters of the three different fiber mats. Although the dispersion value of the carbonized mat is the

lowest, the orientation parameter values steadily decrease as the fiber mat undergoes the post-processing treatments.

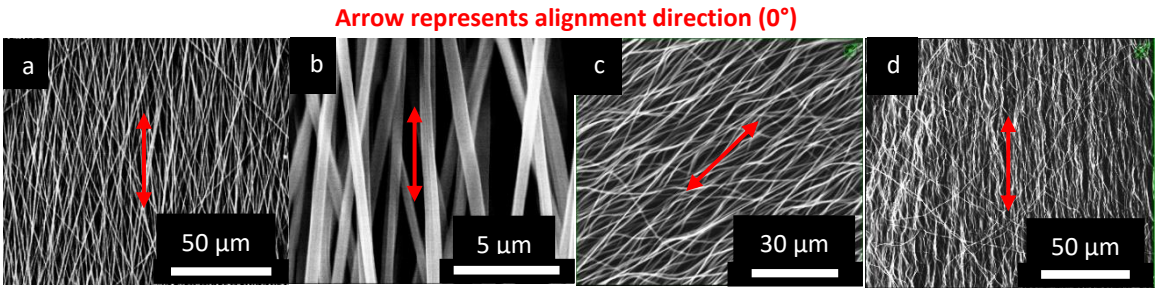

Figure 5.17: SEM micrographs of aligned (a & b) as-spun, (c) oxidized, and (d) carbonized PAN NFs. The average diameter of the as-spun PAN nanofibers was 627 ± 165 nm. The average diameter of the stabilized fibers was 517 ± 90 nm. The average diameter of the carbonized fibers was 355 ± 87 nm.

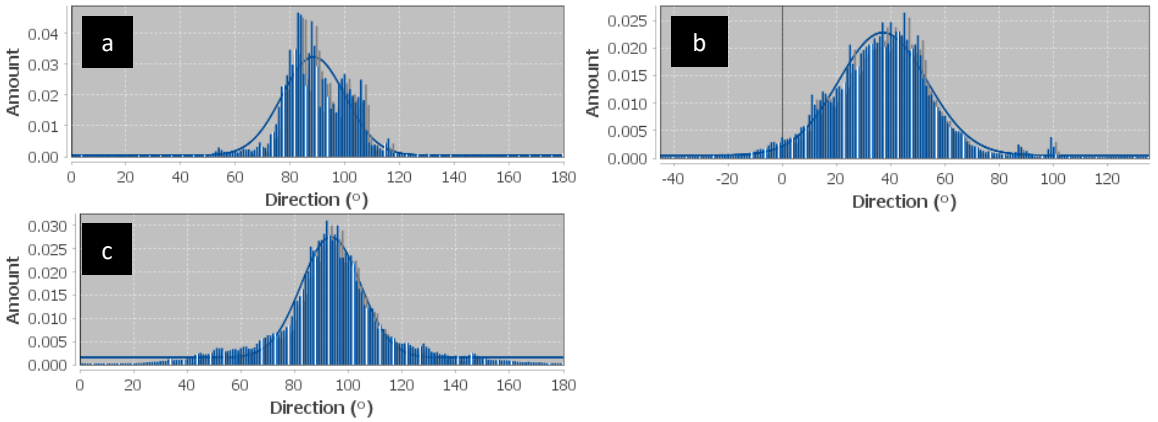

Figure 5.18: Directionality histograms obtained using FIJI for the (a) as-spun, (b) stabilized, and (c) carbonized PAN nanofiber mats. The respective standard deviations of the fitted Gaussian curves for these three mats were ±11.52°, ±16.27°, and ±11.07°. The orientation parameters f_p and g_p for the as-spun mat were 0.805 and 0.763, respectively. The orientation parameters f_p and g_p for the stabilized mat were 0.780 and 0.716, respectively. The orientation parameters f_p and g_p for the carbonized mat were 0.737 and 0.677, respectively.

Once the CNF layups were impregnated with epoxy resin and cured, they, along with neat resin specimens, were tested in tension. Results of the neat resin and CP-19%-Si tests are shown in **Figure 5.19**. It is clear that the CP specimens exhibited significantly higher strengths and moduli compared to the neat resin specimens, although they also exhibited much lower failure strains.

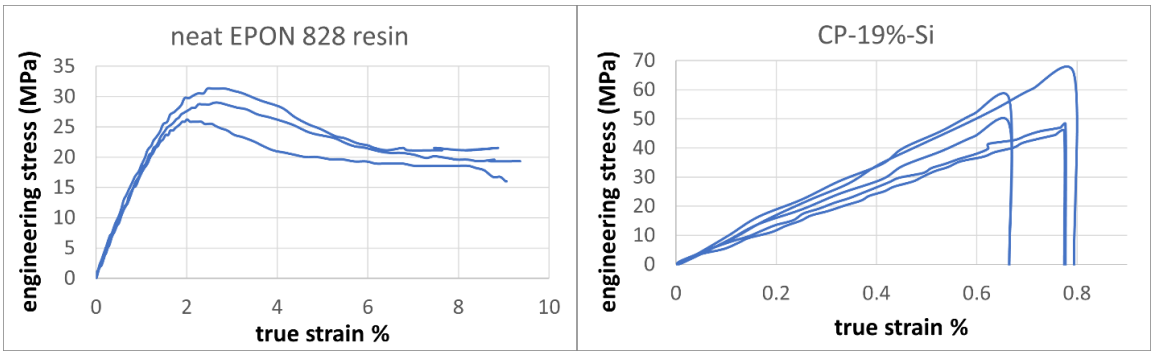

Figure 5.19: Stress-strain curves for the neat epoxy resin and the CP-19%-Si specimens.

The results of the tests on the unidirectional nanocomposite specimens are shown in **Figure 5.20**. Based on these stress-strain curves, the UD-10%-noSi specimens performed best overall, although the UD-10%-Si specimens exhibited the highest moduli. The reason for this is that when the mats were carbonized without being sandwiched between two silicon wafers, they were allowed to shrink and wrinkle more than when they were restricted between the silicon wafers. Thus, when the nanocomposites were loaded in tension, the fibers became somewhat unwrinkled and the UD-10%-noSi specimens were allowed to deform more before the NFs fractured. Although the shrinkage and wrinkling of the nanofibers was thought to be detrimental to mechanical properties, they led to increased material toughness at the expense of material stiffness in this case. However, it would be interesting to note their effects on material properties in the transverse direction.

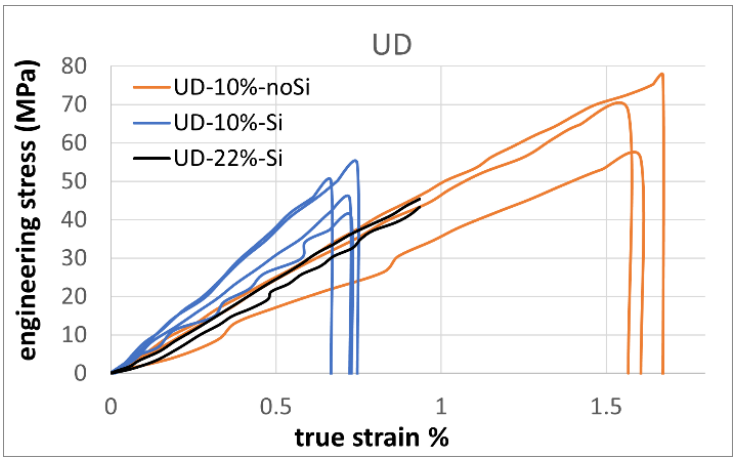

Figure 5.20: Stress-strain curves for the unidirectional CNF/epoxy specimens.

Another surprising result is that for the UD composites made from mats carbonized between two silicon wafers, even when the fiber VF was increased from 10% to 22%, mechanical properties (except failure strain) decreased. The reason for this could be that many of the CNFs were already fractured before curing. Since the substrate speed was increased from 19.4 to 38.0 m/s, the mechanical drawing force from the rotating cylinder may have caused the fibers to fracture prematurely, which has been observed before.[252] If this happened consistently, the number of broken NFs in the aligned mat could be substantial. This would lead to a decrease in tensile strength and modulus and an increase in failure strain of the nanocomposite, which is what was observed.

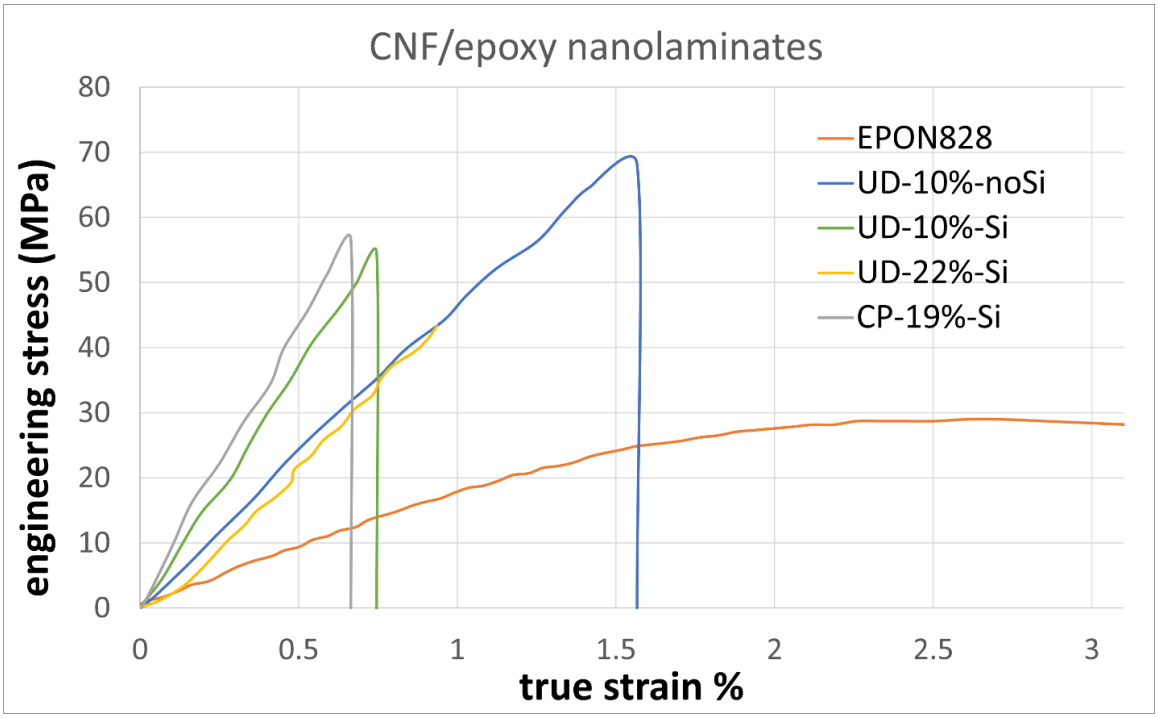

Figure 5.21: Representative stress-strain curves for the neat epoxy resin and CNF/epoxy nanocomposites.

Figure 5.21 shows representative stress-strain curves for the neat epoxy resin and CNF/epoxy nanocomposites. The addition of any volume of CNFs to the epoxy resin substantially increased the strength and modulus of the material. The CP-19%-Si specimens exhibited the highest moduli, even though half of their fibers were aligned orthogonally (90° plies) to the loading direction. Since the other half, which equates to 9.5% of the total composite volume, were oriented longitudinally, strength and modulus values should have been similar to those of the UD-10%-Si specimens. However, they were slightly higher, which means that even the 90° plies contributed somewhat to the 0° tensile strength and stiffness.

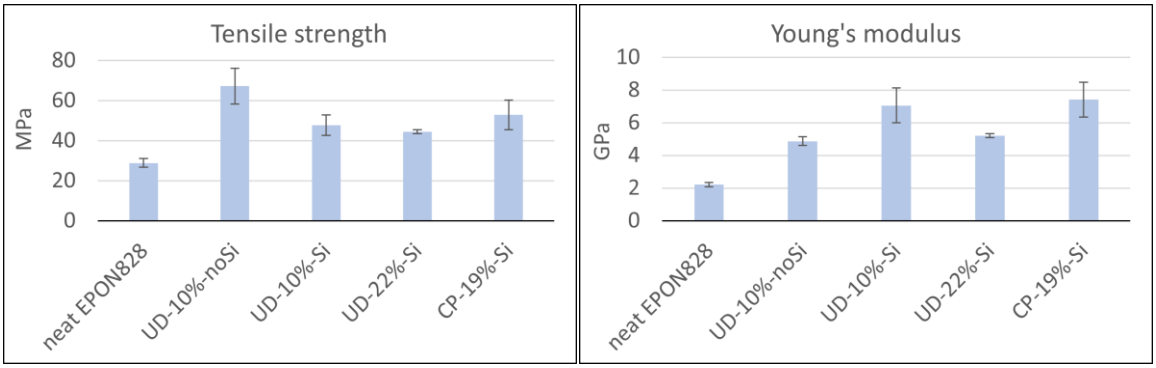

Figure 5.22: Tensile strength and modulus results for the neat epoxy resin and CNF/epoxy nanocomposites.

The mechanical results of the CNF/epoxy nanolaminate investigation are shown in **Figure 5.22** and **Figure 5.23**. Perhaps the most exciting result is the considerable increase in toughness exhibited by the UD-10%-noSi specimens. In this case, the toughness is defined as the area under the curve, which can also be considered the energy needed for failure.

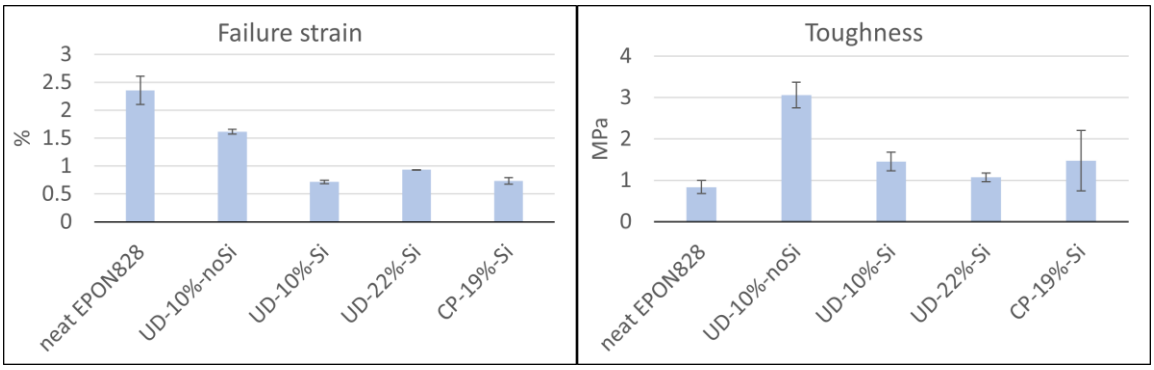

Figure 5.23: Failure strain and toughness results for the neat epoxy resin and CNF/epoxy nanocomposites.

5.4.1 Discussion

Arguably the most common technique for evaluating the failure mechanisms of materials is to investigate the fracture surfaces. This was done on all failed specimens using an SEM. On the neat epoxy resin specimens, hackle patterns characteristic of brittle resin failure are dominant (see **Figure 5.24**). However, in comparison to the CNF/epoxy nanocomposites, the EPON828 resin did not fail in a brittle manner. Based on the stress-

strain curves, the epoxy resin actually yielded before failing, although the yield and failure strengths were much lower than the failure strengths of the nanocomposites.

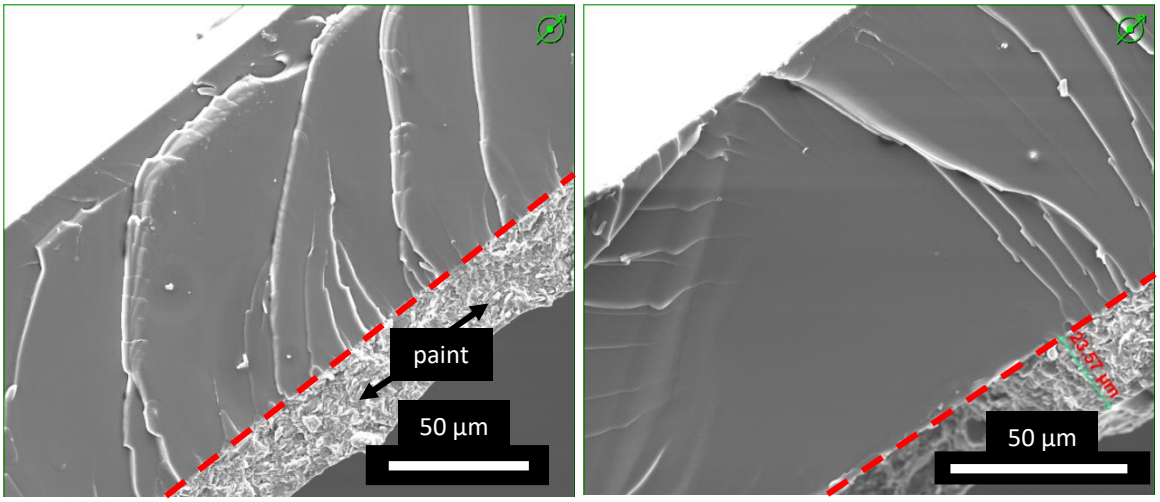

Figure 5.24: Fracture surface of a neat EPON828 specimen. The dashed line separates the epoxy and the layer of spray paint that was applied for DIC.

The fracture surface of a UD-10%-noSi specimen shows an even distribution of the NFs through the thickness of the specimen (see **Figure 5.25**). Also, the resin seems to have fully impregnated the NF mat, and little fiber pullout is evident, although there are some small voids where NFs have pulled out from the matrix. This indicates adequate NF-matrix adhesion.

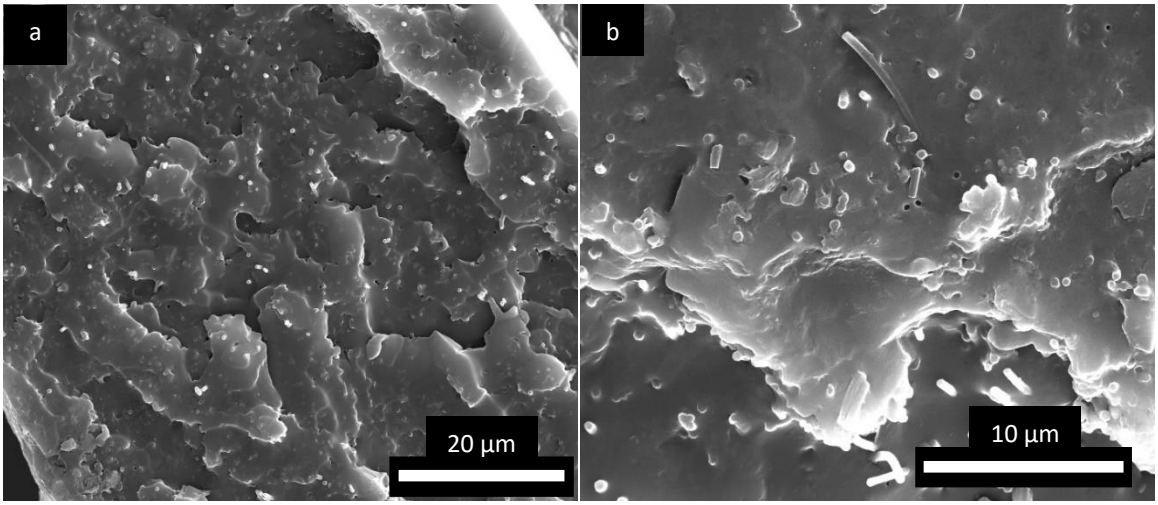

Figure 5.25: Fracture surface of a UD-10%-noSi specimen.

On the other hand, the fracture surface of a UD-10%-Si specimen portray two clearly distinguishable UD plies, which do not make up a large portion of the total specimen thickness. There are large regions of unreinforced resin. In addition, some microvoids are present, which is a sign of incomplete resin impregnation, which occurred due to the tighter packing of the CNF preforms carbonized between the silicon wafers compared to that of the CNFs left uncovered during carbonization.

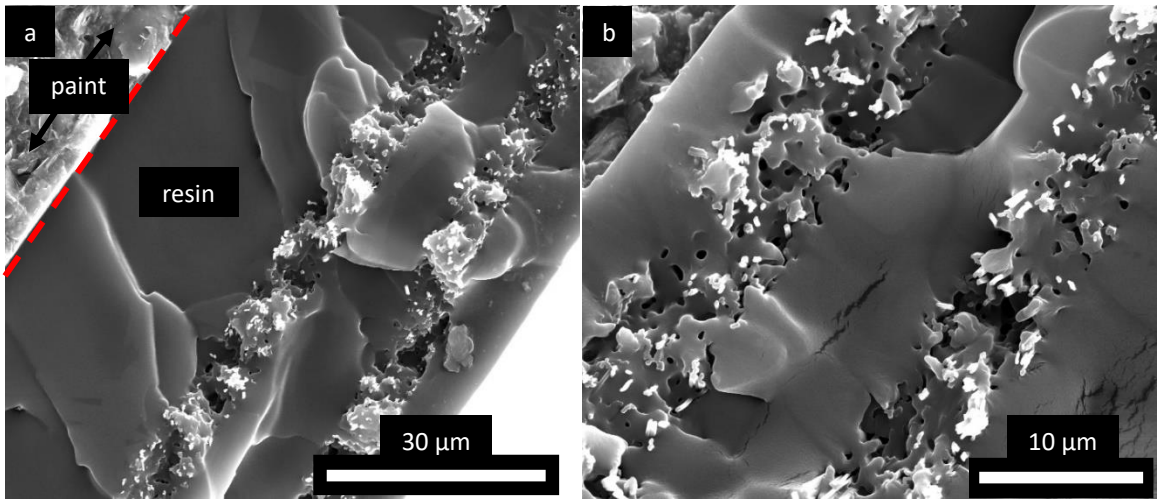

Figure 5.26: Fracture surface of a UD-10%-Si specimen.

Figure 5.27 shows the fracture surface of a UD-22%-Si specimen. In this specimen, the UD plies make up a large portion of the specimen thickness, but there are still some small voids present. The aligned NFs are fairly evenly distributed throughout the specimen, but tensile strength and modulus were still lower than those of the UD-10%-Si specimens. Thus, the previous hypothesis that many fibers were already fractured before testing seems to be even more plausible.

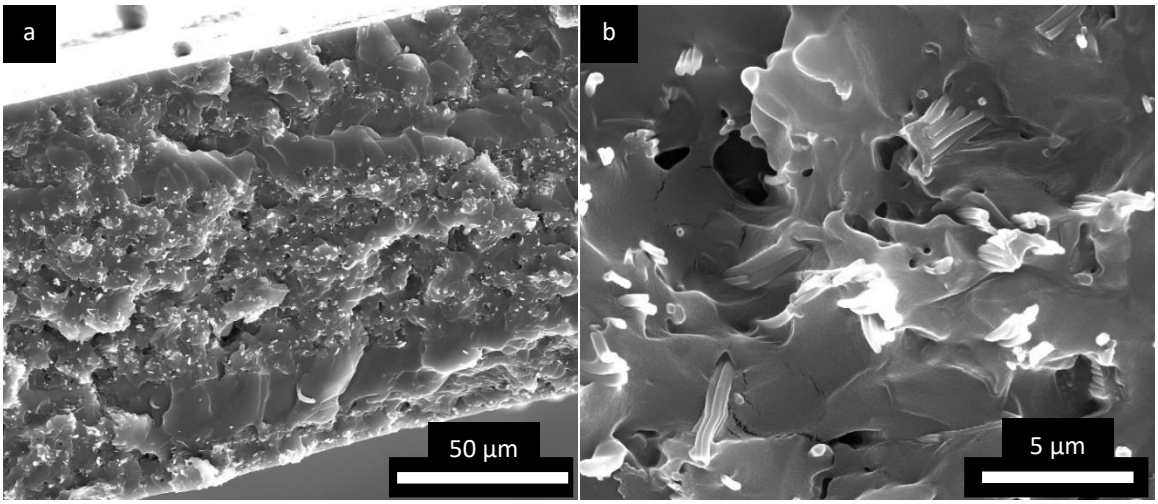

Figure 5.27: Fracture surface of a UD-22%-Si specimen.

On the fracture surface of a cross-ply nanolaminate, shown in **Figure 5.28**, the 0° layers and the 90° layers are clearly distinguishable, as well as the interface between them. There are also some regions where no NFs are present. At higher magnifications, the failure mechanisms of both ply types can be investigated. In the 0° ply region, NF failure is the dominant failure mode, while some NF pullout was present (see **Figure 5.29**). However, there is also a substantial amount of unreinforced resin surrounding the 0° ply. Therefore, there is room for significant improvement in volume fraction.

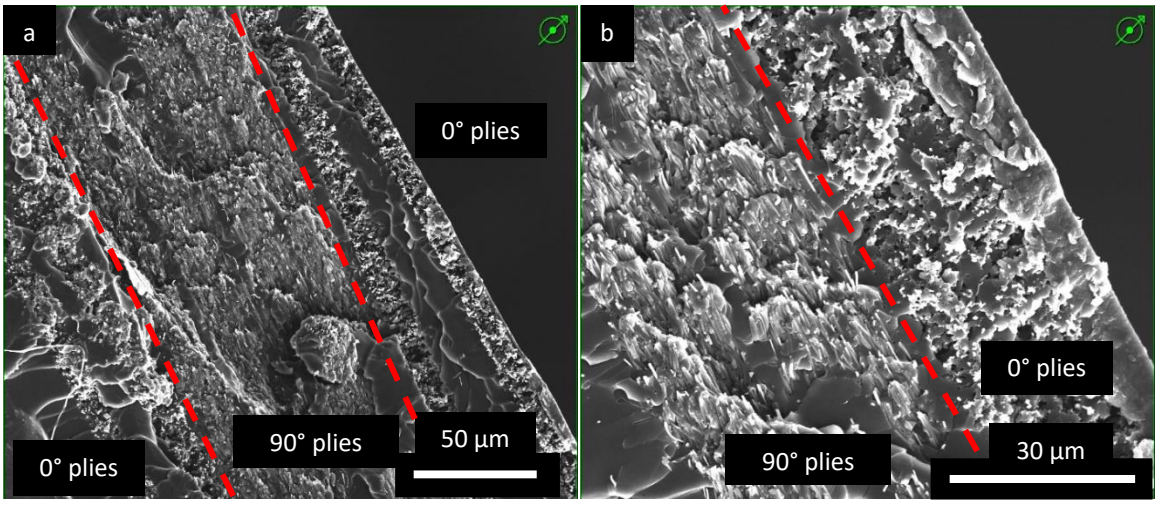

Figure 5.28: Fracture surface of a CP-19%-Si nanolaminate specimen.

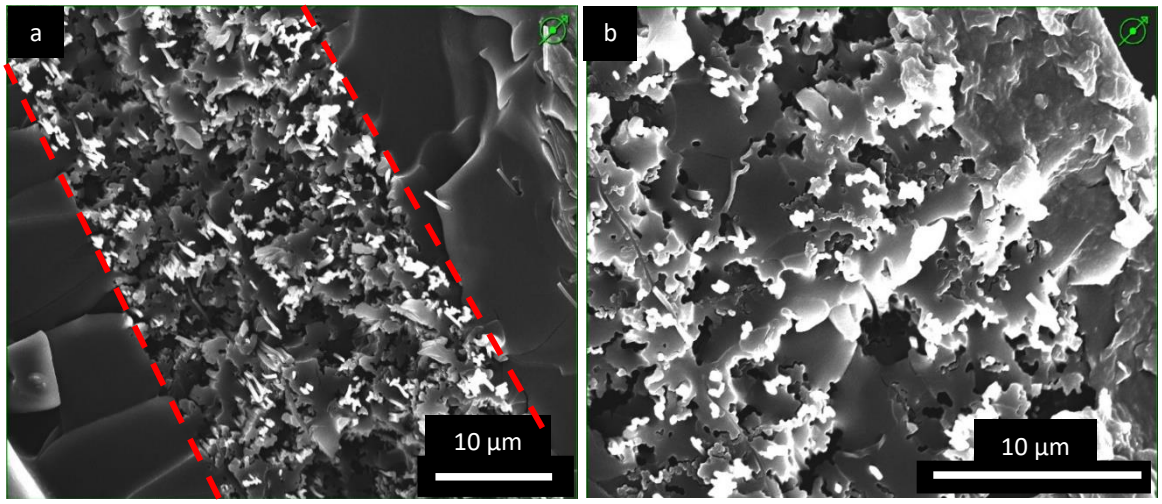

Figure 5.29: Fracture surface of a CP-19%-Si nanolaminate specimen. These images show the failure mechanisms of the 0° plies.

In the 90° ply region, although some nanofiber pullout is shown on the rough surface, there is also significant NF failure (see **Figure 5.30**). There could be two reasons for this: (1) the crack did not propagate totally parallel to the 90° fibers or (2) the 90° fibers were not entirely perpendicular to the loading direction. Based on the manufacturing process, both reasons likely contributed to the 90° fiber breakages. However, these mechanisms would have contributed to the mechanical performance of the CP-19%-Si specimens, which is why they exhibited slightly higher strength and toughness than the UD-10%-Si specimens.

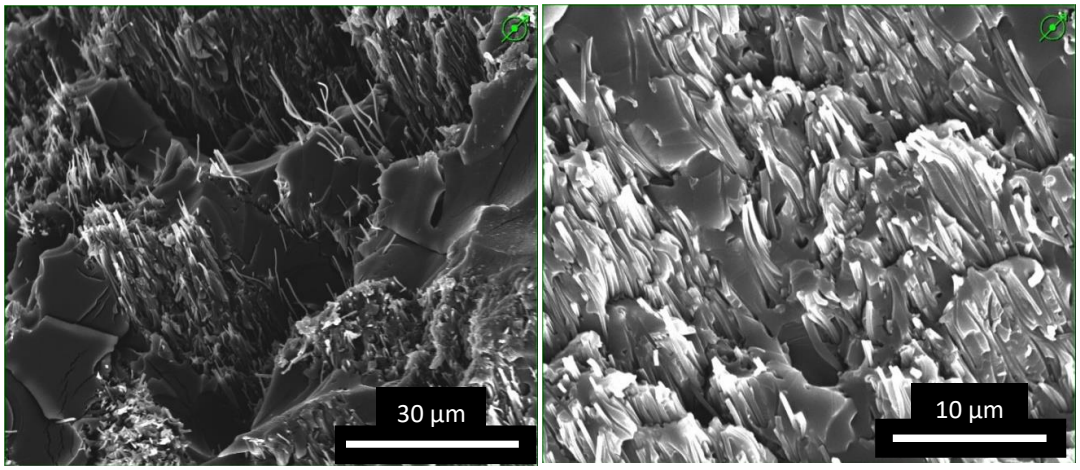

Figure 5.30: Fracture surface of a CP-19%-Si nanolaminate specimen. The images show the failure mechanisms of the 90° plies.

5.5 ANALYSIS OF THE CYANATE ESTER MATRIX NANOCOMPOSITE FABRICATION AND MECHANICAL CHARACTERIZATION

Cyanate ester (CE) resins are highly applicable as advance composite matrices due to their low moisture absorption, low dielectric loss, good flammability characteristics, wide range of processing methods, and high thermal stability.[30,94] Although they are inherently tougher than similar thermosetting resins, they still require toughening for various applications.[30] CEs have been toughened with rubber particles,[97] but this causes a decay of thermo-oxidative properties.[30,94] Engineering thermoplastics with better thermal stabilities have also been mixed with CEs,[26–28,30,94] which leads to phase separation and the formation of semi-interpenetrating networks.[94] However, properties of these blends are highly dependent upon the obtained morphologies, which are effected by molecular weight, curing conditions, and blend composition, making tailorability challenging. In addition, homogenous blends do not allow for the control of anisotropic mechanical properties, which can be achieved in laminated composites.

To create laminated nanocomposites, aligned nanofibers mats were used as unidirectional plies to reinforce a CE resin matrix. The representative stress-strain curves of the neat CE resin and NF/CE nanolaminates are shown in **Figure 5.31**. Although all three of the PAN NF-reinforced nanolaminate materials exhibited slightly increased moduli compared to the neat resin, they also exhibited lower strengths and failure strains, which significantly decreased their toughnesses. In contrast, the PI NF-reinforced nanolaminate materials both exhibited significantly higher failure strains and increased tensile strengths. This improved their toughnesses substantially compared to the neat CE resin.

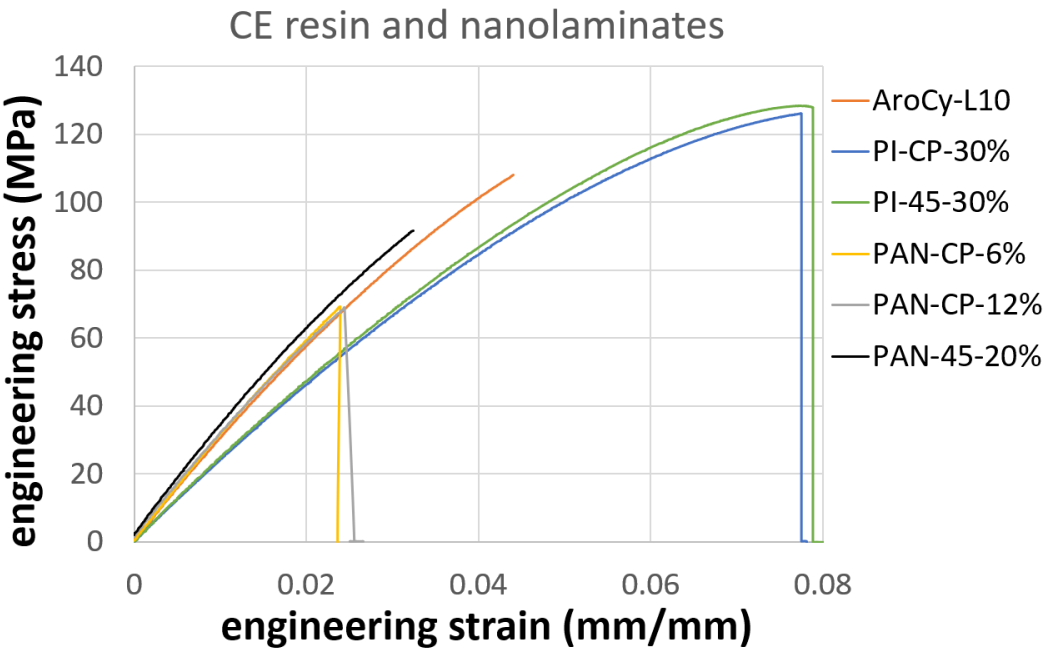

Figure 5.31: Representative stress-strain curves for the neat CE resin and the CE-matrix nanolaminates.

It is interesting to note that the PAN-CP-6% and PAN-CP-12% specimens exhibited nearly identical properties, even though the VF was doubled to 12% in the latter specimens. Another noteworthy result is that the PAN NF-reinforced composites did not reach the same high VF as those reinforced with PI NFs, even though the same manufacturing process was used to fabricate all nanolaminates. The most impressive results are the 80.0% and 61.1% increases in toughness for the PI-CP-30% and PI-45-30% nanolaminates, respectively.

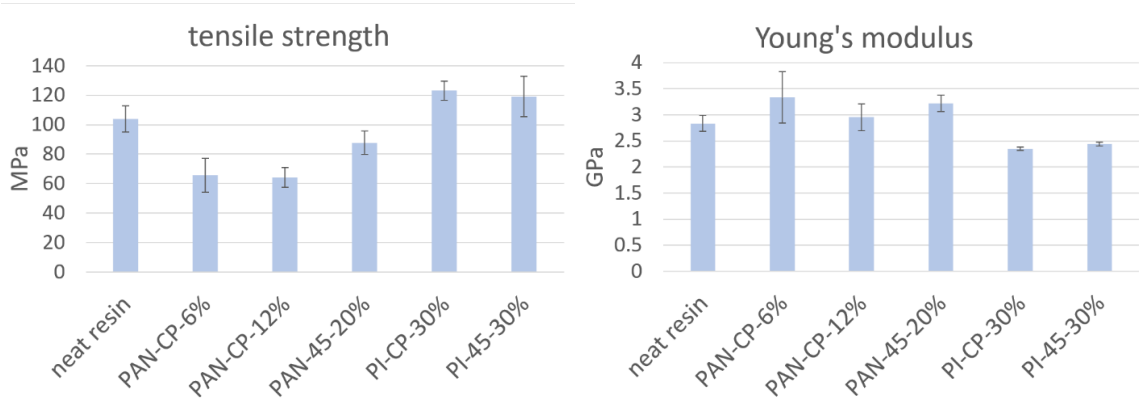

Figure 5.32: Tensile strength and Young's modulus values for the cyanate ester matrix nanolaminates compared to the neat resin.

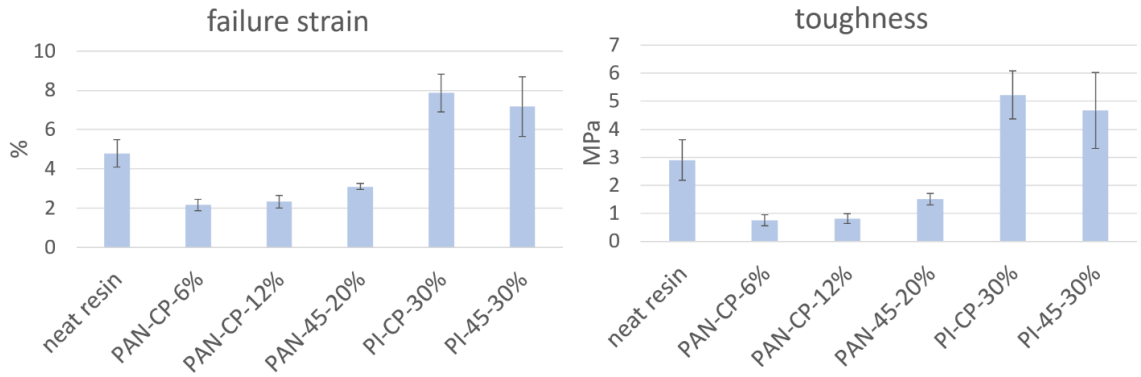

Figure 5.33: Failure strain and toughness values for the cyanate ester matrix nanolaminates compared to the neat resin.

5.5.1 Discussion

In fiber-reinforced polymers, the effectiveness of the reinforcement is highly depending on the fiber volume fraction (VF),[1,7] which is effected by both the diameters and alignment of the fibers. **Figure 5.34** and **Figure 5.35** show SEM images of aligned PAN and PI NF mats, respectively. The average PAN nanofiber diameter was 300±65 nm, while the average PI nanofiber diameter was 381±105 nm.

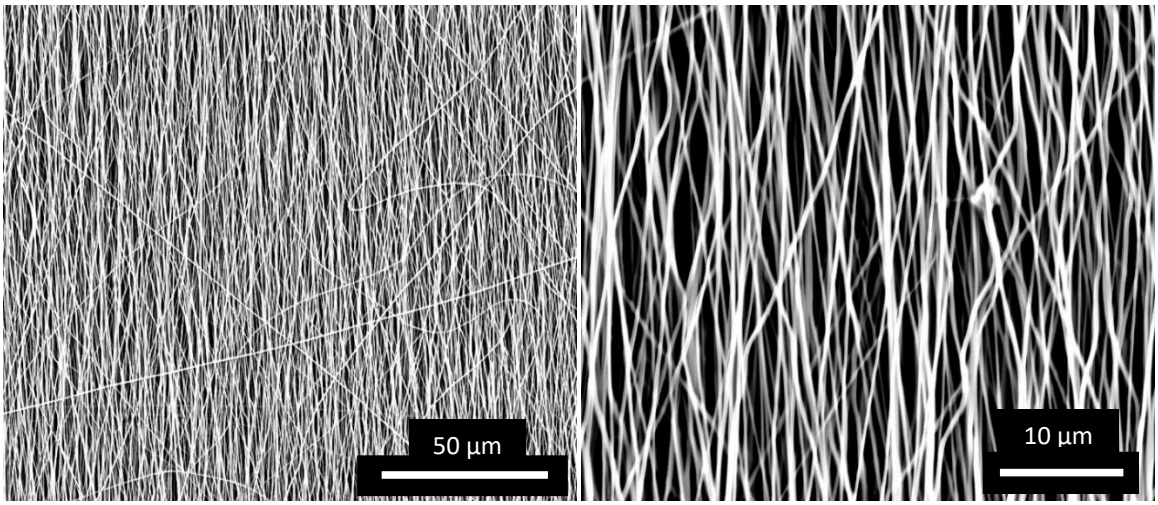

Figure 5.34: SEM micrographs of the aligned PAN NF mats used to manufacture the PAN/CE nanolaminates.

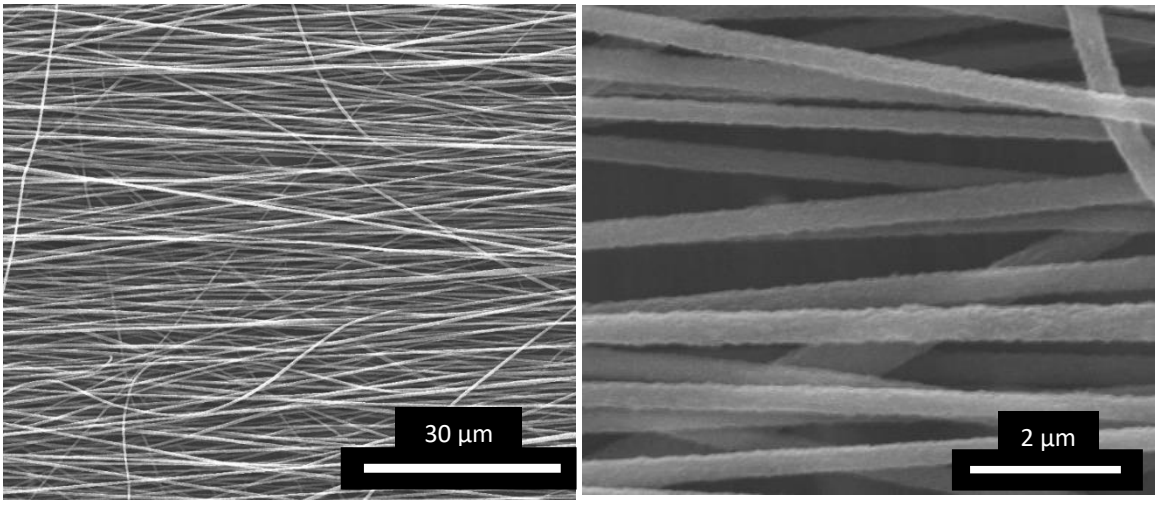

Figure 5.35: SEM micrographs of the aligned PI NFs used to manufacture the PI/CE nanolaminates.

Orientation analysis of the aligned PAN and PI NF mats was also performed. The standard deviation of the fitted Gaussian curve (also called the "dispersion" value) for the PAN mat was 7.72°, while the orientation parameters f_p and g_p were 0.896 and 0.869, respectively. The dispersion value for the PI mat was 6.65°, while the orientation parameters f_p and g_p were 0.845 and 0.821, respectively. As a reminder, perfect fiber orientation would produce f_p and g_p values of 1. Although fiber orientation was not perfect, it was high enough to produce anisotropic mechanical properties.

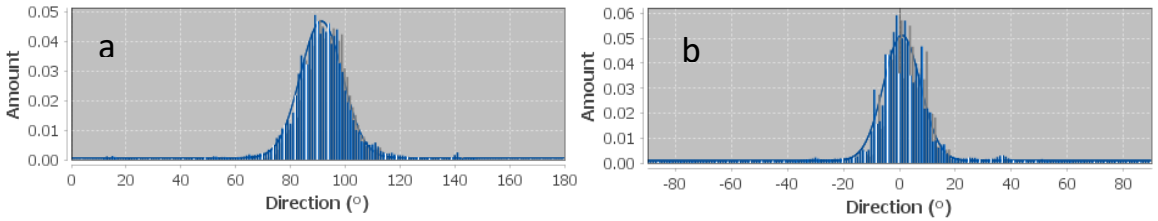

Figure 5.36: Directionality histograms obtained using FIJI for aligned (a) PAN and (b) PI nanofiber mats.

When nanofiber diameters are smaller than the minimum wavelength of visible light (380 nm), the cured nanocomposite can become transparent.[219,240,243] Based on **Figure 5.37**, the PI NF-reinforced nanolaminates show similar amounts of light transmittance as the neat resin. On the other hand, the PAN NF-reinforced nanolaminates let through significantly less light, even at volume fractions of only 6%. This is

noteworthy because the as-spun PAN mats actually had a smaller average fiber diameter than the as-spun PI mats. Also, **Figure 5.37** shows that after resin impregnation, the material is almost completely transparent, but after curing, the nanocomposite has changed to a cloudy yellow color. This may have been caused by the high curing temperatures.

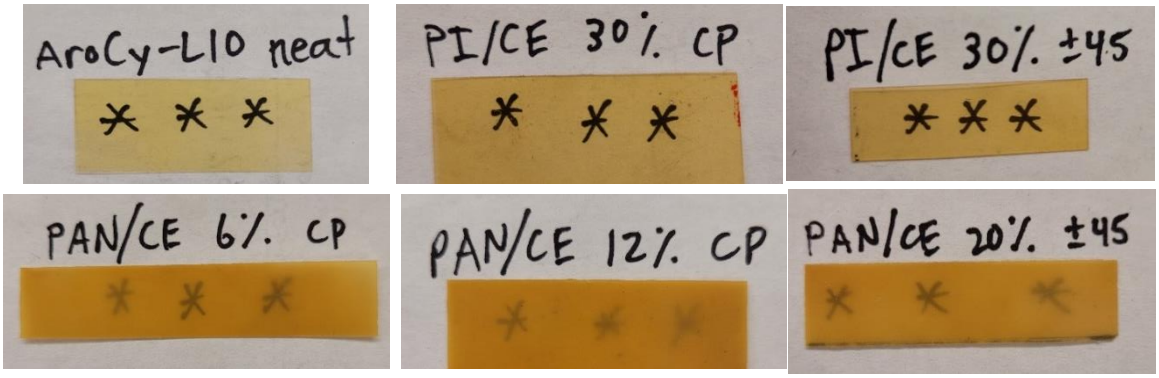

Figure 5.37: Photographs showing the transparencies of the CE resin matrix nanolaminates compared to the neat CE resin. The three stars are drawn on the sheet of paper behind each material.

To test this hypothesis, a PAN NF mat was placed between two glass plates and baked in an oven for 3 hours at the curing temperature of the CE resin (177°C, 350°F). After cooling, the PAN mat had changed from white to yellow in color and become stiffer and brittle to the touch. **Figure 5.38** compares the fracture edges of as-spun PAN mats that were sheared with scissors and those of the baked mats broken in tension by hand. Typically, when a tensile load is applied to a random as-spun NF mat, they fibers will align to a certain extent, and the fracture edge will be very crooked. However, both fracture edges in **Figure 5.38** are relatively straight, and the mats show similar degrees of random alignment. This means that the heat-treated NFs broke at relatively low strains before stretching or causing the NFs to axially align with the loading direction. This can be explained by the cyclization of the PAN fibers, which begins around 180°C (very close to the curing temperature of 177°C) and causes the molecular structure to become

more rigid.[156,157,276] This would explain why the PAN NF-reinforced composites exhibited slightly higher moduli but lower failure strains compared to the neat resin specimens.

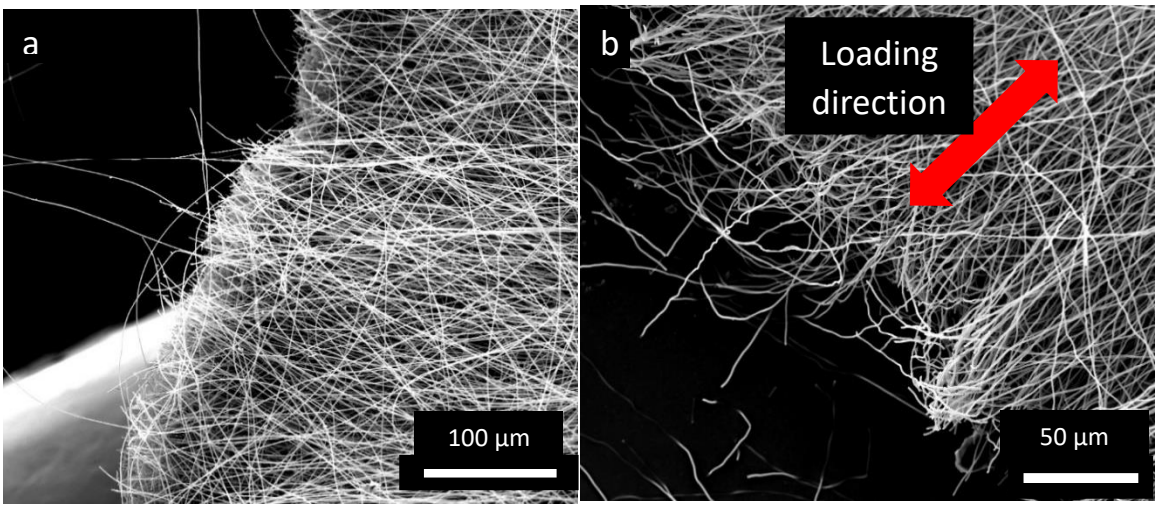

Figure 5.38: (a) as-spun random PAN NF mat that was sheared with scissors. (b) PAN NF mat baked at 350°F for 3 hours between two pieces of glass and broken in tension by hand.

Fracture surface examination of the neat CE resin specimens shows significant hackle patterning, which is characteristic of brittle failure (see **Figure 5.39**). The fracture surfaces of the nanolaminates, on the other hand, are much rougher and bumpier.

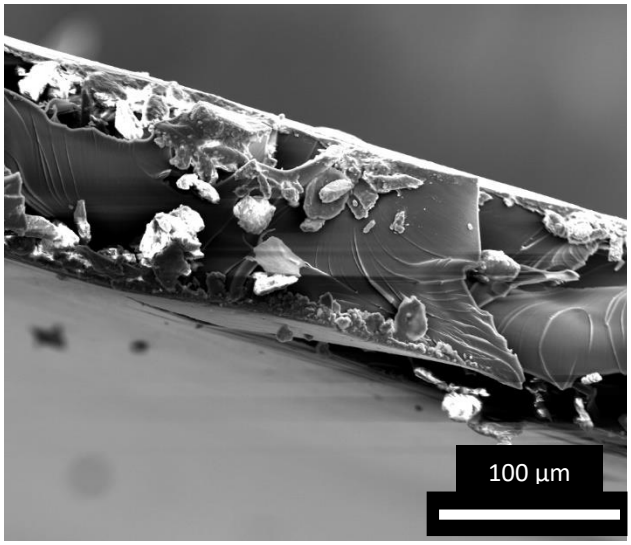

Figure 5.39: Fracture surface of a neat AroCy-L10 CE resin specimen.

The fracture surfaces of the PAN cross-ply nanolaminates are shown in **Figure 5.40**. Although the CP-6% nanolaminate has more, both surfaces show loose NFs, which is a sign of poor fiber-matrix bonding. The CP-12% fracture surface shows distinct 0° and 90° plies, which is a promising step toward laminating nanofiber-reinforced composites and being able to control their anisotropy.

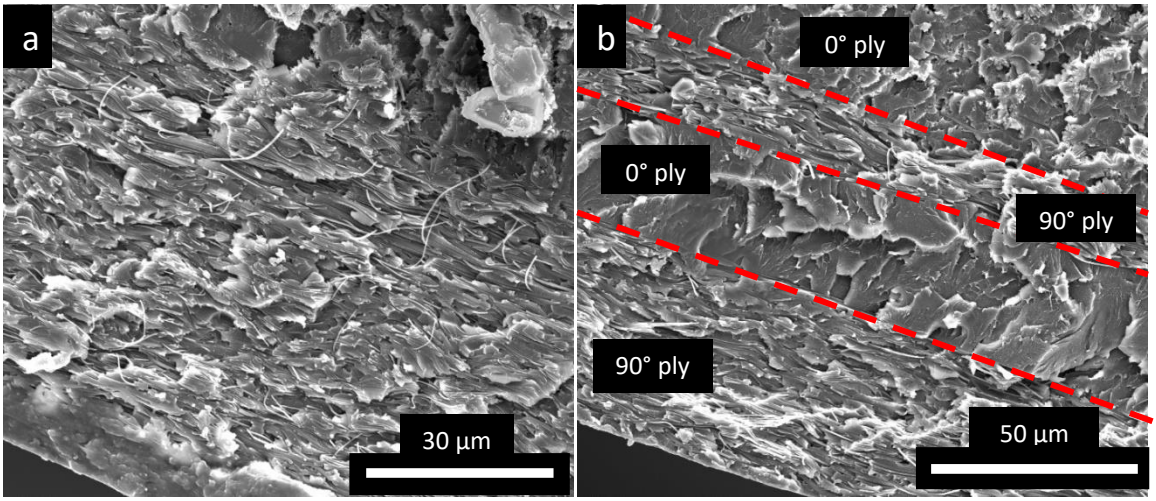

Figure 5.40: Fracture surfaces of (a) PAN-CP-6% and (b) PAN-CP-12% nanolaminate specimens.

The fracture surface of a PAN-45-20% nanolaminate is shown in **Figure 5.41**. The surface is extremely rough and somewhat porous, showing signs of fiber-pullout, which indicates suboptimal fiber-matrix bonding. However, due to the increased VF of this nanolaminate, it exhibited improved properties compared to the PAN-CP-6% and PAN-CP-12% nanolaminates, even though it did not include any fibers in the 0° direction.

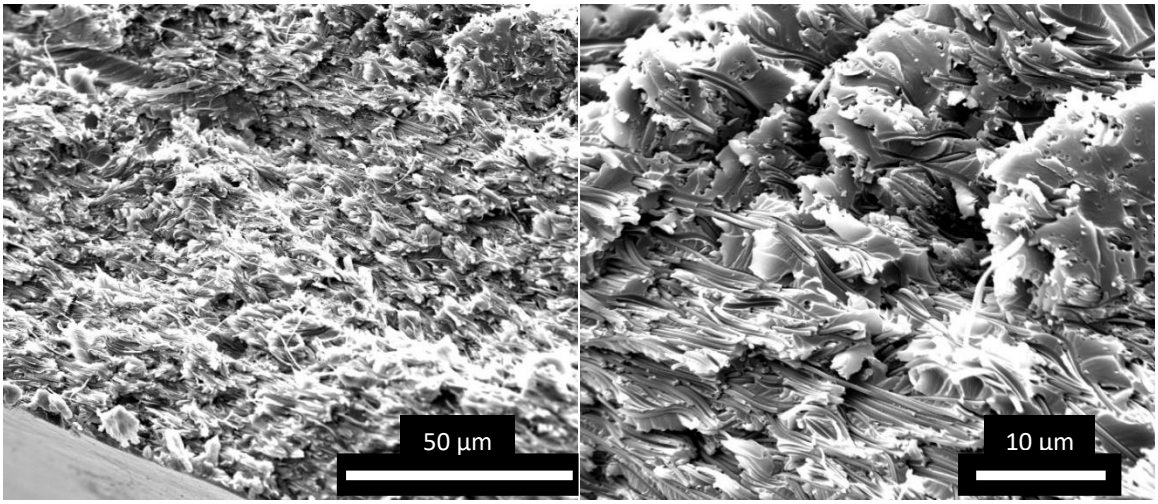

Figure 5.41: Fracture surface of a PAN-45-20% nanolaminate.

On the fracture surface of a PI-CP-30% nanolaminate, some hackle patterning is present. However, the surface is also very rough, which is representative of fiber-toughened tensile failure with no fiber pullout (see **Figure 5.42**). This means that there was strong nanofiber-matrix adhesion, which is why properties were improved substantially compared to the untoughened resin.

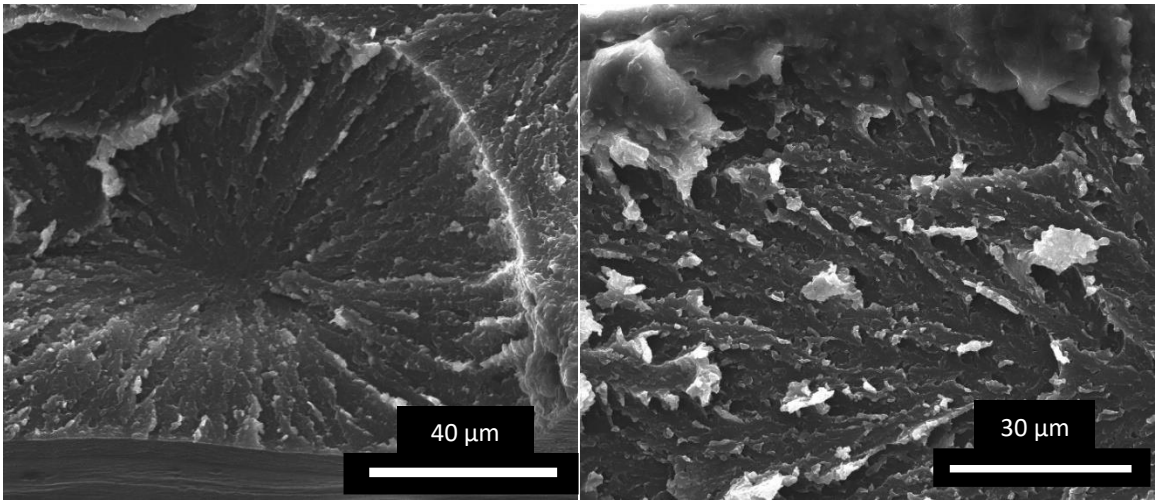

Figure 5.42: Fracture surfaces of a PI-CP-30% nanolaminate specimen.

The fracture surface of the PI-45-30% specimen also shows slight hackle patterning, but there is also significant evidence of NF tensile failure (see **Figure 5.43**). In fact, based on the morphologies of the NFs, it looks like they experienced substantial

plastic deformation before fracturing, which contributed to the increased failure strain and toughness compared to the neat CE resin.

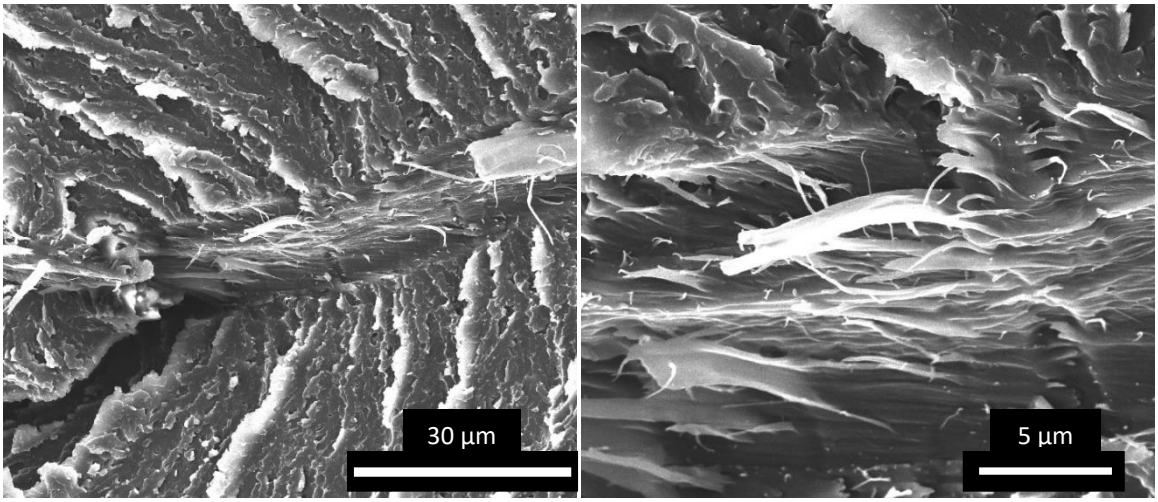

Figure 5.43: Fracture surfaces of a PI-45-30% nanolaminate specimen.

Although it seems that the fibrous morphologies were maintained in the PI/CE nanolaminates, AroCy® L-10 CE resin is capable of dissolving many high-temperature, amorphous thermoplastics, including polysulfone, polyethersulfone, polyetherimide, and thermoplastic polyimide.[277] Of particular interest, AroCy-L10 is known to dissolve Matrimid® 5218 (manufactured by Huntsman), which is a fully imidized soluble thermoplastic polyimide.[278] Since the APS-C2 used in this study to electrospin NFs is also an imidized soluble thermoplastic polyimide, the morphology of the thermoplastic phase must be observed. But first, the molecular structures of APS-C2 and Matrimid 5218 are compared, as shown in **Figure 5.44**. One significant difference is the presence of fluorine atoms in the 4,4′-(hexafluoroisopropylidene)diphthalic anhydride (6FDA) and 6FOBDA molecules. Meanwhile, Matrimid 5218 has no fluorine.

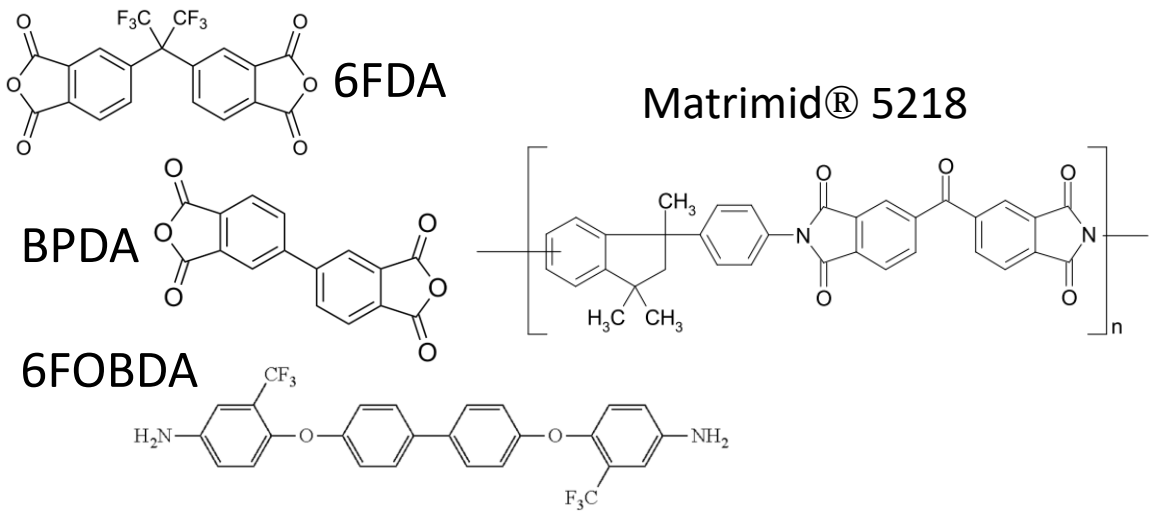

Figure 5.44: Molecular structures of APS-C2 (6FDA/BPDA/6FOBDA = 80/20/100) and Matrimid® 5218.[278]

To further investigate how powdered APS-C2 would be affected in an AroCy-L10 matrix during curing, the two components were mixed and cured the same way as the nanolaminates (i.e., between two aluminum plates). However, the maximum weight ratio of PI powder in this mixture that could be reasonably achieved was only 13.6%, which equates to a PI volume fraction in the cured composite of about 11.7%. This is much lower than what was obtained for the laminated nanocomposites (30% PI fiber VF). However, based on examination of the cured composite, the PI powder seems to have at least partially dissolved in the CE resin during curing (see **Figure 5.45**). Nonetheless, the fracture surface of a PI-45-30% specimen in **Figure 5.43** clearly shows that the nanofibrous morphology was maintained. In this study, the solubility of the PI NFs in the CE resin matrix led to excellent NF-matrix adhesion and an extremely effective toughening mechanism, while maintaining the anisotropic fibrous morphology.

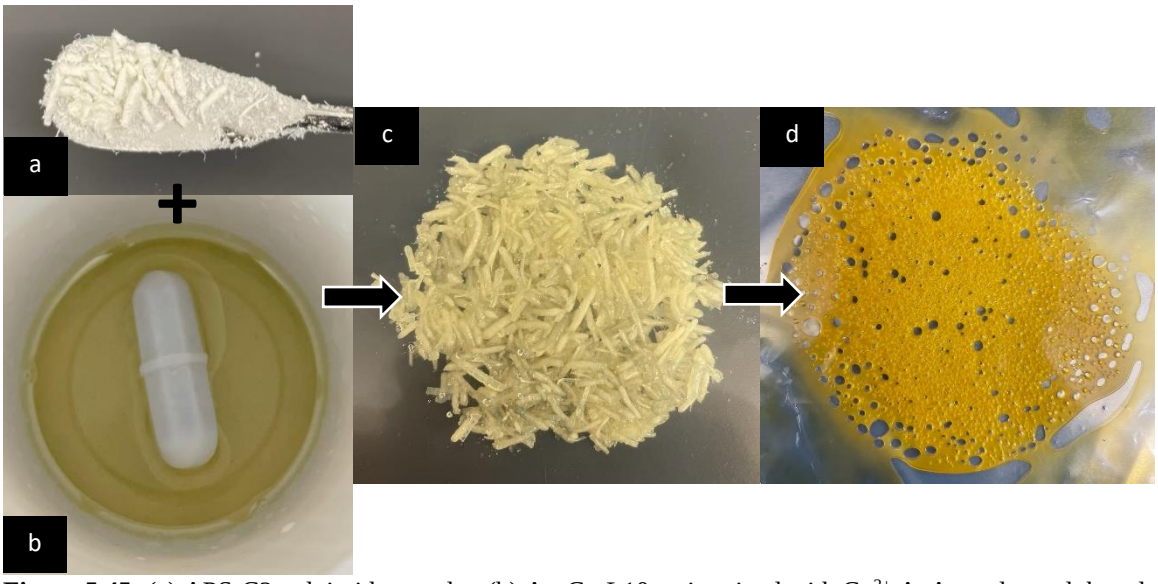

Figure 5.45: (a) APS-C2 polyimide powder. (b) AroCy-L10 resin mixed with Co^{3+} AcAc and nonylphenol catalysts. (c) APS-C2 mixed with CE resin at a 13.6% weight ratio (11.7% PI VF). (d) That same mixture after curing.

5.6 HIGH-SPEED VIDEO OBSERVATION OF JET INSTABILITIES AND NANOFIBER DEPOSITION

As mentioned previously, high alignment of continuous nanofibers is critically needed to produce nanolaminates with controlled anisotropy. However, the instabilities of the electrospinning jet inhibit the development of high orientation,[48,247] although their mechanisms are not yet fully understood.[279,280] To gain a better understanding, high-speed videos of the electrospinning jets were obtained while depositing onto both stationary and rotating collectors.

Observation of frames from different videos obtained allows for the qualitative comparison of the jet instabilities. When collecting onto a moving substrate, there is a threshold surface speed at which the whipping region of the jet becomes smaller due to the drawing force imparted by the collector. This can be seen in **Figure 5.46**. When the rotating cylinder reaches a certain RPM, the mechanical drawing force pulls the polymer jet into a straight line after only a small section of whipping instabilities. When the

rotational speed is too low, however, the bending instabilities grow linearly as they approach the collector to fill a conical-shaped envelope, similar to when electrospinning onto a stationary substrate.

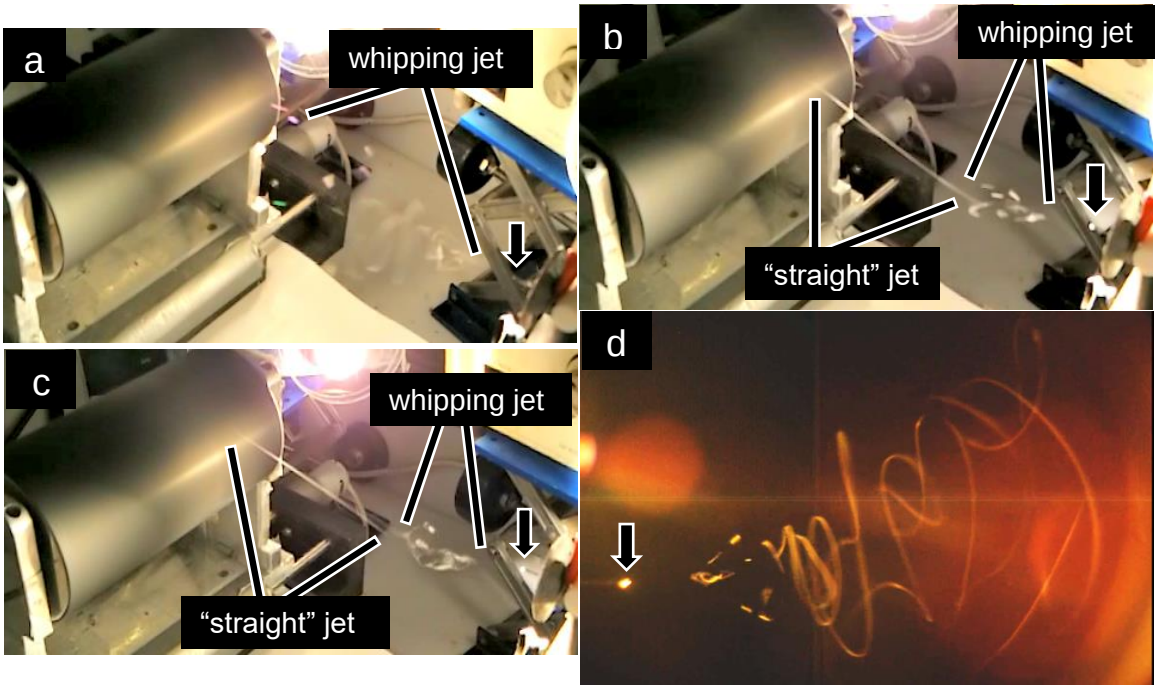

Figure 5.46: Single frames from videos taken with a Samsung Galaxy S8+ at 480 fps of PAN 10wt% + DMF with a 20 gauge needle with cylinder speeds of approximately (a) 1800 RPM, (b) 2400 RPM, and (c) 3300 RPM. (d) Frame from a 1000 fps high-speed video taken with the Redlake camera while electrospinning onto a stationary plate. The arrows indicate the needle tips.

Although no quantitative results were obtained from these videos, visualizing the electrospinning jet can help validate computational models of the process. With high-resolution, slow-motion videos, quantitative analysis can even be achieved.[281,282] In addition, visualizing the electrospinning jet can allow for optimization of processing parameters to eliminate its instabilities, which can lead to the production of highly aligned continuous nanofibers.[283]

5.7 CONCLUSIONS

The results of the alignment study provide valuable relationships between electrospinning parameters and the degree of nanofiber alignment, along with fiber

diameter. The fiber orientation increased for increasing substrate speeds, and high alignment was maintained on substrates as wide as 60 mm, which are applicable to nanocomposite fabrication. Also, the nanofiber diameters decreased at higher rotational speeds. However, ultrahigh substrate speeds may have caused the fibers to prematurely fracture during collection, which is why the UD CNF/epoxy nanocomposites reinforced with aligned mats collected at higher RPMs showed decreased tensile strength and modulus.

In general, the results of the CNF/epoxy nanocomposite investigation were positive. Cross-ply nanolaminates were successfully manufactured, and the 0° and 90° were distinguishable when observing the fracture surfaces. One unanticipated result is the fact that the UD nanocomposites reinforced with CNF mats that were allowed to shrink and wrinkle more during carbonization showed substantially higher strength and toughness that those reinforced with mats that were semi-restricted during carbonization. Although the wrinkling caused an inherent decrease in the degree of alignment, the unwrinkling mechanism allowed the nanocomposite to deform further in the longitudinal direction before failure.

Table 5.6: Mechanical testing results for the neat epoxy resin and CNF/epoxy nanocomposites.

Material	Tensile strength		Young's modulus		Failure strain		Toughness	
	Value (MPa)	Percent increase compared to resin (%)	Value (GPa)	Percent increase compared to resin (%)	Value (%)	Percent increase compared to resin (%)	Value (MPa)	Percent increase compared to resin (%)
EPON828 (neat resin)	28.83 ± 2.09	-	2.20 ± 0.13	-	2.36 ± 0.25	-	0.84 ± 0.16	-
UD-10%-	67.19	133.0	4.87 ±	120.8	1.61 ±	-31.5	3.06 ±	266.3

noSi	± 8.94		0.26		0.04		0.31	
UD-10%-Si	47.66 ± 5.19	65.3	7.05 ± 1.07	219.9	0.72 ± 0.03	-69.6	1.45 ± 0.23	74.4
UD-22%-Si	44.37 ± 1.03	53.9	5.20 ± 0.11	135.8	0.94 ± 0.000 08	-60.3	1.08 ± 0.10	28.6
CP-19%-Si	52.80 ± 7.34	83.1	7.40 ± 1.06	235.9	0.74 ± 0.06	-68.8	1.48 ± 0.73	76.7

The CE-matrix nanocomposite investigation also provided insightful results. Although the addition of PAN NFs to the CE matrix caused the reduction of tensile properties (other than modulus) due to the thermal cyclization of PAN, the PI NFs provided significant toughening. The PI/CE nanocomposites also show excellent thermal stability and have the potential to be used in high-temperature applications. Finally, the lamination of aligned nanofiber plies in this study, which demonstrates for the first time the feasibility of fabricating continuous nanofiber-reinforced nanolaminates, facilitated high fiber volume fraction and controlled anisotropy. The establishment of these properties in polymer matrix nanocomposites is an essential step towards mimicking the highly desirable mechanics of conventional composite laminates at smaller scales.

Table 5.7: Mechanical testing results for the neat CE resin and CE-matrix nanolaminates.

Material	**Tensile strength**		**Young's modulus**		**Failure strain**		**Toughness**	
	Value (MPa)	**Percent increase compared to resin (%)**	**Value (GPa)**	**Percent increase compared to resin (%)**	**Value (%)**	**Percent increase compared to resin (%)**	**Value (MPa)**	**Percent increase compared to resin (%)**
AroCy-L10 (neat resin)	104.0 ± 8.9	-	2.83 ± 0.15	-	4.80 ± 0.69	-	2.90 ± 0.72	-

PAN-CP-6%	65.8 ± 11.6	-36.7	3.34 ± 0.49	17.7	2.16 ± 0.29	-55.0	0.76 ± 0.19	-73.8
PAN-CP-12%	64.1 ± 6.7	-38.4	2.95 ± 0.26	4.2	2.33 ± 0.33	-51.4	0.82 ± 0.17	-71.8
PAN-45-20%	87.7 ± 8.0	-15.7	3.22 ± 0.16	13.7	3.10 ± 0.16	-35.4	1.51 ± 0.20	-48.0
PI-CP-30%	123.2 ± 6.5	18.5	2.34 ± 0.03	-17.1	7.87 ± 0.97	64.1	5.22 ± 0.85	80.0
PI-45-30%	119.2 ± 13.8	14.6	2.44 ± 0.04	-13.8	7.18 ± 1.53	49.6	4.67 ± 1.36	61.1

CHAPTER 6. SUMMARY AND FUTURE WORK

Although fiber-reinforced laminates are some of the most advanced structural materials available today, they are susceptible to delamination, which can cause catastrophic failure. Continuous nanofiber interleaves have been shown to suppress delamination, but primarily in 2D composite plates subject to single mode loadings. This has limited the use of nanofiber interleaves in practical applications. As such, this work investigates their effect on the performance of composite structures, whose geometries can induce additional complex interlaminar stresses. Mechanical testing results on NF-interleaved composite structures can serve as a critical step towards their implementation of in commercial applications. These applications include structures that experience high temperatures, but high-temperature resins are even more prone to microcracking. Nonetheless, composites made from high-temperature resins have hardly been studied with respect to nanofiber reinforcement. Subsequently, in addition to studying conventional carbon/epoxy material, a high-temperature carbon/cyanate ester (CE) material was reinforced with nanofiber interleaves for the first time. Epoxy and cyanate ester resins were also used to manufacture continuous nanofiber-reinforced nanolaminates. These laminated nanocomposites represent the first of their kind, and they prove the feasibility of developing nanocomposites with high fiber volume fraction and controlled anisotropy.

6.1 CONCLUSIONS

6.1.1 Continuous Nanofiber-Reinforcement of High-Temperature Composite Laminates

Continuous nanofiber interleaves have been shown to significantly improve the mechanical properties of conventional composite laminates, such as advanced

carbon/epoxy composites, by successfully suppressing delamination. However, studies on high-temperature composites, which are useful for next-generation applications, are extremely limited. In fact, I could not find a single publication outlining the nanofiber reinforcement of cyanate ester matrix composite laminates. In this work, the effect of nanofiber interleaving in both traditional carbon/epoxy and high-temperature carbon/CE composite materials was investigated.

In CHAPTER 3, continuous nanofiber interleaves were used to reinforce the midplane of unidirectional composites in an attempt to improve their interlaminar fracture toughness (IFT). Mode I IFT was highly dependent on the polymer nanofiber material and the thickness of the nanofiber interleaf. Only thin, polyacrylonitrile (PAN) nanofiber interleaves provided improved fracture toughness in carbon/epoxy, while thicker, polyimide (PI) nanofiber interleaves were able to toughen the carbon/CE material. Although initiation G_{IC} was mostly unaffected by the NF interleaving due to the bluntness of the pre-crack, propagation G_I was increased significantly due to the presence of significant carbon fiber bridging, nanofiber bridging, and crack deflection. Similar results were obtained from the mode II IFT testing, in which carbon/epoxy reinforced with PAN nanofibers and carbon/CE reinforced with PI nanofibers exhibited improved performance compared to the pristine materials. Fracture surface analysis indicated poor adhesion between the epoxy resin and the PAN NFs, while the CE resin bonded extremely well with the PI NFs. Despite spending very little effort optimizing the material properties, nanofiber interleaves were able to significantly improve the fracture toughness of composites made from resins that *had already been toughened* by the manufacturers. In addition, despite the considerable aging of the epoxy resin, which

hindered its adhesion to the NFs, the interleaves were still able to provide notable delamination resistance. Most importantly, the carbon/CE reinforced with PI nanofibers represents a novel material combination that is expected to be widely applicable for high-temperature service and can even experience enhanced ability to absorb energy at high temperatures due to the presence of the thermally stable thermoplastic continuous nanofiber reinforcement.

6.1.2 Translation of Material Improvements via Nanofiber-Reinforcement to Composite Structures

Most studies on delamination suppression via nanofiber interleaving have focused on modes I and II IFT testing of 2D plates, but composite structures can experience mixed-mode failure due to complex stress distributions that depend on their geometries. Delamination in laminates under mixed mode interlaminar stresses can initiate at free edges during in-plane loadings due to their mechanisms, but it can also occur in structural volumes due to direct out-of-plane loadings or the presence of certain discontinuities and geometries. Since laminated composites can be constructed with an infinite number of layups, a laminate can be considered the most basic structural form. Rounded edges or holes also provide an added layer of complexity to the mechanisms of delamination. Lastly, curved beams are especially prone to delamination in the bent region. Although some research has been performed on tensile testing of laminates interleaved with continuous NFs, only a few different types of layups have been studied. Research on NF-reinforced notched laminates is even more limited. Finally, to the best of my knowledge, not a single study on continuous nanofiber interleaving of curved beams has been published.

In CHAPTER 4, the effect of nanofiber reinforcement on the structural properties of multidirectional laminates with and without holes and of L-bend beams was investigated. Although mechanical improvements were minor, and sometimes negative, for the carbon/epoxy material reinforced with PAN nanofibers due to poor nanofiber-matrix adhesion, the improvements observed with the carbon/cyanate ester material reinforced with PI nanofiber interleaves were substantial for all structures tested. This represents the first instance of successfully translating nanofiber-reinforcement for improving material properties to the performance of composite structures. In addition, a relatively wide variety of structures built from two different composite materials were used to prove the feasibility of this translation, and significant improvements were observed without extensive optimization of nanofibers and their properties.

6.1.3 Nanofiber Alignment and Developed Laminated Nanocomposites Reinforced with Continuous Nanofibers

Continuous electrospun nanofibers can exhibit extraordinary mechanical properties. Due to a decreased chance of defects and increased molecular orientation, nanoscale fibers can exhibit enhanced strength and stiffness, and even simultaneous improvements in strength and toughness at ultrafine diameters. Their high surface area-to-volume ratio enables excellent bonding with polymer matrices, and their continuity can provide a better reinforcing effect than that of other discontinuous nanomaterials, such as carbon nanotubes. However, continuous nanofibers typically deposit as randomly oriented nonwoven mats during electrospinning. Although these mats can be used as reinforcement in polymer matrices to improve properties, the achieved fiber volume fraction has been low up to now. To obtain higher volume fraction and mimic the controlled anisotropy exhibited by conventional composite laminates, near perfect

nanofiber alignment is needed. The electrospinning process provides a suitable way to achieve a degree of orientation, but most methods are limited by either the quantity of fibers that can be collected or the degree of alignment.

In CHAPTER 5, an extensive study on continuous electrospun nanofiber alignment was performed using a high-production rate rotating cylinder collector. The effects of several relevant electrospinning parameters on the degree of fiber alignment and on fiber diameter were determined. Results of this study were used as a guide to manufacture laminated nanocomposites, which were subsequently tested in tension. Although it is difficult to maintain nanofiber alignment in polymer matrices, fracture surface analysis showed clearly distinguishable oriented nanofiber plies and obtained fiber volume fractions reached 22% for carbon nanofibers in epoxy and 30% for polyimide nanofibers in cyanate ester. Mechanical results were also generally positive, in which most nanocomposites exhibited significantly enhanced strength, modulus, and energy to failure compared to the respective neat resins. Finally, the PI nanofiber-reinforced cyanate ester is particularly applicable to new-age high-temperature applications due to the high thermal stabilities of both the fibers and the polymer matrix.

6.1.4 Templated Carbon Nanofibers with Nanomaterials to Improve Graphitic Structure

Electrospun polymer nanofibers do not always possess inherently excellent mechanical properties. To enhance certain properties, such as strength, stiffness, conductivity, thermal stability, etc., nanofibers can be modified in several ways. Composite nanofibers can be fabricated through the addition of various nanoparticles. However, achieving high volume fraction of nanoparticles is usually detrimental to electrospinning as it significantly increases solution viscosity and non-uniformity. Post-

processing treatments can be applied to polymer precursors to develop continuous carbon, metallic, and even ceramic nanofibers. Carbon nanofibers (CNFs) have received significant attention due to their prospective excellent strength and stiffness based on the properties of commercial carbon fibers, but CNFs produced from electrospun polymer precursors, mainly polyacrylonitrile, exhibit poor graphitic structures compared to those of conventional carbon fibers. One technique to improve their graphitic order is to increase carbonization temperatures, but this requires expensive, specialized equipment and vast amounts of energy. An alternative approach proposed earlier at UNL involves the addition of small quantities of carbon-based nanomaterials that can act as templating agents to increase the size and orientation of graphitic crystallites in CNFs, leading to enhanced structure and mechanical and transport properties. Recently, two-dimensional nanomaterials have received considerable attention due to their unique properties and ability to adhere well with polymer matrices.

In the exploratory research presented in APPENDIX D, continuous nanofibers templated with graphene nanoribbons (GNRs) and MXenes were fabricated. Although GNRs maintained their excellent graphitic order within the fiber matrix, they showed a high tendency to agglomerate, even at concentrations as low as 1%. In contrast, MXenes were much more evenly distributed throughout the fibers, but they showed less potential to drastically increase graphitization in CNFs. With more research on these nanomaterials, their templating effects may be improved, leading to the development of carbon nanofibers with superior graphitic structures and mechanical properties.

6.2 FUTURE DIRECTIONS

6.2.1 Continuous Nanofiber-Reinforced Composite Structures

The results of Chapters CHAPTER 3 and CHAPTER 4 prove the feasibility of toughening composite structures with continuous nanofiber interleaves. However, very little time was spent optimizing either material or structural properties. Future work could involve investigating the effects of certain interleaf parameters, such as thickness, fiber diameter distribution, and location (both area-wise and through the thickness) to further improve both interlaminar fracture toughness and the performance of composite structures.

The breadth of the research could also be increased by testing other structural elements, such as bearing joints, ply drops and tapers, and beams with distinctive cross-sections. In addition to quasi-static tests, structural responses under fatigue loadings could be determined. Although there are a handful of standardized tests for composite structures, many new ones would have to be developed to allow for a one-to-one comparison of pristine and nanofiber-reinforced structures. During these tests, the failure mechanisms, particularly delamination and its onset, should be closely monitored to determine if and how delamination is suppressed by the nanofiber interleaves. Since high-temperature resins can be prone to microcracking in service, their hot/wet properties could be studied through thermomechanical cycling or thermal aging in humid conditions. Finally, the results of further experimental research could aid in the development of a representative computational model of a complete, nanofiber-interleaved composite structure. All of these projects would ultimately contribute to the

use of nanofiber-reinforced composite laminates for industrial structural applications, which has yet to be realized.

6.2.2 Electrospinning Aligned Nanofibers for Laminated Nanocomposites

The results of CHAPTER 5 were extremely encouraging regarding the reinforcement of polymer matrices with continuous aligned nanofibers. It was shown that nanofiber alignment, even in relatively large and thick mats, can be maximized through proper choice of electrospinning parameters, which allowed for the production of nanolaminates with high fiber volume fraction and controlled anisotropy. However, the lack of complete understanding of the physics that govern electrospinning jets and their instabilities limits the obtainable nanofiber orientation. With high-speed video observation and further modeling-assisted optimization, the whipping jet instabilities can be completely eliminated by collecting onto a substrate moving at the appropriate speed, which can simultaneously increase fiber alignment, increase fiber packing and volume fraction, and decrease fiber diameter. As such, future research should focus on optimizing nanofiber alignment over large areas and maintaining orientation in polymer matrices. In turn, nanomanufacturing of laminated nanocomposites with never-before-seen volume fractions and tailorable anisotropy can be achieved.

6.2.3 Templated Carbon Nanofibers

APPENDIX D explored the potential of both graphene nanoribbons (GNRs) and Ti_3C_2 nanoparticles (MXenes) to serve as templating nanomaterials in carbon nanofibers. Although the GNRs exhibited excellent graphitic structure, they showed a tendency to agglomerate within the nanofibers. The MXenes, on the other hand, were much more uniformly dispersed in the polymer fibers, but they only slightly increased the graphitic

order of the carbon nanofibers. However, this was only at weight fractions of 2%. In future work, the MXene concentration can be increased, and special efforts should be focused on deagglomerating the GNRs. If these goals are achieved, drastic improvements in the graphitic structures of carbon nanofibers could revolutionize the field of continuous nanofiber-reinforced composite materials.

REFERENCES

(1) Campbell, F. C. *Structural Composite Materials*; Materials Park, OH, 2010.

(2) Nagavally, R. R. Composite Materials - History, Types, Fabrication Techniques, Advantages, and Applications. *Int. J. Mech. Prod. Eng.* **2016**, 25–30.

(3) Jones, R. M. *Mechanics of Composite Materials*, 2nd ed.; CRC Press: Boca Raton, FL, 1998.

(4) Vinson, J. R.; Sierakowski, R. L. *The Behavior Of Structures Composed Of Composite Materials*, 2nd ed.; Dordrecht: Springer, Netherlands, 2002.

(5) Rajak, D. K.; Pagar, D. D.; Menezes, P. L.; Linul, E. Fiber-Reinforced Polymer Composites: Manufacturing, Properties, and Applications. *Polymers (Basel).* **2019**, *11*. https://doi.org/10.3390/polym11101667.

(6) Hegde, S.; Satish Shenoy, B.; Chethan, K. N. Review on Carbon Fiber Reinforced Polymer (CFRP) and Their Mechanical Performance. *Mater. Today Proc.* **2019**, *19*, 658–662. https://doi.org/10.1016/j.matpr.2019.07.749.

(7) Gibson, R. F. *Principles of Composite Material Mechanics*; McGraw-Hill, 1994.

(8) Campbell, F. C. Introduction to Composite Materials. In *Structural Composite Materials*; ASM International, 2010; pp 1–29.

(9) Mathapati/ Swami, S. Review on: Analysis for Laminated Composite Plate. *Indian J. Appl. Res.* **2015**, *5* (5), 19–22.

(10) Visal, S.; Deokar, S. A Review Paper on Properties of Carbon Fiber Reinforced Polymers. *Int. J. Innov. Res. Sci. Technol.* **2019**, *2* (12).

(11) *Handbook of Composites*, 2nd ed.; Peters, S. T., Ed.; Chapman & Hall, 2002. https://doi.org/10.1007/978-1-4615-6389-1.

(12) Grand View Research. *Composites Market Size, Share & Trends Analysis Report By Product (Carbon, Glass), By Manufacturing Process (Layup, Filament, RTM), By End Use, By Region, And Segment Forecasts, 2021 - 2028*; 2021.

(13) Kerr, M.; Chawla, N.; Chawla, K. K. The Cyclic Fatigue of High-Performance Fibers. *JOM* **2005**, *57* (2), 67–71. https://doi.org/10.1007/s11837-005-0219-6.

(14) Das, T. K.; Ghosh, P.; Das, N. C. Preparation, Development, Outcomes, and Application Versatility of Carbon Fiber-Based Polymer Composites: A Review. *Adv. Compos. Hybrid Mater.* **2019**, *2* (2), 214–233. https://doi.org/10.1007/s42114-018-0072-z.

(15) Strong, A. B. Thermoplastic Composites. In *Fundamentals of Composites Manufacturing: Materials, Methods, and Applications*; Society of Manufacturing Engineers: Dearborn, MI, 2008.

(16) Matmatch. Thermoplastics vs. Thermosetting Polymers: Properties, Processing and Applications https://matmatch.com/learn/material/thermoplastics-vs-thermosetting-polymers.

(17) Ibeh, C. C. Introduction and History of the Plastics Industry. In *Thermoplastic Materials: Properties, Manufacturing Methods, and Applications*; CRC Press: Boca Raton, FL, 2011.

(18) SpecialChem. Epoxy Resins: A to Z Technical Review of Thermosetting Polymer https://omnexus.specialchem.com/selection-guide/epoxy-resins-a-to-z-technical-review-of-thermosetting-polymer.

(19) 2017 DoD Advanced Composites Maintainers TIM Recap.

(20) Mangalgiri, P. D. Polymer-Matrix Composites for High-Temperature

Applications. *Def. Sci. J.* **2005**, *55* (2), 175–193. https://doi.org/10.14429/dsj.55.1980.

(21) Lau, K. S. Y. High-Performance Polyimides and High Temperature Resistant Polymers. In *Handbook of Thermoset Plastics*; Elsevier Inc., 2014; pp 297–424. https://doi.org/10.1016/B978-1-4557-3107-7.00010-5.

(22) Chang, I. Y.; Lees, J. K. Recent Development in Thermoplastic Composites: A Review of Matrix Systems and Processing Methods. *J. Thermoplast. Compos. Mater.* **1988**, *1* (3), 277–296. https://doi.org/10.1177/089270578800100305.

(23) Shimokawa, T.; Katoh, H.; Hamaguchi, Y.; Sanbongi, S.; Mizuno, H.; Nakamura, H.; Asagumo, R.; Tamura, H. Effect of Thermal Cycling on Microcracking and Strength Degradation of High-Temperature Polymer Composite Materials for Use in Next-Generation SST Structures. *J. Compos. Mater.* **2002**, *36* (7), 885–895. https://doi.org/10.1177/0021998302036007469.

(24) Timmerman, J. F.; Hayes, B. S.; Seferis, J. C. Cure Temperature Effects on Cryogenic Microcracking of Polymeric Composite Materials. *Polym. Compos.* **2003**, *24* (1), 132–139. https://doi.org/10.1002/pc.10013.

(25) Kinloch, A. J.; Taylor, C. The Toughening of Cyanate-Ester Polymers. Part I Physical Modification Using Particles, Fibres and Woven-Mats. *J. Mater. Sci.* **2002**, *37* (3), 433–460. https://doi.org/10.1023/A:1013735103120.

(26) Kinloch, A. J.; Taylor, A. C. The Toughening of Cyanate-Ester Polymers. Part II: Chemical Modification. *J. Mater. Sci.* **2003**, *38* (1), 65–79. https://doi.org/10.1023/A:1021109731672.

(27) Hwang, J. W.; Park, S. D.; Cho, K.; Kim, J. K.; Park, C. E.; Oh, T. S. Toughening

of Cyanate Ester Resins with Cyanated Polysulfones. *Polymer (Guildf).* **1997**, *38* (8), 1835–1843.

(28) Diberardino, M. Toughening Mechanisms in a High Temperature Cyanate Ester Resin Modified with a Thermoplastic Polyimide, Lehigh University, 1993.

(29) Huang, Y.; Hunston, D. L.; Kinloch, A. J.; Riew, C. K. Mechanisms of Toughening Thermoset Resins. **1993**, 1–35. https://doi.org/10.1021/ba-1993-0233.ch001.

(30) Hamerton, I.; Hay, J. N. Recent Technological Developments in Cyanate Ester Resins. *High Performance Polymers*. 1998, pp 163–174. https://doi.org/10.1088/0954-0083/10/2/001.

(31) Shrivastava, R.; Singh, K. K. Interlaminar Fracture Toughness Characterization of Laminated Composites: A Review. *Polym. Rev.* **2020**, *60* (3), 542–593. https://doi.org/10.1080/15583724.2019.1677708.

(32) Carlsson, L. A.; Pipes, R. B.; Adams, D. F. Ch. 14: Characterization of Delamination Failure. In *Experimental Characterization of Advanced Composite Materials*; CRC Press: New Jersey, 2003.

(33) Wisnom, M. R. The Role of Delamination in Failure of Fibre-Reinforced Composites. *Philos. Trans. R. Soc. A Math. Phys. Eng. Sci.* **2012**, *370* (1965), 1850–1870. https://doi.org/10.1098/rsta.2011.0441.

(34) Mittelstedt, C.; Becker, W. Free-Edge Effects in Composite Laminates. *Appl. Mech. Rev.* **2007**, *60* (1–6), 217–245. https://doi.org/10.1115/1.2777169.

(35) Pagano, N. J. On the Calculation of Interlaminar Normal Stress in Composite Laminate. *J. Compos. Mater.* **1974**, *8* (1), 65–81.

https://doi.org/10.1177/002199837400800106.

(36) Wu, X. F. Fracture of Advanced Polymer Composites with Nanofiber Reinforced Interfaces. **2003**, No. August, 326.

(37) Shivakumar, K.; Panduranga, R. Interleaved Polymer Matrix Composites - A Review. *54th AIAA/ASME/ASCE/AHS/ASC Struct. Struct. Dyn. Mater. Conf.* **2013**, No. May 2015. https://doi.org/10.2514/6.2013-1903.

(38) Jeevanandam, J.; Barhoum, A.; Chan, Y. S.; Dufresne, A.; Danquah, M. K. Review on Nanoparticles and Nanostructured Materials: History, Sources, Toxicity and Regulations. *Beilstein J. Nanotechnol.* **2018**, *9* (1), 1050–1074. https://doi.org/10.3762/bjnano.9.98.

(39) Saeed, K.; Khan, I. Carbon Nanotubes-Properties and Applications: A Review. *Carbon Lett.* **2013**, *14* (3), 131–144. https://doi.org/10.5714/cl.2013.14.3.131.

(40) Lau, K. T.; Hui, D. The Revolutionary Creation of New Advanced Materials - Carbon Nanotube Composites. *Compos. Part B* **2002**, *33* (4), 263–277. https://doi.org/10.1016/S1359-8368(02)00012-4.

(41) Dzenis, Y. Structural Nanocomposites. *Science (80-.).* **2008**, *319* (25 January), 419–420. https://doi.org/10.1126/science.1151434.

(42) Wicks, S. S.; de Villoria, R. G.; Wardle, B. L. Interlaminar and Intralaminar Reinforcement of Composite Laminates with Aligned Carbon Nanotubes. *Compos. Sci. Technol.* **2010**, *70* (1), 20–28. https://doi.org/10.1016/j.compscitech.2009.09.001.

(43) Almuhammadi, K.; Alfano, M.; Yang, Y.; Lubineau, G. Analysis of Interlaminar Fracture Toughness and Damage Mechanisms in Composite Laminates Reinforced

with Sprayed Multi-Walled Carbon Nanotubes. *Mater. Des.* **2014**, *53*, 921–927. https://doi.org/10.1016/j.matdes.2013.07.081.

(44) Arai, M.; Noro, Y.; Sugimoto, K. ichi; Endo, M. Mode I and Mode II Interlaminar Fracture Toughness of CFRP Laminates Toughened by Carbon Nanofiber Interlayer. *Compos. Sci. Technol.* **2008**, *68* (2), 516–525. https://doi.org/10.1016/j.compscitech.2007.06.007.

(45) Palazzetti, R.; Zucchelli, A. Electrospun Nanofibers as Reinforcement for Composite Laminates Materials – A Review. *Compos. Struct.* **2017**, *182* (June), 711–727. https://doi.org/10.1016/j.compstruct.2017.09.021.

(46) Barhoum, A.; Pal, K.; Rahier, H.; Uludag, H.; Kim, I. S.; Bechelany, M. Nanofibers as New-Generation Materials: From Spinning and Nano-Spinning Fabrication Techniques to Emerging Applications. *Applied Materials Today*. Elsevier Ltd December 1, 2019, pp 1–35. https://doi.org/10.1016/j.apmt.2019.06.015.

(47) Martin, C. R. Template Synthesis of Electronically Conductive Polymer Nanostructures. *Acc. Chem. Res.* **1995**, *28* (2), 61–68. https://doi.org/10.1021/ar00050a002.

(48) Yarin, A. L.; Koombhongse, S.; Reneker, D. H. Bending Instability in Electrospinning of Nanofibers. *J. Appl. Phys.* **2001**, *89*, 3018–3026. https://doi.org/10.1063/1.1333035.

(49) Haider, A.; Haider, S.; Kang, I. K. A Comprehensive Review Summarizing the Effect of Electrospinning Parameters and Potential Applications of Nanofibers in Biomedical and Biotechnology. *Arab. J. Chem.* **2018**, *11* (8), 1165–1188.

https://doi.org/10.1016/j.arabjc.2015.11.015.

(50) Huang, Z. M.; Zhang, Y. Z.; Kotaki, M.; Ramakrishna, S. A Review on Polymer Nanofibers by Electrospinning and Their Applications in Nanocomposites. *Compos. Sci. Technol.* **2003**, *63* (15), 2223–2253. https://doi.org/10.1016/S0266-3538(03)00178-7.

(51) Xue, J.; Wu, T.; Dai, Y.; Xia, Y. Electrospinning and Electrospun Nanofibers: Methods, Materials, and Applications. *Chem Rev.* **2019**, *119* (9), 5298–5415. https://doi.org/10.1021/acs.chemrev.8b00593.

(52) Dzenis, Y. Spinning Continuous Fibers for Nanotechnology. *Mater. Sci.* **2004**, *304* (June), 1917–1919. https://doi.org/10.1126/science.1099074.

(53) Kenry; Lim, C. T. Nanofiber Technology: Current Status and Emerging Developments. *Prog. Polym. Sci.* **2017**, *70*, 1–17. https://doi.org/10.1016/j.progpolymsci.2017.03.002.

(54) Thenmozhi, S.; Dharmaraj, N.; Kadirvelu, K.; Kim, H. Y. Electrospun Nanofibers: New Generation Materials for Advanced Applications. *Materials Science and Engineering B: Solid-State Materials for Advanced Technology*. 2017. https://doi.org/10.1016/j.mseb.2017.01.001.

(55) Brennan, D. A.; Shirvani, K.; Rhoads, C. D.; Lofland, S. E.; Beachley, V. Z. Electrospinning and Post-Drawn Processing Effects on the Molecular Organization and Mechanical Properties of Polyacrylonitrile (PAN) Nanofibers. *MRS Commun.* **2019**, *9* (2), 764–772. https://doi.org/10.1557/mrc.2019.67.

(56) Zucchelli, A.; Focarete, M. L.; Gualandi, C.; Ramakrishna, S. Electrospun Nanofibers for Enhancing Structural Performance of Composite Materials. *Polym.*

Adv. Technol. **2011**, *22* (3), 339–349. https://doi.org/10.1002/pat.1837.

(57) Khan, I.; Saeed, K.; Khan, I. Nanoparticles: Properties, Applications and Toxicities. *Arab. J. Chem.* **2019**, *12* (7), 908–931. https://doi.org/10.1016/j.arabjc.2017.05.011.

(58) Papkov, D.; Zou, Y.; Andalib, M. N.; Goponenko, A.; Cheng, S. Z. D.; Dzenis, Y. A. Simultaneously Strong and Tough Ultrafine Continuous Nanofibers. *ACS Nano* **2013**, *7* (4), 3324–3331. https://doi.org/10.1021/nn400028p.

(59) Dzenis, Y.; Cheng, Stephen, Z. D.; Harris, F. *ADVANCED SINGLE-POLYMER NANOFIBER-REINFORCED COMPOSITE - TOWARDS NEXT GENERATION ULTRALIGHT SUPERSTRONG/TOUGH STRUCTURAL MATERIAL*; 2015.

(60) Jiang, S.; Chen, Y.; Duan, G.; Mei, C.; Greiner, A.; Agarwal, S. Electrospun Nanofiber Reinforced Composites: A Review. *Polym. Chem.* **2018**, *9* (20), 2685–2720. https://doi.org/10.1039/c8py00378e.

(61) Dzenis, Y. A.; Reneker, D. H. United States Patent 6265333: Delamination Resistant Composites Prepared by Small Diameter Fiber Reinforcement at Ply Interfaces. 6265333, 2001.

(62) Pozegic, T. R.; King, S. G.; Fotouhi, M.; Stolojan, V.; Silva, S. R. P.; Hamerton, I. Delivering Interlaminar Reinforcement in Composites through Electrospun Nanofibres. *Adv. Manuf. Polym. Compos. Sci.* **2019**, *5* (4), 155–171. https://doi.org/10.1080/20550340.2019.1665226.

(63) Daelemans, L.; van der Heijden, S.; De Baere, I.; Rahier, H.; Van Paepegem, W.; De Clerck, K. Nanofibre Bridging as a Toughening Mechanism in Carbon/Epoxy Composite Laminates Interleaved with Electrospun Polyamide Nanofibrous Veils.

Compos. Sci. Technol. **2015**, *117* (July), 244–256. https://doi.org/10.1016/j.compscitech.2015.06.021.

(64) Daelemans, L.; Van Paepegem, W.; De Clerck, K. *Effect of Interleaved Polymer Nanofibers on the Properties of Glass and Carbon Fiber Composites*; INC, 2020. https://doi.org/10.1016/b978-0-12-819904-6.00011-6.

(65) Daelemans, L.; van der Heijden, S.; De Baere, I.; Rahier, H.; Van Paepegem, W.; De Clerck, K. Improved Fatigue Delamination Behaviour of Composite Laminates with Electrospun Thermoplastic Nanofibrous Interleaves Using the Central Cut-Ply Method. *Compos. Part A Appl. Sci. Manuf.* **2017**, *94*, 10–20. https://doi.org/10.1016/j.compositesa.2016.12.004.

(66) Shivakumar, K.; Lingaiah, S.; Chen, H.; Akangah, P.; Swaminathan, G.; Russell, L. Polymer Nanofabric Interleaved Composite Laminates. *AIAA J.* **2009**, *47* (7), 1723–1729. https://doi.org/10.2514/1.41791.

(67) Saghafi, H.; Fotouhi, M.; Minak, G. Improvement of the Impact Properties of Composite Laminates by Means of Nano-Modification of the Matrix-A Review. *Appl. Sci.* **2018**, *8* (12). https://doi.org/10.3390/app8122406.

(68) Neisiany, R. E.; Khorasani, S. N.; Naeimirad, M.; Lee, J. K. Y.; Ramakrishna, S. Improving Mechanical Properties of Carbon/Epoxy Composite by Incorporating Functionalized Electrospun Polyacrylonitrile Nanofibers. *Macromol. Mater. Eng.* **2017**, *302* (5), 1–11. https://doi.org/10.1002/mame.201600551.

(69) Jurf, R. A.; Pipes, R. B. Interlaminar Fracture of Composite Materials. *J. Compos. Mater.* **1982**, *16* (September), 386–394.

(70) Pagano, N. J.; Pipes, R. B. Some Observations on the Interlaminar Strength of

Composite Laminates. *Int. J. Mech. Sci.* **1973**, *15* (8). https://doi.org/10.1016/0020-7403(73)90099-4.

(71) Jones, R. M. *Mechanics of Composite Materials*, 2nd ed.; CRC Press: Boca Raton, FL, 1999.

(72) Nettles, A. T. Basic Mechanics of Laminated Composite Plates. *NASA Ref. Publ.* **1994**, No. 1351.

(73) Preiß, E. *Fracture Toughness of Freestanding Metallic Thin Films Studied by Bulge Testing*; 2018.

(74) Herakovich, C. T. Edge Effects and Delamination Failures. *J. Strain Anal. Eng. Des.* **1989**, *24* (4), 245–252. https://doi.org/10.1243/03093247V244245.

(75) Pagano, N. J.; Pipes, R. B. The Influence of Stacking Sequence on Laminate Strength. *J. Compos. Mater.* **1971**, *5* (1), 50–57. https://doi.org/10.1177/002199837100500105.

(76) Allegri, G.; Yasaee, M.; Partridge, I. K.; Hallett, S. R. A Novel Model of Delamination Bridging via Z-Pins in Composite Laminates. *Int. J. Solids Struct.* **2014**, *51* (19–20), 3314–3332. https://doi.org/10.1016/j.ijsolstr.2014.05.017.

(77) Mignery, L. A.; Tan, T. M.; Sun, C. T. Use of Stitching To Suppress Delamination in Laminated Composites. *ASTM Spec. Tech. Publ.* **1985**, 371–385. https://doi.org/10.1520/stp36315s.

(78) Wu, X. F. Fracture of Advanced Polymer Composites with Nanofiber Reinforced Interfaces, University of Nebraska-Lincoln, 2003.

(79) Khan, B.; Potter, K.; Wisnom, M. R. Suppression of Delamination at Ply Drops in Tapered Composites by Ply Chamfering. *J. Compos. Mater.* **2006**, *40* (2), 157–

174. https://doi.org/10.1177/0021998305053459.

(80) Masters, J. E. Improved Impact and Delamination Resistance through Interleafing. *Key Eng. Mater.* **1991**, *37*, 317–348. https://doi.org/10.4028/www.scientific.net/KEM.37.317.

(81) Yasaee, M.; Bond, I. P.; Trask, R. S.; Greenhalgh, E. S. Mode I Interfacial Toughening through Discontinuous Interleaves for Damage Suppression and Control. *Compos. Part A Appl. Sci. Manuf.* **2012**, *43* (1), 198–207. https://doi.org/10.1016/j.compositesa.2011.10.009.

(82) Shah, D. K.; Chan, W. S.; Joshi, S. P. Delamination Detection and Suppression in a Composite Laminate Using Piezoceramic Layers. *Smart Mater. Struct.* **1994**, *3* (3), 293–301. https://doi.org/10.1088/0964-1726/3/3/005.

(83) Wang, X.; Song, M. Toughening of Polymers by Graphene. *Nanomater. Energy* **2013**, *2* (5), 265–278. https://doi.org/10.1680/nme.13.00024.

(84) Rosso, P.; Ye, L.; Friedrich, K.; Sprenger, S. A Toughened Epoxy Resin by Silica Nanoparticle Reinforcement. *J. Appl. Polym. Sci.* **2006**, *100* (3), 1849–1855. https://doi.org/https://doi.org/10.1002/app.22805.

(85) No Title https://app.dimensions.ai/discover/publication?search_mode=content&search_text=composites AND nanofibers&search_type=kws&search_field=text_search.

(86) Monteserín, C.; Blanco, M.; Murillo, N.; Pérez-Márquez, A.; Maudes, J.; Gayoso, J.; Laza, J. M.; Aranzabe, E.; Vilas, J. L. Effect of Different Types of Electrospun Polyamide 6 Nanofibres on the Mechanical Properties of Carbon Fibre/Epoxy Composites. *Polymers (Basel).* **2018**, *10* (11).

https://doi.org/10.3390/polym10111190.

(87) Daelemans, L.; Van Der Heijden, S.; De Baere, I.; Rahier, H.; Van Paepegem, W.; De Clerck, K. Damage-Resistant Composites Using Electrospun Nanofibers: A Multiscale Analysis of the Toughening Mechanisms. *ACS Appl. Mater. Interfaces* **2016**, *8* (18), 11806–11818. https://doi.org/10.1021/acsami.6b02247.

(88) Daelemans, L.; Heijden, S. Van Der; Baere, I. De; Rahier, H.; Paepegem, W. Van; Clerck, K. De. Using Aligned Nanofibres for Identifying the Toughening Micromechanisms in Nanofibre Interleaved Laminates. *Compos. Sci. Technol.* **2016**, *124*, 17–26. https://doi.org/10.1016/j.compscitech.2015.11.021.

(89) van der Heijden, S.; Daelemans, L.; De Schoenmaker, B.; De Baere, I.; Rahier, H.; Van Paepegem, W.; De Clerck, K. Interlaminar Toughening of Resin Transfer Moulded Glass Fibre Epoxy Laminates by Polycaprolactone Electrospun Nanofibres. *Compos. Sci. Technol.* **2014**, *104*, 66–73. https://doi.org/10.1016/j.compscitech.2014.09.005.

(90) Razavi, S. M. J.; Neisiany, R. E.; Khorasani, S. N.; Ramakrishna, S.; Berto, F. Effect of Neat and Reinforced Polyacrylonitrile Nanofibers Incorporation on Interlaminar Fracture Toughness of Carbon/Epoxy Composite. *Theor. Appl. Mech. Lett.* **2018**, *8* (2), 126–131. https://doi.org/10.1016/j.taml.2018.02.008.

(91) Daelemans, L.; Kizildag, N.; Van Paepegem, W.; D'hooge, D. R.; De Clerck, K. Interdiffusing Core-Shell Nanofiber Interleaved Composites for Excellent Mode I and Mode II Delamination Resistance. *Compos. Sci. Technol.* **2019**, *175* (February), 143–150. https://doi.org/10.1016/j.compscitech.2019.03.019.

(92) Wilson, D. PMR-15 Processing, Properties and Problems—a Review. *Br. Polym.*

J. **1988**, *20* (5), 405–416. https://doi.org/https://doi.org/10.1002/pi.4980200505.

(93) Ju, J.; Morgan, R. J. Characterization of Microcrack Development in BMI-Carbon Fiber Composite under Stress and Thermal Cycling. *J. Compos. Mater.* **2004**, *38* (22), 2007–2024. https://doi.org/10.1177/0021998304044773.

(94) Inamdar, A.; Cherukattu, J.; Anand, A.; Kandasubramanian, B. Thermoplastic-Toughened High-Temperature Cyanate Esters and Their Application in Advanced Composites. *Ind. Eng. Chem. Res.* **2018**, *57* (13), 4479–4504. https://doi.org/10.1021/acs.iecr.7b05202.

(95) Ogihara, S.; Takeda, N.; Kobayashi, S.; Kobayashi, A. Damage Mechanics Characterization of Transverse Cracking Behavior in Quasi-Isotropic CFRP Laminates with Interlaminar-Toughened Layers. *Int. J. Fatigue* **2002**, *24* (2–4), 93–98. https://doi.org/10.1016/S0142-1123(01)00063-9.

(96) Wang, D.; Xiong, X.; Ren, R.; Ma, X.; Han, A.; Chen, P. Characterization and Properties of High-Temperature Resistant Structure Adhesive Based on Novel Toughened Bismaleimide Resins. *High Perform. Polym.* **2020**, 1–9. https://doi.org/10.1177/0954008320970271.

(97) Feng, Y.; Fang, Z. P.; Gu, A. Toughening of Cyanate Ester Resin by Carboxyl Terminated Nitrile Rubber. *Polym. Adv. Technol.* **2004**, *15* (10), 628–631. https://doi.org/10.1002/pat.519.

(98) Wu, H.; Pan, W.; Lin, D.; Li, H. Electrospinning of Ceramic Nanofibers: Fabrication, Assembly and Applications. *J. Adv. Ceram.* **2012**, *1* (1), 2–23. https://doi.org/10.1007/s40145-012-0002-4.

(99) Toriello, M.; Afsari, M.; Shon, H. K.; Tijing, L. D. Progress on the Fabrication and

Application of Electrospun Nanofiber Composites. *Membranes (Basel).* **2020**, *10* (9), 1–35. https://doi.org/10.3390/membranes10090204.

(100) Panda, P. K. Ceramic Nanofibers by Electrospinning Technique—a Review. *Trans. Indian Ceram. Soc.* **2007**, *66* (2), 65–76. https://doi.org/10.1080/0371750X.2007.11012252.

(101) Dersch, R.; Schaper, A.; Greiner, A.; Wendorff, J. H. Functional Nanofibers by Electrospinning. *New York* **2003**, *44* (23), 53–54.

(102) Song, M. Y.; Kim, D. K.; Ihn, K. J.; Jo, S. M.; Kim, D. Y. Electrospun TiO2 Electrodes for Dye-Sensitized Solar Cells. *Nanotechnology* **2004**, *15* (12), 1861–1865. https://doi.org/10.1088/0957-4484/15/12/030.

(103) Srivastava, R. K. *Electrospinning of Patterned and 3D Nanofibers*; Elsevier Ltd., 2017. https://doi.org/10.1016/B978-0-08-100907-9.00016-7.

(104) Dzenis, Y.; Wen, Y. Continuous Carbon Nanofibers for Nanofiber Composites. *MRS Online Proc. Libr.* **2001**, *702*.

(105) Ding, Y.; Hou, H.; Zhao, Y.; Zhu, Z.; Fong, H. Electrospun Polyimide Nanofibers and Their Applications. *Prog. Polym. Sci.* **2016**, *61*, 67–103. https://doi.org/10.1016/j.progpolymsci.2016.06.006.

(106) Zhang, M.; Niu, H.; Wu, D. Polyimide Fibers with High Strength and High Modulus: Preparation, Structures, Properties, and Applications. *Macromol. Rapid Commun.* **2018**, *39* (20), 1–14. https://doi.org/10.1002/marc.201800141.

(107) Tamai, S.; Yamaguchi, A.; Ohta, M. Melt Processible Polyimides and Their Chemical Structures. *Polymer (Guildf).* **1996**, *37* (16), 3683–3692. https://doi.org/10.1016/0032-3861(96)00178-4.

(108) Zhang, R.; Liu, C.; Hsu, P. C.; Zhang, C.; Liu, N.; Zhang, J.; Lee, H. R.; Lu, Y.; Qiu, Y.; Chu, S.; et al. Nanofiber Air Filters with High-Temperature Stability for Efficient PM2.5 Removal from the Pollution Sources. *Nano Lett.* **2016**, *16* (6), 3642–3649. https://doi.org/10.1021/acs.nanolett.6b00771.

(109) Huang, C.; Wang, S.; Zhang, H.; Li, T.; Chen, S.; Lai, C.; Hou, H. High Strength Electrospun Polymer Nanofibers Made from BPDA-PDA Polyimide. *Eur. Polym. J.* **2006**, *42* (5), 1099–1104. https://doi.org/10.1016/j.eurpolymj.2005.11.005.

(110) Chen, S.; Hu, P.; Greiner, A.; Cheng, C.; Cheng, H.; Chen, F.; Hou, H. Electrospun Nanofiber Belts Made from High Performance Copolyimide. *Nanotechnology* **2008**, *19* (1). https://doi.org/10.1088/0957-4484/19/01/015604.

(111) He, Y.; Han, D.; Chen, J.; Ding, Y.; Jiang, S.; Hu, C.; Chen, S.; Hou, H. Highly Strong and Highly Tough Electrospun Polyimide/Polyimide Composite Nanofibers from Binary Blend of Polyamic Acids. *RSC Adv.* **2014**, *4* (104), 59936–59942. https://doi.org/10.1039/c4ra10075a.

(112) Yao, J.; Pantano, M. F.; Pugno, N. M.; Bastiaansen, C. W. M.; Peijs, T. High-Performance Electrospun Co-Polyimide Nanofibers. *Polymer (Guildf).* **2015**, *76*, 105–112. https://doi.org/10.1016/j.polymer.2015.08.053.

(113) Cheng, C.; Chen, J.; Chen, F.; Hu, P.; Wu, X.-F.; Reneker, D. H.; Hou, H. High-Strength and High-Toughness Polyimide Nanofibers: Synthesis and Characterization. *J. Appl. Polym. Sci.* **2010**, *116* (5), 2658–2667. https://doi.org/10.1002/app.

(114) Goponenko, A. V.; Hou, H.; Dzenis, Y. A. Avoiding Fusion of Electrospun 3,3′,4,4′-Biphenyltetracarboxylic Dianhydride-4,4′-Oxydianiline Copolymer

Nanofibers during Conversion to Polyimide. *Polymer (Guildf).* **2011**, *52*, 3776–3782.

(115) Wimmer, G.; Kitzmüller, W.; Pinter, G.; Wettemann, T.; Pettermann, H. E. Computational and Experimental Investigation of Delamination in L-Shaped Laminated Composite Components. *Eng. Fract. Mech.* **2009**, *76* (18), 2810–2820. https://doi.org/10.1016/j.engfracmech.2009.06.007.

(116) Xiao, Y.; Ishikawa, T. Bearing Strength and Failure Behavior of Bolted Composite Joints (Part I: Experimental Investigation). *Compos. Sci. Technol.* **2005**, *65* (7–8), 1022–1031. https://doi.org/10.1016/j.compscitech.2005.02.011.

(117) ASTM D5528. *Standard Test Method for Mode I Interlaminar Fracture Toughness of Unidirectional Fiber-Reinforced Polymer Matrix Composites*; 2014; pp 1–12. https://doi.org/10.1520/D5528-13.2.

(118) ASTM D7905. Standard Test Method for Determination of the Mode II Interlaminar Fracture Toughness of Unidirectional Fiber-Reinforced Polymer Matrix Composites. *ASTM Int.* **2014**, *i*, 1–18. https://doi.org/10.1520/D7905.

(119) ASTM D6671. *Standard Test Method for Mixed Mode I-Mode II Interlaminar Fracture Toughness of Unidirectional Fiber Reinforced Polymer Matrix Composites*; 2006; pp 1–15. https://doi.org/10.1520/D6671.

(120) ASTM D3039. Standard Test Method for Tensile Properties of Polymer Matrix Composite Materials. *ASTM Int.* **2014**, 1–13. https://doi.org/10.1520/D3039.

(121) Dhurvey, P.; Mittal, N. D. Review on Various Studies of Composite Laminates with Ply Drop-Off. *ARPN J. Eng. Appl. Sci.* **2013**, *8* (8), 595–605.

(122) He, K.; Hoa, S. V.; Ganesan, R. The Study of Tapered Laminated Composite

Structures: A Review. *Compos. Sci. Technol.* **2000**, *60* (14), 2643–2657. https://doi.org/10.1016/S0266-3538(00)00138-X.

(123) Thomsen, O. .; Bozhevolnaya, E.; Lyckegaard, A. *SANDWICH STRUCTURES 7: ADVANCING WITH SANDWICH STRUCTURES AND MATERIALS*; Springer, 2005.

(124) Galińska, A. Mechanical Joining of Fibre Reinforced Polymer Composites to Metals—a Review. Part II: Riveting, Clinching, Non-Adhesive Form-Locked Joints, Pin and Loop Joining. *Polymers (Basel).* **2020**, *12* (10), 1–48. https://doi.org/10.3390/polym12102252.

(125) Chang, F.; Scott, R. A.; Springer, G. S. Strength of Mechanically Fastened Composite Joints. *J. Compos. Mater.* **1982**, *16*, 470–494.

(126) Camanho, P. P.; Matthews, F. L. Delamination Onset Prediction in Mechanically Fastened Joints in Composite Laminates. *Journal of Composite Materials*. 1999, pp 906–927. https://doi.org/10.1177/002199839903301002.

(127) Galińska, A. Mechanical Joining of Fibre Reinforced Polymer Composites to Metals—a Review. Part i: Bolted Joining. *Polymers (Basel).* **2020**, *12* (10), 1–48. https://doi.org/10.3390/polym12102252.

(128) Cohen, D.; Toombes, Y. T.; Johnson, A. K.; Hansen, M. F. Pressurized Ring Test for Composite Pressure Vessel Hoop Strength and Stiffness Evaluation. *J. Compos. Technol. Res.* **1995**, *17* (4), 331–340. https://doi.org/10.1520/ctr10453j.

(129) Cohen, D. Multi-Axial Composite Tube Test Method. *ASTM Int.* **2002**, 17–29.

(130) Icardi, U.; Bertetto, A. M. An Evaluation of the Influence of Geometry and of Material Properties at Free Edges and at Corners of Composite Laminates.

Comput. Struct. **1995**, *57* (4), 555–571. https://doi.org/10.1016/0045-7949(95)00069-S.

(131) Dimitrov, A.; Andrä, H.; Schnack, E. Singularities near Three-Dimensional Corners in Composite Laminates. *Int. J. Fract.* **2002**, *115* (4), 361–375. https://doi.org/10.1023/A:1016320103641.

(132) Mathews, M. J.; Swanson, S. R. Characterization of the Interlaminar Fracture Toughness of a Laminated Carbon/Epoxy Composite. *Compos. Sci. Technol.* **2007**, *67* (7–8), 1489–1498. https://doi.org/10.1016/j.compscitech.2006.07.035.

(133) Anderson, T. L. *Fracture Mechanics*, Fourth.; CRC Press: Boca Raton, FL, 2017.

(134) Meireman, T.; Daelemans, L.; Rijckaert, S.; Rahier, H.; Van Paepegem, W.; De Clerck, K. Delamination Resistant Composites by Interleaving Bio-Based Long-Chain Polyamide Nanofibers through Optimal Control of Fiber Diameter and Fiber Morphology. *Compos. Sci. Technol.* **2020**, *193*, 108126. https://doi.org/10.1016/j.compscitech.2020.108126.

(135) Beckermann, G. W.; Pickering, K. L. Mode I and Mode II Interlaminar Fracture Toughness of Composite Laminates Interleaved with Electrospun Nanofibre Veils. *Compos. Part A Appl. Sci. Manuf.* **2015**, *72*, 11–21. https://doi.org/10.1016/j.compositesa.2015.01.028.

(136) Wu, X.; Zholobko, O. Experimental Study of the Probabilistic Fatigue Residual Strength of a Carbon Fiber-Reinforced Polymer Matrix Composite. *J. Compos. Sci.* **2020**.

(137) ASTM D3518. Standard Test Method for In-Plane Shear Response of Polymer Matrix Composite Materials by Tensile Test of a +-45° Laminate. *ASTM Int.* **2007**,

94 (Reapproved), 1–7. https://doi.org/10.1520/D3518.

(138) Whitney, J. M.; Browning, C. E.; Hoogsteden, W. Double Cantilever Beam Tests for Characterizing Mode I Delamination of Composite Materials. *J. Reinf. Plast. Compos.* **1982**, *1* (4), 297–313. https://doi.org/10.1177/073168448200100402.

(139) Prasad, M. S. S.; Venkatesha, C. S.; Jayaraju, T. Experimental Methods of Determining Fracture Toughness of Fiber Reinforced Polymer Composites under Various Loading Conditions. *J. Miner. Mater. Charact. Eng.* **2011**, *10* (13), 1263–1275. https://doi.org/10.4236/jmmce.2011.1013099.

(140) Obrien, T. K.; Martin, R. H. *Results of ASTM Round Robin Testing for Mode I Interlaminar Fracture Toughness of Composite Materials*; 1992.

(141) Berry, J. P. Determination of Fracture Surface Energies by the Cleavage Technique. *J. Appl. Phys.* **1963**, *34* (1), 62–68. https://doi.org/10.1063/1.1729091.

(142) Williams, J. G. On the Calculation of Energy Release Rates for Cracked Laminates. *Int. J. Fract.* **1988**, *36* (2), 101–119. https://doi.org/10.1007/BF00017790.

(143) Hashemi, S.; Kinloch, A. J.; Williams, J. G. Corrections Needed in Double-Cantilever Beam Tests for Assessing the Interlaminar Failure of Fibre-Composites. *J. Mater. Sci. Lett.* **1989**, *8* (2), 125–129. https://doi.org/10.1007/BF00730701.

(144) Kageyama, K.; Hojo, M. Proposed Methods for Interlaminar Fracture Toughness Tests of Composite Laminates. *Achiev. Compos. Japan United States* **1990**, 227–234.

(145) Davies, P.; Blackman, B. R. K.; Brunner, A. J. Standard Test Methods for Delamination Resistance of Composite Materials: Current Status. *Appl. Compos.*

Mater. **1998**, *5* (6), 345–364. https://doi.org/10.1023/A:1008869811626.

(146) Tada, H.; Paris, P. C.; Irwin, G. R. *The Stress Analysis of Cracks Handbook*; ASME Press: New York, 2000. https://doi.org/10.1115/1.801535.ch2.

(147) Kelkar, A. D.; Mohan, R.; Bolick, R.; Shendokar, S. Effect of Nanoparticles and Nanofibers on Mode I Fracture Toughness of Fiber Glass Reinforced Polymeric Matrix Composites. *Mater. Sci. Eng. B Solid-State Mater. Adv. Technol.* **2010**, *168* (1), 85–89. https://doi.org/10.1016/j.mseb.2010.01.015.

(148) Bilge, K.; Papila, M. *Interlayer Toughening Mechanisms of Composite Materials*; Elsevier Ltd., 2015. https://doi.org/10.1016/B978-1-78242-279-2.00010-X.

(149) Toray Advanced Composites. RS3C-T1100GC CE Prepreg Properties from Toray.

(150) Meireman, T.; Daelemans, L.; Rijckaert, S.; Rahier, H.; Van Paepegem, W.; De Clerck, K. Delamination Resistant Composites by Interleaving Bio-Based Long-Chain Polyamide Nanofibers through Optimal Control of Fiber Diameter and Fiber Morphology. *Compos. Sci. Technol.* **2020**, *193* (January), 108126. https://doi.org/10.1016/j.compscitech.2020.108126.

(151) Nilakantan, G.; Nutt, S. Reuse and Upcycling of Thermoset Prepreg Scrap: Case Study with out-of-Autoclave Carbon Fiber/Epoxy Prepreg. *J. Compos. Mater.* **2018**, *52* (3), 341–360. https://doi.org/10.1177/0021998317707253.

(152) Nakagawa, T.; Ko, S.; Salviato, M. IMPACT OF PREPREG AGING ON THE MECHANICAL AND FRACTURE BEHAVIOR IMPACT OF PREPREG AGING ON THE MECHANICAL AND FRACTURE BEHAVIOR OF CHOPPED FIBER COMPOSITES. **2022**, No. March.

(153) Grunenfelder, L. K.; Centea, T.; Hubert, P.; Nutt, S. R. Effect of Room-

Temperature out-Time on Tow Impregnation in an out-of-Autoclave Prepreg. *Compos. Part A Appl. Sci. Manuf.* **2013**, *45*, 119–126. https://doi.org/10.1016/j.compositesa.2012.10.001.

(154) Patz Materials & Technologies. PMT-F3 Data Sheet.

(155) van der Heijden, S.; Daelemans, L.; De Bruycker, K.; Simal, R.; De Baere, I.; Van Paepegem, W.; Rahier, H.; De Clerck, K. Novel Composite Materials with Tunable Delamination Resistance Using Functionalizable Electrospun SBS Fibers. *Compos. Struct.* **2017**, *159*, 12–20. https://doi.org/10.1016/j.compstruct.2016.09.057.

(156) Mathur, R. B.; Bahl, O. P.; Sivaram, P. Thermal Degradation of Polyacrylonitrile Fibres. *Curr. Sci.* **1992**, *62* (10), 662–669.

(157) Intsituto Granado de Tecnologia da Poliacrilonitrila. Polyacrylonitrile properties http://www.igtpan.com/Ingles/propriedade-poli.asp (accessed May 16, 2022).

(158) ASTM D790. Standard Test Methods for Flexural Properties of Unreinforced and Reinforced Plastics and Electrical Insulating Materials. *ASTM Int.* **2002**, 1–12. https://doi.org/10.1520/D0790-17.2.

(159) Carlsson, L. A.; Gillespie, J. W.; Pipes, R. B. On the Analysis and Design of the End Notched Flexure (ENF) Specimen for Mode II Testing. *J. Compos. Mater.* **1986**, *20* (6), 594–604. https://doi.org/10.1177/002199838602000606.

(160) Carlsson, L. A.; Gillespie, J. W.; Trethewey, B. R. Mode II Interlaminar Fracture of Graphite/Epoxy and Graphite/PEEK. *J. Reinf. Plast. Compos.* **1986**, *5* (3), 170–187. https://doi.org/10.1177/073168448600500302.

(161) O'Brien, T.; Murri, G.; Salpekar, S. Interlaminar Shear Fracture Toughness and

Fatigue Thresholds for Composite Materials. *Compos. Mater. Fatigue Fract. Second Vol.* **2008**, 222-222–229. https://doi.org/10.1520/stp10418s.

(162) Davies, P.; Sims, G. D.; Blackman, B. R. K.; Brunner, A. J.; Kageyama, K.; Hojo, M.; Tanaka, K.; Murri, G.; Rousseau, C.; Gieseke, B.; et al. Comparison of Test Configurations for Determination of Mode II Interlaminar Fracture Toughness Results from International Collaborative Test Programme. *Plast. Rubber Compos. Process. Appl.* **1999**, *28* (9), 432–437. https://doi.org/10.1179/146580199101540600.

(163) Gibson, R. F. *Principles of Composite Material Mechanics*, 3rd ed.; 2012.

(164) Suo, Z.; Bao, G.; Fan, B. Delamination R-Curve Phenomena Due to Damage. *J. Mech. Phys. Solids* **1992**, *40* (1), 1–16. https://doi.org/https://doi.org/10.1016/0022-5096(92)90198-B.

(165) Zehnder, A. T. *Fracture Mechanics*; 2012.

(166) Schuecker, C.; Davidson, B. D. Evaluation of the Accuracy of the Four-Point Bend End-Notched Flexure Test for Mode II Delamination Toughness Determination. *Compos. Sci. Technol.* **2000**, *60* (11), 2137–2146. https://doi.org/10.1016/S0266-3538(00)00113-5.

(167) Alfred Franklin, V.; Christopher, T. Generation of R-Curve from 4ENF Specimens: An Experimental Study. *J. Compos.* **2014**, *2014* (November), 1–10. https://doi.org/10.1155/2014/956268.

(168) Zhang, J.; Yang, T.; Lin, T.; Wang, C. H. Phase Morphology of Nanofibre Interlayers: Critical Factor for Toughening Carbon/Epoxy Composites. *Compos. Sci. Technol.* **2012**, *72* (2), 256–262.

https://doi.org/10.1016/j.compscitech.2011.11.010.

(169) Blanchfield, J. P.; Allegri, G. Fatigue Delamination Initiation in L-Bend CFRP Coupons. *16th Eur. Conf. Compos. Mater. ECCM 2014* **2014**, No. June, 22–26.

(170) Gözlüklü, B.; Coker, D. Modeling of the Dynamic Delamination of L-Shaped Unidirectional Laminated Composites. *Compos. Struct.* **2012**, *94* (4), 1430–1442. https://doi.org/10.1016/j.compstruct.2011.11.015.

(171) Roozbehjavan, P.; Tavakol, B.; Ahmed, A.; Koushyar, H.; Das, R.; Joven, R.; Minaie, B. Experimental and Numerical Study of Distortion in Flat, L-Shaped, and U-Shaped Carbon Fiber-Epoxy Composite Parts. *J. Appl. Polym. Sci.* **2014**, *131* (13). https://doi.org/10.1002/app.40439.

(172) Geleta, T. N.; Woo, K.; Lee, B. Delamination Behavior of L-Shaped Laminated Composites. *Int. J. Aeronaut. Sp. Sci.* **2018**, *19* (2), 363–374. https://doi.org/10.1007/s42405-018-0038-y.

(173) Raju, R.; Prusty, B. G.; Kelly, D. W.; Peng, G. D.; Lyons, D. Failure Characterisation of L-Bend Curved Composite Laminates. *Trans. R. Inst. Nav. Archit. Part B Int. J. Small Cr. Technol.* **2010**, *152* (2). https://doi.org/10.3940/rina.ijsct.2010.b2.107.

(174) Zhong, Q. F. D. Y. C.; Hu, X. H.; Cao, D. F.; Li, S. X. Delamination and Matrix Cracking in L-Shaped Cross-Ply Composite Laminates under Four-Point Bending. 2.

(175) O'Higgins, R. M.; Padhi, G. S.; McCarthy, M. A.; McCarthy, C. T. Experimental and Numerical Study of Open-Hole Tensile Strength of Carbon/Epoxy Composites. *Probl. Peredachi Informatsii* **2004**, *40* (2), 50–62.

https://doi.org/10.1023/B.

(176) Hallett, S. R.; Green, B. G.; Jiang, W. G.; Wisnom, M. R. An Experimental and Numerical Investigation into the Damage Mechanisms in Notched Composites. *Compos. Part A Appl. Sci. Manuf.* **2009**, *40* (5), 613–624. https://doi.org/10.1016/j.compositesa.2009.02.021.

(177) Wisnom, M. R.; Hallett, S. R. The Role of Delamination in Strength, Failure Mechanism and Hole Size Effect in Open Hole Tensile Tests on Quasi-Isotropic Laminates. *Compos. Part A Appl. Sci. Manuf.* **2009**, *40* (4), 335–342. https://doi.org/10.1016/j.compositesa.2008.12.013.

(178) Salleh, Z.; Berhan, M. N.; Hyie, K. M.; Taib, Y. M.; Kalam, A.; Roselina, N. R. N. Open Hole Tensile Properties of Kenaf Composite and Kenaf/Fibreglass Hybrid Composite Laminates. *Procedia Eng.* **2013**, *68*, 399–404. https://doi.org/10.1016/j.proeng.2013.12.198.

(179) Fan, H. T.; Wang, H. Predicting the Open-Hole Tensile Strength of Composite Plates Based on Probabilistic Neural Network. *Appl. Compos. Mater.* **2014**, *21* (6), 827–840. https://doi.org/10.1007/s10443-014-9387-2.

(180) ASTM D5766. Standard Test Method for Open-Hole Tensile Strength of Polymer Matrix Composite. *ASTM Int.* **2011**, *11* (Reapproved), 1–7. https://doi.org/10.1520/D5766.

(181) Davies, P.; Carlsson, L. A. Delamination of Composite Cylinders. *Major Accompl. Compos. Mater. Sandw. Struct. An Anthol. ONR Spons. Res.* **2009**, 67–85. https://doi.org/10.1007/978-90-481-3141-9_4.

(182) Foral, R. F.; Gilbreath, D. R. Delamination Failure Modes in Filament-Wound

Composite Tubes. *ASTM Int.* **1989**, 313–325.

(183) Raju. Delamination Damage Analysis of Curved Composites Subjected to Compressive Load Using Cohesive Zone Modelling. *QuEST Glob.* **2014**.

(184) Rasheed, H. A.; Tassoulas, J. L. Delamination Growth in Long Composite Tubes under External Pressure. *Int. J. Fract.* **2001**, *108* (1), 1–23. https://doi.org/10.1023/A:1007514920510.

(185) Atlihan, G. Buckling Analysis of Delaminated Composite Beams. *Indian J. Eng. Mater. Sci.* **2013**, *20* (4), 276–282.

(186) Hamed, M. A.; Nosier, A.; Farrahi, G. H. Separation of Delamination Modes in Composite Beams with Symmetric Delaminations. *Mater. Des.* **2006**, *27* (10), 900–910. https://doi.org/10.1016/j.matdes.2005.03.006.

(187) Roy, T.; Chakraborty, D. Delamination in FRP Laminates with Holes under Transverse Impact. *Mater. Des.* **2008**, *29* (1), 124–132. https://doi.org/10.1016/j.matdes.2006.11.016.

(188) Bilge, K.; Venkataraman, S.; Menceloglu, Y. Z.; Papila, M. Global and Local Nanofibrous Interlayer Toughened Composites for Higher In-Plane Strength. *Compos. Part A Appl. Sci. Manuf.* **2014**, *58*, 73–76. https://doi.org/10.1016/j.compositesa.2013.12.001.

(189) Cox, B. N.; Massabò, R.; Kedward, K. T. Suppression of Delaminations in Curved Structures by Stitching. *Compos. Part A Appl. Sci. Manuf.* **1996**, *27* (12 PART A), 1133–1138. https://doi.org/10.1016/1359-835X(96)00084-X.

(190) Guzman de Villoria, R.; Hallander, P.; Ydrefors, L.; Nordin, P.; Wardle, B. L. In-Plane Strength Enhancement of Laminated Composites via Aligned Carbon

Nanotube Interlaminar Reinforcement. *Compos. Sci. Technol.* **2016**, *133*, 33–39. https://doi.org/10.1016/j.compscitech.2016.07.006.

(191) Gumgol, U.; Umarfarooq, M. A.; Huddar, D.; Vastrad, J. V.; Wilkinson, A.; Shivakumar Gouda, P. S. Influence of Kenaf and GO on Interlaminar Radial Stresses in Glass/Epoxy L-Bend Laminates. *SN Appl. Sci.* **2019**, *1* (1), 1–8. https://doi.org/10.1007/s42452-018-0108-6.

(192) Lekhnitskiy, S. G. *Anisotropic Plates*; 1968.

(193) ASTM D6415. Standard Test Method for Measuring the Curved Beam Strength of a Fiber-Reinforced Polymer-Matrix Composite. *ASTM Int.* **2021**, No. D6415. https://doi.org/10.1520/D6415.

(194) De Schoenmaker, B.; Van Der Heijden, S.; De Baere, I.; Van Paepegem, W.; De Clerck, K. Effect of Electrospun Polyamide 6 Nanofibres on the Mechanical Properties of a Glass Fibre/Epoxy Composite. *Polym. Test.* **2013**, *32* (8), 1495–1501. https://doi.org/10.1016/j.polymertesting.2013.09.015.

(195) Manh, C. V.; Choi, H. J. Enhancement of Interlaminar Fracture Toughness of Carbon Fiber/Epoxy Composites Using Silk Fibroin Electrospun Nanofibers. *Polym. - Plast. Technol. Eng.* **2016**, *55* (10), 1048–1056. https://doi.org/10.1080/03602559.2015.1132459.

(196) Shao, Y.; Yashiro, T.; Okubo, K.; Fujii, T. Effect of Cellulose Nano Fiber (CNF) on Fatigue Performance of Carbon Fiber Fabric Composites. *Compos. Part A Appl. Sci. Manuf.* **2015**, *76*, 244–254. https://doi.org/10.1016/j.compositesa.2015.05.033.

(197) Sun, C. T.; Zhou, S. G. Failure of Quasi-Isotropic Composite Laminates with Free Edges. *J. Reinf. Plast. Compos.* **1988**, *7* (6), 515–557.

https://doi.org/10.1177/073168448800700602.

(198) Kannan, V. K.; Murali, V.; Rajadurai, A.; Nageswara Rao, B. Tension and Compression Strength Evaluation of Composite Plates with Circular Holes. *J. Reinf. Plast. Compos.* **2010**, *29* (10), 1500–1514. https://doi.org/10.1177/0731684409337904.

(199) Kim, J. S. A Comparison Study of Composite Laminated Plates with Holes Under Tension, California Polytechnic State University, 2017.

(200) Huang, C.; Ju, S.; He, M.; Zheng, Q.; He, Y.; Xiao, J.; Zhang, J.; Jiang, D. Identification of Failure Modes of Composite Thin-Ply Laminates Containing Circular Hole under Tension by Acoustic Emission Signals. *Compos. Struct.* **2018**, *206* (April), 70–79. https://doi.org/10.1016/j.compstruct.2018.08.019.

(201) Green, B. G.; Wisnom, M. R.; Hallett, S. R. An Experimental Investigation into the Tensile Strength Scaling of Notched Composites. *Compos. Part A Appl. Sci. Manuf.* **2007**, *38* (3), 867–878. https://doi.org/10.1016/j.compositesa.2006.07.008.

(202) Shalev, D.; Reifsnider, K. L. Study of the Onset of Delamination at Holes in Composite Laminates. *J. Compos. Mater.* **1990**, *24* (1), 42–71. https://doi.org/10.1177/002199839002400103.

(203) Chang, K. Y.; Llu, S.; Chang, fu K. Damage Tolerance of Laminated Composites Containing an Open Hole and Subjected to Tensile Loadings. *J. Compos. Mater.* **1991**, *25* (3), 274–301. https://doi.org/10.1177/002199839102500303.

(204) Zhao, Y. Stress and Strength of Laminated Composite Containing a Circular Hole., Louisiana State University, 1998.

(205) Toubal, L.; Karama, M.; Lorrain, B. Stress Concentration in a Circular Hole in

Composite Plate. *Compos. Struct.* **2005**, *68* (1), 31–36. https://doi.org/10.1016/j.compstruct.2004.02.016.

(206) Liu, D. F.; Tang, Y. J.; Cong, W. L. A Review of Mechanical Drilling for Composite Laminates. *Compos. Struct.* **2012**, *94* (4), 1265–1279. https://doi.org/10.1016/j.compstruct.2011.11.024.

(207) Geng, D.; Liu, Y.; Shao, Z.; Lu, Z.; Cai, J.; Li, X.; Jiang, X.; Zhang, D. Delamination Formation, Evaluation and Suppression during Drilling of Composite Laminates: A Review. *Compos. Struct.* **2019**, *216* (January), 168–186. https://doi.org/10.1016/j.compstruct.2019.02.099.

(208) Kedward, K. T.; Wilson, R. S.; McLean, S. K. Flexure of Simply Curved Composite Shapes. *Composites* **1989**, *20* (6), 527–536. https://doi.org/https://doi.org/10.1016/0010-4361(89)90911-7.

(209) Martin, R. H. Delamination Failure in a Unidirectional Curved Composite Laminate. *ASTM Spec. Tech. Publ.* **1992**, No. 1120, 365–383. https://doi.org/10.1520/stp20170s.

(210) Hiel, C. C.; Sumich, M.; Chappell, D. P. A Curved Beam Test Specimen for Determining the Interlaminar Tensile Strength of a Laminated Composite. *J. Compos. Mater.* **1991**, *25* (7), 854–868. https://doi.org/10.1177/002199839102500705.

(211) Jackson, W. C.; Martin, R. H. Interlaminar Tensile Strength Specimen. *ASTM Spec. Tech. Publ.* **1993**, No. 1206, 333–354. https://doi.org/10.1520/stp12638s.

(212) Hassan, M. H.; Othman, A. R. Contribution of Processing Parameters on Void Content in the Vacuum Bagging Configurations of L-Shaped Composite

Laminates. *Int. J. Adv. Manuf. Technol.* **2017**, *93* (1–4), 1333–1345. https://doi.org/10.1007/s00170-017-0585-6.

(213) Hancox, N. L. Thermal Effects on Polymer Matrix Composites: Part 1. Thermal Cycling. *Mater. Des.* **1998**, *19*, 8591.

(214) Nahm, S. Use Of Dynamic Mechanical Analysis in Thermoset Resin Development (For Composites Applications). *Compos. Conv. trade show* **2001**, 1–13.

(215) Franck, A. *Viscoelasticity and Dynamic Mechanical Testing*; 1993.

(216) Goertzen, W. K.; Kessler, M. R. Thermal and Mechanical Evaluation of Cyanate Ester Composites with Low-Temperature Processability. *Compos. Part A Appl. Sci. Manuf.* **2007**, *38* (3), 779–784. https://doi.org/10.1016/j.compositesa.2006.09.005.

(217) Chung, K.; Seferis, J. C. Evaluation of Thermal Degradation on Carbon Fiber/Cyanate Ester Composites. *Polym. Degrad. Stab.* **2001**, *71* (3), 425–434. https://doi.org/10.1016/S0141-3910(00)00194-4.

(218) Özden, E.; Menceloğlu, Y. Z.; Papila, M. Engineering Chemistry of Electrospun Nanofibers and Interfaces in Nanocomposites for Superior Mechanical Properties. *ACS Appl. Mater. Interfaces* **2010**, *2* (7), 1788–1793. https://doi.org/10.1021/am100288r.

(219) Wu, M.; Wu, Y.; Liu, Z.; Liu, H. Optically Transparent Poly(Methyl Methacrylate) Composite Films Reinforced with Electrospun Polyacrylonitrile Nanofibers. *J. Compos. Mater.* **2012**, *46* (21), 2731–2738. https://doi.org/10.1177/0021998311431995.

(220) Liao, H.; Wu, Y.; Wu, M.; Zhan, X.; Liu, H. Aligned Electrospun Cellulose Fibers

Reinforced Epoxy Resin Composite Films with High Visible Light Transmittance. *Cellulose* **2012**, *19* (1), 111–119. https://doi.org/10.1007/s10570-011-9604-1.

(221) Tang, C.; Wu, M.; Wu, Y.; Liu, H. Effects of Fiber Surface Chemistry and Size on the Structure and Properties of Poly(Vinyl Alcohol) Composite Films Reinforced with Electrospun Fibers. *Compos. Part A Appl. Sci. Manuf.* **2011**, *42* (9), 1100–1109. https://doi.org/10.1016/j.compositesa.2011.04.015.

(222) Alarifi, I. M.; Khan, W. S.; Rahman, A. S.; Kostogorova-Beller, Y.; Asmatulu, R. Synthesis, Analysis and Simulation of Carbonized Electrospun Nanofibers Infused Carbon Prepreg Composites for Improved Mechanical and Thermal Properties. *Fibers Polym.* **2016**, *17* (9), 1449–1455. https://doi.org/10.1007/s12221-016-6179-3.

(223) Beylergil, B.; Tanoğlu, M.; Aktaş, E. Modification of Carbon Fibre/Epoxy Composites by Polyvinyl Alcohol (PVA) Based Electrospun Nanofibres. *Adv. Compos. Lett.* **2016**, *25* (3), 69–76. https://doi.org/10.1177/096369351602500303.

(224) Lipol, L. S.; Rahman, M. Electrospinning and Electrospun Nanofibers. *World J. Nano Sci. Eng.* **2016**, *6*, 45–50. https://doi.org/10.4236/wjnse.2016.62005.

(225) Alubaidy, A.; Venkatakrishnan, K.; Tan, B. Nanofibers Reinforced Polymer Composite Microstructures. *Intech* **2016**, *I*, 13. https://doi.org/10.5772/57101.

(226) Ren, C. PAN Nanofibers and Nanofiber Reinforced Composites, University of Nebraska-Lincoln, 2013.

(227) Crosby, A. J.; Lee, J. Y. Polymer Nanocomposites: The “Nano” Effect on Mechanical Properties. *Polym. Rev.* **2007**, *47* (2), 217–229. https://doi.org/10.1080/15583720701271278.

(228) Puggal, S.; Dhall, N.; Singh, N.; Litt, M. S. A Review on Polymer Nanocomposites: Synthesis, Characterization and Mechanical Properties. *Indian J. Sci. Technol.* **2016**, *9* (4). https://doi.org/10.17485/ijst/2016/v9i4/81100.

(229) Bradford, P. D.; Wang, X.; Zhao, H.; Maria, J. P.; Jia, Q.; Zhu, Y. T. A Novel Approach to Fabricate High Volume Fraction Nanocomposites with Long Aligned Carbon Nanotubes. *Compos. Sci. Technol.* **2010**, *70* (13), 1980–1985. https://doi.org/10.1016/j.compscitech.2010.07.020.

(230) Gonnet, P.; Liang, Z.; Choi, E. S.; Kadambala, R. S.; Zhang, C.; Brooks, J. S.; Wang, B.; Kramer, L. Thermal Conductivity of Magnetically Aligned Carbon Nanotube Buckypapers and Nanocomposites. *Curr. Appl. Phys.* **2006**, *6* (1), 119–122. https://doi.org/10.1016/j.cap.2005.01.053.

(231) Ürk, D.; Demir, E.; Bulut, O.; Çakıroğlu, D.; Cebeci, F.; Lütfi Öveçoğlu, M.; Cebeci, H. Understanding the Polymer Type and CNT Orientation Effect on the Dynamic Mechanical Properties of High Volume Fraction CNT Polymer Nanocomposites. *Compos. Struct.* **2016**, *155*, 255–262. https://doi.org/10.1016/j.compstruct.2016.05.087.

(232) Cheng, Q. F.; Wang, J. P.; Wen, J. J.; Liu, C. H.; Jiang, K. L.; Li, Q. Q.; Fan, S. S. Carbon Nanotube/Epoxy Composites Fabricated by Resin Transfer Molding. *Carbon N. Y.* **2010**, *48* (1), 260–266. https://doi.org/10.1016/j.carbon.2009.09.014.

(233) Sui, C.; Pan, Z.; Headrick, R. J.; Yang, Y.; Wang, C.; Yuan, J.; He, X.; Pasquali, M.; Lou, J. Aligned-SWCNT Film Laminated Nanocomposites: Role of the Film on Mechanical and Electrical Properties. *Carbon N. Y.* **2018**, *139*, 680–687. https://doi.org/10.1016/j.carbon.2018.07.025.

(234) Mora, R. J.; Vilatela, J. J.; Windle, A. H. Properties of Composites of Carbon Nanotube Fibres. *Compos. Sci. Technol.* **2009**, *69* (10), 1558–1563. https://doi.org/10.1016/j.compscitech.2008.11.038.

(235) Bogdanovich, A. E.; Bradford, P. D. Carbon Nanotube Yarn and 3-D Braid Composites. Part I: Tensile Testing and Mechanical Properties Analysis. *Compos. Part A Appl. Sci. Manuf.* **2010**, *41* (2), 230–237. https://doi.org/10.1016/j.compositesa.2009.10.002.

(236) Wang, Z.; Liang, Z.; Wang, B.; Zhang, C.; Kramer, L. Processing and Property Investigation of Single-Walled Carbon Nanotube (SWNT) Buckypaper/Epoxy Resin Matrix Nanocomposites. *Compos. Part A Appl. Sci. Manuf.* **2004**, *35* (10), 1225–1232. https://doi.org/10.1016/j.compositesa.2003.09.029.

(237) Lopes, P. E.; van Hattum, F.; Pereira, C. M. C.; Nóvoa, P. J. R. O.; Forero, S.; Hepp, F.; Pambaguian, L. High CNT Content Composites with CNT Buckypaper and Epoxy Resin Matrix: Impregnation Behaviour Composite Production and Characterization. *Compos. Struct.* **2010**, *92* (6), 1291–1298. https://doi.org/10.1016/j.compstruct.2009.11.003.

(238) Hussain, F.; Hojjati, M.; Okamoto, M.; Gorga, R. E. Review Article: Polymer-Matrix Nanocomposites, Processing, Manufacturing, and Application: An Overview. *J. Compos. Mater.* **2006**, *40* (17), 1511–1575. https://doi.org/10.1177/0021998306067321.

(239) Kim, J. S.; Reneker, D. H. Mechanical Properties of Composites Using Ultrafine Electrospun Fibers. *Polym. Compos.* **1999**, *20* (1), 124–131. https://doi.org/10.1002/pc.10340.

(240) Bergshoef, M. M.; Vancso, G. J. Transparent Nanocomposites with Ultrathin, Electrospun Nylon-4,6 Fiber Reinforcement. *Adv. Mater.* **1999**, *11* (16), 1362–1365. https://doi.org/10.1002/(SICI)1521-4095(199911)11:16<1362::AID-ADMA1362>3.0.CO;2-X.

(241) Neppalli, R.; Marega, C.; Marigo, A.; Bajgai, M. P.; Kim, H. Y.; Causin, V. Poly(ε-Caprolactone) Filled with Electrospun Nylon Fibres: A Model for a Facile Composite Fabrication. *European Polymer Journal*. 2010, pp 968–976. https://doi.org/10.1016/j.eurpolymj.2010.01.004.

(242) Albañil-Sánchez, L.; Cruz-Silva, R.; Piza-Betancourt, J. L.; Romo-Uribe, A. Electrospun Nylon Nanofibers for Polymer Composites. *Emerg. Mater. Res.* **2013**, *2* (1), 53–57. https://doi.org/10.1680/emr.12.00027.

(243) Zheng-Ming Huang; Xiao-fei Wang; Lu-song Che. DEVELOPMENT OF NANOFIBER REINFORCED TRANSPARENT COMPOSITES. *ICCM Int. Conf. Compos. Mater.* **2009**, 10.

(244) Chen, Y.; Han, D.; Ouyang, W.; Chen, S.; Hou, H.; Zhao, Y.; Fong, H. Fabrication and Evaluation of Polyamide 6 Composites with Electrospun Polyimide Nanofibers as Skeletal Framework. *Compos. Part B Eng.* **2012**, *43* (5), 2382–2388. https://doi.org/10.1016/j.compositesb.2011.11.071.

(245) Teo, W. E.; Ramakrishna, S. A Review on Electrospinning Design and Nanofibre Assemblies. *Nanotechnology* **2006**, *17*, R89–R106. https://doi.org/10.1088/0957-4484/17/14/R01.

(246) Yuan, H.; Zhou, Q.; Zhang, Y. Improving Fiber Alignment during Electrospinning. In *Electrospun Nanofibers*; Elsevier Ltd., 2017; pp 125–147.

https://doi.org/10.1016/B978-0-08-100907-9.00006-4.

(247) Reneker, D. H.; Yarin, A. L. Electrospinning Jets and Polymer Nanofibers. *Polymer (Guildf).* **2008**, *49*, 2387–2425. https://doi.org/10.1016/j.polymer.2008.02.002.

(248) Gadu-Maria, F.; Parsi, F. Measurement of Fiber Orientation in Short-Fiber Composites Using Digital Image Processing. *Polym. Compos.* **1993**, *14* (2).

(249) Liu, L.; Dzenis, Y. A. Analysis of the Effects of the Residual Charge and Gap Size on Electrospun Nanofiber Alignment in a Gap Method. *Nanotechnology* **2008**, *19* (35). https://doi.org/10.1088/0957-4484/19/35/355307.

(250) Pan, H.; Li, L.; Hu, L.; Cui, X. Continuous Aligned Polymer Fibers Produced by a Modified Electrospinning Method. *Polymer (Guildf).* **2006**, *47* (14), 4901–4904. https://doi.org/10.1016/j.polymer.2006.05.012.

(251) Theron, A.; Zussman, E.; Yarin, A. L. Electrostatic Field-Assisted Alignment of Electrospun Nanofibres. *Nanotechnology* **2001**, *12* (3), 384–390. https://doi.org/10.1088/0957-4484/12/3/329.

(252) Beachley, V.; Katsanevakis, E.; Zhang, N.; Wen, X. *Biomedical Applications of Polymeric Nanofibers*; Springer, 2012; Vol. 246. https://doi.org/10.1007/12_2011_141.

(253) Matthews, J. A.; Wnek, G. E.; Simpson, D. G.; Bowlin, G. L. Electrospinning of Collagen Nanofibers. *Biomacromolecules* **2002**, *3* (2), 232–238. https://doi.org/10.1021/bm015533u.

(254) Kim, K. W.; Lee, K. H.; Khil, M. S.; Ho, Y. S.; Kim, H. Y. The Effect of Molecular Weight and the Linear Velocity of Drum Surface on the Properties of

Electrospun Poly(Ethylene Terephthalate) Nonwovens. *Fibers Polym.* **2004**, *5* (2), 122–127. https://doi.org/10.1007/BF02902925.

(255) Chew, S. Y.; Wen, J.; Yim, E. K. F.; Leong, K. W. Sustained Release of Proteins from Electrospun Biodegradable Fibers. *Biomacromolecules* **2005**, *6* (4), 2017–2024. https://doi.org/10.1021/bm0501149.

(256) Long, Y.-Z.; Yu, M.; Sun, B.; Gu, C.-Z.; Fan, Z. Recent Advances in Large-Scale Assembly of Semiconducting Inorganic Nanowires and Nanofibers for Electronics, Sensors and Photovoltaics. *Chem. Soc. Rev.* **2012**, *41* (12), 4560–4580. https://doi.org/10.1039/C2CS15335A.

(257) Fennessey, S. F.; Farris, R. J. Fabrication of Aligned and Molecularly Oriented Electrospun Polyacrylonitrile Nanofibers and the Mechanical Behavior of Their Twisted Yarns. *Polymer (Guildf).* **2004**, *45* (12), 4217–4225. https://doi.org/10.1016/j.polymer.2004.04.001.

(258) Boland, E. D.; Wnek, G. E.; Simpson, D. G.; Pawlowski, K. J.; Bowlin, G. L. Tailoring Tissue Engineering Scaffolds Using Electrostatic Processing Techniques: A Study of Poly(Glycolic Acid) Electrospinning. *Journal of Macromolecular Science - Pure and Applied Chemistry*. 2001, pp 1231–1243. https://doi.org/10.1081/MA-100108380.

(259) Sundaray, B.; Subramanian, V.; Natarajan, T. S.; Xiang, R.-Z.; Chang, C.-C.; Fann, W.-S. Electrospinning of Continuous Aligned Polymer Fibers. *Appl. Phys. Lett.* **2004**, *84* (7), 1222–1224. https://doi.org/10.1063/1.1647685.

(260) Yuan, H.; Zhao, S.; Tu, H.; Li, B.; Li, Q.; Feng, B.; Peng, H.; Zhang, Y. Stable Jet Electrospinning for Easy Fabrication of Aligned Ultrafine Fibers. *J. Mater. Chem.*

2012, *22* (37), 19634–19638. https://doi.org/10.1039/C2JM33728B.

(261) Papkov, D. SIZE EFFECTS IN CONTINUOUS POLYACRYLONITRILE-BASED POLYMER, COMPOSITE, AND CARBON NANOFIBERS, University of Nebraska-Lincoln, 2014.

(262) Papkov, D.; Zou, Y.; Andalib, M. N.; Goponenko, A.; Cheng, S. Z. D.; Dzenis, Y. A. Simultaneously Strong and Tough Ultrafine Continuous Nanofibers. *ACS Nano* **2013**, *7* (4), 3324–3331.

(263) Katta, P.; Alessandro, M.; Ramsier, R. D.; Chase, G. G. Continuous Electrospinning of Aligned Polymer Nanofibers onto a Wire Drum Collector. *Nano Lett.* **2004**, *4* (11), 2215–2218. https://doi.org/10.1021/nl0486158.

(264) Zhou, Z.; Lai, C.; Zhang, L.; Qian, Y.; Hou, H.; Reneker, D. H.; Fong, H. Development of Carbon Nanofibers from Aligned Electrospun Polyacrylonitrile Nanofiber Bundles and Characterization of Their Microstructural, Electrical, and Mechanical Properties. *Polymer (Guildf).* **2009**, *50* (13), 2999–3006. https://doi.org/10.1016/j.polymer.2009.04.058.

(265) Reneker, D. H.; Chun, I. Nanometre Diameter Fibres of Polymer, Produced by Electrospinning. *Nanotechnology* **1996**, *7* (3), 216–223. https://doi.org/10.1088/0957-4484/7/3/009.

(266) Yuan, X.; Zhang, Y.; Dong, C.; Sheng, J. Morphology of Ultrafine Polysulfone Fibers Prepared by Electrospinning. *Polym. Int.* **2004**, *53* (11), 1704–1710. https://doi.org/https://doi.org/10.1002/pi.1538.

(267) Baumgarten, P. K. Electrostatic Spinning of Acrylic Microfibers. *J. Colloid Interface Sci.* **1971**, *36* (1), 71–79. https://doi.org/https://doi.org/10.1016/0021-

9797(71)90241-4.

(268) Zhang, C.; Yuan, X.; Wu, L.; Han, Y.; Sheng, J. Study on Morphology of Electrospun Poly(Vinyl Alcohol) Mats. *Eur. Polym. J.* **2005**, *41* (3), 423–432. https://doi.org/10.1016/j.eurpolymj.2004.10.027.

(269) Yördem, O. S.; Papila, M.; Menceloğlu, Y. Z. Effects of Electrospinning Parameters on Polyacrylonitrile Nanofiber Diameter: An Investigation by Response Surface Methodology. *Mater. Des.* **2008**, *29* (1), 34–44. https://doi.org/10.1016/j.matdes.2006.12.013.

(270) Deitzel, J. M.; Kleinmeyer, J.; Harris, D.; Beck Tan, N. C. The Effect of Processing Variables on the Morphology of Electrospun. *Polymer (Guildf).* **2001**, *42*, 261–272.

(271) Buchko, C. J.; Chen, L. C.; Shen, Y.; Martin, D. C. Processing and Microstructural Characterization of Porous Biocompatible Protein Polymer Thin Films. *Polymer (Guildf).* **1999**, *40* (26), 7397–7407. https://doi.org/10.1016/S0032-3861(98)00866-0.

(272) Demir, M. M.; Yilgor, I.; Yilgor, E.; Erman, B. Electrospinning of Polyurethane Fibers. *Polymer (Guildf).* **2002**, *43* (11), 3303–3309. https://doi.org/10.1016/S0032-3861(02)00136-2.

(273) Li, Z.; Wang, C. *One-Dimensional Nanostructures - Chaper 2 - Effects of Working Parameters on Electrospinning*; 2013; Vol. 32.

(274) Yang, Q.; Li, Z.; Hong, Y.; Zhao, Y.; Qiu, S.; Wang, C.; Wei, Y. Influence of Solvents on the Formation of Ultrathin Uniform Poly(Vinyl Pyrrolidone) Nanofibers with Electrospinning. *J. Polym. Sci. Part B Polym. Phys.* **2004**, *42* (20),

3721–3726. https://doi.org/https://doi.org/10.1002/polb.20222.

(275) Sabantina, L.; Rodríguez-Cano, M. Á.; Klöcker, M.; García-Mateos, F. J.; Ternero-Hidalgo, J. J.; Al Mamun; Beermann, F.; Schwakenberg, M.; Voigt, A. L.; Rodríguez-Mirasol, J.; et al. Fixing PAN Nanofiber Mats during Stabilization for Carbonization and Creating Novel Metal/Carbon Composites. *Polymers (Basel).* **2018**, *10* (735). https://doi.org/10.3390/polym10070735.

(276) Qiao, M.; Kong, H.; Ding, X.; Hu, Z.; Zhang, L.; Cao, Y.; Yu, M. Study on the Changes of Structures and Properties of PAN Fibers during the Cyclic Reaction in Supercritical Carbon Dioxide. *Polymers (Basel).* **2019**, *11* (3). https://doi.org/10.3390/polym11030402.

(277) Huntsman. AroCy L-10 Technical Datasheet. 2022.

(278) Huntsman. Matrimid 5218 Technical Datasheet. 2010, pp 1–7.

(279) Kong, C. S.; Choi, S. J.; Lee, H. S.; Kim, H. S. Observation of Electrospinning Behavior of Nanoscale Fibers by a High-Speed Camera. *J. Macromol. Sci. Part B Phys.* **2016**, *55* (2), 201–210. https://doi.org/10.1080/00222348.2016.1138041.

(280) Zhao, W.; Yalcin, B.; Cakmak, M. Dynamic Assembly of Electrically Conductive PEDOT:PSS Nanofibers in Electrospinning Process Studied by High Speed Video. *Synth. Met.* **2015**, *203*, 107–116. https://doi.org/10.1016/j.synthmet.2015.02.018.

(281) Montinaro, M.; Fasano, V.; Moffa, M.; Camposeo, A.; Persano, L.; Lauricella, M.; Succi, S.; Pisignano, D. Sub-Ms Dynamics of the Instability Onset of Electrospinning. *Soft Matter* **2015**, *11* (17), 3424–3431. https://doi.org/10.1039/c4sm02708f.

(282) Uematsu, I.; Uchida, K.; Nakagawa, Y.; Matsumoto, H. Direct Observation and

Quantitative Analysis of the Fiber Formation Process during Electrospinning by a High-Speed Camera. *Ind. Eng. Chem. Res.* **2018**, *57* (36), 12122–12126. https://doi.org/10.1021/acs.iecr.8b02352.

(283) Kiselev, P.; Rosell-Llompart, J. Highly Aligned Electrospun Nanofibers by Elimination of the Whipping Motion. *J. Appl. Polym. Sci.* **2012**, *125*, 2433–2441. https://doi.org/10.1002/app.36519.

(284) ASTM D2584. Standard Test Method for Ignition Loss of Cured Reinforced Resin. *ASTM Int.* **2018**, 1–3. https://doi.org/10.1520/D2584-18.2.

(285) Yao, J.; Bastiaansen, C. W. M.; Peijs, T. High Strength and High Modulus Electrospun Nanofibers. *Fibers* **2014**, *2* (2), 158–187. https://doi.org/10.3390/fib2020158.

(286) Inagaki, M.; Yang, Y.; Kang, F. Carbon Nanofibers Prepared via Electrospinning. *Adv. Mater.* **2012**, *24* (19), 2547–2566. https://doi.org/https://doi.org/10.1002/adma.201104940.

(287) Fitzer, E. Pan-Based Carbon Fibers—Present State and Trend of the Technology from the Viewpoint of Possibilities and Limits to Influence and to Control the Fiber Properties by the Process Parameters. *Carbon N. Y.* **1989**, *27* (5), 621–645. https://doi.org/https://doi.org/10.1016/0008-6223(89)90197-8.

(288) Jain, M. K.; Abhiraman, A. S. Conversion of Acrylonitrile-Based Precursor Fibres to Carbon Fibres. *J. Mater. Sci.* **1987**, *22* (1), 278–300. https://doi.org/10.1007/BF01160584.

(289) Gupta, A. K.; Paliwal, D. K.; Bajaj, P. Acrylic Precursors for Carbon Fibers. *J. Macromol. Sci. Part C* **1991**, *31* (1), 1–89.

https://doi.org/10.1080/15321799108021557.

(290) Li, X.; Yang, Y.; Zhao, Y.; Lou, J.; Zhao, X.; Wang, R.; Liang, Q.; Huang, Z. Electrospinning Fabrication and in Situ Mechanical Investigation of Individual Graphene Nanoribbon Reinforced Carbon Nanofiber. *Carbon N. Y.* **2017**, *114*, 717–723. https://doi.org/10.1016/j.carbon.2016.12.082.

(291) Papkov, D.; Goponenko, A.; Compton, O. C.; An, Z.; Moravsky, A.; Li, X. Z.; Nguyen, S. T.; Dzenis, Y. A. Improved Graphitic Structure of Continuous Carbon Nanofibers via Graphene Oxide Templating. *Adv. Funct. Mater.* **2013**, *23*, 5763–5770. https://doi.org/10.1002/adfm.201300653.

(292) Zussman, E.; Chen, X.; Ding, W.; Calabri, L.; Dikin, D. A.; Quintana, J. P.; Ruoff, R. S. Mechanical and Structural Characterization of Electrospun PAN-Derived Carbon Nanofibers. *Carbon N. Y.* **2005**, *43* (10), 2175–2185. https://doi.org/10.1016/j.carbon.2005.03.031.

(293) Li, L.; Bellan, L. M.; Craighead, H. G.; Frey, M. W. Formation and Properties of Nylon-6 and Nylon-6/Montmorillonite Composite Nanofibers. *Polymer (Guildf).* **2006**, *47* (17), 6208–6217. https://doi.org/10.1016/j.polymer.2006.06.049.

(294) Ding, Y.; Zhang, P.; Jiang, Y.; Xu, F.; Yin, J.; Zuo, Y. Mechanical Properties of Nylon-6/SiO2 Nanofibers Prepared by Electrospinning. *Mater. Lett.* **2009**, *63* (1), 34–36. https://doi.org/10.1016/j.matlet.2008.08.058.

(295) Zoppe, J. O.; Peresin, M. S.; Habibi, Y.; Venditti, R. A.; Rojas, O. J. Reinforcing Poly(ε-Caprolactone) Nanofibers with Cellulose Nanocrystals. *ACS Applied Materials and Interfaces*. 2009, pp 1996–2004. https://doi.org/10.1021/am9003705.

(296) Zhou, C.; Chu, R.; Wu, R.; Wu, Q. Electrospun Polyethylene Oxide/Cellulose Nanocrystal Composite Nanofibrous Mats with Homogeneous and Heterogeneous Microstructures. *Biomacromolecules* **2011**, *12* (7), 2617–2625. https://doi.org/10.1021/bm200401p.

(297) Jiang, L.; Li, K.; Yang, H.; Liu, X.; Li, W.; Xu, W.; Deng, B. Improving Mechanical Properties of Electrospun Cellulose Acetate Nanofiber Membranes by Cellulose Nanocrystals with and without Polyvinylpyrrolidone. *Cellulose* **2020**, *27* (2), 955–967. https://doi.org/10.1007/s10570-019-02830-1.

(298) Mack, J. J.; Viculis, L. M.; Ali, A.; Luoh, R.; Yang, G.; Hahn, H. T.; Ko, F. K.; Kaner, R. B. Graphite Nanoplatelet Reinforcement of Electrospun Polyacrylonitrile Nanofibers. *Adv. Mater.* **2005**, *17* (1), 77–80. https://doi.org/https://doi.org/10.1002/adma.200400133.

(299) Lamastra, F. R.; Puglia, D.; Monti, M.; Vella, A.; Peponi, L.; Kenny, J. M.; Nanni, F. Poly(ε-Caprolactone) Reinforced with Fibres of Poly(Methyl Methacrylate) Loaded with Multiwall Carbon Nanotubes or Graphene Nanoplatelets. *Chemical Engineering Journal*. 2012, pp 140–148. https://doi.org/10.1016/j.cej.2012.04.078.

(300) Hou, H.; Ge, J. J.; Zeng, J.; Li, Q.; Reneker, D. H.; Greiner, A.; Cheng, S. Z. D. Electrospun Polyacrylonitrile Nanofibers Containing a High Concentration of Well-Aligned Multiwall Carbon Nanotubes. *Chem. Mater.* **2005**, *17* (5), 967–973. https://doi.org/10.1021/cm0484955.

(301) Yeo, L. Y.; Friend, J. R. Electrospinning Carbon Nanotube Polymer Composite Nanofibers. *Journal of Experimental Nanoscience*. 2006, pp 177–209. https://doi.org/10.1080/17458080600670015.

(302) Özden-Yenigün, E.; Menceloğlu, Y. Z.; Papila, M. MWCNTs/P(St-Co-GMA) Composite Nanofibers of Engineered Interface Chemistry for Epoxy Matrix Nanocomposites. *ACS Appl. Mater. Interfaces* **2012**, *4* (2), 777–784. https://doi.org/10.1021/am2014162.

(303) Chen, D.; Wang, R.; Tjiu, W. W.; Liu, T. High Performance Polyimide Composite Films Prepared by Homogeneity Reinforcement of Electrospun Nanofibers. *Compos. Sci. Technol.* **2011**, *71* (13), 1556–1562. https://doi.org/10.1016/j.compscitech.2011.06.013.

(304) Tijing, L. D.; Park, C. H.; Kang, S. J.; Amarjargal, A.; Kim, T. H.; Pant, H. R.; Kim, H. J.; Lee, D. H.; Kim, C. S. Improved Mechanical Properties of Solution-Cast Silicone Film Reinforced with Electrospun Polyurethane Nanofiber Containing Carbon Nanotubes. *Appl. Surf. Sci.* **2013**, *264*, 453–458. https://doi.org/10.1016/j.apsusc.2012.10.043.

(305) Borges, A. L. S.; Münchow, E. A.; de Oliveira Souza, A. C.; Yoshida, T.; Vallittu, P. K.; Bottino, M. C. Effect of Random/Aligned Nylon-6/MWCNT Fibers on Dental Resin Composite Reinforcement. *J. Mech. Behav. Biomed. Mater.* **2015**, *48*, 134–144. https://doi.org/10.1016/j.jmbbm.2015.03.019.

(306) Papkov, D.; Beese, A. M.; Goponenko, A.; Zou, Y.; Naraghi, M.; Espinosa, H. D.; Saha, B.; Schatz, G. C.; Moravsky, A.; Loutfy, R.; et al. Extraordinary Improvement of the Carbon Nanofibers Templated with Graphitic Structure of Continuous Double Wall Carbon Nanotubes. *ACS Nano* **2013**, *7* (1), 126–142. https://doi.org/10.1021/nn303423x.

(307) Qiao, B.; Ding, X.; Hou, X.; Wu, S. Study on the Electrospun

CNTs/Polyacrylonitrile-Based Nanofiber Composites. *Journal of Nanomaterials*. 2011. https://doi.org/10.1155/2011/839462.

(308) Chronakis, I. S. Novel Nanocomposites and Nanoceramics Based on Polymer Nanofibers Using Electrospinning Process - A Review. *J. Mater. Process. Technol.* **2005**, *167* (2–3), 283–293. https://doi.org/10.1016/j.jmatprotec.2005.06.053.

(309) Mayerberger, E. A.; Urbanek, O.; Mcdaniel, R. M.; Street, R. M.; Barsoum, M. W.; Schauer, C. L. Preparation and Characterization of Polymer-Ti3C2Tx (MXene) Composite Nanofibers Produced via Electrospinning. *J. Appl. Polym. Sci.* **2017**, *2017*, 45295. https://doi.org/10.1002/app.45295.

(310) Eskizeybek, V.; Yar, A.; Avcı, A. CNT-PAN Hybrid Nanofibrous Mat Interleaved Carbon/Epoxy Laminates with Improved Mode I Interlaminar Fracture Toughness. *Compos. Sci. Technol.* **2018**, *157*, 30–39. https://doi.org/10.1016/j.compscitech.2018.01.021.

(311) Shekhirev, M.; Vo, T. H.; Kunkel, D. A.; Lipatov, A.; Enders, A.; Sinitskii, A. Aggregation of Atomically Precise Graphene Nanoribbons. *RSC Adv.* **2017**, *7*, 54491–54499. https://doi.org/10.1039/c7ra08049b.

(312) Levitt, A. S.; Alhabeb, M.; Hatter, C. B.; Sarycheva, A.; Dion, G.; Gogotsi, Y. Electrospun MXene/Carbon Nanofibers as Supercapacitor Electrodes. *J. Mater. Chem. A* **2019**, *7*, 269–277. https://doi.org/10.1039/c8ta09810g.

(313) Huang, R.; Chen, X.; Dong, Y.; Zhang, X.; Wei, Y.; Yang, Z.; Li, W.; Guo, Y.; Liu, J.; Yang, Z.; et al. MXene Composite Nanofibers for Cell Culture and Tissue Engineering. *ACS Appl. Bio Mater.* **2020**, *3* (4), 2125–2131.

https://doi.org/10.1021/acsabm.0c00007.

(314) Awasthi, G. P.; Maharjan, B.; Shrestha, S.; Bhattarai, D. P.; Yoon, D.; Park, C. H.; Kim, C. S. Synthesis, Characterizations, and Biocompatibility Evaluation of Polycaprolactone–MXene Electrospun Fibers. *Colloids Surfaces A Physicochem. Eng. Asp.* **2020**, *586* (July 2019), 124282. https://doi.org/10.1016/j.colsurfa.2019.124282.

(315) Sobolčiak, P.; Ali, A.; Hassan, M. K.; Helal, M. I.; Tanvir, A.; Popelka, A.; Al-Maadeed, M. A.; Krupa, I.; Mahmoud, K. A. 2D Ti3C2Tx (MXene)-Reinforced Polyvinyl Alcohol (PVA) Nanofibers with Enhanced Mechanical and Electrical Properties. *PLoS One* **2017**, *12* (8). https://doi.org/10.1371/journal.pone.0183705.

(316) Mayerberger, E. A.; Street, R. M.; McDaniel, R. M.; Barsoum, M. W.; Schauer, C. L. Antibacterial Properties of Electrospun Ti3C2Tz (MXene)/Chitosan Nanofibers. *RSC Adv.* **2018**, *8* (62), 35386–35394. https://doi.org/10.1039/c8ra06274a.

(317) Rostron, P.; Gaber, S.; Gaber, D. Raman Spectroscopy, Review. *Int. J. Eng. Tech. Res.* **2016**, *6* (1).

(318) Papkov, D.; Pellerin, C.; Dzenis, Y. A. Polarized Raman Analysis of Polymer Chain Orientation in Ultrafine Individual Nanofibers with Variable Low Crystallinity. *Macromolecules* **2018**, *51* (21), 8746–8751. https://doi.org/10.1021/acs.macromol.8b01869.

(319) Hodkiewicz, J. Characterizing Carbon Materials with Raman Spectroscopy. *Thermo Fish. Sci.* **2010**. https://doi.org/10.1088/0022-3727/46/12/122001.

(320) Higginbotham, A. L.; Kosynkin, D. V; Sinitskii, A.; Sun, Z.; Tour, J. M. Lower-Defect Graphene Oxide Nanotubes from Multiwalled Carbon Nanotubes. *ACS*

Nano **2010**, *4* (4), 2059–2069.

(321) Kosynkin, D. V.; Lu, W.; Sinitskii, A.; Pera, G.; Sun, Z.; Tour, J. M. Highly Conductive Graphene Nanoribbons by Longitudinal Splitting of Carbon Nanotubes Using Potassium Vapor. *ACS Nano* **2011**, *5* (2), 968–974. https://doi.org/10.1021/nn102326c.

(322) Kuila, T.; Bose, S.; Mishra, A. K.; Khanra, P.; Kim, N. H.; Lee, J. H. Chemical Functionalization of Graphene and Its Applications. *Prog. Mater. Sci.* **2012**, *57* (7), 1061–1105. https://doi.org/10.1016/j.pmatsci.2012.03.002.

(323) Tuinstra, F.; Koenig, J. L. Characterization of Graphite Fiber Surfaces with Raman Spectroscopy. *J. Compos. Mater.* **1970**, *4* (4), 492–499. https://doi.org/10.1177/002199837000400405.

APPENDIX A – DATA FROM INTERLAMINAR FRACTURE TOUGHNESS TESTING

Table A.1: Electrospinning parameters for NF interleaves that produced negative DCB results.

Material abbrev.	Areal weight (g/m^2)	Total spin time (hours)	Needle gauge	Collector distance (cm)	Applied voltage (kV)	Flow rate (mL/h)	Temp (°C)	% Relative humidity
PMTF3-PAN2	2.1	2	23	16	8.0	0.280	21.7	42.2
PMTF3-PAN6	5.8	4	23	17	9.0	0.390	24.0	48.0
PMTF3-PAN12	12.5	8	23	17	9.0	0.390	23.7	43.4
PMTF3-PI1	0.8	1	23	16	10.5	0.160	21.7	20.6
PMTF3-PI2	1.9	2	23	16	10.5	0.180	21.7	26.4
PMTF3-PI10	9.9	8	23	17	8.5	0.240	21.5	59.0
RS3C-PAN1	0.9	1	23	15	9.5	0.220-0.260	22.2	15.6
RS3C-PAN2	1.5	2	23	15	9.5	0.180-0.220	21.7	19.8
RS3C-PAN7	7.1	8	23	15	9.5	0.200-0.300	21.8	23.3

Table A.2: Electrospinning parameters for NF interleaves that produced negative ENF results.

Material abbrev.	Areal weight (g/m^2)	Total spin time (hours)	Needle gauge	Collector distance (cm)	Applied voltage (kV)	Flow rate (mL/h)	Temp (°C)	% Relative humidity
PMTF3-PAN2	1.3	2	23	16	9.5	0.160-0.200	21.5	25.4

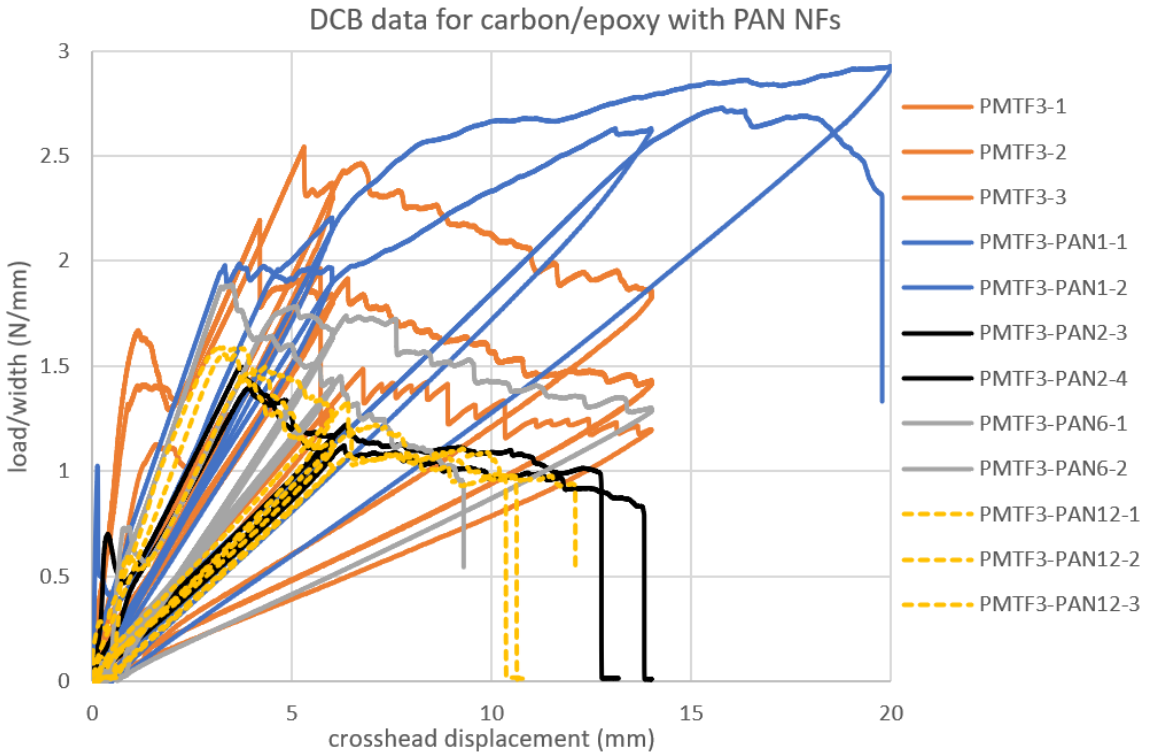

Figure A.1: DCB data for the carbon/epoxy material reinforced with PAN NFs.

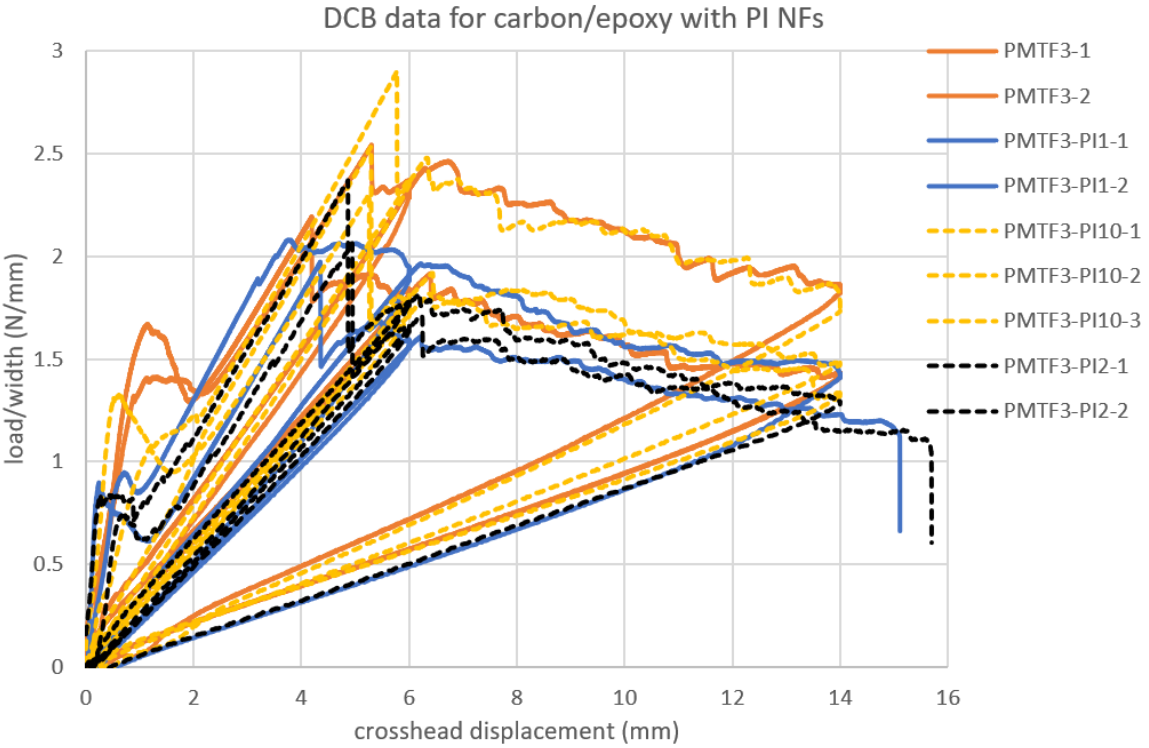

Figure A.2: DCB data for the carbon/epoxy material reinforced with PI NFs.

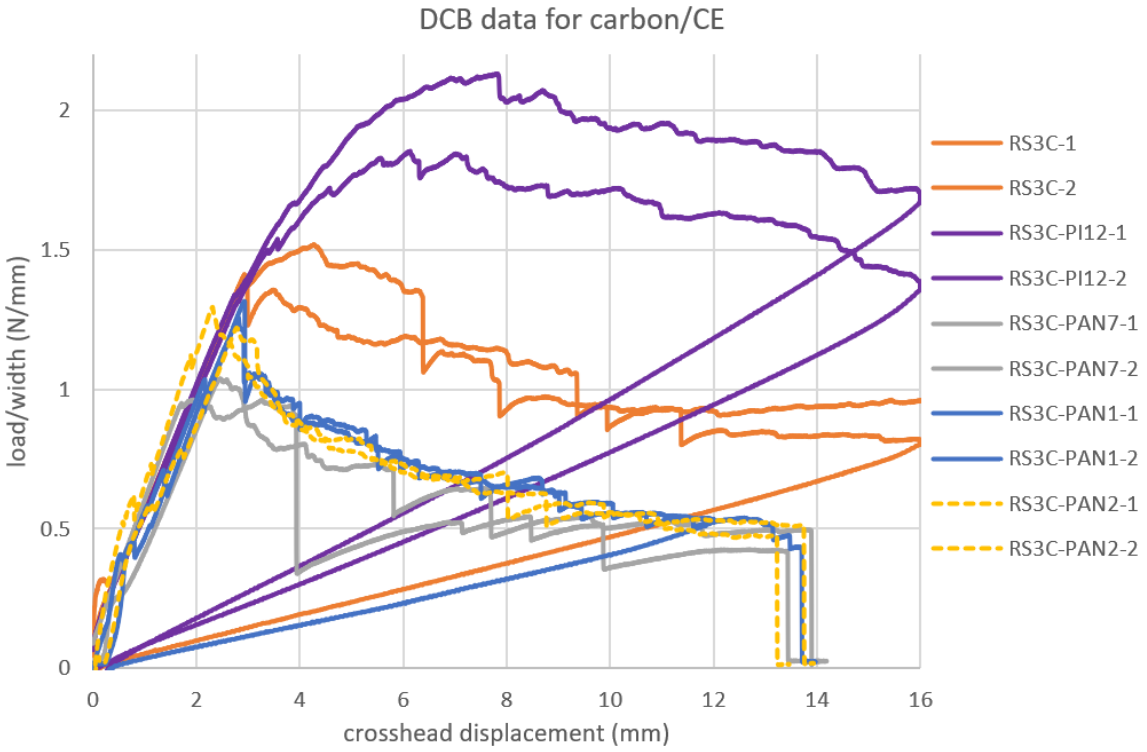

Figure A.3: DCB data for the carbon/CE material.

APPENDIX B – NANOCOMPOSITE MANUFACTURING

To fabricate the nanocomposites, aligned nanofiber mats were carefully folded over to increase the thickness and double the number of layers of the NF preforms, and, subsequently, the number of plies in the nanocomposite layup. Mats were stacked in either unidirectional or cross-ply layups and the aluminum foil substrates were carefully peeled away. To obtain carbon nanofibers, the PAN NF layups were stabilized in an oven at 270°C for 3 hours and then carbonized in nitrogen at 1000°C for 3.5 hours using an MTI GSL-1700X tube furnace. The carbonization schedule can be found in **Table B.1**. Before stabilization and carbonization, all CNF layups, except one unidirectional one, were sandwiched between two silicon wafers to minimize mat shrinkage and wrinkling.

Table B.1: Carbonization schedule. The time column indicates the time it took for the oven to go from the temperature in the same row to the temperature in the following row.

Segment #	Temperature (°C)	Time (minutes)
1	0	5
2	150	15
3	150	60
4	300	30
5	300	150
6	1000	210
7	1000	120
8	0	~720

Figure B.1: MTI GSL-1700X tube furnace in which nanofibers were carbonized.

As-spun and carbonized layup preforms were laid on a perfluoroalkoxy (PFA) film before the resin was dropped on the center of them and covered with another PFA film. The resin was spread throughout the preforms by rolling a pen over the top film. Care was taken to not disturb the fibers while ensuring all the air bubbles were rolled out.

Figure B.2: Aligned PAN NF mats. (top) as-spun. (bottom left) folded over once to create a $[0_2]$ layup. (bottom right) folded over twice to create a $[0_4]$ layup. The fiber direction is horizontal.

To cure the CNF/epoxy composites, the impregnated CNFs sandwiched between two PFA films was placed in a Carver, Inc model 2699 press-clave and cured under 25 in. Hg vacuum pressure and 75 psi surface pressure at 80°C (176°F) for 2 hours and 120°C (248°F) for 2 hours. Once the heat was turned off, the vacuum and surface pressure were left on while the composite cooled overnight.

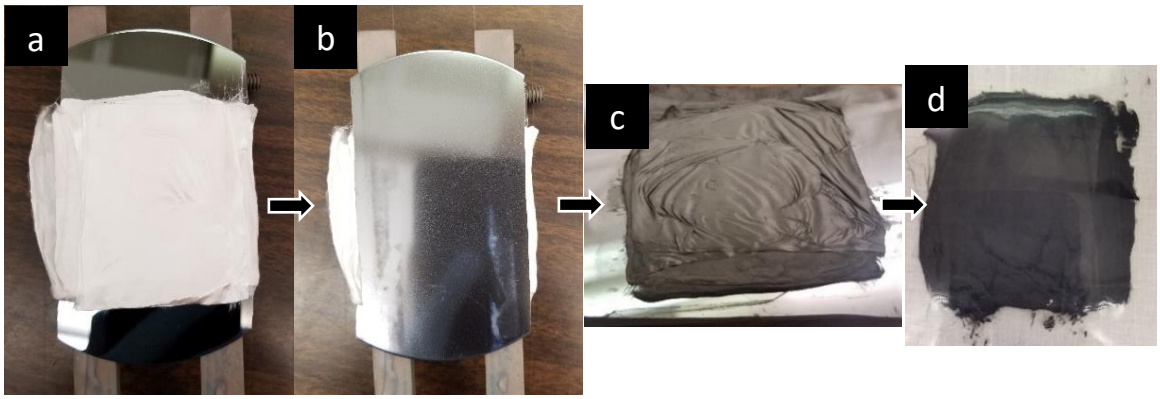

Figure B.3: CNF/epoxy composite manufacturing steps: (a) as-spun layup on a silicon wafer, (b) as-spun layup sandwiched between silicon wafers, (c) carbonized layup before resin impregnation, and (d) cured CNF/epoxy composite.

To cure the CE matrix composites, the impregnated PAN or PI NFs sandwiched between two PFA films were placed between two aluminum plates and placed in an oven to cure at 100°C (212°F) for 3 hours and 177°C (350°F) for another 3 hours. Once the heat was turned off, the layup was left between the plates in the oven while it cooled.

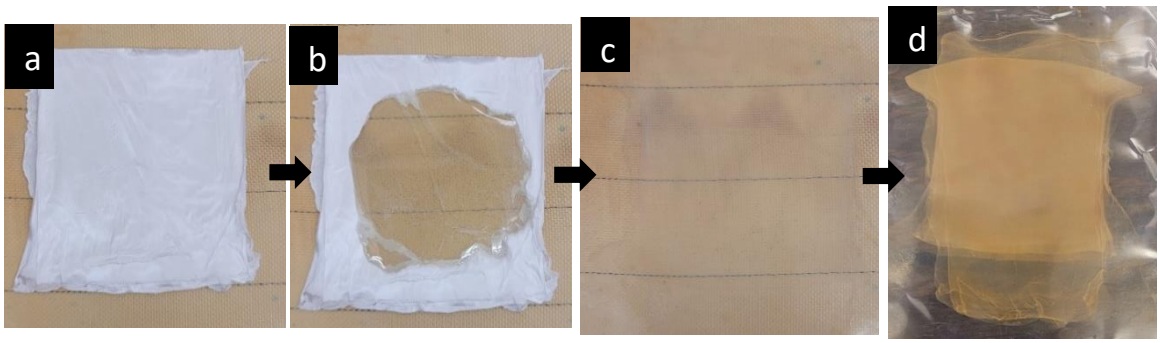

Figure B.4: PAN/CE nanolaminate manufacturing. (a) PAN [$0_4/90_4$] preform, (b) PAN [$0_4/90_4$] preform partially impregnated with AroCy-L10 CE resin, (c) the preform fully impregnated with resin before curing, and (d) the cured [$0_4/90_4$] nanolaminate.

B.1. DETERMINATION OF FIBER VOLUME FRACTION

The effectiveness of the reinforcement in composites is highly dependent on the nanofiber volume fraction (VF). Existing methods for VF quantification include both thermal[284] and optical techniques. Thermal techniques involve heating the composite until the resin decomposes, comparing the original mass to the mass after heating. However, with high-temperature nanocomposites, this method presents a challenge

because the high thermal stability of both matrix and fiber reinforcement makes it difficult to decompose components separately. Optical techniques require examination of a cross-section of a composite to compare the 2D area fractions of fiber and matrix. Although this method is suitable for conventional laminates due to their high fiber alignment and larger fiber diameters, nanofiber-reinforced composites have yet to possess comparable fiber orientation and the fiber diameters are 1-2 orders of magnitude smaller than high-performance microfibers.

In this work, an alternative method is adopted where the weight fractions and densities of the components are used to estimate fiber volume fraction assuming zero void volume fraction. This is a reasonable assumption for the nanocomposites in this study because adequate resin impregnation through the NFs was achieved. This is revealed by the complete wetting out of the NF layups before curing. In addition, fracture surface analysis of the failed nanocomposite specimens did not indicate that any microvoids were present. Lastly, although the resin spread out during curing, the CNF and PAN NF layups maintained their original size, which means the PI NF layup likely did, too, meaning the measured areal weights of the dry NF preforms were maintained during curing of the nanocomposites.

The fiber volume fractions of all nanocomposites were estimated using the following procedure:

1) Measure the areal weight of the nanofiber mat, AW_{NF}.
2) Measure the areal weight of the cured nanocomposite, AW_{comp}.
3) Calculate the weight fractions of the fiber, w_f, and matrix, w_m.
$$w_f = \frac{AW_{NF} \times (number\ of\ layers)}{AW_{comp}}\ ;\ w_m = 1 - w_f$$
4) Using the weight fractions and densities of the constituent materials, calculate the matrix volume fraction, V_m.

$$V_m = \frac{1}{1 + \left(\frac{w_f \rho_m}{w_m \rho_f}\right)}$$

5) Calculate the fiber volume fraction, V_f (or VF).

$$V_f = 1 - V_m$$

APPENDIX C – TABULATED RESULTS OF THE NANOFIBER ALIGNMENT INVESTIGATION

Table C.1: Results of the substrate speed study.

Substrate speed (m/s)	Cylinder RPM	Dispersion (°)	f_p	g_p	Avg. diameter (μm)
0	0	28.06	0.2628	0.2241	-
6.4363	1490	8.34	0.3258	0.2984	0.948±0.240
10.4105	2410	7.04	0.4160	0.3724	-
14.3414	3320	5.66	0.5680	0.5490	0.745±0.150
19.0066	4400	4.56	0.6580	0.6555	-
24.0607	5570	4.09	0.7396	0.7287	0.719±0.210
29.2875	6780	4.04	0.8100	0.7921	-
34.0392	7880	3.92	0.8674	0.8648	0.710±0.180
37.6677	8720	3.08	0.9315	0.9238	0.666±0.150

Table C.2: Results of the spin time study.

Spin time (min)	Dispersion (°)	f_p	g_p
15	3.13	0.9417	0.9310
30	3.04	0.9168	0.9050
45	3.7	0.9096	0.8948
60	3.62	0.8938	0.8805
75	4.79	0.8817	0.8597
90	5.52	0.8775	0.8543
105	6.04	0.8624	0.8350

Table C.3: Results of the substrate width study.

Substrate width (mm)	Dispersion (°) (8700 RPM)	Dispersion (°) (3300 RPM)	f_p (8700 RPM)	g_p (8700 RPM)	f_p (3300 RPM)	g_p (3300 RPM)
4	1.6	-	0.9829	0.9791	-	-

10	4.7	8.11	0.9687	0.9640	0.7313	0.6828
20	4.31	-	0.9456	0.9367	-	-
30	4.76	10.9	0.9169	0.8996	0.6622	0.6153
40	6.84	-	0.8909	0.8698	-	-
50	6.75	13.8	0.8516	0.8334	0.5658	0.5289
60	6.87	-	0.8280	0.7977	-	-

Table C.4: Results of the voltage study, showing the different flow rates used.

Applied voltage (kV)	Dispersion (°)	Avg. diameter (µm)	Flow rate (mL/h)	f_p	g_p
7	7.55	-	0.34	0.4789	0.4935
8	5.33	0.824±0.295	0.31	0.7889	0.7629
9	2.93	0.666±0.150	0.34	0.9117	0.8993
10	3.04	-	0.37	0.8700	0.8578
11	5.43	0.471±0.083	0.39	0.7562	0.7296
12	7.56	0.4640.084	0.50	0.6684	0.6441

Table C.5: Results of the polymer concentration study.

PAN concentration (wt%)	Dispersion (°)	Avg. diameter (µm)	f_p	g_p
8	13.64	0.381±0.150	0.5008	0.4965
9	8.16	-	0.5782	0.5471
10	6.75	0.666±0.150	0.6281	0.6021
11	5.32	0.577±0.120	0.6724	0.6441
12	2.2	-	0.6332	0.6548

APPENDIX D – CONTINUOUS NANOFIBERS TEMPLATED WITH CARBON-BASED NANOMATERIALS

D.1. METHODS OF IMPROVING STRUCTURE AND MECHANICAL PROPERTIES OF NANOFIBERS

Continuous electrospun nanofibers have been proven to be an effective reinforcement of polymer matrix composites, both in the resin-rich interlaminar region of laminates and as bulk reinforcement of polymer resins. However, mechanical improvements have not always been exceptional. One of the primary reasons for this is that polymer fibers processed from solution are often not intrinsically suitable for high-performance structural reinforcement. Thus, electrospun polymer nanofibers themselves are sometimes incapable of achieving high mechanical performance.[56] Although some polymers with better mechanical properties can be electrospun, their expensive material costs may outweigh the structural benefits.[56] Additionally, the size-dependent mechanical properties of fibers can produce significant improvements in strength, modulus, and toughness of NFs with diameters below 500 nm due to increased molecular orientation, decreased crystallinity, and fewer probability of defects.[58] However, NF diameters are highly dependent on the electrospinning parameters, and ultrafine diameters are difficult, sometimes impossible, to produce uniformly, especially in large batches applicable to composite reinforcement. Therefore, several other methods have been developed to improve the mechanical properties of individual electrospun nanofibers.

D.1.1. Post-Processing Treatment

The first method for improving the mechanical properties of NFs is to subject them to a post-processing treatment. One of the most common post-processing methods is carbonization, which is capable of producing carbon nanofibers (CNFs) from several

polymer precursors, including polyacrylonitrile (PAN), polyimide (PI), poly(vinyl alcohol) (PVA), poly(vinylidene fluoride) (PVDF), and polybenzimidazol (PBI).[285,286] The most popular precursor is PAN, which is also used to manufacture most commercial high-performance carbon fibers due to its high carbon yield and the enhanced strength of the resulting fibers.[287–289]

Carbon nanofibers (CNFs) have recently attracted high interest due to their potentially high specific strength. They can be used in a variety of applications, including protective textiles, energy storage, electronics, and carbon-based structural composites.[290,291] CNF processing methods involve the oxidative stabilization and carbonization of polymer precursor fibers produced through a multitude of methods, including melt blowing, centrifugal spinning, and electrospinning.[290] Of these, electrospinning provides a top-down, cost-effective method to produce continuous, uniform, polymer nanofibers that can be carbonized to create continuous CNFs. Nonetheless, electrospun, PAN-based CNFs produced up to now have possessed much lower strengths and stiffnesses compared to commercial PAN-based carbon fibers due to their poor graphitic structure.[104,292] To produce fibers with higher elastic moduli and thermal and electrical conductivities, enhanced graphitic order is needed. In addition, preferential axial alignment of the graphitic nanocrystallites within the fibers is required for increasing fiber strength.[291]

One way to improve the graphitic structure of CNFs is to increase the carbonization temperature. Higher carbonization temperatures have been shown to increase the size and alignment of graphitic crystallites in PAN-based carbon fibers, which helps increase modulus and conductivity. However, high graphitic order in

electrospun nanofibers can only be achieved at temperatures around 3000°C, which requires specialized, expensive equipment, and the process is extremely energy intensive.[291] If manufacturing costs are to be decreased, improved graphitic alignment should be seen at lower carbonization temperatures.

D.1.2. Adding Nanoreinforcement

The second approach to improve nanofiber properties is by adding a nanoreinforcing material to the electrospun NFs. Several types of nanomaterials have been used to reinforce electrospun NFs, including montmorillonite,[293] SiO_2,[294] and cellulose nanocrystals.[295–297] Although these nanomaterials improved fiber mechanical properties, the most popular nanomaterials used to reinforce electrospun NFs are carbon-based due to their superior strengths and stiffnesses. Graphite[298] nanoplatelets have been used to improve the modulus of polymer nanofibers, while poly(methyl methacrylate) NFs reinforced with graphene[299] nanoplatelets have provided a larger increase in the modulus of a polycaprolactone matrix than unmodified PMMA NFs. Carbon nanotubes (CNTs) have also been used to enhance the mechanical properties of polymer nanofibers.[300,301] Improvements have been also measured in bulk NF composites that were reinforced with fibers modified by carbon nanoinclusions.[299,302–305] Although many of these improvements were substantial, results did not meet expectations considering the extraordinary properties of CNTs. In almost all of these studies, reinforcement volume fractions were limited by the tendency of the nanoparticles to agglomerate, which can lead to nonuniform dispersion throughout the fibers. The addition of CNTs and other nanoparticles can also significantly increase the viscosities of the polymeric solutions, which can make electrospinning of quality nanofibers difficult, if not impossible. To

avoid these issues, significant mechanical improvements must be achieved with low filler volume fractions.

D.1.3. Adding Templating Agent

Another approach that removes the shortcomings of the methods discussed above has been proposed by Dzenis lab at UNL.[291,306] This technique involves adding a small amount of nanofiller that can interact with the polymer chains inside the NFs during electrospinning to create improvements in macromolecular alignment. Carbon-based nanofillers are of special interest as small quantities of these materials can both orient the polymer chains and simultaneously serve as a "templating" agent for the formation of graphitic crystallites during carbonization of continuous carbon nanofibers (CNFs).[291] As mentioned above, poor graphitic structure and orientation are the main factor limiting the mechanical and physical properties of CNFs. By increasing the size and/or alignment of graphitic crystallites at lower carbonization temperatures, efficiently-processed CNFs with enhanced mechanical properties can be obtained.

The most common nanotemplating agent added to electrospun NFs are carbon nanotubes (CNTs)[306–308] due to their extraordinary mechanical properties, such as ultra-high strength and stiffness.[60,306] Other carbon-based nanomaterials, including graphene oxide (GO)[291] and graphene nanoribbons (GNRs),[290] have also been used to template NFs to improve their graphitic structure at lower carbonization temperatures. One group found that a small amount (1wt%) of 2D transition metal carbides (MXenes)[309] could significantly increase the crystal structure of electrospun poly(ethylene oxide) NFs without any post-processing treatments. Although these results are promising, further investigation to verify the results is needed.

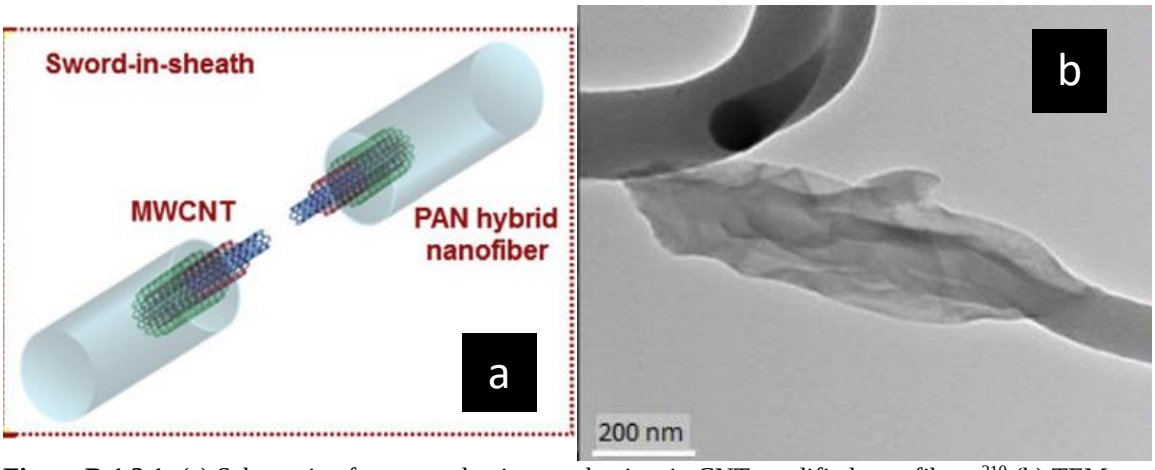

Figure D.1.3.1: (a) Schematic of nanotoughening mechanism in CNT-modified nanofibers.[310] (b) TEM image of a graphene oxide templated carbon nanofiber.[291]

Although several carbon nanomaterials have been used to template electrospun NFs, there are some challenges that remain. For example, most nanoparticles tend to agglomerate, making it difficult to achieve their uniform dispersion throughout the nanofibers.[311] Attempts to deagglomerate the nanoparticles could add a costly and time-consuming step to the manufacturing process of templated nanofibers. In addition, ensuring that the nanomaterials are aligned with the fiber axis is not straight forward due to their small dimensions, even with respect to the ultrafine diameters of the NFs. Due to brittle nature of electrospun CNFs, it is very difficult to obtain the mechanical properties of single CNFs by a tensile test,[60] so other characterization methods are required. Lastly, synthesis of carbon-based nanoparticles can be complicated and costly.

D.1.4. Summary and Problem Formulation

Electrospun polymer nanofibers do not often inherently possess exceptional mechanical properties. Their properties can be improved at ultrafine diameters, but achieving these diameters consistently is challenging. Therefore, carbon nanofibers with improved strength and stiffness are often manufactured from polymer precursor nanofibers. However, their properties are limited by their poor graphitic structure and

orientation. An alternative approach to enhancing nanofiber properties involves adding a nanoreinforcing material, but their volume fractions are usually low due to their tendency to agglomerate and increase the viscosity of the electrospinning solution. At the same time, as demonstrated by earlier research at UNL, carbon-based nanomaterials have the ability to serve as templating agents, which, even at low volume fractions, can help organize the polymer chains and assist with the formation of oriented graphitic crystallites within the nanofibers during carbonization. Although these improvements can subsequently improve the mechanical properties of the continuous nanofibers, these studies are fairly limited, and some challenges remain. More research is needed to potentially uncover extraordinary improvements in the structure and mechanical properties of continuous nanofibers.

In this exploratory appendix, continuous electrospun nanofibers were modified with two types of two-dimensional nanoinclusions: graphene nanoribbons (GNRs) and Ti_3C_2 MXenes. GNRs have been successfully incorporated in PAN-based CNFs carbonized at 850°C to increase tensile strength and modulus due to improved graphitic order and decreased porosity.[290] However, the results of this single study must be verified before GNR-templated CNFs can be implemented in practical composite applications. On the other hand, nanofibers modified with MXenes have several applications, including composites, supercapacitor electrodes,[312] cell culture, tissue engineering,[313] wound dressing, bone regeneration, and cancer therapy.[314] This is due to the fact that MXene-modified nanofibers can exhibit superior elastic modulus, electrical conductivity,[315] antibacterial properties,[316] biocompatibility, wettability, biomineralization, and protein absorption.[314] Results of the study outlined in this work can provide further data on

graphitic order in continuous carbon nanofibers templated with 2D carbon-based nanomaterials and carbonized at lower temperatures. This will contribute to the development of efficiently-processed continuous carbon nanofibers that possess enhanced graphitic structures, potentially comparable to those exhibited by commercial carbon fibers, which are the some of the strongest commercial materials available.

D.2. EXPERIMENTAL METHODS

D.2.1. Materials

A polymer solution was created by mixing polyacrylonitrile (PAN, 150,000MW) from Pfaltz & Bauer and dimethylformamide (DMF) from Sigma Aldrich. The solution was mixed at a 10wt% PAN concentration and stirred for 24 hours at 45°C to completely dissolve the PAN. Another solution, this one with 1% (wt% of PAN) graphene nanoribbons (GNRs) added was prepared by first adding a small amount (e.g., 0.01 g) of GNR powder, then adding PAN powder (e.g., 1.0 g) to a vial. Next, the correct amount of DMF (e.g., 10.0 g) was added, and the solution was stirred overnight at 45°C. This solution was prepared to ensure the electrospun NFs would be 1 wt% GNR. A similar method was used to create a solution with 9.5% PAN+2% (wt% of PAN) Ti_3C_2 (MXenes), although the MXenes were previously mixed with DMF. This solution would produce 2wt% MXene PAN NFs. The GNRs and MXenes were obtained from the Sinitzkii Lab in the Department of Chemistry at the University of Nebraska-Lincoln.

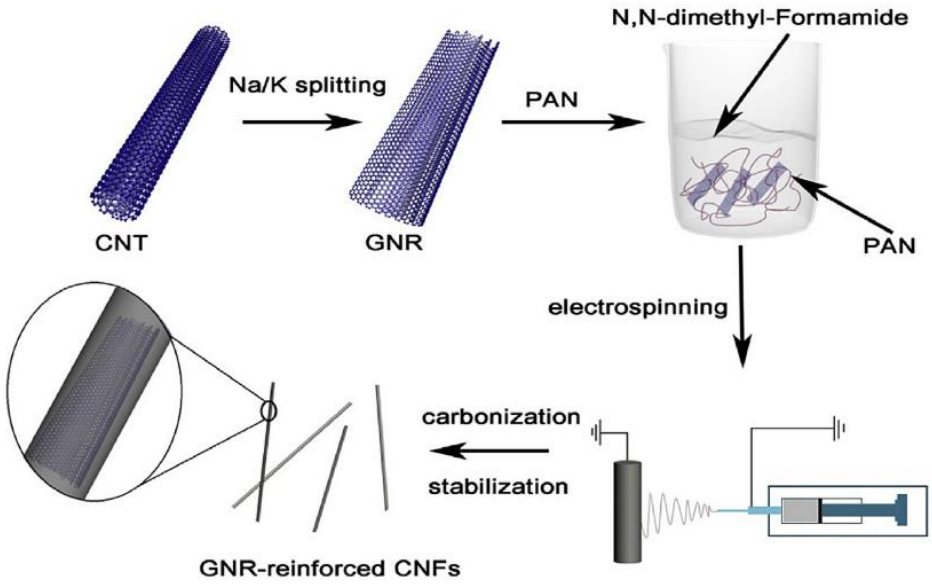

Figure D.2.1.1: Schematic of manufacturing process for GNR-reinforced carbon nanofibers.[290]

The 10%PAN+1%GNR solution was examined with an optical microscope to determine how the GNRs were dispersed. It was then sonicated 3 times for 30 minutes each and stirred at room temperature overnight. Again, the sonicated solution was examined using an optical microscope.

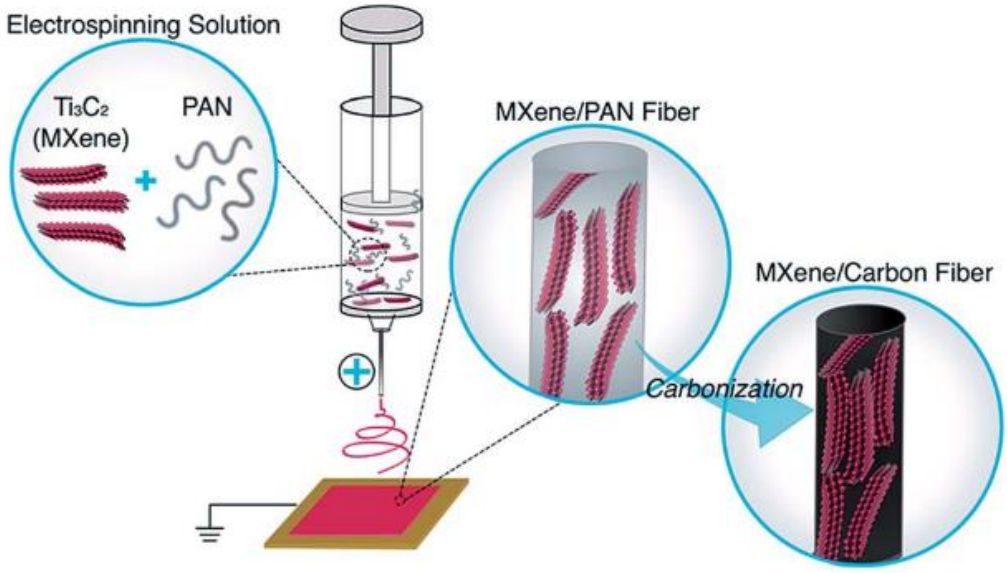

Figure D.2.1.2: Schematic of manufacturing process for MXene-reinforced carbon nanofibers.[312]

Table D.2.1.1: List of materials tested.

Polymer material	Polymer concentration (wt%)	Solvent	Additive and wt% of polymer wt.	Sonicated (Y/N)	Abbreviation
PAN	10	DMF	-	N	Pristine PAN
PAN	10	DMF	GNR 1%	Y	PAN+1%GNR
PAN	9.5	DMF	MXene 2%	N	PAN+2%MXene

D.2.2. Electrospinning

Nanofibers were electrospun onto both a stationary plate to create random NFs and a rotating cylinder to create aligned NFs. The aligned nanofibers were spun using an E-SPIN Super-ES-2 Nanofiber Unit. The rotating aluminum cylinder was covered in aluminum foil, had a diameter of 8.25 cm, and was rotated at ~8800 RPM, which equates to a surface speed of around 38.0 m/s. All NF mats were electrospun for 3 minutes each, except those that were carbonized, which were spun for 30 minutes. All nanofibers, along with powdered PAN and GNRs, were examined with SEM and optical microscopy. MXene-templated NFs were examined with TEM.

Table D.2.2.1: Electrospinning parameters used to fabricate random and aligned NFs.

Material	Needle gauge	Flow rate (mL/h)	Collector distance (cm)	Applied voltage (kV)	Temperature (°C)	Humidity (% RH)
Pristine PAN	23	0.340	18	9.0	22-23	46-48
PAN+1%GNR	23	0.340	18	9.0	22-23	46-48
PAN+2%MXene	23	0.340	18	9.0	22-23	46-48

D.2.3. Stabilization and Carbonization

Both random pristine and 2%MXene PAN nanofiber mats were left on their foil substrates and stabilized in an oven at 270°C for 3 hours. After cooling, the mats were removed from the foil and placed in an MTI GSL-1700X tube furnace to carbonize in a nitrogen environment at 1000°C and 7.80e+2 Torr for 3.5 hours. The carbonization schedule can be found in **Table B.1**.

D.2.4. Raman Spectroscopy

Raman spectroscopy is a branch of vibrational spectroscopy that allows for highly sensitive structural identification of trace amounts of chemicals based on their unique vibrational characteristics. When a photon from incident light strikes a molecule, it becomes scattered. Raman is based on measuring the shift in the energy, or wavelength, of the outgoing photon, which depends upon the chemical composition of the molecules that cause the scattering. The intensity of Raman scattering is proportional to the magnitude of the change in the molecular polarization, which is caused by the displacement of the constituent atoms from their equilibrium positions as a result of the molecular vibrations. A Raman spectrometer is composed of a light source, a monochromator, a sample holder, and a detector.[317]

In this work, Raman spectroscopy was performed using a Horiba Scientific LabRAM HR Evolution Raman Spectrometer. Focusing was performed first optically under x100 magnification and then by maximizing either the nitrile band intensity for PAN samples or the G band intensity for GNR, MXene, or carbonized samples. Spectra were obtained at several points in each sample using a 633 nm laser with a 600 lines/mm diffraction grating and a 100μm hole size. Each test included 10 accumulations each with an acquisition time of 10 seconds. Using the baseline subtraction tool in the LabSpec6 software, the background intensity was removed from all spectra. Several spectra from each sample were averaged and plotted in Excel to allow for comparison. Relevant peaks were fit with Lorentzian curves to determine their Raman shift values, intensities, and full width at half maximums (FWHMs).

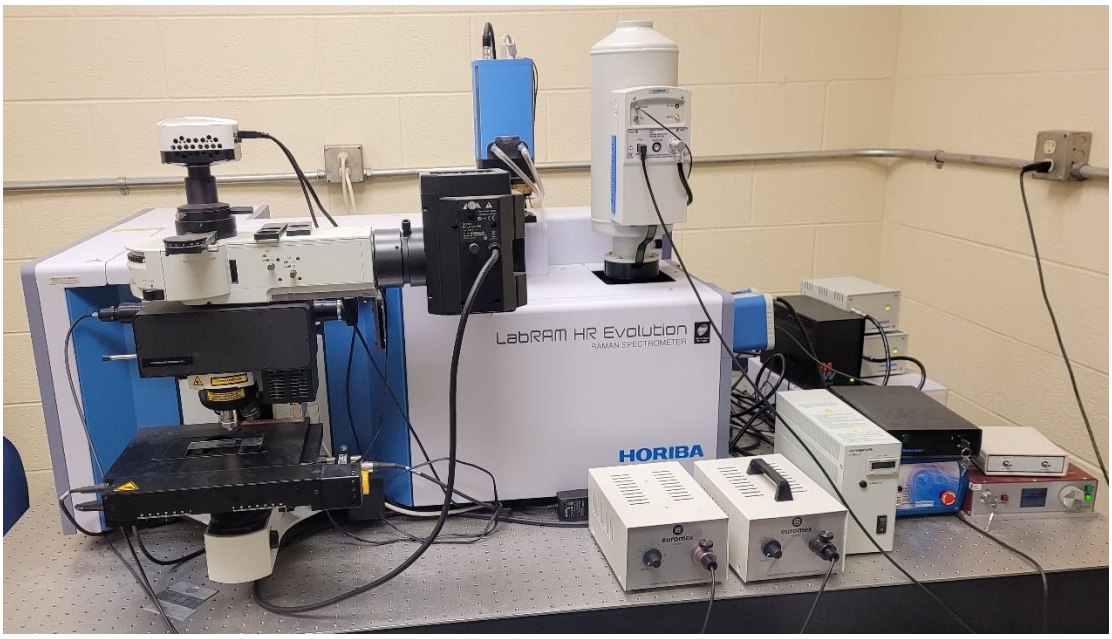

Figure D.2.4.1: Horiba Scientific LabRAM HR Evolution Raman spectrometer.

D.3. RESULTS

D.3.1. Graphene Nanoribbons Results

To be able to determine the material composition at the points in the electrospun GNR/PAN nanofibers where Raman spectra were obtained, spectra were also obtained from both PAN and GNR powder (see **Figure D.3.1.1**). PAN can be characterized by the nitrile stretching mode (2242 cm^{-1}) and several strong overlapping bands in the 2800-3000 cm^{-1} range, corresponding to different CH stretching vibrations. Both regions can be used for orientation studies, but the nitrile band is preferred due to its spectral isolation from other bands.[318] Polymer chain orientation can also be characterized by the intensity ratio of the band at 1355 cm^{-1} and the nitrile band, in which an increase in the $I_{1355}/I_{nitrile}$ is indicative of higher molecular orientation and can also be caused by increased crystallinity.[318] Based on the results of a study performed in our group,[318] chain orientation, determined by the $I_{1355}/I_{nitrile}$ ratio, increases rapidly as PAN fiber diameters decrease below 500 nm, which is the reason for the observed increases in nanofiber

modulus. At the thinnest diameters (~140 nm), substantial increases in the band ratio were found, indicating drastic improvements in polymer chain orientation.[318] Electrospun nanofibers with diameters in this range (<250 nm) have exhibited simultaneous improvements in strength and toughness.[262] Therefore, higher modulus, and, potentially, other properties, can be expected in NFs smaller than 500 nm in diameter, and Raman spectroscopy can be used to analyze these mechanical enhancements through polymer structure control during nanomanufacturing.[318] Although these results are extremely promising for nanofiber research and Raman spectroscopy as a characterization tool, polymer orientation is not the primary focus of this chapter. Rather, improving the graphitization of carbon nanofibers serves as the primary goal.

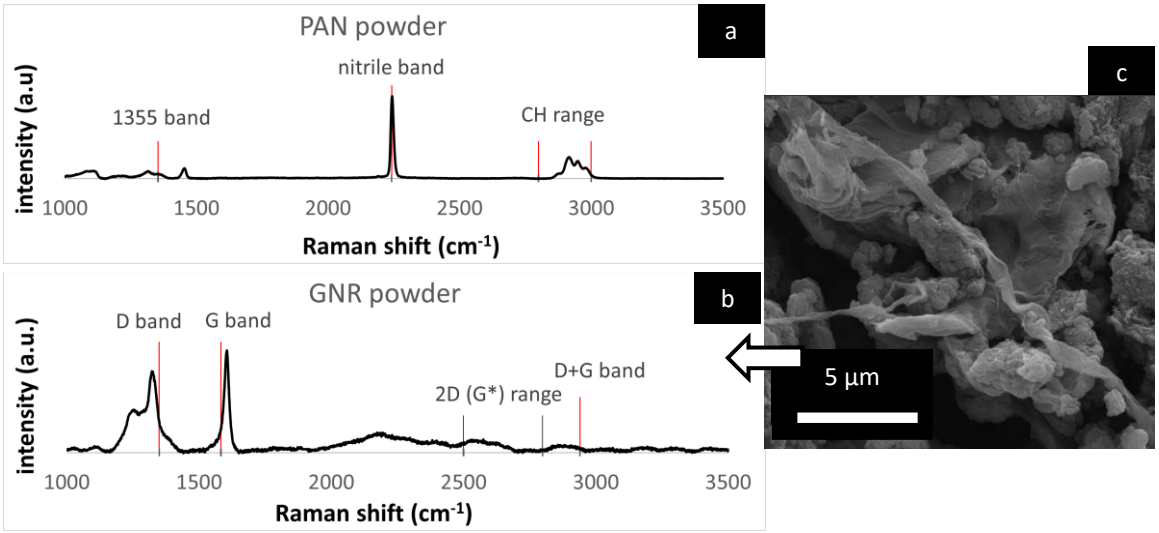

Figure D.3.1.1: Raman spectra of powdered (a) PAN and (b) graphene nanoribbons. (c) SEM image of a bundle of GNRs.

Carbon materials can be characterized by several different vibrational modes, or Raman bands. These include the D band (1350 cm^{-1}), the G band (1582 cm^{-1}), the 2D (also called G* or G') range (2500-2800 cm^{-1}), the D' band (1620 cm^{-1}), and the D+G band (~2940 cm^{-1}).[319] The D band (1350 cm^{-1}), which is also called the disorder or defect band, is commonly present in carbon fiber and nanotubes. It represents a hybridized

vibrational mode associated with the graphene edges and indicates the presence of some disorder in the graphene structure. Its intensity relative to that of the G band is often used to measure the quality of CNTs. The G band (1582 cm^{-1}) is characteristic of graphite and indicates the presence of sp^2 bonded carbon in planar sheets. Since the energies of the sp^2 bonds are higher than those of the sp^3 bonds in diamond, the vibrational frequencies of the bonds is shifted, which causes the Raman band to shift from 1332 cm^{-1} in diamond to 1582 cm^{-1} in graphite. In addition, the G* band (~2700 cm^{-1}) is more pronounced in graphene than in graphite, the D' band represents surface defect modes, and the D+G band exists as the sum of the D and G vibrational modes.[319] Most of these bands, especially the D and G bands, are evident in the Raman spectrum obtained from the GNR powder shown in **Figure D.3.1.1**. The spectra in this figure will be used for comparison to those obtained from the templated nanofibers.

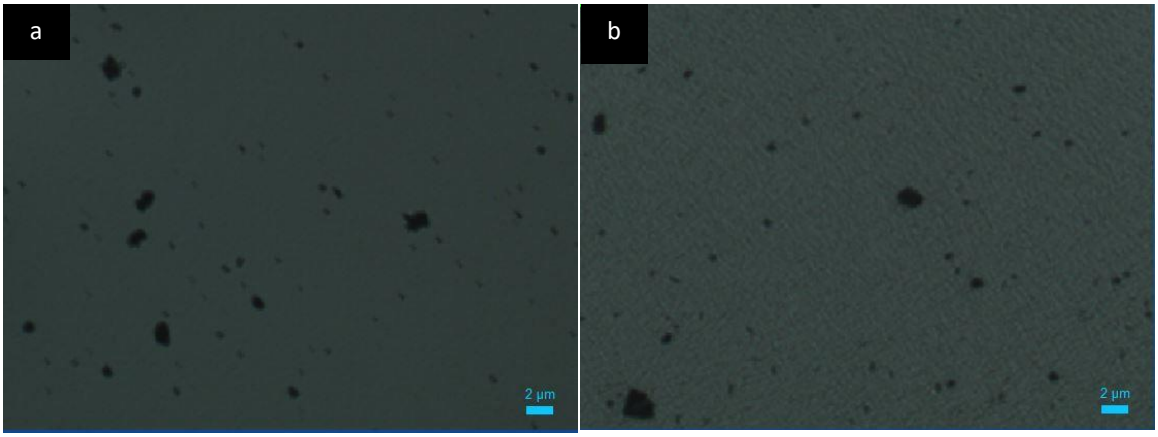

Figure D.3.1.2: Optical microscope image of 10wt% PAN + 1% (wt% of PAN) GNR in DMF solutions (a) before sonication and (b) after sonication.

Since GNRs tend to agglomerate in solution,[320] the PAN/GNR solution was sonicated for 90 minutes in an attempt to aid in more uniform dispersion of the GNRs. **Figure D.3.1.2** shows optical microscope images of the 10%PAN+1%GNR solution before and after sonication. Qualitatively, the solutions look fairly similar, and the

particle sizes appear to be comparable. The particle density is also rather low. Optical microscopy of a drop cast of the sonicated solution shows a higher particle density, but the particles remain somewhat round and large, different from the ribbonlike morphology observed by Kosynkin et al.[321]

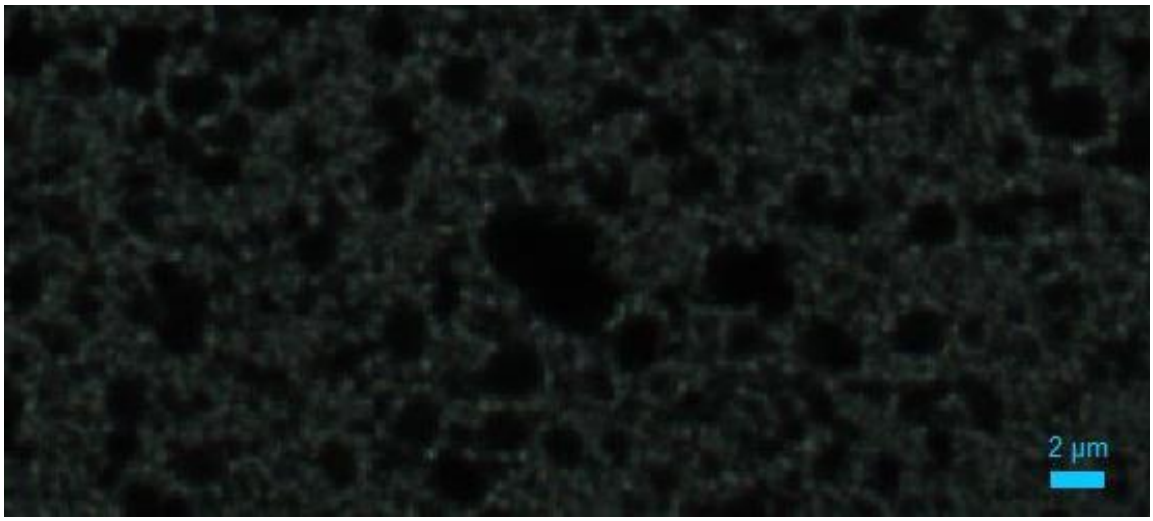

Figure D.3.1.3: Optical microscope image of the 10wt% PAN + 1% (wt% of PAN) GNR in DMF after sonication and evaporation of DMF solvent.

After electrospinning both pristine PAN and PAN+1%GNR nanofibers, they were again examined with an optical microscope. Unfortunately, agglomerates of GNRs within the fibers, which will be called "dark spots" from here forward, are evident.

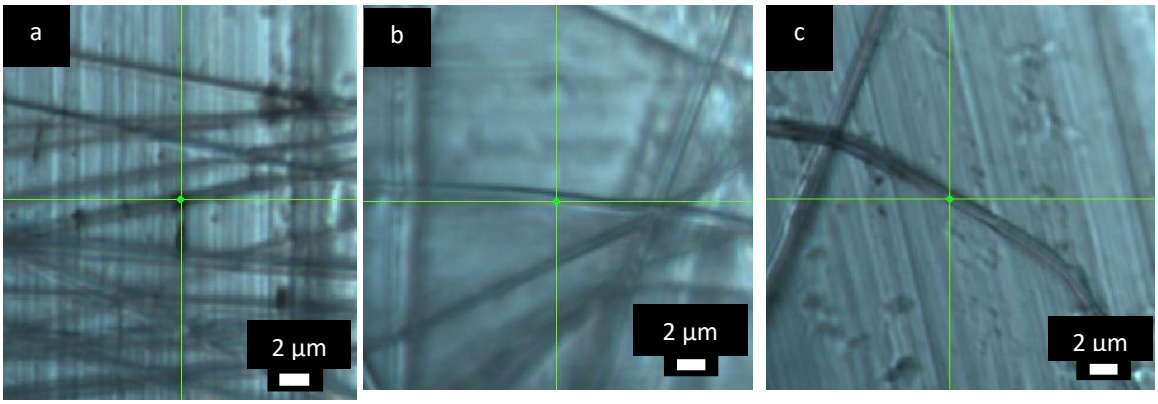

Figure D.3.1.4: Locations of obtained spectra for (a) an aligned PAN+1%GNR fiber "dark spot," (b) a random PAN+1%GNR fiber (not a dark spot: PAN only), and (c) a random pristine PAN fiber.

To confirm these dark spots were actually agglomerates of GNRs, Raman spectroscopy was performed on several points along the templated fibers. Some spectra were obtained from the dark spot locations, and others were obtained at points where no dark spot was visible (PAN only locations).

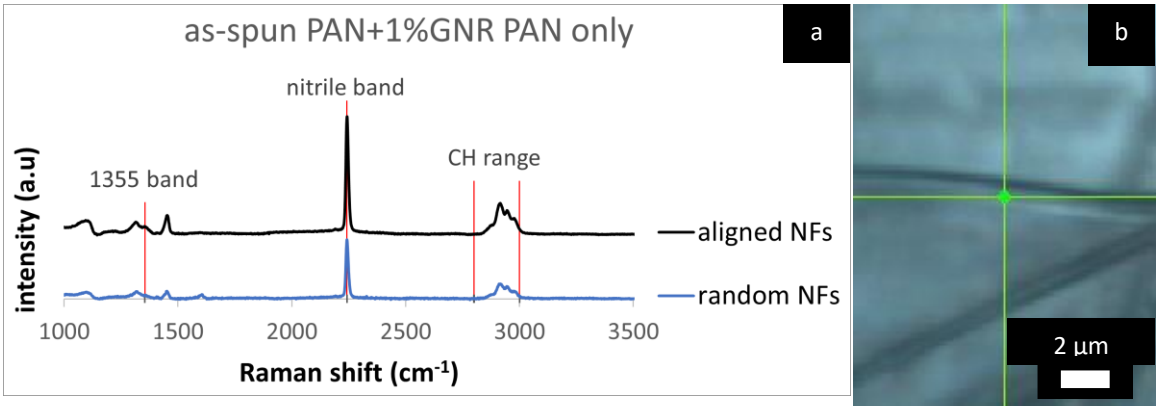

Figure D.3.1.5: (a) Raman spectra of as-spun PAN+1%GNR PAN only spots. (b) optical microscope image of a PAN+1%GNR PAN only location. The vertical lines indicate points or ranges of relevant vibrational modes.

As shown in **Figure D.3.1.5**, Raman spectra obtained from PAN only locations in the PAN+1%GNR fibers were nearly identical to the spectra obtained from the PAN powder. Although the aligned fibers exhibited more intense nitrile and CH stretching modes, which are evident of increases molecular orientation, it is clear that GNRs were not present in these regions.

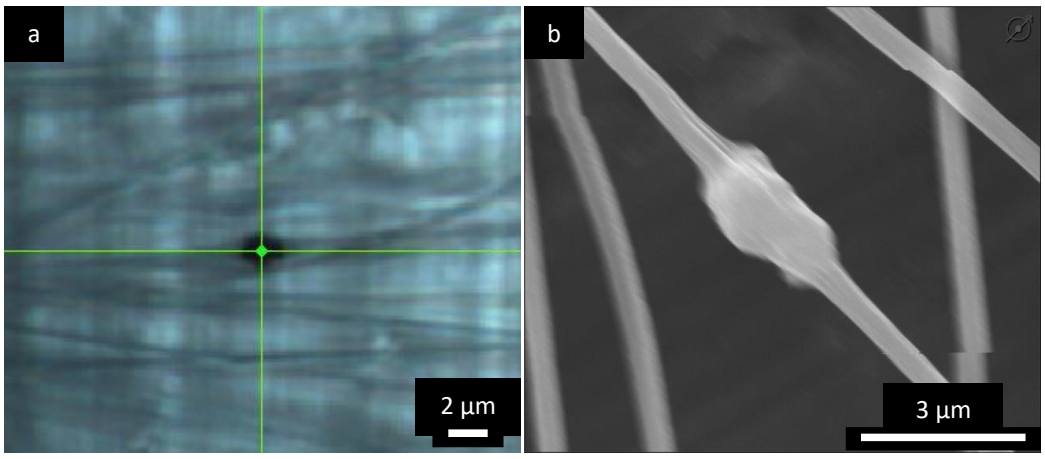

Figure D.3.1.6: (a) Optical microscope image of a large "dark spot" in a PAN+1%GNR nanofiber. (b) SEM micrograph of a bulge in a fiber from the same mat.

On the other hand, at the dark spot locations, the characteristic D and G bands were much more intense than the nitrile bands (see **Figure D.3.1.7**) Also, the dark spots in the aligned nanofibers exhibited more intense D and G bands than those in the random NFs. The intensity ratio R of the D and G bands (I_D/I_G) at dark spot locations is also higher in the aligned fibers. This is characteristic of enlarged in-plane crystal size.[306] Although the nanofibers were not carbonized, the agglomeration of the GNRs caused them to restack and form graphitic crystallites. This process, which occurs through $\pi - \pi$ stacking and van de Waals interactions if the sheet are not well separated from each other, has been observed before.[322] The R value (I_D/I_G) was first connected to the in-plane crystal size L_a (R proportional to L_a^{-1}) by Tuinstra and Koenig,[323] and has subsequently been used several times for this purpose.[306] Although the aligned dark spots exhibit improved graphitic structures, the GNR agglomerates, which can be much larger than the fiber diameter (see **Figure D.3.1.6**), are detrimental to the uniformity of nanofiber morphology, graphitic structure, and mechanical properties.

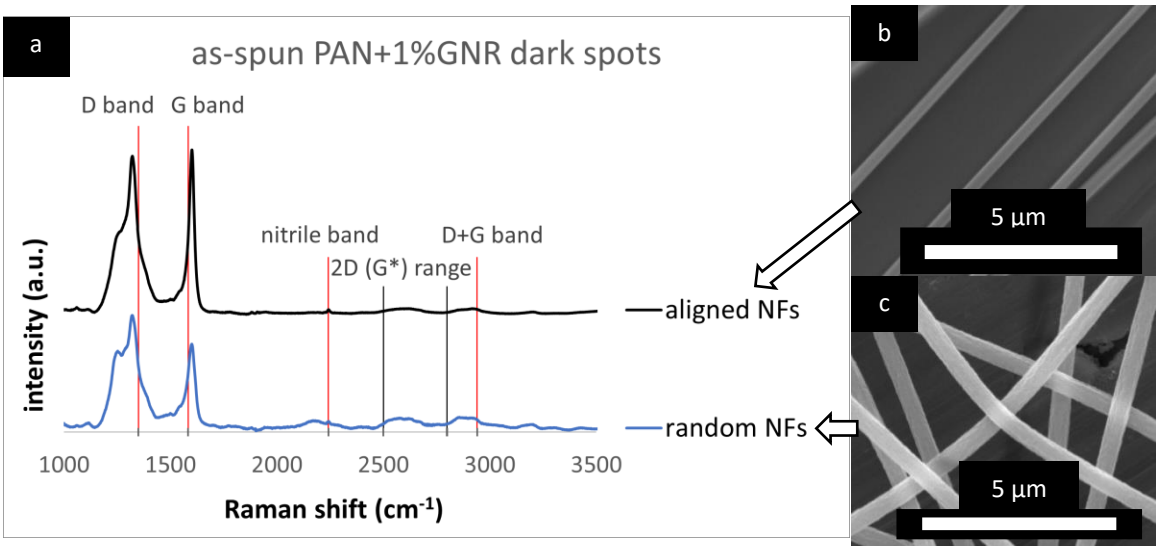

Figure D.3.1.7: (a) Raman spectra of as-spun PAN+1%GNR "dark spots." SEM images of PAN+1%GNR (b) random and (c) aligned nanofibers. The vertical lines indicate points or ranges of relevant vibrational modes.

The graphitic structure of carbonized pristine PAN was compared to that of both the as-spun aligned and random dark spots (see **Figure D.3.1.8**). As expected, the graphitic structure of the pristine CNFs is poor, which is supported by the low-intensity and wide D and G bands. Although the GNR dark spots exhibit dramatically more intense and sharper D and G band peaks, which indicate superior graphitic order, they are only present in scarce locations along the fiber, where agglomerations of GNRs formed graphitic crystals. When templated nanofibers were carbonized, their Raman spectra, although not explicitly shown here, exhibited slightly lower D and G band intensities and nearly identical R values to those observed on the spectra of pristine carbonized PAN. The reason for this is that the GNRs only improved graphitic structure in highly localized and limited regions along the fibers. If the Raman spectrum was obtained in any region other than where the GNR agglomerations existed, which is suspected to have happened during all of the tests in this work, it would look identical to those obtained from pristine CNFs. Thus, more uniform dispersion of the GNRs in both the polymeric solutions and the electrospun nanofibers is critically needed to enhance the graphitic structure more uniformly throughout the fibers.

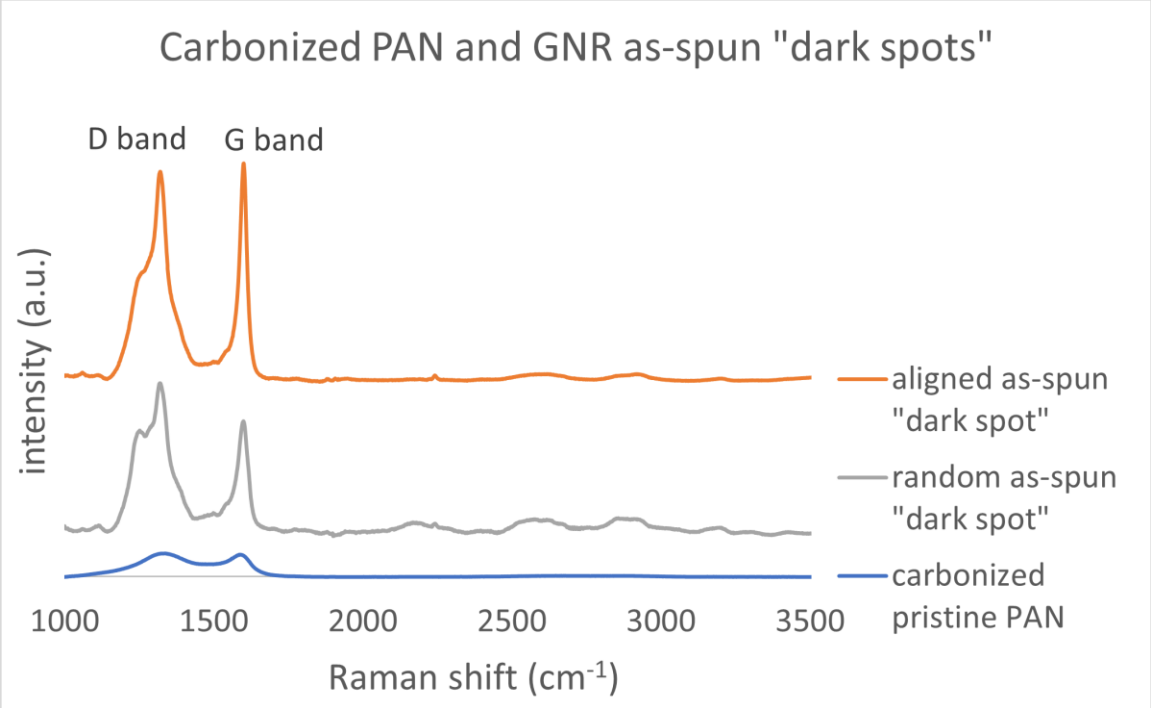

Figure D.3.1.8: Raman spectra of as-spun GNR dark spots and carbonized pristine PAN nanofibers.

D.3.2. MXenes Results

Polyacrylonitrile nanofibers modified with 2wt% MXenes were electrospun onto a stationary substrate. Resulting random nanofiber mats were examined with SEM and energy dispersive x-ray spectroscopy (EDS or EDX). As shown in **Figure D.3.2.1**, nanofiber morphology was highly uniform. EDS mapping also showed a significant amount of titanium atoms uniformly dispersed throughout the electrospun fibers. This indicates that the Ti_3C_2 MXene particles were uniformly distributed within the fibers.

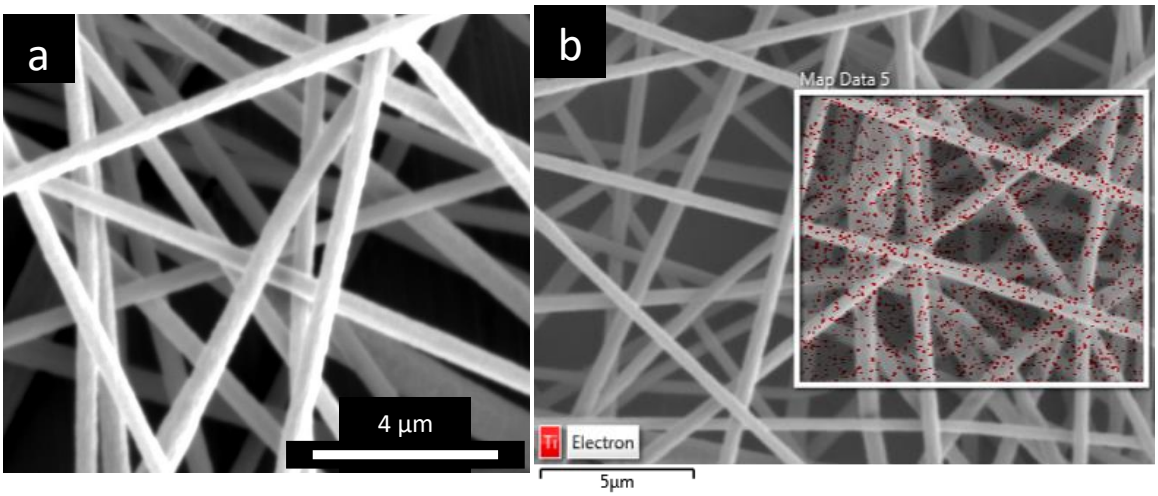

Figure D.3.2.1: SEM images of PAN+2%MXene nanofibers. (b) Dispersion pattern of Ti_3C_2 shown by EDS mapping where Ti is red.

The conclusion of uniform MXene distribution within the nanofibers was reinforced visually with transmission electron microscopy (TEM), as shown in **Figure D.3.2.2**)

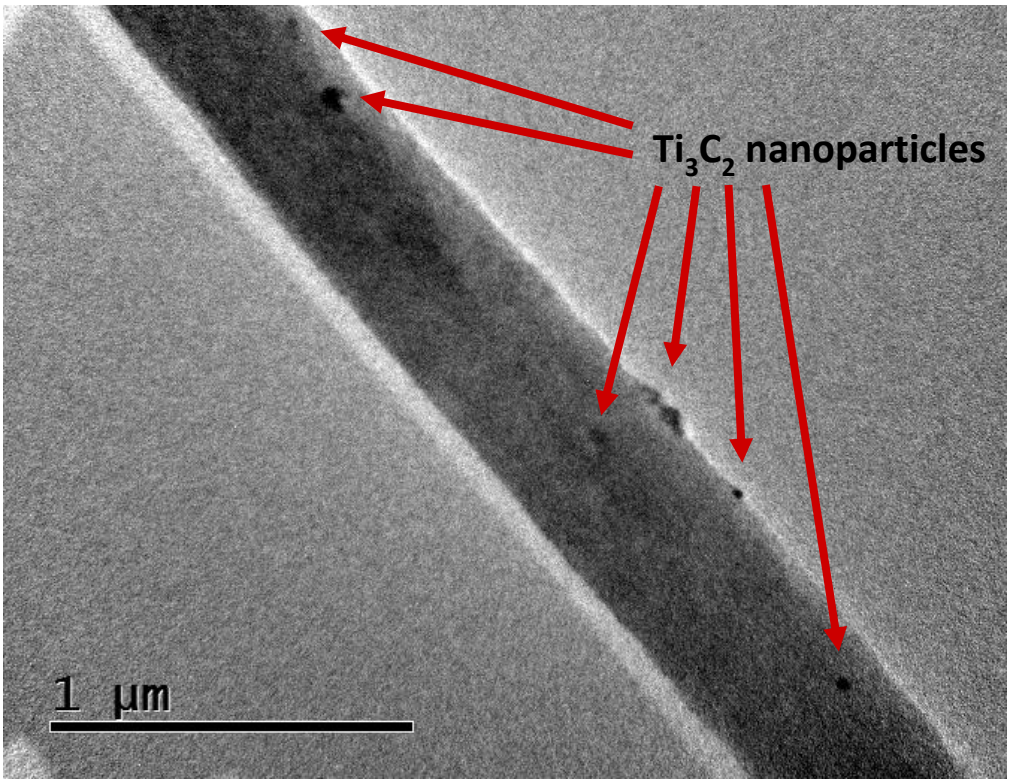

Figure D.3.2.2: TEM image of a PAN+2%MXene nanofiber.

Once it was determined that the MXene particles were relatively well dispersed throughout the nanofibers, the fiber mats were carbonized to create CNFs. Raman spectroscopy was performed on several spots in pristine PAN and PAN+2%MXene nanofibers. Average Raman spectra are shown in **Figure D.3.2.3**.

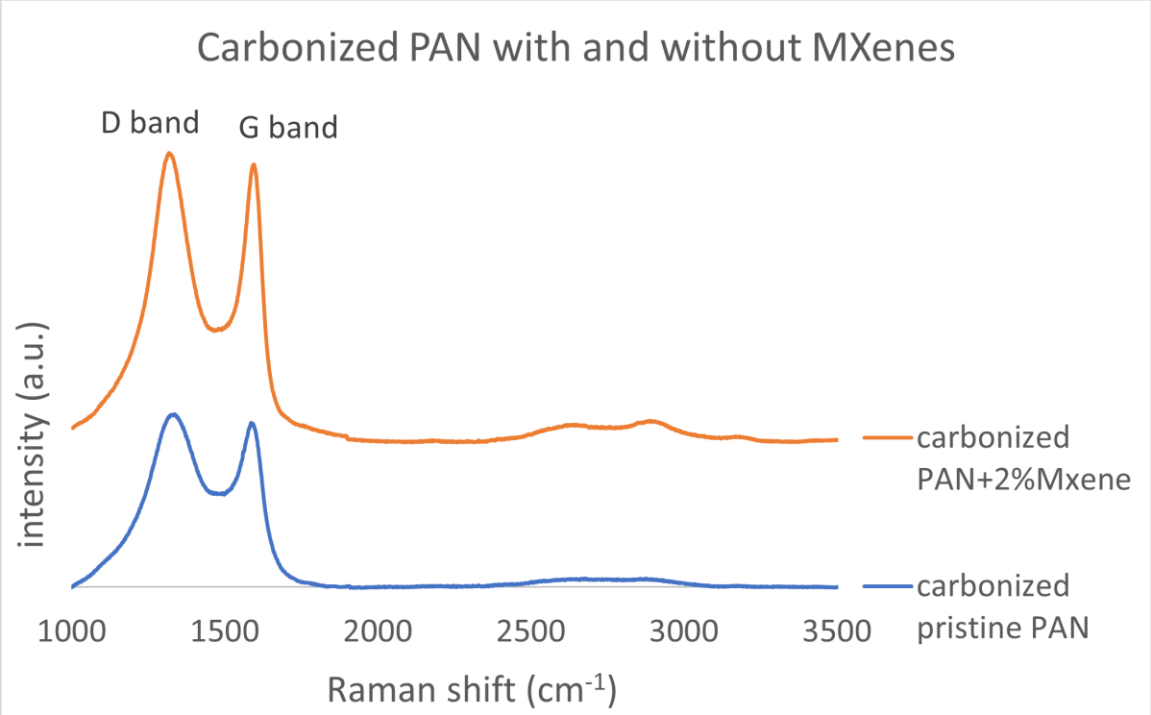

Figure D.3.2.3: Qualitative comparison of the average Raman spectra for carbonized pristine PAN and PAN+2%MXene nanofibers.

Qualitatively, the CNFs templated with 2wt% MXenes exhibit more intense D and G band peaks, which may indicate better graphitic order. However, Lorentzian curves must be fit to the data for all relevant peaks in both spectra to allow for quantitative comparison (see **Figure D.3.2.4** and **Figure D.3.2.5**).

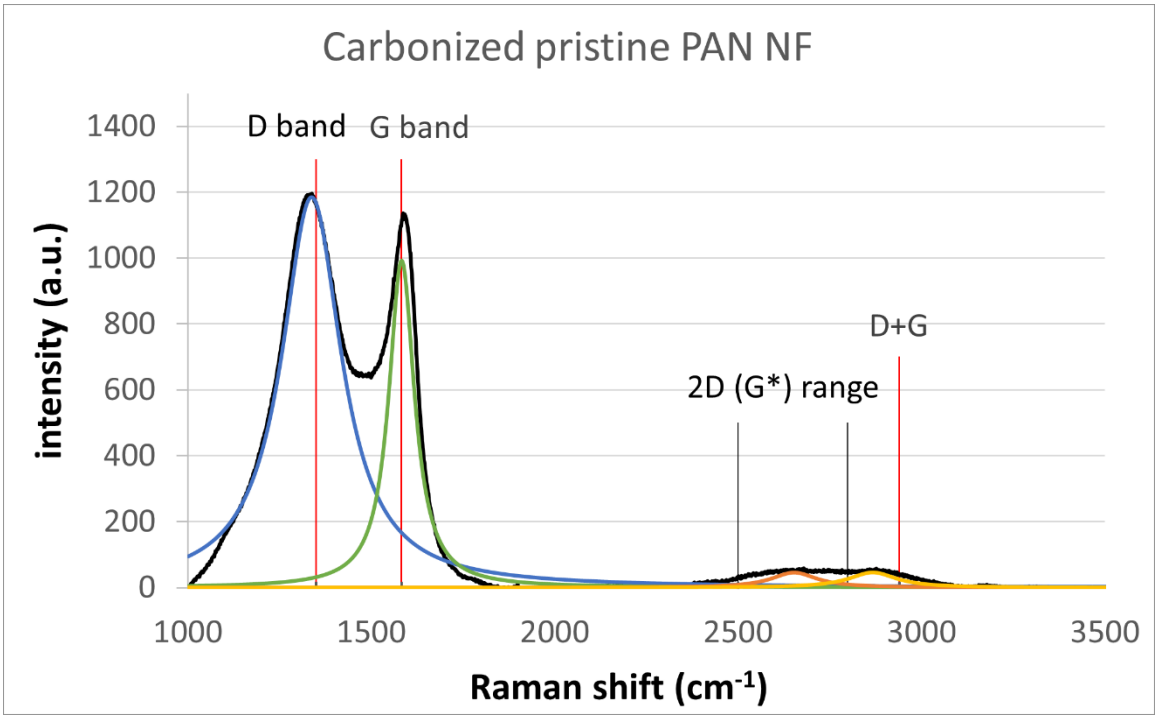

Figure D.3.2.4: Average Raman spectrum for carbonized pristine PAN NFs showing the four fitted Lorentzian curves. The vertical lines indicate points or ranges of relevant vibrational modes.

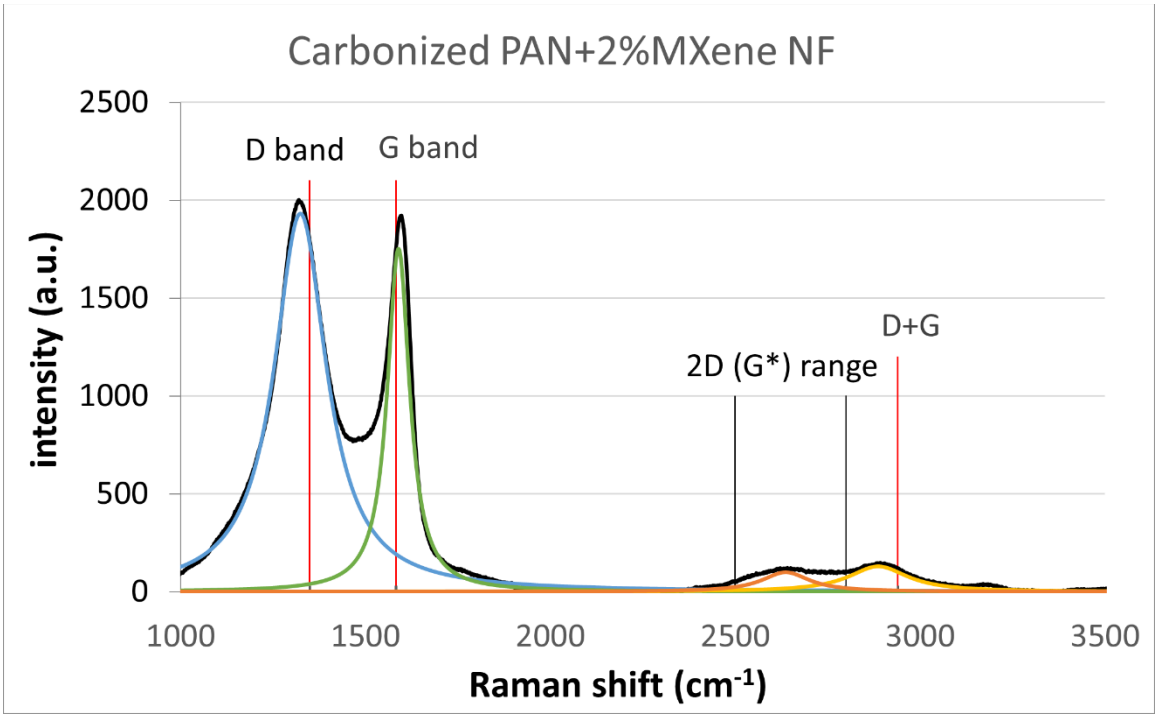

Figure D.3.2.5: Average Raman spectrum for carbonized PAN+2%MXene NFs showing the four fitted Lorentzian curves. The vertical lines indicate points or ranges of relevant vibrational modes.

The characteristics of the fitted Lorentzian curves from the pristine PAN and PAN+2%MXene nanofiber spectra indicate a significant improvement in the graphitic structure of the templated carbon nanofiber (see **Table D.3.2.1**). The spectra obtained from the MXene-templated fibers show significantly stronger D and G bands, along with a smaller R value, which signifies larger average in-plane crystal size L_a.[306] The enhanced graphitization in the templated CNFs is also indicated by their narrower G band, measured by the full width at half the maximum.[291]

Table D.3.2.1: Quantitative comparison of the Raman spectra characteristics for pristine PAN and PAN+2%MXene nanofibers.

Characteristic	Pristine PAN	PAN+2%MXenes	Percent increase (%)
I_D	1185.087	1931.747	63.005
I_G	992.4464	1752.802	76.614
$R = I_D/I_G$	1.194107	1.102091	-7.706
FWHM of G band (cm^{-1})	85.03	72.67	-14.536

D.4. CONCLUSIONS

Templating continuous carbon nanofibers with two-dimensional carbon-based nanomaterials could provide significant improvements in their graphitic structures and, in turn, their mechanical properties and electrical properties. Two potential templating materials, graphene nanoribbons and Ti_3C_2 MXenes, were added to electrospun nanofibers at low weight fractions. Subsequent optical microscopy, SEM, TEM, and Raman spectroscopy were performed to determine the distribution of the nanoparticles in the nanofibers and their effect on the graphitic structure. Although GNRs exhibit strong graphitic order, they tend to agglomerate both in solution and in the electrospun nanofibers, even at 1% weight fractions. MXenes, on the other hand, showed much more uniform dispersion throughout the nanofibers, and their effect on the graphitic structure of the CNFs was significant. With better dispersion of GNRs or higher concentrations of

MXenes, further enhancements in graphitization in continuous CNFs could be observed. This may lead to the development of nanoscale carbon fibers with similar graphitic structures to those of commercial carbon fibers, potentially revolutionizing the fiber-reinforced composites industry as we know it.

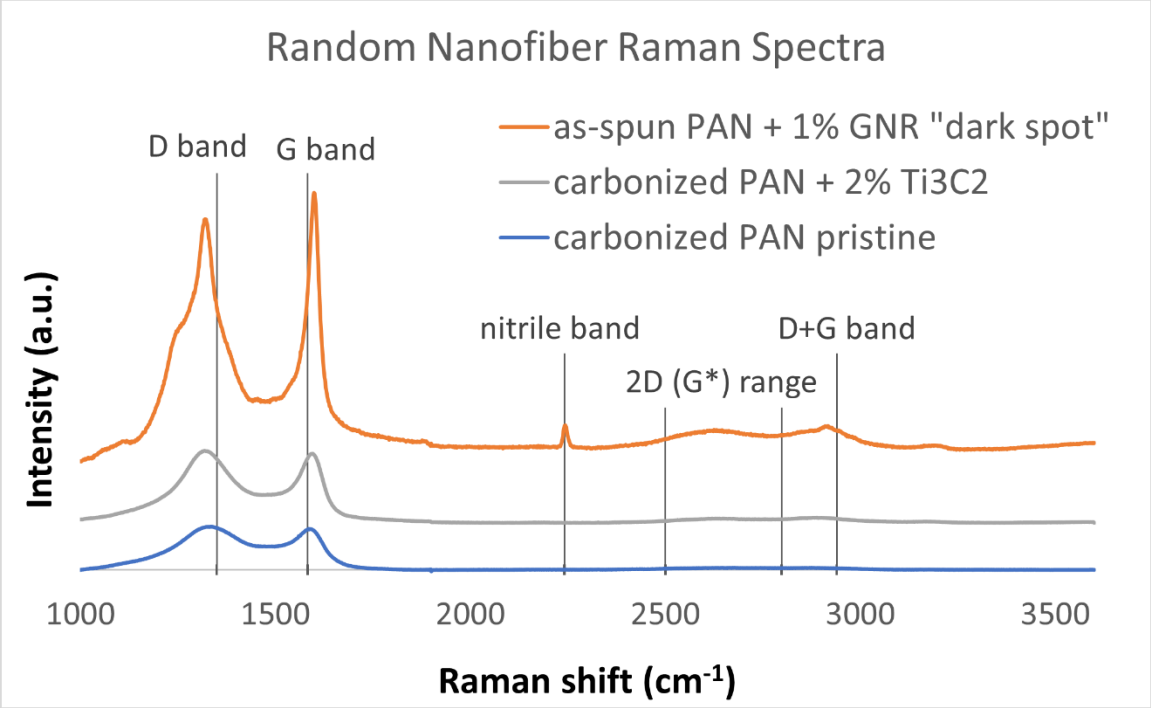

Figure D.4.1: Average Raman spectra of as-spun aligned PAN+1%GNR "dark spots," carbonized PAN+2%MXene, and carbonized pristine PAN random nanofibers.